

POLITECNICO DI TORINO



BEHAVIORAL MODELING AND DIGITAL
BASE-BAND PREDISTORTION OF RF
POWER AMPLIFIERS

PhD Thesis

Eduardo Gonçalves de Lima

Advisor:

Prof. Giovanni Ghione
Prof. Marco Pirola

January 2009

Contents

1	Introduction	1
1.1	Organization of the thesis	3
2	RF Power Amplifier behavioral modeling	5
2.1	Circuit-equivalent description of a Power Amplifier	6
2.2	Memoryless PA behavioral modeling	9
2.3	Nonlinear dynamic approaches to PA behavioral modeling	12
2.3.1	Tapped delay neural networks	13
2.3.2	Volterra series	16
2.3.3	Comparison between Volterra series and three layer perceptrons . .	23
2.4	Simplifications of the general Volterra series	24
2.4.1	Changing the initial trajectory $x_0(t)$ where the nonlinearity is expanded in a Taylor series	25
2.4.2	Block-oriented approximations	28
2.4.3	Approximation by one-dimensional functions	35
2.4.4	Pruning using physical knowledge	38
3	Low-pass equivalent PA behavioral model with feedback topology	46
3.1	Motivations for the development of the LPE feedback model	46
3.2	LPE feedback model derivation and theoretical justification	48
3.3	Digital implementation and parameter extraction	57
4	A new approach to the derivation of PA behavioral models	60
4.1	Parity definitions for complex-valued functions	61

4.2	Odd-order symmetry of RF devices under narrow-band excitations	62
4.3	Theoretical development	66
4.3.1	Memoryless polynomial models	66
4.3.2	One-dimensional polynomial approximations	71
4.3.3	Volterra series	73
4.3.4	Dynamic deviation reduction of Volterra series	75
4.4	Possible improvements in PA behavioral model performances	76
5	Simulation and experimental results for PA behavioral modeling	78
5.1	Comparative results of state-of-the-art PA behavioral models	83
5.1.1	Case study 1: one carrier WCDMA input signal	84
5.1.2	Case study 2: two carrier WCDMA input signal	99
5.2	Validation of the low-pass equivalent PA behavioral model with feedback topology described in Chapter 3	114
5.2.1	Case study 1: input-output data simulated in a known RF feedback model	114
5.2.2	Case study 2: input-output data measured in a PA with GaN based technology	115
5.3	Validation of the new approach in deriving PA behavioral models presented in Chapter 4	123
5.3.1	Case study 1: one carrier WCDMA input signal	124
5.3.2	Case study 2: two carrier WCDMA input signal	141
5.3.3	Case Study 3: a (weak) extrapolation test	159
6	Digital Base-band Predistortion of RF Power Amplifiers	164
6.1	Basic concepts in predistortion schemes	165
6.2	DPD topology selection	166
6.2.1	Inversion of static nonlinearities	171
6.2.2	Inversion of nonlinear dynamic 1D approximations	172
6.2.3	The p th-order inverses of Volterra series	174
6.3	DPD parameter identification	177
6.3.1	Direct learning algorithm	177

6.3.2	Indirect learning algorithm	178
6.4	Experimental validation	180
6.4.1	Case study 1: physically derived pruned Volterra DPD topology . .	182
6.4.2	Case study 2: DPD topologies with polynomial approximations at base-band and RF levels	192
6.4.3	Case study 3: arbitrary topology selection for the PA or for the DPD models	200
6.5	Practical implementation and adaptive strategies	209
7	Conclusions	210

Abstract

In modern wireless communication systems, the information modulates both amplitude and phase of a carrier to improve the spectral efficiency. However, due to the non constant envelope, there is a trade-off between linearity and power efficiency. Unless a linearization scheme is implemented in the transmitter chain, the power amplifier (PA) must be driven at lower input levels to satisfy stringent linearity requirements, causing the detriment of the power efficiency. Among the available linearization techniques, digital base-band predistortion (DPD) is a cost-effective choice. For both the design of communication systems and for DPD purposes, a behavioral model for the PA, having low computational complexity and relating the complex-valued envelopes at its input and output, is required. This thesis is dedicated to the behavioral modeling and DPD of RF PAs, focusing on model topology selection and parametric identification procedures.

A detailed description of the available PA behavioral models in literature is first presented. Particular attention is paid to the Volterra series, mainly to the different approaches followed to the reduction of its number of parameters. A comparative analysis, using experimental data measured in an RF laboratory, is performed. Then, a low-pass equivalent PA behavioral model of feedback topology is described. The motivations for its development, model implementation, parameter identification and experimental validation are then addressed. Later, a new approach in deriving PA behavioral models is proposed. Instead of approximating the RF system by a polynomial operator and then looking for the components that fall in the PA pass-band to get a low-pass equivalent behavioral model, a direct derivation of a low-pass equivalent PA behavioral model is proposed in which a polynomial approximation is done at base-band level. This approach justifies the use of additional odd-order terms not present when the polynomial approximation is done at RF level. The previously described models are extended to include the additional terms and the corresponding improvements in modeling accuracy by their inclusion are experimentally validated. Finally, the basic concepts of DPD and a bibliographical revision on the topic are presented, together with the experimental validation of the effectiveness of different DPD schemes in improving linearization metrics of RF PAs.

Acknowledgements

It is a pleasure to thank the people who made this thesis possible.

I wish to express my gratitude to Prof. Marco Pirola and Prof. Giovanni Ghione for their support and guidance throughout the three years I spent as a PhD student at Politecnico di Torino.

I am deeply indebted to Prof. José Carlos Pedro for his very helpful and enthusiastic guidance, encouragement and interest in my work during the period I spent at University of Aveiro, and for his invaluable suggestions for the development of this work. I would like to thank Prof. Telmo Reis Cunha from University of Aveiro for all the support and help he provided me and for the fruitful discussions we had.

I would also like to thank Hugo Miguel Teixeira and Roberto Quaglia for their assistance in the acquisition of the experimental data used in this thesis.

Finally, I would like to thank my family, in special my parents José and Sebastiana.

Chapter 1

Introduction

Modern wireless communication systems deal with a huge amount of information at very high data-rate. Among the most popular applications are the third generation (3G) cellular systems, like the wideband code division multiple access (WCDMA), and the wireless local area networks (WLANs)[1]. Due to the overcrowded spectrum, the bandwidth reserved for those systems is limited and determined by regulatory agencies. The first trade-off in the design of modern wireless communication systems is between data-rate and occupied bandwidth [2]. Spectral efficiency can be improved if the information is associated both to the amplitude and phase of the RF carrier, which motivates its adoption by the majority of the 3G cellular systems. Nevertheless, a non constant envelope implies linearity in the transmitter chain to avoid inference between adjacent channels in the receiver chain. Regulatory agencies determine stringent linearity requirements. On the other hand, for improving the power efficiency, the power amplifier (PA) present in the transmitter chain is usually driven near saturation, where its nonlinear behavior manifests at a significant level. The second trade-off in the design of such systems is between linearity and power efficiency. In this context, the PA plays a key role and its study has attracted the interest of several researchers in last years. Unless a linearization scheme is implemented, the PA must be back-off, e.g. driven at lower input levels to satisfy these linearity requirements, causing the detriment of the power efficiency and, for instance, increasing the size and weight consumed by the battery in a handset. Among the available linearization techniques, digital base-band predistortion (DPD) is a cost-effective choice. It consists in the digitally distortion of the envelope signal before the RF modulation, so

that the signal at the PA output is within the specifics of the chosen standard.

For both the design of communication systems and for linearization purposes, a model for the PA is required. In the literature, PA models with different levels of system description and computational complexity can be found. The physics-based models are the most detailed descriptions. For a complete characterization of a PA at a physical level, the partial-differential equations of diffusion and charge transport for the active device modeling, and partial-differential wave equations for the passive device modeling should be included, and the resulting model would have a very high computational complexity. An intermediate description at the circuit-equivalent level is available specifically for the solid-state power amplifiers (SSPA). It includes the Kirchoff's laws and the constitutive equations of the elementary devices. Finally, a less detailed description at system level is possible leading to the so-called behavioral or black-block models. They describe the PA based on measurements with no or little *a priori* information about its internal structure. Behavioral models are classified in literature based on the nature of the signals involved. If they relate the real-valued RF signals at the PA input and output, they are called RF or instantaneous behavioral models. Instead, if it is the relationship between the complex-valued envelope at the PA input and output being modeled, they are called envelope, base-band or low-pass equivalent behavioral models [3].

The most suited PA model for the cited applications is the low-pass equivalent behavioral model. In the computer-aided design (CAD) of communication systems, the whole system, including the transmitter chain, physical channel and receiver chain, are simulated to evaluate overall performance indicators like bit-error rate (BER), eye diagram and constellation diagram. In such system level simulations, the single devices, being the PA one example, are modeled by blocks that relate the complex-envelope information at their outputs to the complex-envelope information applied to their inputs. Even if a circuit-level model of the PA could be used in a co-simulation environment, this is a very time consuming simulation and would be justified only in the final stage of the design. A convenient choice is to use a low-pass equivalent behavioral PA model that performs the desired block operation. In DPD applications, the implementation of the inverse of the base-band characteristic of a PA is the final goal. This can be accomplished by inverting a PA low-pass equivalent model, or deriving directly a behavioral model for the DPD.

1.1 Organization of the thesis

This thesis is dedicated to the behavioral modeling and digital base-band predistortion of RF PAs. After the above introductory motivations for their study, a brief description of the topics discussed in next chapters is presented here.

Chapter 2 starts by a circuit-equivalent description of an RF PA with the aim of identifying the requirements to be satisfied by a behavioral model for an accurate description of the PA. Then, a detailed description of the available PA behavioral models in literature is presented. Emphasis is put on the Volterra-based models, specifically to the different approaches followed to the simplification of the general Volterra series aimed to overcome its main drawback: the huge number of parameters to be identified.

Chapter 3 is dedicated exclusively to a particular low-pass equivalent PA behavioral model with feedback topology, proposed in [4], in which I have participated. The motivations for the development of a such feedback model are first presented. The model derivation, starting by a PA description in a feedback topology at RF level, is then detailed. Theoretical justifications for its validity, based on nonlinear Volterra analysis, are provided. In the sequence, its digital implementation and parameter identification are discussed. Its application to DPD purposes will be addressed in Chapter 6.

Chapter 4 proposes a new approach to the derivation of PA behavioral models. Instead of approximating the RF system by a polynomial operator and then looking for the components that fall in the PA pass-band to get a low-pass equivalent behavioral model, it is proposed a direct derivation of a base-band PA behavioral model in which a polynomial approximation is done at base-band level. This procedure justifies the use of new terms not present when the polynomial approximation is done at RF level. These new terms have already being studied in literature, but erroneously addressed as even-order terms. A discussion on the possible improvements in PA behavioral modeling by the inclusion of these additional odd-order terms is presented, and the previously described models are extended to include them. Its application to DPD purposes will be addressed in Chapter 6.

Chapter 5 is dedicated to the simulation and experimental validation of the theory presented in Chapters 2, 3 and 4. First, a comparative analysis of the available PA

behavioral models that derive from polynomial approximations at RF level is done, using experimental data measured in an RF laboratory. Then, the low-pass equivalent PA behavioral with feedback topology is validated using simulated and experimental input-output data. Finally, the improvements in PA behavioral modeling by the inclusion of the additional odd-order terms, proposed and theoretically justified in Chapter 4, are proved based on experimental input-output data measured in an RF PA.

Chapter 6 addresses the digital base-band predistortion (DPD) of RF PAs. The basic concepts of DPD and a bibliographical revision on the topic are firstly presented. Emphasis is put on DPD topology selection and parameter identification. The effectiveness of different DPD schemes in improving linearization metrics of RF PAs are then experimentally investigated.

Finally, Chapter 7 summarizes the main contributions and conclusions of this thesis.

Chapter 2

RF Power Amplifier behavioral modeling

This chapter presents a detailed description of the available literature on RF PA behavioral modeling.

Following the methodology of the review article on PA behavioral modeling in [3], a simplified equivalent circuit description of an RF PA is presented, in Section 2.1, before the introduction of the different approaches to PA behavioral modeling. Its purpose is to first identify the different nonlinear dynamics that could be present in a physical PA and then, whenever possible, impose the minimum requirements for their accurate modeling. The concepts underlying the distinction between linear memory and nonlinear memory effects [3], intimately related to the physical frequency bands from where the non flatness frequency response is generated – in the PA pass-band for the linear memory effects or everywhere else for the nonlinear memory ones – are presented.

The description of PA behavioral models begins with the memoryless case in Section 2.2. It is discussed, among others, the limitations of the memoryless approximation and the nonparametric or parametric identification. Then, the two largely adopted approaches to the PA behavioral modeling including memory effects, namely neural networks and Volterra series, are individually described and compared in Section 2.3. Attention is then turned, in Section 2.4, to the Volterra-based models and four different approaches are presented to the simplification of the general Volterra series to overcome its main drawback: the large number of parameters. These approaches include the use of block-

oriented structures, one-dimensional approximations, the change in the initial trajectory $x_0(t)$ from where the nonlinearity is expanded in a Taylor series and the exploitation of physical knowledge for the Volterra model pruning.

Most of the behavioral models described in this chapter were implemented using the Matlab software from The MathWorks, Inc. to fit experimental input-output data measured in an RF PA. Their comparative performance results are reported in Chapter 5.

2.1 Circuit-equivalent description of a Power Amplifier

This section investigates the different behaviors that could be exhibited by a real RF PA. The analysis are based on the simplified PA circuit-equivalent presented in [5] and shown in Figure 2.1.

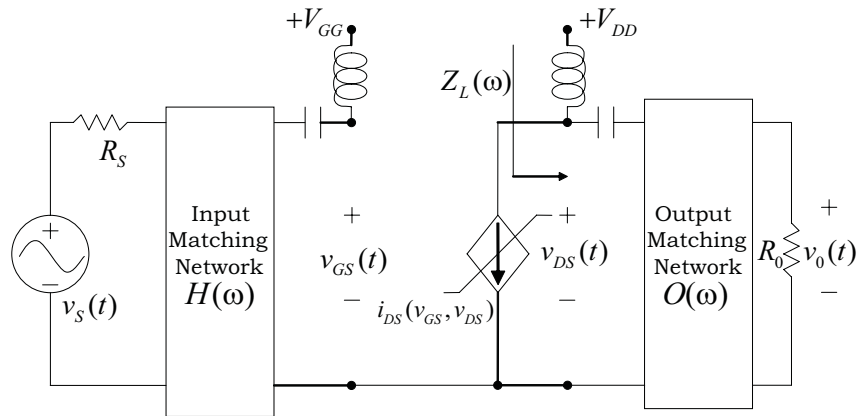


Figure 2.1: Simplified FET based PA equivalent circuit [5]

The circuit shown in Figure 2.1 can be divided into three fundamental parts: the matching networks, the active device and the bias circuitry.

The input and output frequency-selective matching networks are responsible for the PA band-pass behavior, e.g. only band-pass inputs can produce any measurable output and the only observable outputs are also band-pass signals. The output matching network is usually designed to maximize the output power delivered to the load, while the input matching network is designed to match the source and transistor's input impedances. If the bandwidth of the matching networks is wider than the one of the input signal, an

assumption usually called narrow-band input or wide-band system, only a small portion of the available matching network bandwidth is excited by the input signal and the pass-band behavior of the matching networks can be accurately represented by a flat response. On the other hand, if the bandwidth of the input signal is comparable with those of the matching networks, their pass-band behaviors must be represented by linear filters.

The active device shown in Figure 2.1 is a very simplified circuit-equivalent description of a field-effect transistor (FET). It assumes that the parasitic or extrinsic elements are negligible and that the intrinsic active device is unilateral and has a unique nonlinearity represented by a nonlinear current source dependent on two voltages: the voltage across the gate-source v_{gs} and drain-source v_{ds} terminals.

The bias-tee is used to isolate the DC sources from the RF signals and to avoid that DC current could flow into the RF source. Some dynamic effects observed in the PA pass-band output are usually attributed to the base-band frequency response of the bias circuitry [6], [7], [8] and [9]. One way of studying this phenomenon is by the observation of the AM-AM conversion at different bias conditions [10] and [11]. The AM-AM conversion shows the instantaneous output amplitude as a function of the instantaneous input amplitude. Circuit simulations in [10] show that while a static AM-AM conversion is obtained in conditions where the bias-tee approximates its ideal behavior, the AM-AM conversion shows hysteresis when the bias-tee is excited in base-band frequencies where its behavior is far away from the ideal. Additionally, in [11] circuit analysis were performed to determine the bias conditions for a clockwise or counter-clockwise time evolution of the hysteresis cycle in the AM-AM conversion.

Now, if the nonlinear voltage-controlled current source $i_{ds}(v_{gs}, v_{ds})$ in Figure 2.1 is expanded in a Taylor series around the DC operation point I_{ds} , then analytic Volterra-based circuit analysis [6] can be used for the study of the mildly nonlinear class AB operation of the PA. Particularly, the Taylor series expansion of $i_{ds}(v_{gs}, v_{ds})$ truncated to 3rd order is:

$$\begin{aligned} i_{ds} = & I_{ds} + G_{m1}v_{gs} + G_{d1}v_{ds} + G_{m2}v_{gs}^2 + G_{md}v_{gs}v_{ds} + G_{d2}v_{ds}^2 \\ & + G_{m3}v_{gs}^3 + G_{m2d}v_{gs}^2v_{ds} + G_{md2}v_{gs}v_{ds}^2 + G_{d3}v_{ds}^3 \end{aligned} \quad (2.1)$$

According to [12], under the assumption that the bandwidth of the envelope signal is

much lower than the carrier frequency, only odd-order kernels affect the pass-band behavior of a PA. Applying the harmonic input method, combined with the nonlinear current method, to the circuit in Figure 2.1, the first-order $S_1(\omega)$ and third-order $S_3(\omega_1, \omega_2, \omega_3)$ nonlinear transfer functions (NLTFs), e.g. the frequency-domain representation of the Volterra kernels, relating the input $v_s(t)$ and output $v_0(t)$ voltages, are given by [5]:

$$S_1(\omega) = -H(\omega)G_{m1}\frac{Z_L(\omega)}{D(\omega)}O(\omega) \quad (2.2)$$

where $D(\omega) = 1 + G_{d1}Z_L(\omega)$ and:

$$\begin{aligned} S_3(\omega_1, \omega_2, \omega_3) &= -H(\omega_1)H(\omega_2)H(\omega_3)\frac{Z_L(\omega_1 + \omega_2 + \omega_3)}{D(\omega_1 + \omega_2 + \omega_3)}O(\omega_1 + \omega_2 + \omega_3) \\ &\quad \times \{(G_{m3} + G_{m2d}A_v + G_{md2}A_v^2 + G_{d3}A_v^3) \\ &\quad - \frac{1}{3}(G_{md} + 2G_{d2}A_v)(G_{m2} + G_{md}A_v + G_{d2}A_v^2) \\ &\quad \times \left[\frac{Z_L(\omega_1 + \omega_2)}{D(\omega_1 + \omega_2)} + \frac{Z_L(\omega_1 + \omega_3)}{D(\omega_1 + \omega_3)} + \frac{Z_L(\omega_2 + \omega_3)}{D(\omega_2 + \omega_3)} \right] \} \end{aligned} \quad (2.3)$$

where $A_v(\omega) = -G_{m1}\frac{Z_L(\omega)}{D(\omega)}$ is assumed constant within the signal bandwidth.

The terms $H(\omega)$, $Z_L(\omega)$, $D(\omega)$ and $O(\omega)$ in (2.2), and the terms $H(\omega_1)H(\omega_2)H(\omega_3)$, $Z_L(\omega_1 + \omega_2 + \omega_3)$, $D(\omega_1 + \omega_2 + \omega_3)$ and $O(\omega_1 + \omega_2 + \omega_3)$ in (2.3) describe the so-called linear memory effects [3]. Linear memory effects, also called short-term memory, refers only to the dynamic effects whose frequency is inside the PA pass-band and the terminology linear indicates that these effects could be present even in small-signal operation. Besides the matching networks, shown in Figure 2.1, reactive elements in the active device, not shown in this simplified equivalent circuit, also contribute to the linear memory effects. Under the assumption of narrow-band input or wide-band PA system, the linear memory effects are negligible.

The terms $Z_L(\omega_1 + \omega_2)$, $D(\omega_1 + \omega_2)$, $Z_L(\omega_1 + \omega_3)$, $D(\omega_1 + \omega_3)$, $Z_L(\omega_2 + \omega_3)$ and $D(\omega_2 + \omega_3)$ in (2.3), describe the so-called nonlinear memory effects [3]. Nonlinear memory effects are due to dynamics whose frequency is in the base-band or harmonic bands and the terminology nonlinear indicates that these effects manifest themselves only in nonlinear operation regimes (see that no terms of (2.2) were included here). Nonlinear memory effects due to base-band frequencies are also called long-term memory effects. Besides the bias circuitry explained above and shown in Figure 2.1, low-frequency dispersion, trapping effects and self-heating in the active device also contribute to base-band dynamics [6], [7],

[8] and [9]. On the other hand, the output matching network can contribute to dynamics at the second harmonic band. A more insightful look at this nonlinear dynamic behavior is possible if the pass-band nature of the input signal is exploited together with a property of linear systems. In particular, linear circuits can only change the amplitude and phase of the frequencies already present, but can not create new spectral lines. So, given the PA pass-band input, a nonlinear operation must be performed to change the spectral content of the input signal to include also base-band or harmonic frequencies. Linear frequency-dependent devices can affect the amplitude and phase at these just created base-band and harmonic frequencies. However, these effects will only be observed in the PA pass-band output after the action of another nonlinearity that mixes these signals back to the pass-band [3]. Such dynamic nonlinear behavior can be represented by a cascade connection of a linear filter between two static nonlinearities [7] or by the feedback topology shown in Figure 2.2. This feedback topology was presented in [5] and its first- and third-order NLFTs were shown to be structurally equivalent to the respective NLFTs in (2.2) and (2.3), obtained for the PA simplified equivalent circuit shown in Figure 2.1.

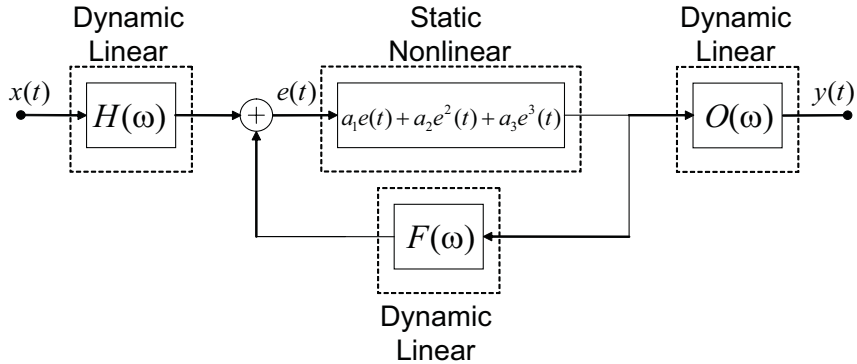


Figure 2.2: Nonlinear feedback topology of an RF PA [5]

2.2 Memoryless PA behavioral modeling

This section discusses the memoryless models used for the description of the relationship between the complex-valued envelopes at the PA input and output. Here, both the amplitude of the signal at the PA output and the phase difference between output and input signals are functions of only the instantaneous amplitude of the signal applied to the

PA input. The nonlinear functions describing the output amplitude and phase difference dependences on the instantaneous input amplitude are usually called AM-AM conversion and AM-PM conversion, respectively.

If the word memoryless is interpreted rigorously as frequency-independent, then it can be shown [13] that a memoryless nonlinear system can not affect the phase and so the experimental observation of a phase modulation at the output signal as a function of the amplitude of the input signal can not take place in memoryless systems. In fact, no physical device is really frequency-independent. However, under the assumption of narrow-band input (or equivalently, wide-band system), a PA model in which the instantaneous complex-envelope at the output depends only on the instantaneous complex-envelope at the input could be a good approximation for that PA. Good approximation if, besides the narrow-band input assumption, nonlinear memory effects are negligible. Here, as is usually done in PA behavioral modeling literature, the terminology memoryless has a less rigorous interpretation and is used to refer to these models, sometimes also called quasi-memoryless models, in which the output complex-envelope depends only on the instantaneous input complex-envelope.

The block diagram of a memoryless PA model described by the AM-AM and AM-PM conversions, called series or polar model [14], is shown in Figure 2.3.

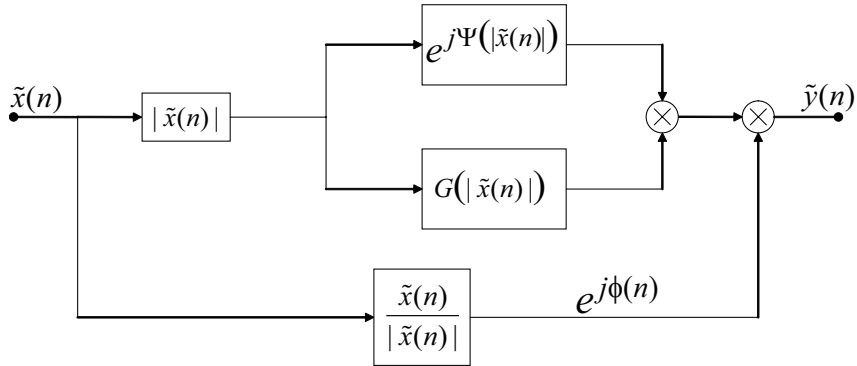


Figure 2.3: Polar representation of a memoryless PA behavioral model [14]

Using standard trigonometric identities, the equivalent parallel or quadrature model is obtained [14]. Its block diagram is shown in Figure 2.4. The relationship between the static nonlinearities of the polar model, $G(|\tilde{x}(n)|)$ and $\Psi(|\tilde{x}(n)|)$, and of the quadrature

model, $S_I(|\tilde{x}(n)|)$ and $S_Q(|\tilde{x}(n)|)$, are given by:

$$S_I(|\tilde{x}(n)|) = G(|\tilde{x}(n)|) \cos \Psi(|\tilde{x}(n)|) \quad (2.4)$$

and

$$S_Q(|\tilde{x}(n)|) = G(|\tilde{x}(n)|) \sin \Psi(|\tilde{x}(n)|) \quad (2.5)$$

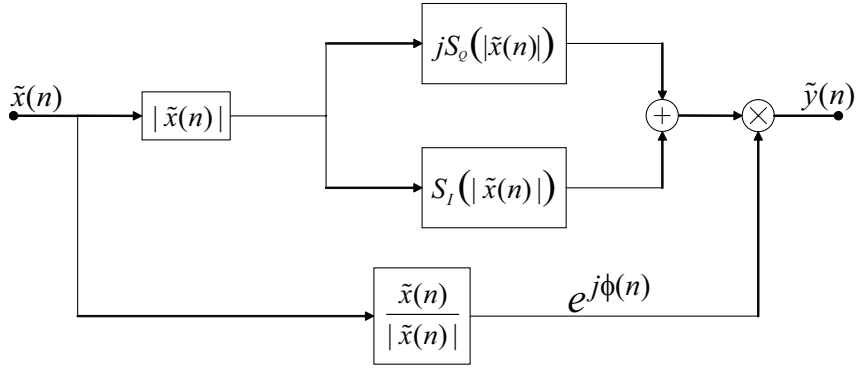


Figure 2.4: Quadrature representation of a memoryless PA behavioral model [14]

The extraction of the static nonlinearities is done traditionally by one-tone power sweep measurements using a Vector Network Analyzer (VNA) and a power meter to calibrate the power, e.g. through different measurements at constant envelope. The measured points can be directly implemented by two Look-Up-Tables (LUTs) with appropriate interpolation strategies (nonparametric model) or used to fit *a priori* chosen nonlinear parametric functions. Among these nonlinear parametric functions are the real-valued rational functions of the Saleh model [15], the real-valued Bessel functions of the first kind reported in [16] and the complex-valued polynomials largely reported in literature, for example in [3] and [17]. If the extraction is done based on one-tone root-mean square (RMS) power measurements and the signals in the intended model implementation represent instantaneous (peak) envelope voltages, then the measured power axes must be interpreted as half the square of the instantaneous envelope. In dBV units, this means that a 3 dB correction in both abscissa and ordinate are necessary.

A second possibility for the extraction of the static nonlinearities is based on a single time-domain measurement with a non constant envelope input signal, which could be as simple as a two-tone or a narrow-band complex-envelope modulated signal, using a Vector Signal Analyzer (VSA). A large set of sampled time-domain input and output

data are then used for the parameter identification of some *a priori* chosen nonlinear parametric function, using linear identification techniques, for example via Least Squares (LS). In fact, if the narrow-band input approximation is adequate, the spectral content of the input signal used for model extraction do not affect, in a considerable amount, the parameter identification and, as a consequence, the model extraction based on constant or non constant envelope measurements are expected to provide similar results.

A third possibility for model identification is also based on non constant envelope input signal, but now the measurements are time-averaged, stationary phasor responses, instead of instantaneous time-domain measurements. A two-tone power measurement using a VNA belongs to this group of measurements. For instance, if the PA is modeled by a third-order polynomial of complex-valued coefficients, then the linear complex gain can be obtained by a one-tone power measurement in small-signal operation, and the complex-coefficient scaling the third-order polynomial term is related, by a closed-form expression, to the power measured at the PA output at one of its third-order intermodulation (IM3) frequencies, $2\omega_2 - \omega_1$ or $2\omega_1 - \omega_2$, in the presence of a two-tone excitation at frequencies ω_1 and ω_2 . If the memoryless assumption is satisfied, then the measured power at the IM3 frequencies are the same.

2.3 Nonlinear dynamic approaches to PA behavioral modeling

In many cases, modern communication systems involve modulated signals whose bandwidth are wide enough so that the frequency response of the PA has to be taken into account. In such cases, the memoryless behavioral models have limited accuracy and models addressing nonlinear dynamic effects are needed.

This section addresses the nonlinear dynamic models that have been used for PA behavioral modeling. Various classes of systems are investigated in nonlinear system theory [18], including the homomorphic systems, order statistic filters, morphological filters, neural networks and polynomial filters. Among these classes of nonlinear systems, the latter two have received a particular interest by the microwave community, specially

for the behavioral modeling and digital base-band predistortion of RF PAs and, hence, are the subjects studied in here. This section is organized as follows: it starts with a description of non recursive neural networks, then presents the Volterra series approach and concludes with a comparison between these two classes of nonlinear systems.

2.3.1 Tapped delay neural networks

Artificial neural networks (ANNs) have been used to model nonlinear dynamic systems in many fields, such as biomedical, aerospace, automotive, financial, electronics and telecommunications. Although recursive ANNs, also called recurrent neural networks (RNNs), have been used to model the relationship between voltages and currents in microwave circuits [19], here only the use of non recursive neural networks, called tapped delay (or feed-forward) neural networks, is presented. Indeed, it was already shown in [20] that multilayer feed-forward neural networks are universal approximators.

Two different architectures for multi-input tapped delay neural networks (TDNNs) with one hidden layer were reported in literature for the behavioral modeling of PA: the perceptrons [21], [22] and the radial basis networks [23].

The schematic diagrams of multi-input three layer perceptron (TLP) and multi-input three layer radial basis network (TLRBN) are shown in Figures 2.5 and 2.6, respectively.

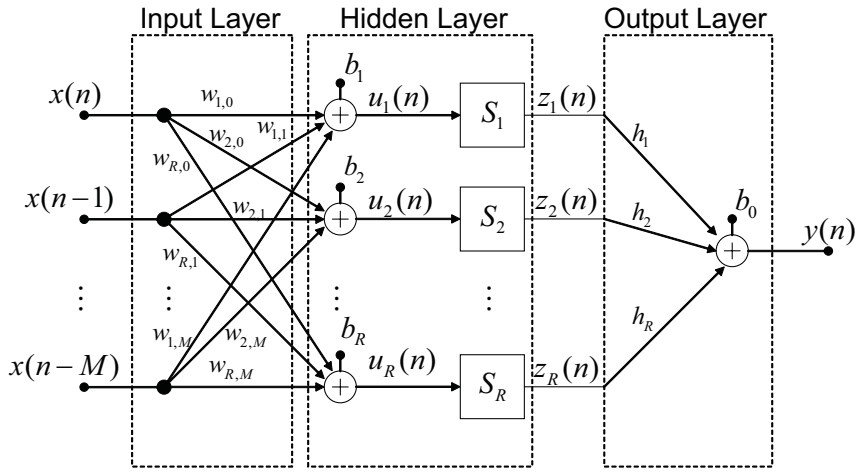


Figure 2.5: Schematic diagram of a three layer perceptron (TLP)

The difference between a perceptron and a radial basis network is in the mapping of the input signals $x(n - m)$ (for $m = 0, \dots, M$ where M is the finite memory length)

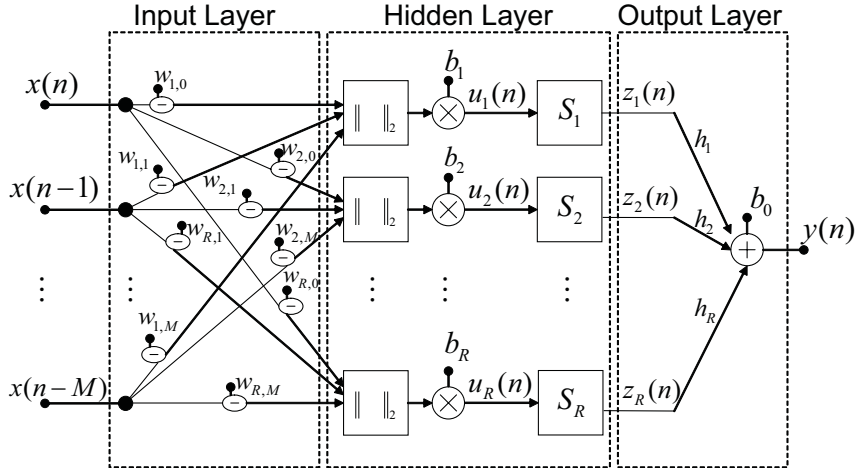


Figure 2.6: Schematic diagram of a three layer radial basis network (TLRBN)

into the one-dimensional signals $u_r(n)$ (for $r = 1, \dots, R$ where R is the number of hidden neurons) performed in the hidden layer. In the perceptron case, the one-dimensional signals $u_r(n)$ are given by the weighted sum (a linear combination) of the inputs $x(n-m)$ plus a bias:

$$u_r(n) = \sum_{m=0}^M w_{r,m}x(n-m) + b_r \quad (2.6)$$

or, in other words, (2.6) shows that in a perceptron each $u_r(n)$ signal is the convolution of the input signal with a finite impulse response $w_{r,m}$, plus a bias b_r . In the case of the radial basis network, the one-dimensional signals $u_r(n)$ are given by:

$$u_r(n) = b_r \|\bar{x} - \bar{w}_r\|_2 = b_r \sqrt{\sum_{m=0}^M [x(n-m) - w_{r,m}]^2} \quad (2.7)$$

where $\bar{x} = [x(n) \ x(n-1) \ \dots \ x(n-M)]$ and $\bar{w}_r = [w_{r,0} \ w_{r,1} \ \dots \ w_{r,M}]$.

Each unit or neuron S_r in the hidden layer in Figures 2.5 and 2.6 is represented by a one-dimensional static nonlinear function, called activation function. Different choices can be made for the activation function: sigmoidal and Gaussian functions are the traditional choices for perceptrons and radial basis networks, respectively.

A commonly used sigmoidal function is the hyperbolic tangent sigmoid function given by:

$$S_r(u_r) = \frac{2}{1 + e^{-2u_r}} - 1 \quad (2.8)$$

which is mathematically equivalent to a hyperbolic tangent function. A Gaussian function

could be:

$$S_r(u_r) = \exp -u_r^2 \quad (2.9)$$

The output layer usually has a linear transfer function. In this case, the output signal $y(n)$ is given by a linear combination of the signals $z_r(n)$ at the output of the activation functions S_r , plus a bias b_0 :

$$y(n) = \sum_{r=1}^R h_r z_r(n) + b_0 \quad (2.10)$$

The TDNN is nonlinear in its parameters, namely the weights, $w_{r,m}$ and h_r , and the bias, b_r and b_0 . In neural network terminology, the parameter extraction is called learning or training procedure. Typically, the backpropagation algorithm [24] is the training algorithm used for the TLP, while the Orthogonal Least Squares algorithm [25] is the corresponding one for the radial basis network.

Concerning low-pass equivalent PA behavioral models, the complex-valued inputs could be directly applied to a TDNN or first decomposed into their two real-valued components: the magnitude and phase for a polar representation or the in-phase and quadrature components for a rectangular representation.

In the first approach, the TDNN has complex-valued parameters and a single complex-valued output. This was the choice adopted in [21] for the behavioral modeling of a PA. The complex backpropagation algorithm [26] was used during the learning process.

Following the second approach, [22] first decomposed the complex-valued PA input signal into its real-valued in-phase I_x and quadrature Q_x components and then applied both I_x and Q_x components, together with their delayed samples, as inputs to a real-valued TLP with two outputs that estimate the in-phase I_y and quadrature Q_y components of the complex-valued signal at the PA output. Also following this second approach, in [23] only the amplitude of the envelope at the PA input, including its instantaneous and delayed values, is applied as input to a real-valued TLRBN with two outputs that estimate the amplitude and phase difference (respect to the instantaneous phase of the envelope at the PA input) of the envelope at the PA output.

As shown in [3], a TLP is equivalent to a parallel connection of cascades of a linear filter and a static nonlinearity, as shown in Figure 2.7. The static nonlinearities $f_r[v_r(n)]$ account for the bias b_r , the activation functions S_r , the weights h_r , and also the bias b_0 .

This structure is known as Parallel Wiener.

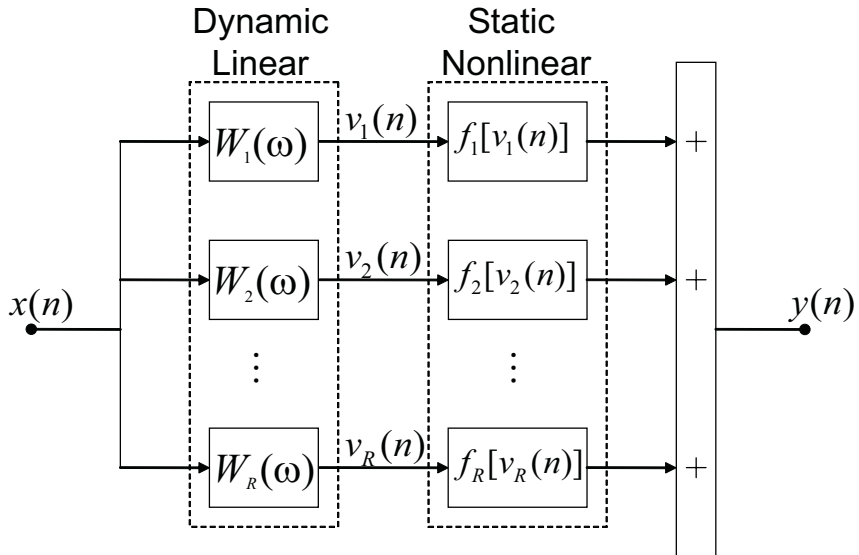


Figure 2.7: Schematic diagram of the Parallel Wiener representation of a TLP

2.3.2 Volterra series

A Volterra series is the combination of a static nonlinear system expressed in a Taylor series and a one-dimensional convolution integral representation for dynamic linear systems. The resulting multi-dimensional convolution integrals have been used in different areas of study [18], [27], [28] for the description of time-invariant, causal, nonlinear dynamic systems with fading memory [29].

A linear time-invariant (LTI) system is completely characterized by its impulse response $h(t)$, and its output $y(t)$ is expressed as the one-dimensional convolution integral of the input signal $x(t)$ with $h(t)$:

$$y(t) = \int_{-\infty}^{\infty} h(\tau)x(t - \tau)d\tau \quad (2.11)$$

If the LTI system is assumed to be causal, e.g. the output does not depend on future values of the input signal, then the lower limit in the integral in (2.11) is set to zero. Furthermore, if the system is assumed to have a finite impulse response of duration M , then the upper limit in the integral in (2.11) is truncated to M . By now, causality and finite memory length are always assumed.

On the other hand, if a nonlinear static (or memoryless) system can be expressed in a convergent Taylor series around an initial point $x_0(t)$:

$$y(t) = \sum_{p=0}^{\infty} c_p [x(t) - x_0(t)]^p \quad (2.12)$$

then the resulting power series is an optimal approximation (in a uniform sense) for that system near the initial point $x_0(t)$ where it was expanded. Concerning PA behavioral modeling, the term c_0 is always zero since the PA output is zero whenever the PA input is zero, and hence it will be omitted in the next equations. Additionally, the power series is truncated to the polynomial order P_0 .

The extension of (2.12) to the inclusion of the dynamic behavior in (2.11), around the initial trajectory (or state) $x_0(t) = 0$ for $-\infty < t < \infty$, gives the Volterra series:

$$y(t) = \sum_{p=1}^{P_0} \int_0^M \cdots \int_0^M h_p(\tau_1, \dots, \tau_p) x(t - \tau_1) \cdots x(t - \tau_p) d\tau_1 \cdots d\tau_p \quad (2.13)$$

The multi-dimensional functions $h_p(\tau_1, \dots, \tau_p)$ are called the Volterra kernels of the system and they completely characterize a nonlinear system represented by a Volterra series. Equation (2.13) is the functional formulation of the Volterra series. Another common representation is in terms of the Volterra operators $H_p[x(n)]$:

$$y(t) = \sum_{p=1}^{P_0} H_p[x(n)] \quad (2.14)$$

in which:

$$H_p[x(n)] = \int_0^M \cdots \int_0^M h_p(\tau_1, \dots, \tau_p) x(t - \tau_1) \cdots x(t - \tau_p) d\tau_1 \cdots d\tau_p \quad (2.15)$$

Since for the purposes of this thesis only discrete-time systems are concerned, by now, most of the time, the discrete-time Volterra series is used. Its constitutive equation is given by:

$$y(n) = \sum_{p=1}^{P_0} \sum_{q_1=0}^M \sum_{q_2=q_1}^M \cdots \sum_{q_p=q_{p-1}}^M h_p(q_1, q_2, \dots, q_p) \prod_{j=1}^p x(n - q_j) \quad (2.16)$$

where $x(n)$ and $y(n)$ are the input and output signals at sample time n , respectively, P_0 is the polynomial order truncation and M is the memory length. In (2.16), the assumption that the Volterra kernels, $h_p(q_1, q_2, \dots, q_p)$, are symmetric functions of their arguments was exploited. The kernel symmetry assumption does not imply any loss of generality.

For PA behavioral modeling purposes, assuming a polynomial approximation at the RF system level, (2.16) relates the RF output signal $y(n)$ to the RF input signal $x(n)$. It can be shown, following the procedure described in [12], that the low-pass equivalent representation of (2.16), describing the relationship between the complex-valued envelopes $\tilde{x}(n)$ and $\tilde{y}(n)$ at the PA input and output, respectively, is given by:

$$\begin{aligned} \tilde{y}(n) = & \sum_{p=1}^P \sum_{q_1=0}^M \sum_{q_2=q_1}^M \cdots \sum_{q_p=q_{p-1}}^M \sum_{q_{p+1}=0}^M \sum_{q_{p+2}=q_{p+1}}^M \cdots \sum_{q_{2p-1}=q_{2p-2}}^M \\ & \times \tilde{h}_{2p-1}(q_1, q_2, \dots, q_{2p-1}) \prod_{j_1=1}^p \tilde{x}(n - q_{j_1}) \prod_{j_2=p+1}^{2p-1} \tilde{x}^*(n - q_{j_2}) \end{aligned} \quad (2.17)$$

where $2P - 1 = P_0$ is the polynomial order truncation and $\tilde{h}_{2p-1}(q_1, q_2, \dots, q_{2p-1})$ are the low-pass equivalent Volterra kernels, a generalization of the low-pass equivalent impulse response from linear systems to nonlinear systems. Kernel symmetry was assumed in (2.17).

The discrete-time Volterra series has the important property of being linear in its parameters $\tilde{h}_{2p-1}(q_1, q_2, \dots, q_{2p-1})$. Therefore, using time-domain complex-envelope input-output data, a direct extraction of the low-pass equivalent Volterra kernels can be done using linear system identification techniques, via batch algorithms like the least-squares (LS) and minimum mean-square error (MMSE), or via adaptive algorithms like least-mean-square (LMS) and recursive least-squares (RLS)[18].

Unfortunately, the number of parameters in (2.17) increases very fast with the polynomial order $2P - 1$ and the memory length M . This is sometimes called *curse of dimensionality* for polynomial approximation in system identification language [30]. Specifically, the number of complex-valued parameters in (2.17) as a function of M and P is given by [17]:

$$\sum_{p=0}^{P-1} \frac{[(M+p)!]^2 (M+p+1)}{(M!)^2 (p!)^2 (p+1)} \quad (2.18)$$

The direct extraction of the Volterra parameters using linear identification techniques could not be satisfactory when the number of parameters is large. For instance, the two traditional methods for batch linear identification, namely the MMSE and LS described in [18], require the inversion of an auto-correlation matrix. Even with a moderate number of parameters, the inversion of the auto-correlation matrix could be a numerically ill-

conditioned problem and, in that case, the parameter identification is inaccurate. A commonly way to measure this numerical disturb is by the conditioning number of a matrix, defined in 2-norm as the ratio of the highest to the smallest singular value of a matrix. If high powers of the input signal are involved, specially when distinct input samples are used, very small quantities are originated in the auto-correlation matrix and its conditioning number will be very high. In practice, the auto-correlation matrix is not inverted and more robust algorithms, like QR-decomposition or pseudo-inverses [31], are used to perform the MMSE and LS algorithms. These robust algorithms improve considerable the accuracy of the numerical solution, and work well for rank deficient matrices (when a column is linearly dependent on the others). Problems that are nearly, but not exactly, rank deficient are more difficult to handle, and this is the situation of a Volterra series identification with a huge number of parameters. Again, poor estimations can be obtained and small changes in the data can lead to large changes in the computed parameter estimation.

To circumvent the problems associate with the direct parameter identification, a Gram-Schmidt orthogonalization procedure can be used to construct an orthogonal basis for the Volterra operators $H_p[x(n)]$. Since the $H_p[x(n)]$ operators depend on the input signal $x(n)$, the resulting basis is orthogonal only for the input signal used in its construction. Wiener [32] was the first to apply these concepts in nonlinear system theory. He constructed a set of functionals $G_p[x(n)]$, known as Wiener G-functionals, that are orthogonal to each other when the input signal $x(n)$ is an independent, identically distributed (IID) Gaussian sequence with zero mean value and finite variance. In other words, the Wiener G-functionals satisfy:

$$E \{G_l[x(n)]G_p[x(n)]\} = 0 \quad (2.19)$$

for $l \neq p$, if the input is the one just cited. $E(\cdot)$ denotes the mean value or the ensemble average (for ergodic processes, the ensemble average is equal to the time average). The output $y(n)$ is then represented by the sum of the G-functionals:

$$y(n) = \sum_{p=1}^{P_0} G_p[x(n)] \quad (2.20)$$

The orthogonality implies that the p th-order G-functional $G_p[x(n)]$ can be estimated independently of the G-functionals of other orders and also that, if higher order terms

are added later, the already estimated functionals do not change. The extraction can be done in the time-domain using the cross-correlation formula of Lee and Schetzen [27]. The relationship between the Wiener kernels and Volterra kernels can be found in [33].

A Volterra PA behavioral model whose kernels are orthogonal to an input signal composed by a large set of different realizations of a multi-sine with constant amplitude but randomized phases was presented in [34] and [35]. The particular chosen input, when applied to a nonlinear system with fading memory and the realization set is large enough, gives the same output as the one obtained when the applied input is a white Gaussian [36]. Furthermore, it is easier to generate and process multi-sine in an RF laboratory than a white Gaussian noise, since sinusoids or combination of sinusoids are the largely used signals in microwave instrumentations. The identification procedure exploited the orthogonalization property and each particular kernel was obtained individually and independently of the others, using higher order cross-correlations between the input and output signals, as well as higher order auto-correlations of the input signal.

Looking back to the Wiener kernels, it can be shown that they are non-explosive [27], e.g. they satisfy the inequality:

$$\int_0^M \cdots \int_0^M k_p^2(\tau_1, \dots, \tau_p) d\tau_1 \cdots d\tau_p < \infty \quad (2.21)$$

This is sufficient to expand each Wiener kernel $k_p(t - \tau_1, \dots, \tau_p)$ (for $p = 1, \dots, P_0$) in a set of p -dimensional orthogonal functions. For the particular choice of the orthonormal set of Laguerre functions and for a white Gaussian input signal, in [27] it is presented an experimental setup for the identification of the Wiener kernels. The orthogonality is exploited and the Wiener kernels of each order are obtained individually and independently of the others. The Laguerre functions are chosen because they are easily synthesizable by a tandem connection of all-pass electrical circuits.

In [37], the Volterra kernels are first expanded in an orthogonal set of L discrete-time Laguerre functions and then the discrete-time Volterra series given by (2.17) is rewritten with the truncation factor L instead of the memory length M . All the parameters are then extracted at once using least squares (LS). Since the orthogonality is not exploited in the parameter extraction, this identification strategy is not limited to a particular input signal. There, the discrete-time Laguerre functions are chosen because the number of functions

in the basis (given by L) necessary to accurately model the system is usually lower than the system memory length M . More specifically, the discrete-time Laguerre functions are orthogonalized exponentials, e.g. the dynamic behavior is modeled by transfer functions that decay exponentially to zero at a controllable rate, while in the Volterra series the dynamic behavior is modeled by FIR filters of memory length M , e.g. by Dirac impulse transfer functions. Since in stable systems the impulse response decays exponentially, it is expected that a more parsimonious model could be obtained if the system impulse response would be represented by a sum of decaying exponentials, specially if the *a priori* fixed real-valued poles of the discrete-time Laguerre filters are close to the dominant poles of the system being modeled. A low-pass equivalent PA behavioral model using a Volterra series with the kernels expanded in a set of discrete-time Laguerre functions was presented in [38]. The parameter extraction was based on LS and the input signal was an amplitude and phase modulated signal satisfying a wireless communications standard. If the same approach is followed, but now discrete-time Kautz filters are used, the *a priori* fixed poles could also be complex-valued and a better performance is observed if the system being modeled presents oscillatory behavior, e.g. has complex-valued dominant poles. A low-pass equivalent PA behavioral model using a Volterra series with the kernels expanded in a set of discrete-time Kautz functions was presented in [39]. Again, all the parameters were extracted at once by LS.

Moreover, in [40] it is proved that a parallel connection of branches composed by a cascade of a linear filter followed by a static nonlinearity, sometimes called Parallel Wiener structure and shown in Figure 2.8, can be an arbitrarily close approximation, in the mean-square sense, to a Volterra series. An iterative strategy was proposed in [28] for the extraction of parallel cascade structures. The parameters are extracted in a number of steps larger than or equal to the number of parallel branches and, at each step, the parameters of just one parallel branch are identified. More specifically, the parameters in the cascade connection of the first branch are extracted to best fit the measured input-output data, for example using the iterative procedure presented in [41] that will be detailed later in Subsection 2.4.2 and whose flowchart is shown in Figure 2.14. Then, a residual error signal is calculated as the difference between the measured output and the output of the extracted cascade branch. The procedure is repeated for the second branch,

but now to best fit the residual error signal, and after that a new residual signal error is calculated. The procedure continues until the *a priori* maximum number of branches are extracted or the residual error signal is inferior to a threshold. A PA PW structure, extracted using this iterative procedure, was reported in [42].

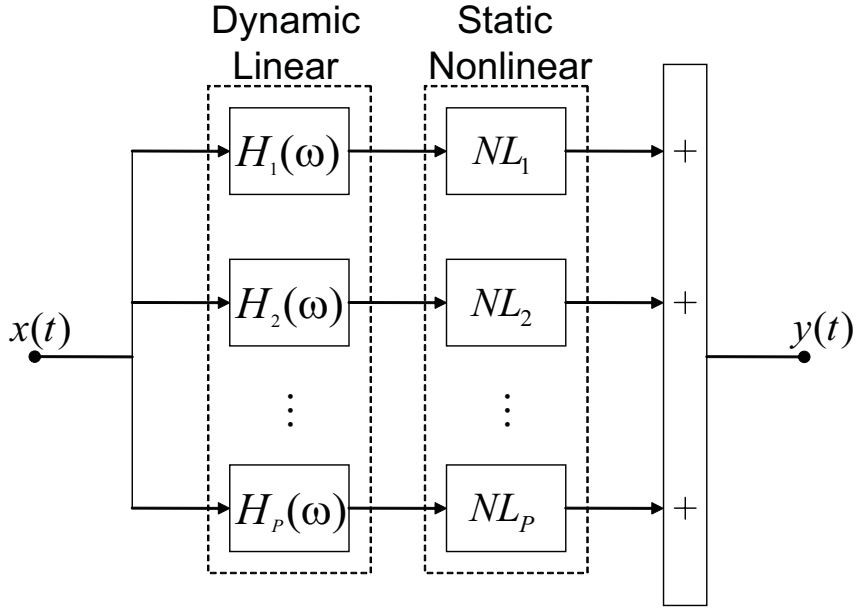


Figure 2.8: Parallel Wiener structure

However, even if the numerical problems suffered by the identification process in the presence of a large number of parameters can be addressed by orthogonal approaches, hardware limitations in practical applications obviate the use of Volterra series with high polynomial order and long memory length due to the very stringent time interval to process the information in a real-time implementation of the model. By now, (2.17) will be referred to as the general Volterra series and its use is limited to mild nonlinear systems. To circumvent this limitation of the general Volterra series, in this way allowing to the modeling of nonlinear systems with higher polynomial order and longer memory length, the adopted strategy, in a considerable large number of published works concerning PA behavioral modeling, consist in the performance of simplifications of the general Volterra series. Section 2.4 is dedicated exclusively to a detailed discussion on the different approaches to the reduction of the number of parameters in a general Volterra series.

2.3.3 Comparison between Volterra series and three layer perceptrons

As already pointed out, both the TLP and the discrete-time Volterra series can be represented by parallel connections of a linear filter in cascade with a static nonlinearity, the so-called Parallel Wiener structure. Now, two situations in which they are equivalent are presented [43]. In the first scenario, the TLP shown in Figure 2.5 has polynomial activation functions given by:

$$S_r(v_r) = \alpha_{r,1}v_r + \alpha_{r,2}v_r^2 + \cdots + \alpha_{r,P}v_r^P \quad (2.22)$$

where $v_r(n) = u_r(n) - b_r$, P is the polynomial order truncation and the coefficients $\alpha_{r,p}$ are distinct for each activation function. If the bias, b_r and b_0 , are all set to zero, the resulting TLP is equivalent to a Volterra series with the NLTFS, $H_p(\omega_1, \dots, \omega_p)$, given by:

$$H_p(\omega_1, \dots, \omega_p) = \sum_{r=1}^R h_r \alpha_{r,p} W_r(\omega_1) \cdots W_r(\omega_p) \quad (2.23)$$

where $W_r(\omega)$ (for $r = 1, \dots, R$) are linear filters whose discrete-time finite impulse response is given by $w_{r,m}$ (for $m = 0, \dots, M$).

In the second scenario, a TLP with non polynomial but analytic (e.g. the function is equal to its Taylor series in the vicinity from where it was expanded) activation functions also have an equivalent Volterra series representation if the activation functions are expanded in a Taylor series around the bias b_r :

$$S_r(v_r) = \sum_{p=1}^P \alpha_{r,p}(b_r) v_r^p \quad (2.24)$$

where $v_r(n) = u_r(n) - b_r$, P is the polynomial order truncation and the dependence of the Taylor coefficients $\alpha_{r,p}(b_r)$ on the bias b_r are explicitly shown. The corresponding NLTFS, e.g. the frequency-domain representation of the Volterra kernels, are given by:

$$H_p(\omega_1, \dots, \omega_p) = \sum_{r=1}^R h_r \alpha_{r,p}(b_r) W_r(\omega_1) \cdots W_r(\omega_p) \quad (2.25)$$

The neural networks have the advantage of being parsimonious in the number of parameters and can be the choice for the modeling of PA in strong nonlinear regimes.

Additionally, neural networks have more general validity than polynomial approximators, specially in extrapolation contexts where the polynomials are known by their catastrophic behaviors. However, they are nonlinear in their parameters and so they require nonlinear identification strategies, which demand for complex computational algorithms that could be trapped in local optimum solutions depending on the initial conditions. Finally, they constitute a pure black-box approach, in the sense that no physical knowledge could be exploited, for instance, to help in the selection of the number of hidden neurons.

On the other hand, Volterra series are linear in their parameters but the linear parameter identification that guarantees analytically the optimum solution could be inaccurate due to numerical ill-conditioning in the presence of a large number of parameters. Nevertheless, analytical nonlinear Volterra analysis, like the harmonic input method and the nonlinear current method [6], are available and can be used to guide in the reduction of the number of parameters in a general Volterra series.

At this point, it is convenient to introduce the general Wiener model presented in [27] and shown in Figure 2.9. In Figure 2.9, Section A is a single-input multi-output linear system that contains all the modeled memory, Section B is a multi-input multi-output memoryless nonlinear system modeled by R M -dimensional functions $f_r[z_1(t), \dots, z_M(t)]$, and Section C is a multi-input single-output amplification and summation system. Both the three-layer perceptron and the Volterra series are particular instances of this general Wiener model. In the TLP, the multi-dimensional functions $f_r[z_1(t), \dots, z_M(t)]$ are constrained to be one-dimensional functions that share a common shape. In the Volterra series, the multi-dimensional functions $f_r[z_1(t), \dots, z_M(t)]$ are constrained to be analytic functions in the sense that, for the specific choice of the amplification coefficients a_r (for $r = 1, \dots, R$), they should be expandable in a convergent multi-dimensional power series of the signals $z_m(t)$, for $m = 1, \dots, M$.

2.4 Simplifications of the general Volterra series

Four different approaches are presented in this section to the reduction of the number of parameters in the general Volterra series. These approaches are: the change in the initial trajectory $x_0(t)$ from where the nonlinearity is expanded in a Taylor series, the

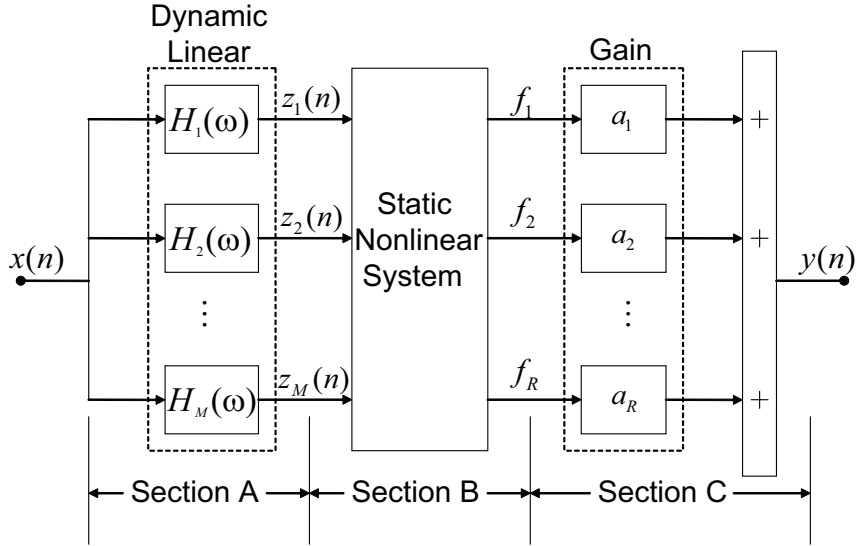


Figure 2.9: General Wiener model of a nonlinear system [27]

use of block-oriented structures, one-dimensional approximations and the exploitation of physical knowledge for the Volterra model pruning.

2.4.1 Changing the initial trajectory $x_0(t)$ where the nonlinearity is expanded in a Taylor series

The general Volterra series, presented in Subsection 2.3.2, is the combination of a static nonlinear system expanded in a Taylor series around an initial trajectory or state $x_0(t) = 0$ for $-\infty < t < \infty$, and the one-dimensional convolution integral representation for dynamic linear systems. A modified Volterra series can be obtained by choosing another initial trajectory or state $x_0(t)$. The initial trajectory could be a unique choice and then represented by a single waveform defined over the whole time domain $-\infty < t < \infty$ (the Volterra series is an example). In this case, the kernels are time-invariant functions. On the other hand, the initial trajectory could be a time dependent choice, e.g. at each time instant a different waveform, defined over a time interval equals to the memory span of the system being modeled, is chosen as the initial trajectory. In the latter case, time-varying kernels are obtained. A convenient choice belonging to the latter case is to use a constant trajectory over the memory span of the system, but with a time-varying DC value equals to the nonlinear memoryless operation point [44], [45]. This particular choice

was exploited in [46], [47], [48] and [49] to reduce the computational complexity (in terms of number of parameters) of the general Volterra series. The study of their approaches is the scope of this subsection.

Firstly, the dynamic deviation function $e(t, \tau_i)$ is defined as:

$$e(t, \tau_i) = x(t - \tau_i) - x(t) \quad (2.26)$$

Then, substituting (2.26) in the general Volterra series given by (2.13), it is obtained:

$$\begin{aligned} y(t) &= F_{DC}[x(t)] + \sum_{n=1}^{\infty} \int_{-\infty}^{\infty} \cdots \int_{-\infty}^{\infty} \\ &\quad \times g_n[x(t), \tau_1, \dots, \tau_n] e(t, \tau_1) \cdots e(t, \tau_n) d\tau_1 \cdots d\tau_n \end{aligned} \quad (2.27)$$

The function F_{DC} and the time-varying kernels $g_n[x(t), \tau_1, \dots, \tau_n]$, sometimes called dynamic Volterra kernels, are related to the kernels $h_n(\tau_1, \dots, \tau_n)$ of the general Volterra series by [45]:

$$F_{DC}[x(t)] = \sum_{n=1}^{\infty} x^n(t) \int_{-\infty}^{\infty} \cdots \int_{-\infty}^{\infty} h_n(\tau_1, \dots, \tau_n) d\tau_1 \cdots d\tau_n \quad (2.28)$$

and:

$$\begin{aligned} g_n[x(t), \tau_1, \dots, \tau_n] &= \sum_{k=n}^{\infty} x^{(k-n)}(t) \binom{k}{n} \int_{-\infty}^{\infty} \cdots \int_{-\infty}^{\infty} \\ &\quad \times h_k(\tau_1, \dots, \tau_k) d\tau_{n+1} \cdots d\tau_k \end{aligned} \quad (2.29)$$

In the modified series (2.27), the nonlinear static effects are separated from the dynamic ones, while in the general Volterra series these effects are mixed together. Under the assumption of short-term memory, e.g. the PA has a memory span much shorter than the reciprocal of the maximum frequency of the complex-valued envelope applied to the PA input, the product of two dynamic deviations $e(t, \tau_i)$, for each τ_i in the memory span of the PA, are small enough to be considered almost negligible in practice. In this case, a first-order truncation of (2.27) provides an accurate description of the input-output relationship of a PA. The low-pass equivalent representation of the first-order truncation of (2.27) was used in [46], [47] and [48] to characterize the relationship between the

complex-valued envelopes at the PA input and output:

$$\begin{aligned}\tilde{y}(t) &= \tilde{F}_{DC}[\tilde{x}(t), \tilde{x}^*(t)] \\ &+ \int_0^{\tau_{max}} \tilde{g}_1[\tilde{x}(t), \tilde{x}^*(t), \tau] [\tilde{x}(t - \tau) - \tilde{x}(t)] d\tau \\ &+ \int_0^{\tau_{max}} \tilde{g}_2[\tilde{x}(t), \tilde{x}^*(t), \tau] [\tilde{x}^*(t - \tau) - \tilde{x}^*(t)] d\tau\end{aligned}\quad (2.30)$$

where $\tilde{x}(t)$ and $\tilde{y}(t)$ are the complex-envelope at the PA input and output, respectively, $\tilde{g}_1[\tilde{x}(t), \tilde{x}^*(t), \tau]$ and $\tilde{g}_2[\tilde{x}(t), \tilde{x}^*(t), \tau]$ are low-pass equivalent dynamic Volterra kernels, and $(*)$ denotes the complex conjugate operator.

Concerning the identification of the parameters of (2.30), in [46] and [47] one-tone (at frequency f_c) power sweep measurements were used for the static nonlinearity $\tilde{F}_{DC}(\cdot)$ extraction, while the extraction of the parameters $\tilde{g}_1(\cdot)$ and $\tilde{g}_2(\cdot)$ were based on two-tone measurements: a tone with large amplitude at the frequency f_c and another tone with small amplitude at a frequency shifted by Ω respect to f_c . These extraction procedures are valid only for the first-order approximation.

In [49], the same reasoning was applied to the discrete-time Volterra series and, after some mathematical manipulations and regrouping of coefficients, it was presented a new representation for the Volterra series:

$$\begin{aligned}y(n) &= \sum_{p=1}^{P_0} h_p(0, \dots, 0) x^p(n) + \sum_{p=1}^P \sum_{r=1}^{\min(p, R)} x^{p-r}(n) \\ &\times \sum_{q_1=1}^M \dots \sum_{q_r=q_{r-1}}^M h_r(0, \dots, 0, q_1, \dots, q_r) \prod_{j=1}^r x(n - q_j)\end{aligned}\quad (2.31)$$

where $R \leq P_0$ and $\min(p, R)$ indicates the minimum between p and R .

The low-pass equivalent of (2.31), after considering kernel symmetry is:

$$\begin{aligned}\tilde{y}(n) &= \sum_{p=1}^P \tilde{h}_{2p-1}(0, \dots, 0) \tilde{x}^{p+1}(n) [\tilde{x}^*(n)]^p \\ &+ \sum_{p=1}^P \sum_{r=1}^{\min\{2p-1, R\}} \sum_{c=0}^{\min\{2p-1-r, p-1\}} [\tilde{x}(n)]^{2p-1-r-c} [\tilde{x}^*(n)]^c \sum_{q_1=1}^M \dots \sum_{q_r=q_{r-1}}^M \\ &\times \tilde{h}_{2p-1}(0, \dots, 0, q_1, \dots, q_r) \prod_{j=1}^{r-(p-1-c)} \tilde{x}(n - q_{j1}) \prod_{j=2=1}^{\min\{r, p-1-c\}} \tilde{x}^*(n - q_{j2})\end{aligned}\quad (2.32)$$

where the polynomial order is $P_0 = 2P - 1$.

The new Volterra series representations in (2.31) and (2.32) have three truncation factors. Besides the polynomial truncation order P and memory length M already present in the general Volterra series, (2.31) and (2.32) also include the dynamic truncation order R . This truncation factor R indicates the maximum number of delayed inputs that could be involved in the input products. Choosing a dynamic truncation order R lower than the polynomial truncation order P constitutes an effective approach to the reduction of the number of parameters in the general Volterra series.

The new Volterra series representation in (2.32) retains the important property of being linear in its parameters $\tilde{h}_{2p-1}(.)$. So, using time-domain complex-valued envelope input-output data, for *a priori* set of truncation factors, the parameters $\tilde{h}_{2p-1}(.)$ can be extracted using linear system identification techniques.

The equation (2.32) was implemented in the Matlab software to assess the effectiveness of such a parameter reduction approach. The results will be presented in Chapter 5 and (2.32) will be designated by dynamic deviation (DD) model.

2.4.2 Block-oriented approximations

This subsection is dedicated to those models whose topologies involve the cascade connection of only two kinds of elementary subsystems: the dynamic linear and the static nonlinear subsystems. Sometimes called block-oriented or block-structured models, they have been used to model nonlinear dynamic systems in different areas of study [14], [50], [28], [51]. Specific designations for some particular arrangements of the subsystems in the cascade connection are frequently adopted. As examples, the cascade connection of a linear filter followed by a static nonlinearity, shown in Figure 2.10, is known as a Wiener structure, while the cascade connection in which the subsystem disposition is reversed, e.g. a static nonlinearity followed by a linear filter, shown in Figure 2.11, is called a Hammerstein structure. The cascade connection of a static nonlinearity between two linear filters, shown in Figure 2.12, combines the two previously cited topologies and so is referred to as a Wiener-Hammerstein or three-box structure.

In the case where the static nonlinearities are approximated by polynomials, these cascade connections reduce to particular instances of the general Volterra series and the

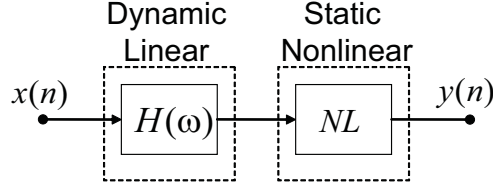


Figure 2.10: Wiener structure

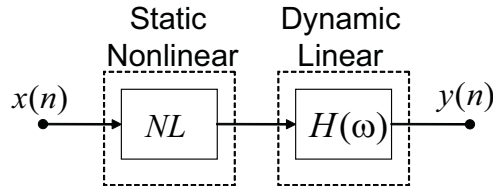


Figure 2.11: Hammerstein structure

a priori choice of one such topology constitutes another approach to the reduction of the number of parameters in the general Volterra series. In PA behavioral modeling literature, examples of PA Wiener models are reported in [52], [53], [54] and [55], PA Hammerstein models in [17], and PA Wiener-Hammerstein models in [56] and [57]. Nowadays versions of commercial computer-aided designs (CADs) dedicated to RF circuit and system designs include block-oriented structures in their libraries with automate model parameter extraction that could be used for PA behavioral modeling.

If the nonlinearity is approximated by a polynomial at the RF level, then the discrete-time low-pass equivalent constitutive equation of a Wiener structure is:

$$\tilde{y}(n) = \sum_{p=1}^P \tilde{b}_{2p-1} \left| \sum_{m=0}^M \tilde{h}(m) \tilde{x}(n-m) \right|^{2p-2} \sum_{m=0}^M \tilde{h}(m) \tilde{x}(n-m) \quad (2.33)$$

and the discrete-time low-pass equivalent constitutive equation of a Hammerstein structure is:

$$\tilde{y}(n) = \sum_{m=0}^M \tilde{h}(m) \sum_{p=1}^P \tilde{b}_{2p-1} |\tilde{x}(n-m)|^{2p-2} \tilde{x}(n-m) \quad (2.34)$$

where, both in (2.33) and (2.34), $\tilde{x}(n)$ and $\tilde{y}(n)$ are the complex-envelope signal at the PA input and output, respectively, $\tilde{h}(m)$ are complex-valued parameters describing the finite impulse response (of length M) of the linear filter and \tilde{b}_{2p-1} are complex-valued coefficients of the polynomial nonlinearity of order $2P - 1$. In the Wiener cascade, the Volterra kernels are separable kernels, e.g. $\tilde{h}_{2p-1}(\tau_1, \dots, \tau_{2p-1}) = \tilde{h}_1(\tau_1) \cdots \tilde{h}_1(\tau_{2p-1})$,

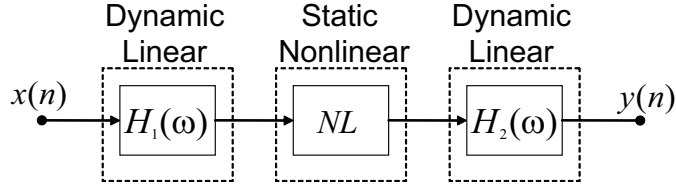


Figure 2.12: Wiener-Hammerstein structure

while in the Hammerstein cascade, only the diagonal kernels have non null values, e.g. $\tilde{h}_{2p-1}(\tau_1, \dots, \tau_{2p-1}) \neq 0$ only if $\tau_1 = \tau_2 = \dots = \tau_{2p-1}$.

The discrete-time low-pass equivalent constitutive equation of a three-box Wiener-Hammerstein structure where the nonlinearity is approximated by a polynomial at the RF level is:

$$\tilde{y}(n) = \sum_{m_2=0}^M \tilde{h}_2(m_2) \sum_{p=1}^P \tilde{b}_{2p-1} \left| \sum_{m_1=0}^M \tilde{h}_1(m_1) \tilde{x}(n - m_1 - m_2) \right|^{2p-2} \sum_{m_1=0}^M \tilde{h}_1(m_1) \tilde{x}(n - m_1 - m_2) \quad (2.35)$$

where $\tilde{h}_1(m_1)$ and $\tilde{h}_2(m_2)$ are complex-valued parameters describing the finite impulse responses, both of length M , of the linear filter before and after the nonlinearity, respectively.

A common property of the block-oriented models is that they are models nonlinear in their parameters. For instance, (2.33) and (2.34) depend nonlinearly on their parameters $\tilde{h}(m)$ and \tilde{b}_{2p-1} , and (2.35) depends nonlinearly on its parameters $\tilde{h}_1(m_1)$, $\tilde{h}_2(m_2)$ and \tilde{b}_{2p-1} . Furthermore, the realization of a system by a block-oriented model is not unique. Indeed, one can multiply the output of the first block in the cascade connection and divide the input of the following block by the same nonzero scalar, and the resulting realization will have the same input-output relation as the original realization, once the linear gain of the overall cascade connection is given by the product of the linear gains of the individual elementary subsystems.

An optimal estimation for the parameters $\tilde{h}(m)$ and \tilde{b}_{2p-1} could be achieved by a nonlinear optimization, for example, the minimization of a quadratic criteria function of the error signal defined as the difference between the desired and modeled output signals. Commonly used nonlinear optimization algorithms include the Levenberg-Marquardt and the Gauss-Newton methods [58]. Nonlinear optimization methods do not guarantee a convergence to a global minimum solution and can be trapped in local minima. Specifically

in the cases of Wiener and Hammerstein structures, a much more efficient optimization is achieved if the algorithm optimizes only the linear filter coefficients $\tilde{h}(m)$, or equivalently, only the nonlinearity coefficients \tilde{b}_{2p-1} , since when the parameters of one block are known, (2.33) and (2.34) become linear in the remaining parameters. This reduced nonlinear optimization is known as separable least squares (SLS) [59], [60]. The SLS algorithm was applied to the parameter extraction of a Hammerstein structure for the modeling of a nonlinear biological system in [51].

Sub-optimal estimations for the block-oriented parameters have also been reported in literature. The designation sub-optimal refers here to the extraction procedures in which the parameters of each elementary block, or of a subsystem of the whole structure, are extracted separately and independently of the others. The solution obtained is not guaranteed to be an optimal one, neither global nor local, to the complete topology being used. However, it represents an optimal solution for the subsystem of the whole structure whose parameters were extracted at the same time. In the particular case of Wiener and Hammerstein models, the obtained solution is equal to the global one if there is no model topology error and the data used for each elementary block extraction only excites the respective behavior (linear dynamic or nonlinear static).

The PA Wiener models in [52], [53] and [54] are extracted using a two steps procedure based on one-tone power sweep and small-signal Vector Network analyzer (VNA) measurements, and are examples of sub-optimal parameter estimations. In this procedure, the static nonlinearity is extracted to fit a one-tone power sweep input-output data at a single frequency, usually at the center frequency of the band of interest, since in this measurement the dynamic effects are absent. The linear filter is then extracted based on small-signal measurements, e.g. phasor voltages are measured at the PA output for a low power one-tone input signal at varying frequency around the center one, since in this measurement the nonlinear effects are absent. This identification procedure is applicable to both Wiener and Hammerstein models, and the particular PA topology is not involved in the computations. It gives a solution that is closer to the optimal one as the real PA topology is closer to the *a priori* selected topology, e.g. the extraction procedure is strongly affected by model topology mismatches. The Ptolemy environment of the Advanced Design System (ADS), version 2006 Update 1, from Agilent Technologies

[61], given a circuit-level simulation, automates the extraction of a two-box model using this procedure. The topology selection, between Wiener and Hammerstein, is left as an user's parameter. This is called there as automatic verification modeling (AVM) or Fast Cosimulation. Furthermore, the estimated parameters following this procedure were also used in [52] and [53] as the initial conditions in a nonlinear optimization for a Wiener PA parameter extraction. There, the linear dynamic block was implemented by an infinite impulse response (IIR) filter and the model was denoted by nonlinear ARMA model.

Concerning the Wiener-Hammerstein or three-box PA model, sub-optimal parameter extraction based on one-tone power sweep measurements at different frequencies have also been presented [14]. The procedure assumes that the AM-AM and AM-PM curves obtained at different frequencies have the same shape, but differ from each other by distinct horizontal and vertical shifts of this single characteristic [56]. Hence, a linear filter placed before the nonlinearity causes the horizontal shifts while a linear filter placed after the nonlinearity models the vertical shifts. The nonlinearity is considered to be the measured one-tone power sweep AM-AM and AM-PM conversions at the frequency f_c , usually the center frequency of the band of interest. Then, for each of the other measured frequencies f_m , the following two costs functions, $E_{mag}(f_m)$ and $E_{phase}(f_m)$, are minimized with respect to the input filter gain $G_{in}(f_m)$ and phase $\Phi_{in}(f_m)$, as well as to the output filter gain $G_{out}(f_m)$ and phase $\Phi_{out}(f_m)$:

$$E_{mag}(f_m) = \sum_{P_{in}=P_{in}^{min}}^{P_{in}^{max}} \{P_{out}(P_{in}, f_m) - P_0[P_{in} + G_{in}(f_m)] - G_{out}(f_m)\}^2 \quad (2.36)$$

$$E_{phase}(f_m) = \sum_{P_{in}=P_{in}^{min}}^{P_{in}^{max}} \{\Phi_{out}(P_{in}, f_m) - \Phi_0[P_{in} + G_{in}(f_m)] - \xi(f_m)\}^2 \quad (2.37)$$

where $\xi(f_m) = \Phi_{out}(f_m) + \Phi_{in}(f_m)$. The $P_0(P_{in}) \equiv P_{out}(P_{in}, f_c)$ and $\Phi_0(P_{in}) \equiv \Phi_{out}(P_{in}, f_c)$ are the extracted nonlinearities, e. g. the measured AM-AM and AM-PM conversions at the frequency f_c , respectively. The summation is over the measured power sweep which ranges from P_{in}^{min} to P_{in}^{max} and all power and gain values are in dB. In (2.37), there is a degree of freedom in the choice of the filter phases, since only the sum of their phases affects the cost function $E_{phase}(f_m)$. The optimized values for the gain and phase of the filters at the frequencies f_m are then used to design either infinite impulse response (IIR) or

finite impulse response (FIR) filters. The system level design component Virtual System Simulator (VSS) of the Applied Wave Research (AWR) Design Environment suite, version 7.05 [62] includes a three-box nonlinear model in its library. From a user point-of-view, the library model either reads a file containing the one-tone power sweep measurements at different frequencies or performs one-tone Harmonic Balance (HB) power sweep simulations at different frequencies in a circuit-equivalent schematic, then automatically extracts a three-box model using the above procedure, and finally allows to the implementation of the extracted three-box model in a system level simulation using FIR or IIR filters. Furthermore, in [57] another suboptimal parameter identification for a three-box structure is presented. It uses the two steps procedure described above for the Wiener cascade and uses spectral analysis for the extraction of the filter after the nonlinearity, called the optimal-filter.

Additional examples of sub-optimal parameter identification for block-oriented models, whose parameter extraction were based on one-tone power sweep measurements at different frequencies, include the extension of memoryless quadrature PA models with non polynomial nonlinearities to account for memory effects by the use of frequency-dependent parameters. Indeed, using rational nonlinearities and two frequency-dependent parameters, in [15] a three-box Wiener-Hammerstein structure for both the in-phase and quadrature paths were obtained. Additionally, in [16] the linear combination, based on frequency-dependent coefficients, of N Bessel functions of the first-kind resulted in a parallel connection of Hammerstein cascade branches for both the in-phase and quadrature paths. The latter topology is usually called Parallel Hammerstein structure.

These sub-optimal extraction based on one-tone measurements at different frequencies can not model the PA nonlinear memory effects due to base-band effects [3]. In fact, each one-tone input signal of frequency f excites the PA dynamics at the frequencies $f_{out} = i \times f$, $i = 0, 1, \dots, n$. So, repeating this measurement at different frequencies will not excite any dynamic behavior of the PA at base-band frequencies.

Now, the attention is turned to sub-optimal procedures for Wiener and Hammerstein parameter extraction that are based on time-domain input-output data, reported in [41] and [50]. Instead of performing a nonlinear optimization, it is proposed an iterative algorithm in which three linear parameter identifications are performed at each iteration.

The flowchart of the algorithm for the Hammerstein and Wiener structures are shown in Figure 2.13 and Figure 2.14, respectively. The initial condition for the algorithms is to consider absent the first block in the cascade connection. The measured time-domain input $x(t)$ and output $y(t)$ signals are first used to extract the inverse of the linear filter, using linear cross-correlation techniques in the Hammerstein case, or the inverse of the polynomial nonlinearity using linear least-squares (LS) in the Wiener case. Then, the measured output signal $y(t)$ is processed by the respective extracted inverse to obtain the intermediate signal $z(t)$ between the two blocks in the cascade connection. After that, the measured input signal $x(t)$ and the calculated intermediate signal $z(t)$ are used for the extraction of the coefficients of the polynomial nonlinearity $p(.)$ by linear LS in the Hammerstein case, or to extract the linear filter impulse response $h(.)$ by linear cross-correlation techniques in the Wiener case. The input signal is now processed by the just extracted first block in the cascade connection to get an updated approximation for the intermediate signal $z(t)$, which will then be used for the extraction of the second block in the cascade connection using again linear identification techniques. The model output $y_m(t)$ is then estimated and compared with the measured output $y(t)$. The process is repeated again, starting from the extraction of the inversion blocks, but now with the intermediate signal $z(t)$ fixed to the last calculated approximation. If the mean-square error E_N between the estimated and measured output signals at iteration N does not decrease with respect to the previously calculated error E_{N-1} at iteration $N - 1$, then the extracted parameters in iteration N are taken as the optimum ones. The application of this iterative procedure requires, in the case of the Hammerstein structure, that the linear filter be of minimum phase so that it has a stable inverse and, in the case of the Wiener structure, that the nonlinearity be invertible, e.g. be a one-to-one mapping in the range of interest. Despite the convergence of this iterative algorithm is not guaranteed, as shown by the counter-example in [63], it represents a computationally efficient extraction procedure that was shown to work well in biomedical engineering applications [64].

In [41], the initial condition for the iterative algorithm was to consider, in both Wiener and Hammerstein cases, absent the first block in the cascade connection. However, concerning PA behavioral modeling, the nonlinear effects dominate over the dynamic ones. A faster convergence of the iterative algorithm is achieved if the initial condition is to

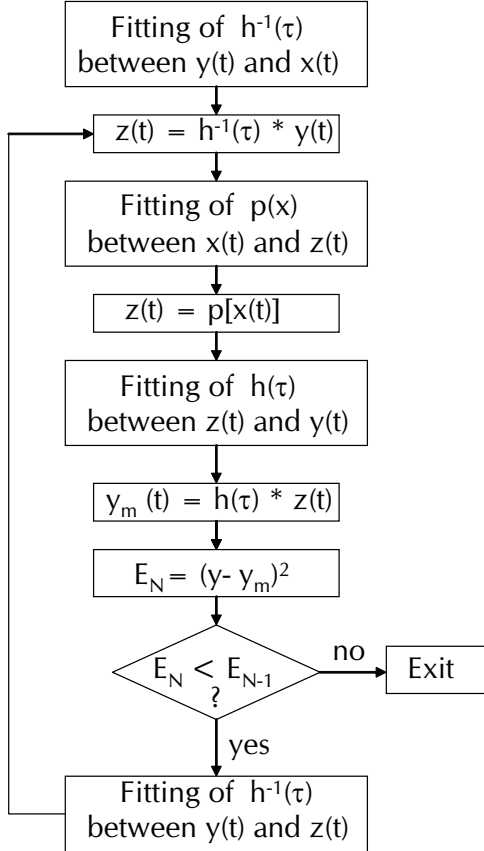


Figure 2.13: Flowchart of the iterative algorithm for the parameter extraction of a Hammerstein structure. (*) denotes the convolution operator.

consider the linear filter absent, in both Wiener and Hammerstein cases, since it results in an initial solution closer to the optimum.

2.4.3 Approximation by one-dimensional functions

This subsection addresses the behavioral models that describe the relationship between the complex-envelopes at the PA input and output by means of a summation of one-dimensional nonlinear functions. Using the same terminology as in [3], those models are classified as 1D approximations of a general multi-dimensional nonlinear function. For illustration of the concept, given the nonlinear multi-dimensional function $f [x(n), x(n - 1), \dots, x(n - M)]$ and:

$$y(n) = f [x(n), x(n - 1), \dots, x(n - M)] \quad (2.38)$$

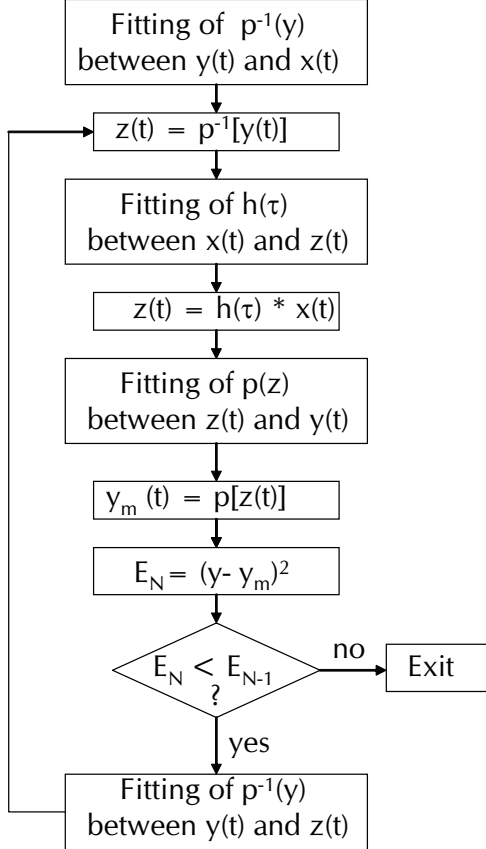


Figure 2.14: Flowchart of the iterative algorithm for the parameter extraction of a Wiener structure. (*) denotes the convolution operator.

where $x(n)$ and $y(n)$ are the real-valued RF signals at the PA input and output, respectively, and M is the memory length, the 1D approximation models considered here perform:

$$y(n) = \sum_{m=0}^M g_m [x(n - M)] \quad (2.39)$$

where $g_m [x(n - M)]$, for $m = 0, \dots, M$ are one-dimensional nonlinear functions.

As already seen, if the nonlinear multi-dimensional function $f(.)$ in (2.38) is expanded in a Taylor series around the initial vector $x_0 = [0, \dots, 0]$, equation (2.38) reduces to the general discrete-time Volterra series in (2.16).

Now, if each nonlinear one-dimensional function $g_m [x(n - M)]$, for $m = 0, \dots, M$ in (2.39) is expanded in a Taylor series around the initial point $x_0 = 0$, and then truncated to the polynomial order P_0 , (2.39) reduces to the memory polynomial (MP) model presented

in [65]:

$$y(n) = \sum_{p=1}^{P_0} \sum_{m=0}^M a_{pm} x^p(n-m) \quad (2.40)$$

where a_{pm} are real-valued coefficients, P_0 and M are the polynomial order truncation and the memory length, respectively.

The low-pass equivalent representation of (2.40) is given by:

$$\tilde{y}(n) = \sum_{p=1}^P \sum_{m=0}^M \tilde{b}_{2p-1,m} |\tilde{x}(n-m)|^{2p-2} \tilde{x}(n-m) \quad (2.41)$$

where $\tilde{x}(n)$ and $\tilde{y}(n)$ are the complex-envelope at the PA input and output, respectively, $\tilde{b}_{2p-1,m}$ are complex-valued coefficients and the polynomial order truncation is $P_0 = 2P-1$.

Even if no physical justification has been given for the validity of such 1D approximation, the memory polynomial model has been widely used for the behavioral modeling of RF PAs [65], [66], [67], [68]. Use of 1D approximations for PA behavioral modeling, but employing non-polynomial nonlinearities has also been reported. Examples of the latter case include the nonlinear impulse response model reported in [69] and [70], and also the model presented in [16].

The MP model can be viewed as particular cases of the more general Parallel Hammerstein and Parallel Wiener topologies. In the first case, as shown in Figure 2.15, the memoryless nonlinearities are simple monomials of a specific polynomial order [3] and then the signals of different nonlinear orders are subject to distinct linear filtering actions. In the second case, as shown in Figure 2.16, each linear filter is implemented by just a simple delay and then a distinct polynomial nonlinearity, containing one or more nonlinear terms, is applied to the different delayed signals.

The model presented in [16] can also be viewed as a particular Parallel Hammerstein topology, in which each memoryless nonlinearity, represented by Bessel functions of the first kind, are multiplied by frequency dependent complex-gains.

The MP model inherits the linearity in the parameters property from the general Volterra series, since it is just a brutal truncation of such general series, in which all the cross products between distinct delayed versions of the input are simple not taken into account. Again, linear system identification techniques, together with time-domain base-band input-output data, can be used for the extraction of the MP parameters $\tilde{b}_{2p-1,m}$.

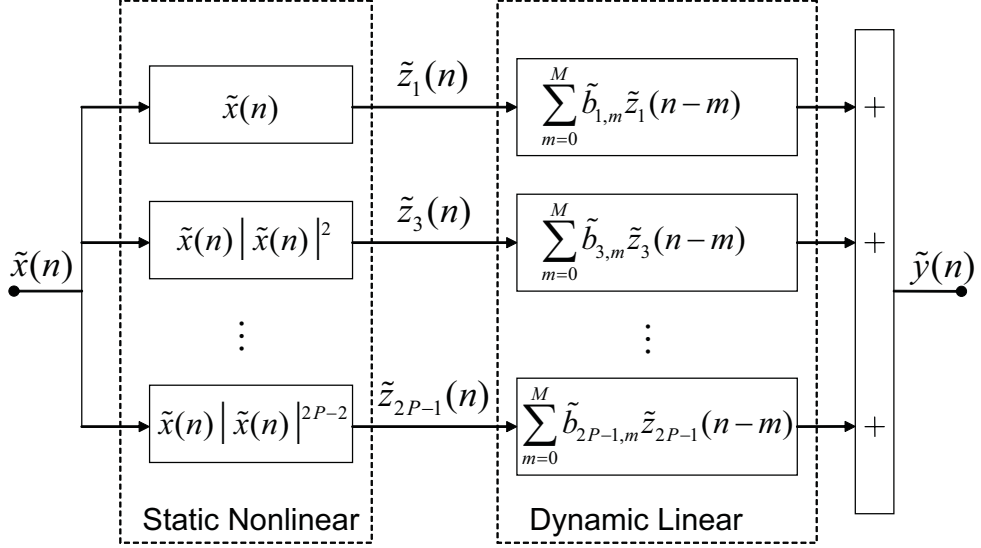


Figure 2.15: Block diagram of the Parallel Hammerstein interpretation of the MP

Concerning the cited 1D approximation models using non polynomial nonlinearities, the model in [16] uses one-tone power sweep measurements for the parameter extraction, and so, as explained earlier, it can not model the PA nonlinear dynamic behavior due to base-band frequencies. Additionally, the nonlinear impulse response models in [69] and [70] were extracted based on time-domain input-output envelope measurements in a PA driven by a modulated unit step function.

As a final remark, Parallel Hammerstein structures using finite-impulse response (FIR) filters are 1D approximations independently of the particular expressions for the static nonlinearities.

2.4.4 Pruning using physical knowledge

This subsection describes the models that use physical informations about the origins of the dynamic and nonlinear effects observed in a real PA to simplify, in terms of number of parameters, the general Volterra series. These physical informations, specially the base-band dynamic influence on the PA pass-band output, are incorporated into the behavioral models either empirically in [9] and [71], or more formally by the Volterra analysis of a circuit-equivalent representation of the PA in [72] and [73].

In [9], the physically identified sources of nonlinear dynamic behaviors in a PA are directly measured as static functions of the input power. Examples of such sources, here

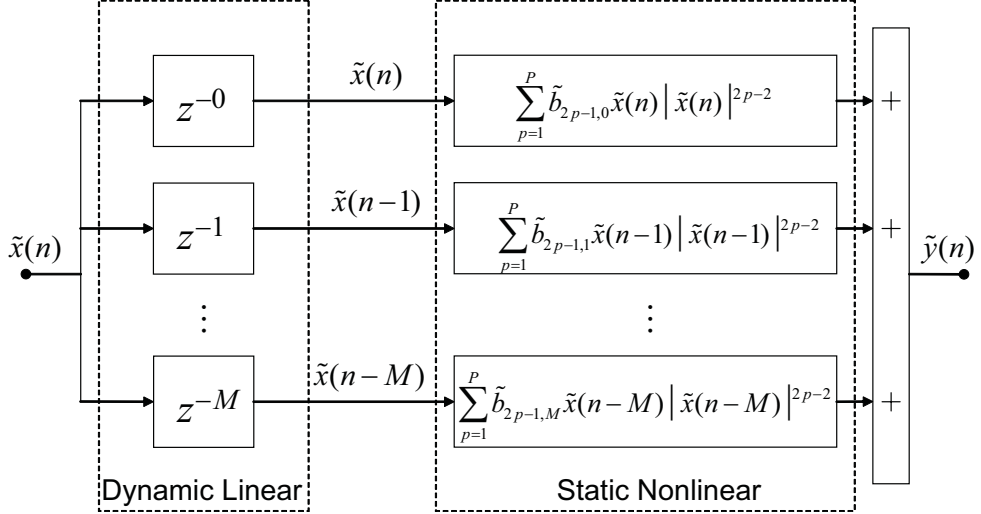


Figure 2.16: Block diagram of the Parallel Wiener interpretation of the MP

denoted by $\tilde{S}(n)$, include the power dissipated in the transistor and the current drawn from the drain (collector) power supply. These sources, identified and measured, excite the dynamics of the active device self-heating and bias circuitry, respectively. Their effects, denoted by the variable $\tilde{Z}(n)$, are the variation of the instantaneous temperature in the first case, and the variation of the drain (collector) power supply in the second case. The thermal self-heating and bias network dynamic behaviors are represented by *a priori* known linear equivalent circuits with frequency response $\tilde{H}_z(\omega)$.

The memoryless PA behavioral model represented by the AM-AM and AM-PM conversions is then extended to take into account these nonlinear dynamic effects. This is done by letting the gain $G(\cdot)$ and phase $\Psi(\cdot)$ characteristics dependent also on the variable $\tilde{Z}(n)$, besides the already present dependence on the instantaneous amplitude of the input envelope $|\tilde{x}(n)|$. Figure 2.17 shows the block diagram of a PA modeled by these bi-dimensional gain $G\left[|\tilde{x}(n)|, \tilde{Z}(n)\right]$ and phase $\Psi\left[|\tilde{x}(n)|, \tilde{Z}(n)\right]$ characteristics, designated as the augmented behavioral characterization (ABC) model in [9]. In Figure 2.17, $\tilde{y}(n)$ is the complex-envelope at the PA output when an arbitrary band-limited signal with complex envelope $\tilde{x}(n) = |\tilde{x}(n)| \exp^{j\phi(n)}$ is applied to the PA input.

The dependence of the gain $G(\cdot)$ and phase $\Psi(\cdot)$ on the additional variable $\tilde{Z}(n)$ is obtained by one-tone power sweep measurements at several temperatures or drain power supply voltages. Bi-dimensional look-up-tables (LUTs) are used to implement the

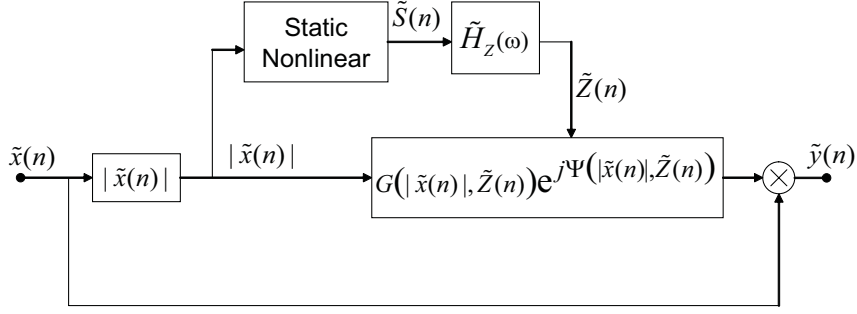


Figure 2.17: Block diagram of the Augmented Behavioral Model proposed in [9]

measured behaviors.

The accuracy of the proposed model is strongly dependent on the *a priori* known circuit-equivalent models. Additionally, the interpolation in the bi-dimensional LUTs should be carefully addressed.

Following this work but employing an approach more black-box oriented, in [74] it was assumed that neither the gain and phase dependence on $\tilde{Z}(n)$ nor the $\tilde{Z}(n)$ dependence on the instantaneous input power could be directly measured, but only derived from input-output time-domain measurements. The relationship between the input and output PA voltages is given by:

$$\tilde{y}(n) = G \left[|\tilde{x}(n)|, \tilde{Z}(n) \right] \tilde{x}(n) \quad (2.42)$$

where $\tilde{x}(n) = |\tilde{x}(n)| \exp^{j\Phi(n)}$ is the complex-envelope signal applied to the PA input at sample time n , $\tilde{y}(n)$ is the complex-envelope measured at the PA output at sample time n and $G(\cdot)$ is a bi-dimensional operator. If the operator $G(\cdot)$ contains complex-valued parameters, it models both the AM-AM and AM-PM conversions. However, if only real parameters are used, then just the AM-AM conversion is modeled.

In the model derivation, the operator $G(\cdot)$ was first expanded in a Taylor series around the steady-state value $\tilde{Z}_\infty(|\tilde{x}(n)|)$ and then truncated to first order. Furthermore, the dependence of $\tilde{Z}(n)$ on the input power was modeled by a linear time-invariant system. As a result, the operator $G(\cdot)$ was approximated by:

$$G \left[|\tilde{x}(n)|, \tilde{Z}(n) \right] \approx G_0 [| \tilde{x}(n) |] [1 + h_z(n) * |\tilde{x}(n)|] \quad (2.43)$$

where $G_0 [| \tilde{x}(n) |]$ is the steady-state operation point, $h_z(n)$ represents a linear impulse response and (*) denotes the convolution operator.

The simplified operator $G(\cdot)$ in (2.43) can be seen as the sum of two contributions: the first is a static nonlinearity and the second is the product of a dynamic linear system by the same static nonlinearity, as is shown in Figure 2.18. The signal applied to both contributions is the amplitude $|\tilde{x}(n)|$ of the complex-envelope signal.

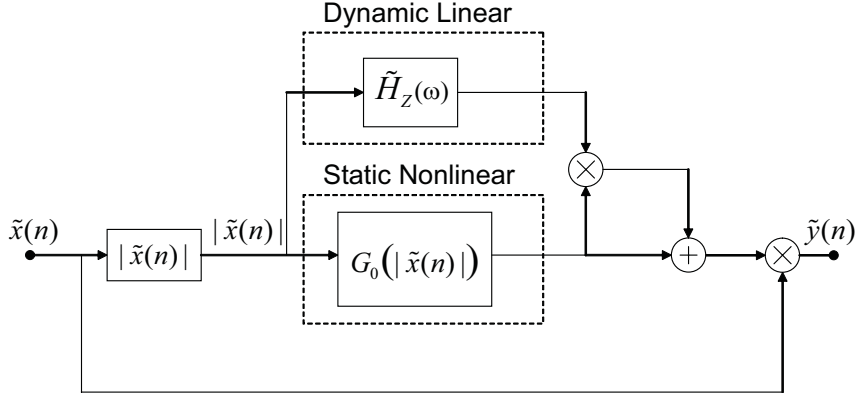


Figure 2.18: Block diagram of the PA Behavioral Model proposed in [74]

The model extraction was performed in two steps. First, the nonlinearity $G_0[|\tilde{x}(n)|]$ was extracted based on measurements under quasi-static conditions. More specifically, when the PA was driven by a modulated ramp signal with a small slope to minimize the memory effects. The filter response was then extracted based on pulsed RF signals with different initial and final power levels within the range of the extracted nonlinearity $G_0[|\tilde{x}(n)|]$.

In [72], another approach was followed to the derivation of a PA behavioral model. Starting from the RF feedback representation of the PA, presented in [5] and shown in Figure 2.2, of recognized validity and supported by physical analysis on the circuit-equivalent PA model shown in Figure 2.1, the respective feed-forward Volterra kernels up to third-order were determined using the harmonic input method [6]. Assuming that the PA has a flat frequency response at the fundamental zone, it was shown that they can be synthesized by the block diagram shown in Figure 2.19. Additionally, the time-domain kernel expressions were presented and the null elements were identified. Also, the nonlinear transfer functions, e.g. the multidimensional Fourier transform of the Volterra kernels were reported and the third-order nonlinear transfer function was shown to be given by a summation of unidimensional functions.

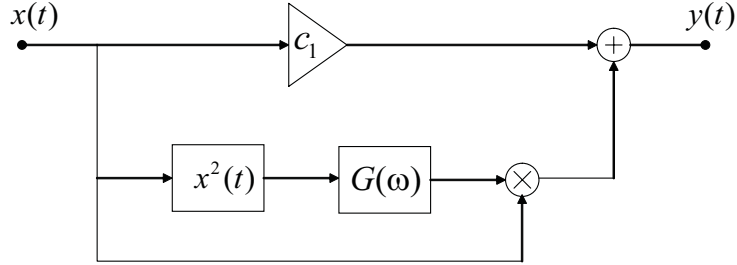


Figure 2.19: 3^{rd} order RF feed-forward model

For the identification of the model parameters, a small-signal one-tone measurement was used for the extraction of the PA constant gain and linear phase. The remaining parameters were extracted based on two-tone, at frequencies ω_1 and ω_2 , measurements. Closed-form expressions relating the power measured at the PA output at its third-order intermodulation (IM3) frequencies, $2\omega_2 - \omega_1$ and $2\omega_1 - \omega_2$, to the model parameters were presented.

In [71], a third-order PA behavioral model is proposed to correctly characterize the IM3 distortion observed in a PA. Considering that different sources contribute to the same observable phenomenon, like the IM3, it presents a model, called multi-slice, in which each source is separately modeled by a slice (or branch). Then, the single slices are added to get the output, as shown in Figure 2.20 for the particular case of two slices.

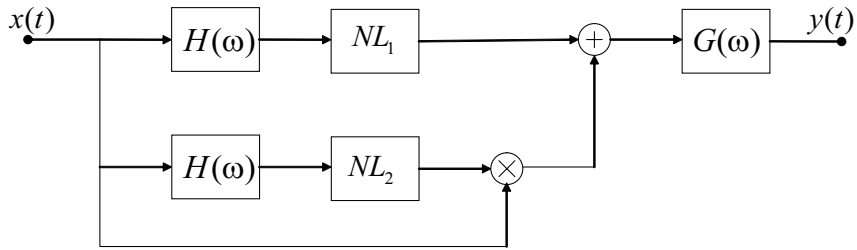


Figure 2.20: 3^{rd} order RF multi-slice model

The structure with two slices shown in Figure 2.20 is not classified as a block-oriented structure because it includes a multiplier in the second slice. It has a topology very similar to the one presented in [72] and shown here in Figure 2.19. The major difference is an inversion in the order of the linear filter and the static nonlinearity prior to the multiplier in the second slice. In fact, as explained in [71], the first slice accounts for the contribution of the dynamic and nonlinear effects physically present at the fundamental

band to the third-order Volterra kernel. This means that the first slice is memoryless if the PA frequency response at fundamental band is assumed flat. On the other hand, the second slice captures the contribution of the second-order dynamic and nonlinear effects, physically originated at base-band or second harmonic frequencies, to the third-order Volterra kernel. Based on this reasoning, it should be more intuitive to put the nonlinearity NL_2 in the second slice before the filter $H(\omega)$, as done in [72], since in this case the NL_2 first translates the band-pass input signal to the base-band, then the non flat base-band frequency response of $H(\omega)$ affects the signal and, finally, the multiplier translates the signal back to the fundamental band. A more recent work from the authors actually has implemented that change [75].

The extraction of the parameters were performed in two steps. The nonlinearity in the first slice was extracted based on two-tone measurements under small-signal operation where no or negligible IM3 asymmetries are observed, since the first slice can not account for asymmetries under the assumption of wide-band system. Then, the parameters of the second slice were extracted to fit the difference between the measured upper and lower IM3s based on two-tone measurements under an operation regime where IM3 asymmetries are observed.

In [73], starting from a nonlinear circuit with one bi-dimensional nonlinearity, similar to the PA simplified circuit-equivalent presented in [5] and shown in Figure 2.2, a combination of the harmonic input and nonlinear current methods [6] was used to obtain the respective Volterra kernels. There, the scope was not to obtain an exact expression for the nonlinear transfer functions or an equivalent system topology for that particular nonlinear circuit. The work focused on the identification of different types of frequency dependence of the nonlinear transfer functions, e.g. if the nonlinear transfer functions are general multi-dimensional functions or if they are expressed as the product of lower-dimensional functions. These results were then exploited in discrete time-domain to identity possible null elements in the discrete-time Volterra Kernels.

The amplifier was assumed to be a wide-band system, e.g. it has a pass-band larger than the RF signal bandwidth and so its frequency response can be considered flat at the fundamental band. Also, the flatness frequency response assumption was extended to all harmonic frequency bands, meaning that the only dynamic behavior modeled was that

due to the base-band frequencies.

In the derivation procedure, as stated by the authors, at each order an appropriate nonlinear current source F_n is used to excite an associated linear network Z and the nonlinear transfer function $k_n(\xi)$ is given by $k_n = ZF_n$. In fact, the appropriate nonlinear current sources are originated from the nonlinear circuit with a bi-dimensional nonlinearity, since for example the third-order nonlinear current source, F_3 , could not be originated from a nonlinear circuit with just one unidimensional nonlinearity. The discrete-time low-pass equivalent PA behavioral model obtained following this procedure is [73]:

$$\tilde{y}(n) = \tilde{h}_1(0)\tilde{x}(n) + \sum_{p=1}^{P-1} \sum_{q_1=0}^M \cdots \sum_{q_p=q_{p-1}}^M \tilde{h}_{2p+1}(q_1, \dots, q_{2p+1}) \prod_{m=1}^p |\tilde{x}(n - q_m)|^2 \tilde{x}(n) \quad (2.44)$$

where $\tilde{x}(n)$ and $\tilde{y}(n)$ are the complex-valued envelopes at the PA input and output, respectively, $\tilde{h}_1(\cdot)$ and $\tilde{h}_{2p+1}(\cdot)$ are complex-valued coefficients. Kernel symmetry was exploited in (2.44).

If, also in [72], the flatness assumption is extended to all harmonic frequency bands, the same (2.44) discrete-time constitutive equation is obtained. Now, following the same procedure but excluding the flatness assumption at the second harmonic band, it is possible to show that the low-pass equivalent discrete-time PA behavioral model, considering a maximum input delay equals M and polynomial order truncation of $2P - 1 = 7$, is given by (2.45) in the next page.

Looking at (2.44) and (2.45), some interesting behaviors can be observed. Remember that the derivations started from a polynomial approximation at RF level. First, the assumption of flat frequency response at fundamental implies that an instantaneous input sample, or its conjugate, is always presented at the output. As a consequence of the presence of an instantaneous input sample at the output, the only 1D terms at the output are those memoryless. So, these physically based behavioral models, under the flatness assumption, do not share the 1D approximation of the models presented in Subsection 2.4.3 where the memory polynomial is the most representative case. In the dynamic deviation (DD) model presented in Subsection 2.4.1, the 1D terms were also just the memoryless terms. Second, the assumption that only base-band and second-harmonic frequencies have dynamics, combined with the discrete-time finite impulse response of the filters, implies that delayed input samples appear in the output always in pairs.

$$\begin{aligned}
\tilde{y}(n) = & \tilde{h}_1(0)\tilde{x}(n) \\
& + \sum_{q_1=0}^M \tilde{h}_3(0^*, q_1, q_1)\tilde{x}^*(n)\tilde{x}^2(n-q_1) \\
& + \sum_{q_1=1}^M \tilde{h}_3(0, q_1, q_1^*)\tilde{x}(n)|\tilde{x}(n-q_1)|^2 \\
& + \sum_{q_1=0}^M \sum_{q_2=q_1}^M \tilde{h}_5(0, q_1, q_1^*, q_2, q_2^*)\tilde{x}(n)|\tilde{x}(n-q_1)|^2|\tilde{x}(n-q_2)|^2 \\
& + \underbrace{\sum_{q_1=0}^M \sum_{q_2=0}^M}_{q_1 \neq q_2} \tilde{h}_5(0, q_1, q_1^*, q_2^*, q_2)\tilde{x}(n)\tilde{x}^2(n-q_1)[\tilde{x}^*(n-q_2)]^2 \\
& + \underbrace{\sum_{q_1=0}^M \sum_{q_2=0}^M}_{q_1+q_2 \geq 1} \tilde{h}_5(0^*, q_1, q_1, q_2, q_2^*)\tilde{x}^*(n)\tilde{x}^2(n-q_1)|\tilde{x}(n-q_2)|^2 \\
& + \sum_{q_1=0}^M \sum_{q_2=q_1}^M \sum_{q_3=q_2}^M \tilde{h}_7(0, q_1, q_1^*, q_2, q_2^*, q_3, q_3^*)\tilde{x}(n)|\tilde{x}(n-q_1)|^2|\tilde{x}(n-q_2)|^2|\tilde{x}(n-q_3)|^2 \\
& + \underbrace{\sum_{q_1=0}^M \sum_{q_2=0}^M \sum_{q_3=0}^M}_{q_1 \neq q_3} \tilde{h}_7(0, q_1, q_1, q_2, q_2^*, q_3^*, q_3)\tilde{x}(n)\tilde{x}^2(n-q_1)|\tilde{x}(n-q_2)|^2[\tilde{x}^*(n-q_3)]^2 \\
& + \underbrace{\sum_{q_1=0}^M \sum_{q_2=0}^M \sum_{q_3=q_2}^M}_{q_1+q_2+q_3 \geq 1} \tilde{h}_7(0^*, q_1, q_1, q_2, q_2^*, q_3, q_3^*)\tilde{x}^*(n)\tilde{x}^2(n-q_1)|\tilde{x}(n-q_2)|^2|\tilde{x}(n-q_3)|^2 \\
& + \underbrace{\sum_{q_1=0}^M \sum_{q_2=0}^M \sum_{q_3=q_2}^M}_{q_1 \neq q_2, q_1 \neq q_3} \tilde{h}_7(0^*, q_1^*, q_1^*, q_2, q_2, q_3, q_3)\tilde{x}^*(n)[\tilde{x}^*(n-q_1)]^2\tilde{x}^2(n-q_2)\tilde{x}^2(n-q_3)
\end{aligned} \tag{2.45}$$

The extraction of the parameters in (2.44) and (2.45) using time-domain base-band data can be performed using linear system identification techniques, like LS. Both (2.44) and (2.45) were implemented in the Matlab software. The results will be reported in Chapter 5. Equation (2.44) will be referred to as physical pruning (PP) model with the assumption that the only dynamic effects are due to base-band frequencies, while equation (2.45) will be referred to as physical pruning (PP) model with the assumption that the dynamic effects are due to base-band and second harmonic frequencies.

Chapter 3

Low-pass equivalent PA behavioral model with feedback topology

This chapter is focused on the particular low-pass equivalent, LPE, PA behavioral model with feedback topology, proposed in [4].

Starting by the motivations for the development of a such feedback model, theoretical justifications for its validity, based on nonlinear Volterra analysis, are then provided. Finally, its implementation and parameter identification are addressed.

3.1 Motivations for the development of the LPE feedback model

In [5], it was shown, based on a circuit-equivalent description of an RF PA, that the feedback topology shown in Figure 3.1 can represent the most important dynamic nonlinear effects observed in a real PA.

The block diagram shown in Figure 3.1 models the relationship between the real-valued band-pass RF signals at the PA input, $x(t)$, and output, $y(t)$. By now, it will be referred to as the RF feedback model. The input frequency-selective matching network, $H(\omega)$, guarantees that only band-pass signals can produce any measurable output, while the output frequency-selective matching network, $O(\omega)$, restricts the observable output to the in-band contributions. The closed-loop between the matching networks can model

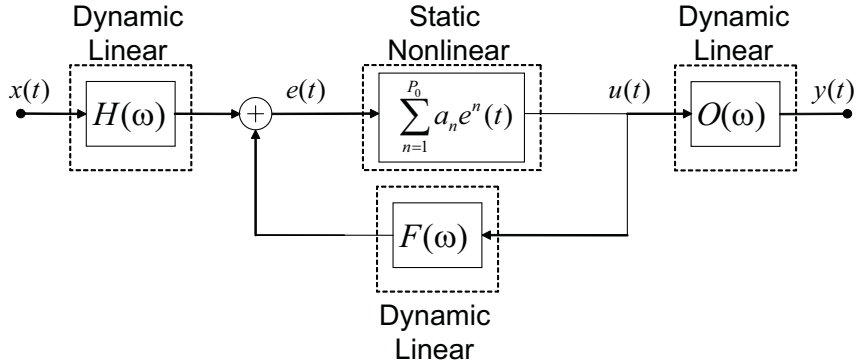


Figure 3.1: RF feedback topology

nonlinear dynamic effects of infinite polynomial order, even if its nonlinear block is a polynomial whose degree is truncated to some finite integer P_0 , and even if its linear block, $F(\omega)$, is band-limited.

The feedback topology contains itself a significant amount of information and hence can be very parsimonious in the number of parameters. Nevertheless, the parameter extraction of the RF feedback model is complicated and its low-pass equivalent model, relating the complex-valued envelopes at its input and output, is not straightforward.

The RF feedback model was used as the starting point for the derivation of some PA behavioral models [76], [77], [72], [78]. A common characteristic of these derived PA behavioral models is that they are approximations with non recursive topology, so that a direct extraction procedure, either based on one-tone and two-tone measurements [72] and [78], or via LS based on time-domain base-band measurements [76] and [77], can be carried out, and the relationship between the complex-valued envelope at the input, $\tilde{x}(t)$, and the output, $\tilde{y}(t)$, can be easily obtained. However, for an accurate representation of a feedback topology by a non recursive (or feed-forward) topology, the complexity – in terms of the number of operations involving the reduced parameter set of the feedback topology – grows very fast as the required polynomial truncation order and memory length increase.

Based on these considerations, the scope of the model presented in this chapter is to obtain a relationship between the complex-valued envelopes at the input and output of the RF feedback model that maintains the feedback topology and, additionally, can be extracted using simple measurements.

3.2 LPE feedback model derivation and theoretical justification

The difficulties in deriving a low-pass equivalent representation for the RF feedback model shown in Figure 3.1 reside in the internal closed-loop, once the matching networks, $H(\omega)$ and $O(\omega)$, are directly represented by their respective low-pass equivalents, $\tilde{H}(\Omega)$ and $\tilde{O}(\Omega)$. In Figure 3.1, the real-valued signal $u(t)$ at the input of the filter $O(\omega)$ is fed-back and then its spectral content is affected by the action of the dynamic linear filter $F(\omega)$. It is reasonable to assume that the filter $F(\omega)$ has a significant spectral content only at a limited spectral range. In accordance to [78], it is assumed that only the base-band, the fundamental band, and the second-harmonic band have non negligible spectral contents. If only complex-valued base-band signals are involved, then the only output that can be fed-back is the one at fundamental band. As a consequence, the filter in the feedback path must be substituted by its low-pass equivalent filter $\tilde{F}_1(\Omega)$. The other two non negligible components of $F(\omega)$, namely the base-band contribution, $F_0(\Omega)$, and the low-pass equivalent of the second-harmonic band contribution, $\tilde{F}_2(\Omega)$, should be included in the direct (or feed-forward) path. Additionally, the signals applied to the filters $F_0(\Omega)$ and $\tilde{F}_2(\Omega)$ – whose spectral content are around the base-band and second-harmonic band, respectively – are not available and must be estimated based on the available signals at the fundamental band. The simplest estimations, e.g. second-degree polynomial approximations, consist in performing the squarer $(.)^2$, for the second-harmonic band estimation and the squarer of the modulus $|.|^2$ for the base-band estimation. These considerations justify the use of the low-pass equivalent, LPE, feedback model whose block diagram is shown in Figure 3.2.

In Figure 3.2, the filters $Q_0(\Omega)$ and $\tilde{Q}_2(\Omega)$ are defined by:

$$Q_0(\Omega) = \frac{F_0(\Omega)}{1 - a_1 F_0(\Omega)} \quad (3.1)$$

and

$$\tilde{Q}_2(\Omega) = \frac{\tilde{F}_2(\Omega)}{1 - a_1 \tilde{F}_2(\Omega)} \quad (3.2)$$

Now, the theoretical validity of the block diagram shown in Figure 3.2 – from now on named as the LPE feedback model – to mimic the pass-band behavior of the RF feedback

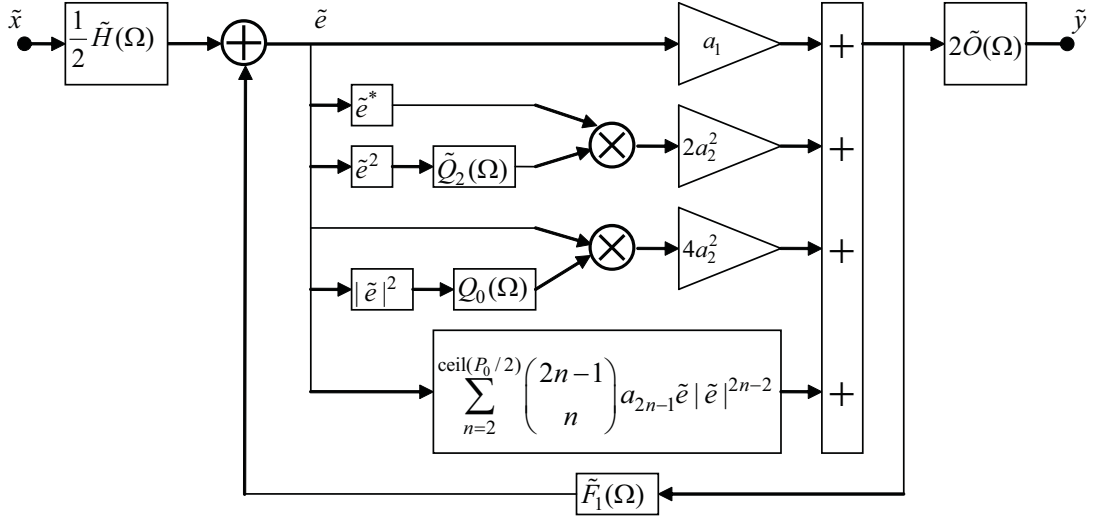


Figure 3.2: Low-pass equivalent feedback topology

model shown in Figure 3.1 is tested using nonlinear Volterra analysis. Specifically, the Volterra kernels of the RF feedback system shown in Figure 3.1, up to the fifth-order, are first obtained using the harmonic input method [6] and then the terms that fall in the pass-band output are collected. According to [12], only odd-order terms are present, and the number of conjugate input samples (instantaneous or past samples) in the low-pass equivalent Volterra kernel expressions is always one less than the number of non conjugate input samples. Figures 3.3 and 3.4 show the feed-forward diagrams of the 1st and 3rd order low-pass equivalent Volterra kernels of the RF feedback model, respectively, while the 5th order in-band response of the RF feedback model is given by the sum of the contributions \tilde{y}_{51} , \tilde{y}_{52} , \tilde{y}_{53} and \tilde{y}_{54} , whose feed-forward diagrams are shown in Figures 3.5, 3.6, 3.7 and 3.8, respectively.

In the feed-forward diagrams of the Volterra kernels, the filter $\tilde{D}_1(\Omega)$ is defined by:

$$\tilde{D}_1(\Omega) = 1 - a_1 \tilde{F}_1(\Omega) \quad (3.3)$$

At this point, the Volterra kernels of the LPE feedback system shown in Figure 3.2, up to the fifth-order, are obtained using a modified harmonic input method. Specifically, if the signal:

$$\tilde{x}(t) = \sum_{i=1}^n \exp(j\Omega_i t) \quad (3.4)$$

is applied to the input of the LPE feedback model, then the n th-order Volterra kernel

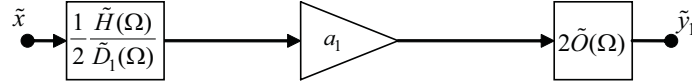


Figure 3.3: Feed-forward diagram of the 1st order low-pass equivalent Volterra kernel of the RF feedback model

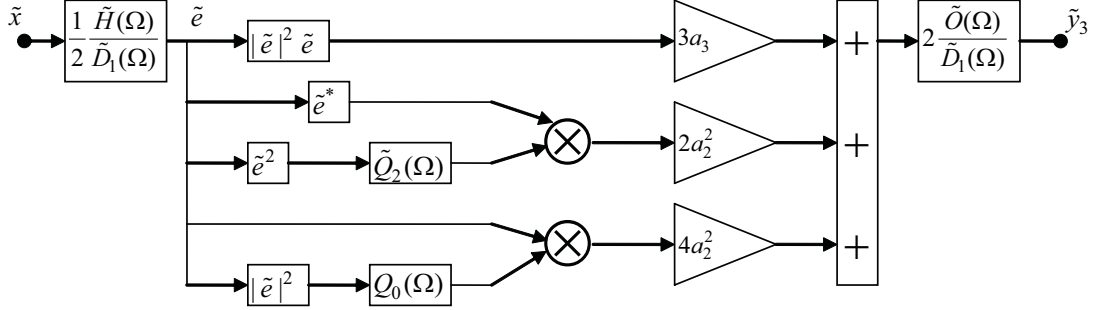


Figure 3.4: Feed-forward diagram of the 3rd order low-pass equivalent Volterra kernel of the RF feedback model

$\tilde{H}_n(\Omega_1, \dots, \Omega_{(n+1)/2}, \Omega_{(n+3)/2}^*, \dots, \Omega_n^*)$, where n is odd, is related to the LPE feedback model response at the frequency $\Omega_d = (\Omega_1 + \dots + \Omega_{(n+1)/2} - \Omega_{(n+3)/2} - \dots - \Omega_n)$, denoted as $\tilde{y}^{\Omega_d}(t)$, by:

$$\tilde{H}_n(\Omega_1, \dots, \Omega_{(n+1)/2}, \Omega_{(n+3)/2}^*, \dots, \Omega_n^*) = \frac{1}{n!} \frac{\tilde{y}^{\Omega_d}(t)}{\exp(j\Omega_i t)} \quad (3.5)$$

Applying this methodology, the obtained expressions for $\tilde{H}_1(\Omega_1)$ and $\tilde{H}_3(\Omega_1, \Omega_2, \Omega_3^*)$ are exactly the same as the respective expressions obtained for the feedback system relating the RF signals, whose block diagrams were presented in Figures 3.3 and 3.4, respectively. Additionally, the fifth-order response of the LPE feedback model is given by the sum of the contributions \tilde{y}_{51} and \tilde{y}_{52} , whose feed-forward diagrams are shown in Figures 3.9 and 3.10, respectively.

By simple inspection, it is immediate to see that all the contributions to the fifth-order response of the LPE feedback system are also present in the fifth-order in-band response of the RF feedback system. In other words, the LPE feedback model shown in Figure 3.2 does not add any extra 5th-order contribution that is not already present in the RF feedback model shown in Figure 3.1. On the other hand, the fifth-order Volterra kernel of the LPE feedback model is just a sub-set of the fifth-order low-pass

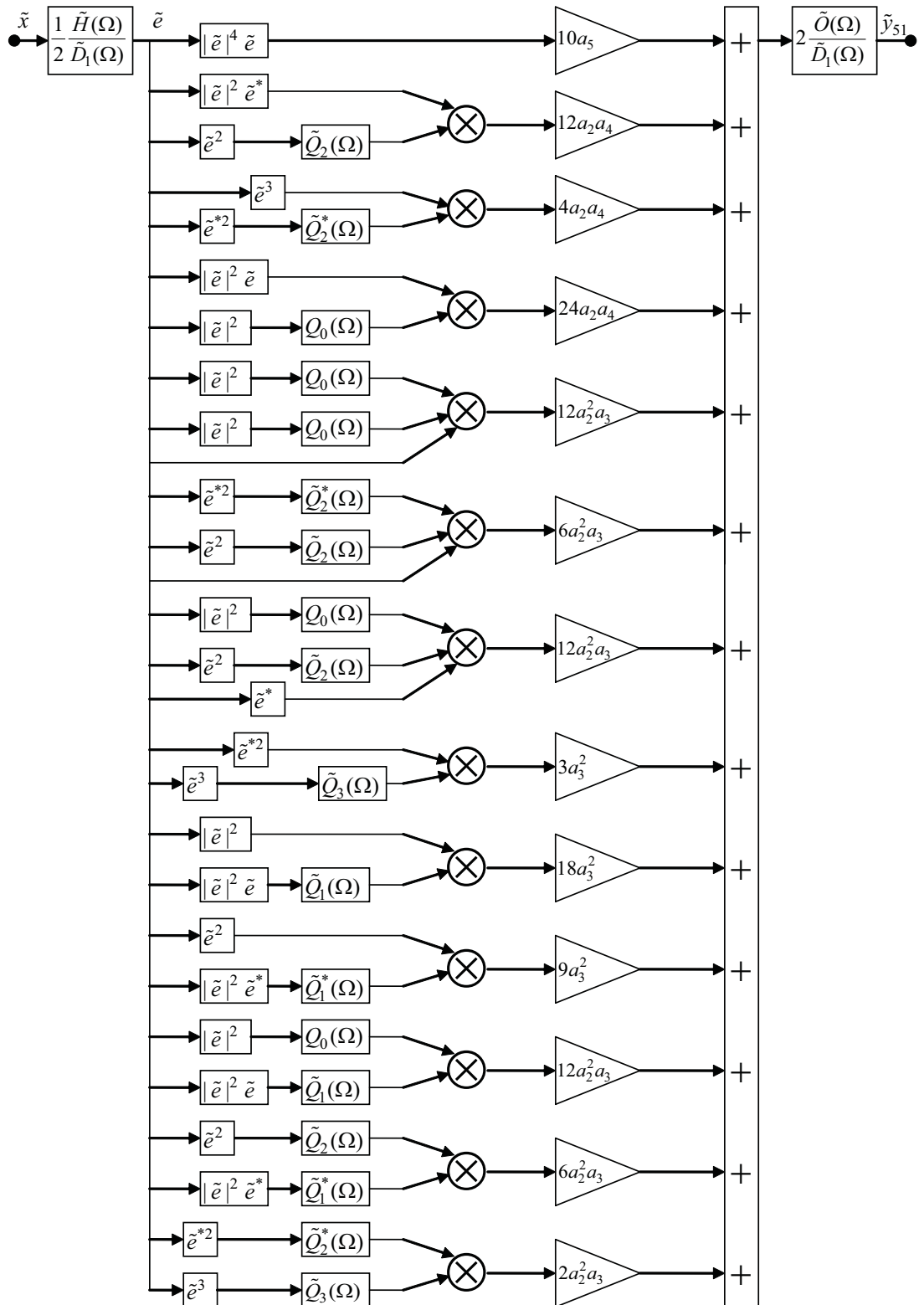


Figure 3.5: Feed-forward diagram of the 5th order low-pass equivalent Volterra kernel of the RF feedback model – part 1

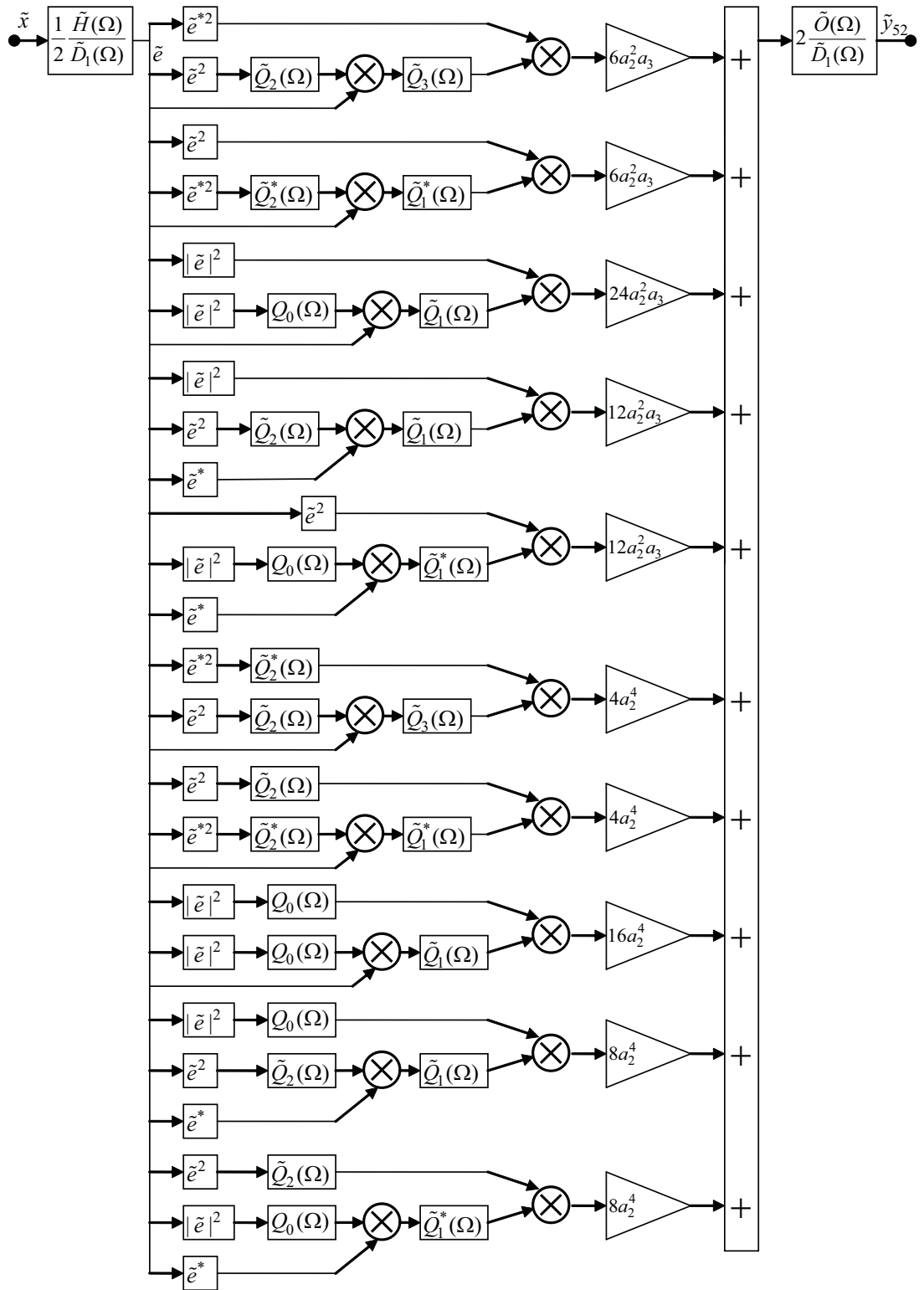


Figure 3.6: Feed-forward diagram of the 5th order low-pass equivalent Volterra kernel of the RF feedback model – part 2

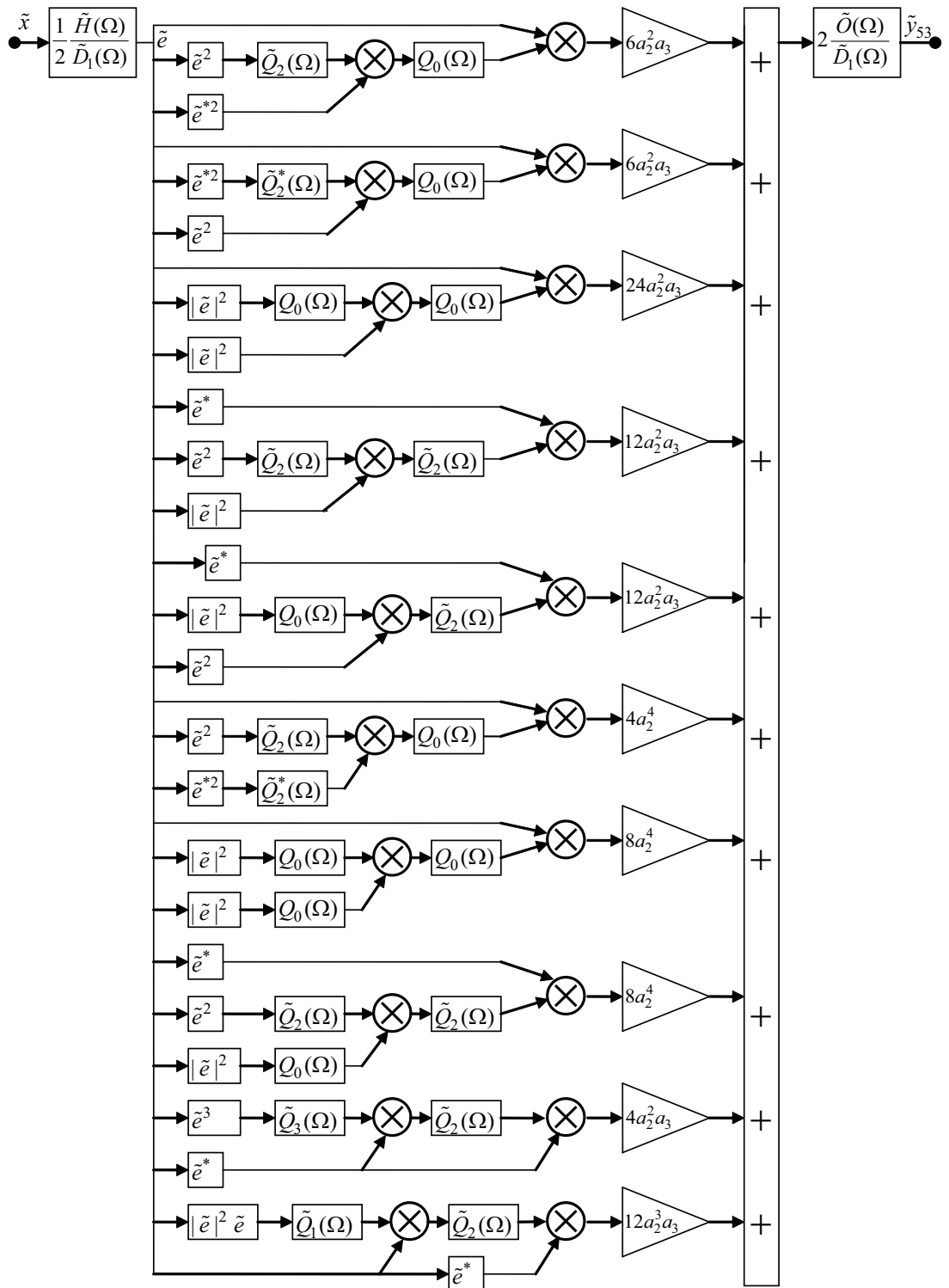


Figure 3.7: Feed-forward diagram of the 5th order low-pass equivalent Volterra kernel of the RF feedback model – part 3

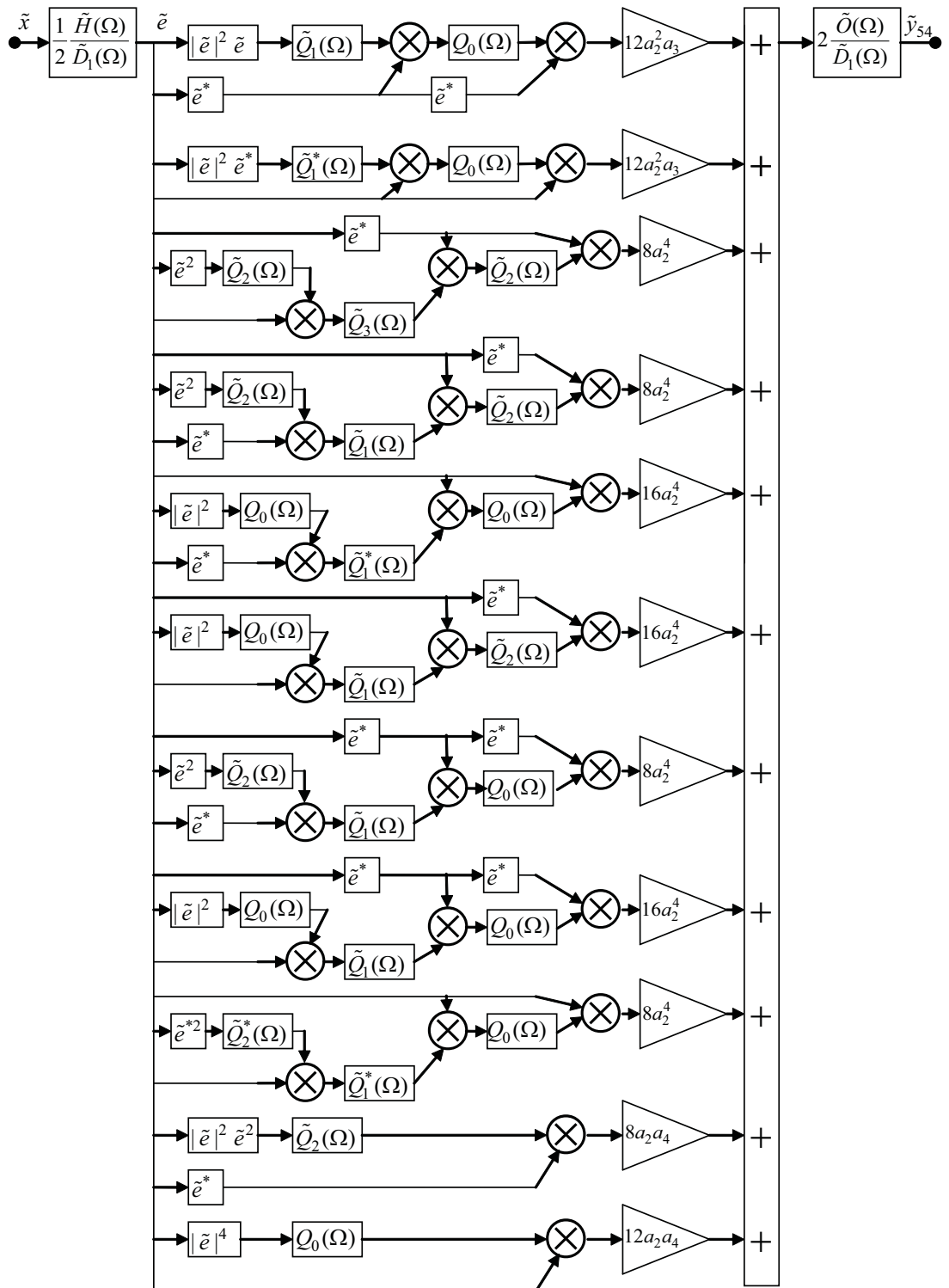


Figure 3.8: Feed-forward diagram of the 5th order low-pass equivalent Volterra kernel of the RF feedback model – part 4

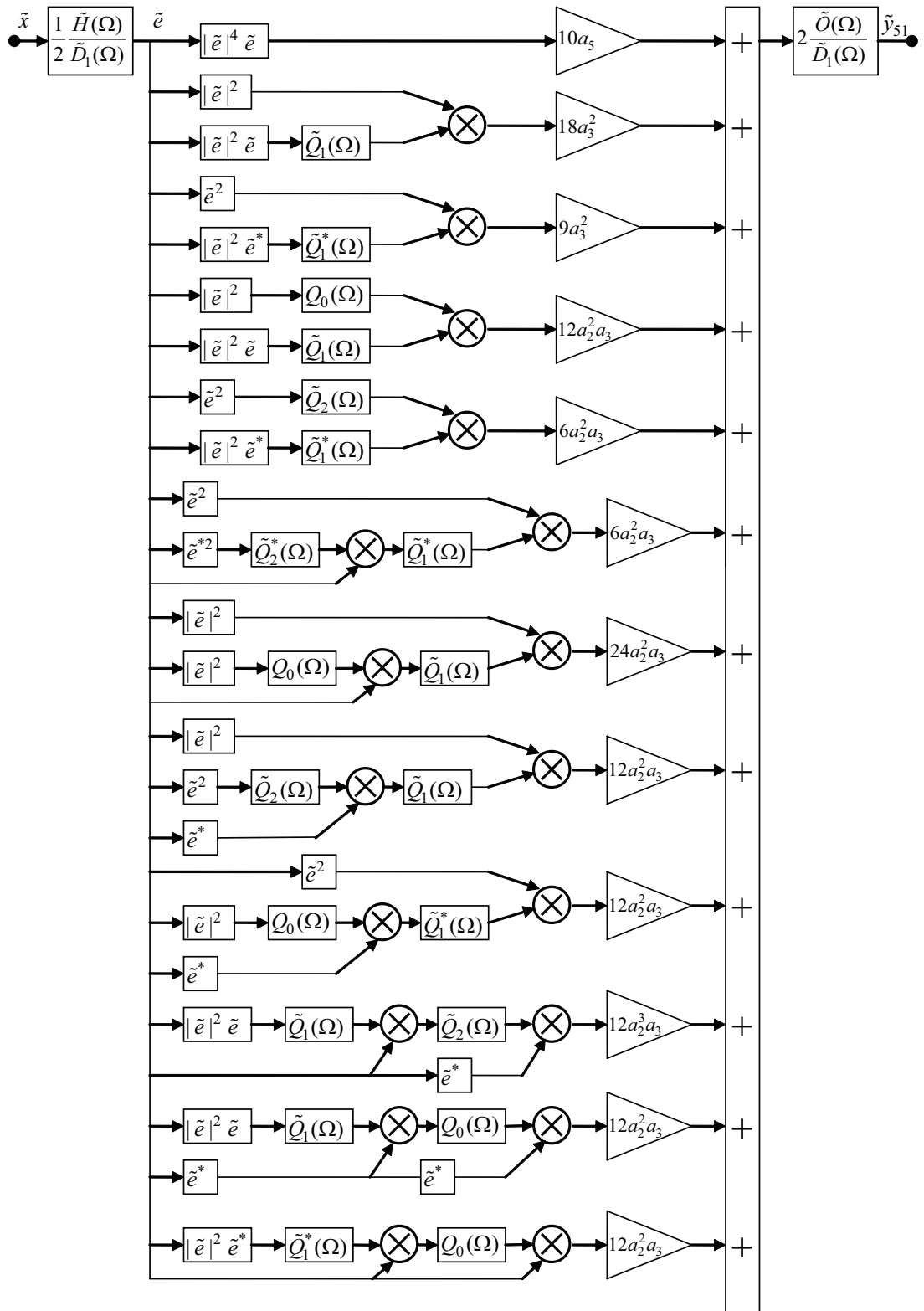


Figure 3.9: Feed-forward diagram of the 5th order Volterra kernel of the LPE feedback model – part 1

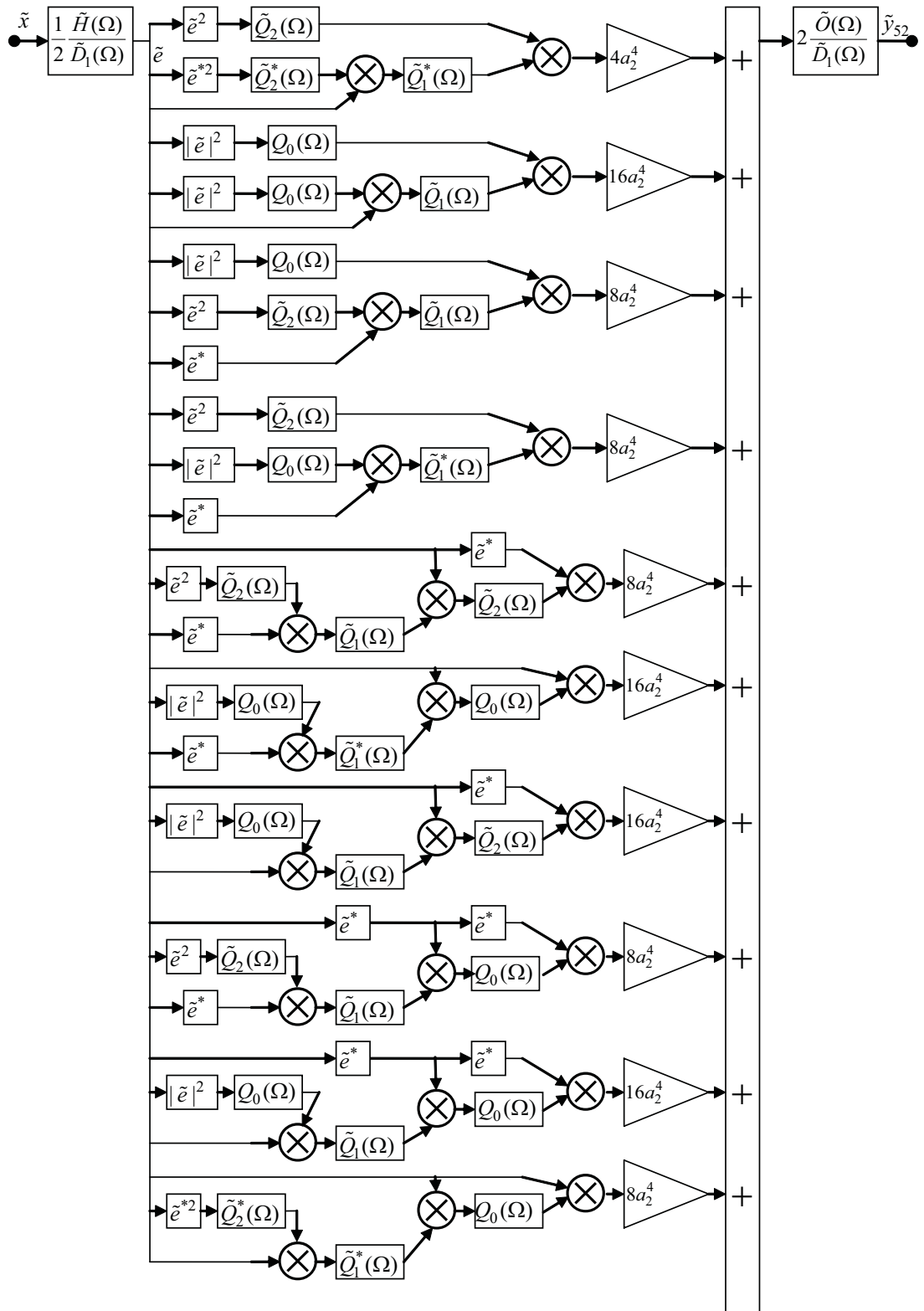


Figure 3.10: Feed-forward diagram of the 5th order Volterra kernel of the LPE feedback model – part 2

equivalent Volterra kernel of the RF feedback model. By a careful observation of the kernel determination procedure, it is evident that the higher order Volterra kernels of both the RF and LPE feedback systems are always built from the lower order kernels. This is enough to guarantee that all the higher order Volterra kernels of the LPE feedback model are a sub-set of the respective higher order low-pass equivalent Volterra kernels of the RF feedback model.

3.3 Digital implementation and parameter extraction

Firstly, all the linear filters present in the LPE feedback model, whose block diagram is shown in Figure 3.2, are approximated by finite-impulse response (FIR) digital filters. The filter $Q_0(\Omega)$ has real-valued coefficients (or taps), since it represents the base-band frequency response of a real filter, while the filters $\tilde{F}_1(\Omega)$ and $\tilde{Q}_2(\Omega)$ have complex-valued coefficients, since they shift either the fundamental or the second-harmonic frequency response of real filters to the base-band – the complex-conjugate symmetry between negative and positive frequencies will probably be lost.

Within this particular scenario, parameter redundancy can be eliminated, according to [72]. Particularly, the complex-valued filter taps, \tilde{q}_{2m} , of the filter $\tilde{Q}_2(\Omega)$, and the real-valued taps, q_{0m} , of the filter $Q_0(\Omega)$, plus the real-valued polynomial coefficients a_2 and a_3 , do not need to be explicitly identified, since, without any loss in modeling capabilities, they can all be represented by just two FIR filters, $G_0(\Omega)$ and $\tilde{G}_2(\Omega)$, whose taps, designated by g_{0m} and \tilde{g}_{2m} , respectively, are given by:

$$g_{0m} = \begin{cases} ka_3 + 4a_2^2 q_{0m}, & \text{for } m = 0 \\ 4a_2^2 q_{0m}, & \text{for } m = 1, \dots, M_0 \end{cases} \quad (3.6)$$

and

$$\tilde{g}_{2m} = \begin{cases} (3 - k)a_3 + 2a_2^2 \tilde{q}_{2m}, & \text{for } m = 0 \\ 2a_2^2 \tilde{q}_{2m}, & \text{for } m = 1, \dots, M_2 \end{cases} \quad (3.7)$$

with $0 \leq k \leq 3$, and where M_0 and M_2 are the memory lengths of the filters $Q_0(\Omega)$ and $\tilde{Q}_2(\Omega)$, respectively.

Additionally, it is assumed that the PA has a flat frequency response at the fundamental zone, e.g. it has a pass-band larger than the input signal bandwidth. Therefore,

the filter $\tilde{F}_1(\Omega)$ is represented by just a complex-valued gain, \tilde{f}_0 .

After these approximations, for the particular case in which the polynomial in the feed-forward path in the RF feedback system is truncated to the third degree ($P_0 = 3$), if one equates the in-phase (or real) and quadrature (or imaginary) components of the complex-valued output $\tilde{y}(t)$, denoted by $I_y(t)$ and $Q_y(t)$, respectively, after some mathematical manipulations it is found that they must obey:

$$I_y^3(t) + a_1(t)I_y^2(t)Q_y(t) + a_2(t)I_y(t)Q_y^2(t) + a_3(t)Q_y^3(t) + a_4(t)I_y(t) + a_5(t)Q_y(t) = a_6(t) \quad (3.8)$$

and

$$I_y^3(t) + b_1(t)I_y^2(t)Q_y(t) + b_2(t)I_y(t)Q_y^2(t) + b_3(t)Q_y^3(t) + b_4(t)I_y(t) + b_5(t)Q_y(t) = b_6(t) \quad (3.9)$$

where the time-varying coefficients $a_j(t)$ and $b_j(t)$ for $j = 1, \dots, 6$ are dependent on the instantaneous and delayed samples of the in-phase, $I_x(t)$, and quadrature, $Q_x(t)$, components of the complex-valued input $\tilde{x}(t)$. Observe that, since in the LPE feedback model there is an instantaneous gain in the feedback path, it was possible to find only implicit equations relating both real and imaginary components of the output signal. Additionally, there is no closed solution to a system of two third-order equations into two unknowns, I_y and Q_y , and hence an iterative numerical algorithm is required to get an approximate solution. For instance, the classical Newton-Raphson algorithm [79] can be used for this purpose. Furthermore, the presence of time-varying coefficients forces the solution of this nonlinear equation system in the implicit form to be performed at each time sample.

For the extraction of the LPE feedback model parameters, in [4] it was presented a procedure based on simple RF measurements. First, a small-signal one-tone measurement is done for the extraction of the PA linear gain and phase. Then, the G_0 and \tilde{G}_2 filter parameters in the feed-forward path are extracted based on two-tone, at frequencies ω_1 and ω_2 , measurements. Closed-form expressions relating the power measured at the PA output at its third-order intermodulation (IM3) frequencies, $2\omega_2 - \omega_1$ and $2\omega_1 - \omega_2$, to the G_0 and \tilde{G}_2 filter parameters were presented in [72]. The complex-valued gain \tilde{f}_0 and higher order real-valued coefficients a_n ($n > 3$), if presented in the feed-forward path, are optimized to adjust the large-signal behavior.

Alternatively, a nonlinear optimization procedure could be implemented to extract all the LPE feedback model coefficients at once, for instance the minimization of a quadratic criteria function of the error signal defined as the difference between the measured and modeled time-domain base-band output signals, using standard nonlinear optimization algorithms like the Levenberg-Marquardt and the Gauss-Newton methods [58].

In Chapter 5, the accuracy of the LPE feedback model in reproducing input-output data simulated in a known RF feedback model, and in fitting experimental input-output base-band data measured in a real RF PA, will be investigated.

Chapter 4

A new approach to the derivation of PA behavioral models

A commonly used approach in deriving a PA behavioral model starts by the expansion in a Volterra series of the system at RF level. Then, attention is payed to the terms at output that fall in the PA pass-band. The final scope is to construct a model that describes the relationship between the base-band complex-valued envelopes at the PA input and output, the so-called PA low-pass equivalent behavioral model. According to [12], only odd-order terms are present and the number of conjugate input samples (instantaneous or past samples) is always one less than the number of non conjugate input samples. This was the methodology followed in Chapters 2 and 3.

In this Chapter, theoretical analysis based on parity properties of complex-valued functions are developed to provide a new insight into the implications of a Volterra (or polynomial) approximation at RF level. Within this rigorous mathematical context, it will be shown that a polynomial approximation at RF level imposes additional constraints on low-pass equivalent PA behavioral models, by no means associated to any physical behavior observed in real PA systems. Then, it is proposed a direct derivation of a low-pass equivalent PA behavioral model in which a polynomial approximation is done at base-band level, to eliminate the unnecessary parity constraint present when the polynomial approximation is done at RF level, justifying, in this way, the use of new odd-order terms. These new terms have already being investigated in literature, but misunderstood as even-order terms [80] and [81]. A discussion on the possible improvements in PA behavioral

modeling by the inclusion of these new odd-order terms is presented, and some of the previously described models are extended to include them.

4.1 Parity definitions for complex-valued functions

This section presents the definitions that extend the concepts of even and odd functions from real-valued functions to complex-valued functions. As a remark, the terminology even and odd refers to the parity of the power functions in a polynomial expansion.

A complex-valued function $\tilde{y}(I_x, Q_x)$ dependent on the two real-valued variables I_x and Q_x has even symmetry if:

$$\begin{aligned}\tilde{y}(I_x, Q_x) &= \tilde{y}(-I_x, -Q_x) \\ I_y(I_x, Q_x) + jQ_y(I_x, Q_x) &= I_y(-I_x, -Q_x) + jQ_y(-I_x, -Q_x)\end{aligned}\quad (4.1)$$

In other words, a complex-valued function $\tilde{y}(I_x, Q_x)$ is even if both its real $I_y(I_x, Q_x)$ and imaginary $Q_y(I_x, Q_x)$ parts are real-valued even functions. On the other hand, a complex-valued function $\tilde{y}(I_x, Q_x)$ has odd symmetry if:

$$\begin{aligned}\tilde{y}(I_x, Q_x) &= -\tilde{y}(-I_x, -Q_x) \\ I_y(I_x, Q_x) + jQ_y(I_x, Q_x) &= -I_y(-I_x, -Q_x) - jQ_y(-I_x, -Q_x)\end{aligned}\quad (4.2)$$

e.g. a complex-valued function $\tilde{y}(I_x, Q_x)$ is odd if both its real $I_y(I_x, Q_x)$ and imaginary $Q_y(I_x, Q_x)$ parts are real-valued odd functions.

The definitions in (4.1) and (4.2) are valid for arbitrary relationship between I_x and Q_x . However, for the purposes here, I_x and Q_x are constrained to be the real and imaginary parts, respectively, of a complex number $\tilde{x} = I_x + jQ_x$.

Now, it is presented a proof of a parity property that will be used soon. Specifically, it is shown that the product of an odd function, $g_1(I_x, Q_x)$, by an even function, $g_2(I_x, Q_x)$, results in an odd function:

$$\begin{aligned}\tilde{y}(I_x, Q_x) &= g_1(I_x, Q_x) \times g_2(I_x, Q_x) \\ \tilde{y}(-I_x, -Q_x) &= g_1(-I_x, -Q_x) \times g_2(-I_x, -Q_x) \\ \tilde{y}(-I_x, -Q_x) &= -g_1(I_x, Q_x) \times g_2(I_x, Q_x) \\ \tilde{y}(-I_x, -Q_x) &= -\tilde{y}(I_x, Q_x)\end{aligned}\quad (4.3)$$

Additionally, it can be easily shown that the composition of any function with an even function is an even function.

4.2 Odd-order symmetry of RF devices under narrow-band excitations

The fundamental property that only odd-order terms can contribute to the pass-band output of RF devices under narrow-band excitations is widely known in the microwave community. A proof of this property was given in [12] for Volterra RF systems and is commonly cited in literature.

Here, the objective is to show that if an arbitrary pass-band input signal $x(t)$ of bandwidth B much lower than its center (or carrier) frequency f_c , also referred to as a narrow-band signal, is subjected to the action of an arbitrary even nonlinearity $F[x(t)]$ (a polynomial with even powers is just a particular case), then the resulting signal $y(t)$ will present a null spectrum in the pass-band or in-band, e.g. a null spectrum around and near the carrier frequency f_c . This is mathematically equivalent to proof that the odd-order coefficients of a Chebyshev series of the signal at the output of an even nonlinearity driven by a narrow-band input signal are zero.

The proof starts by the definition of a Chebyshev series [82], [83], which is related to a Fourier series of only cosine terms through a change of variable.

If a narrow-band input signal $x(t)$:

$$x(t) = A(t) \cos[2\pi f_c t + \alpha(t)] \quad (4.4)$$

is fed to an arbitrary even nonlinearity $F(\cdot)$, then the resulting signal $y(t)$ is:

$$y(t) = F[x(t)] \quad (4.5)$$

Define:

$$\theta(t) = 2\pi f_c t + \alpha(t) \quad (4.6)$$

Make the change of variable ¹:

$$x = A \cos(\theta) \quad (4.7)$$

The signal y at the nonlinearity output is a periodic even function of the new variable θ :

$$y = F(A \cos \theta) \quad (4.8)$$

and hence can be represented by the Fourier series of only cosine terms:

$$y(A \cos \theta) = \frac{1}{2}a_0(A) + \sum_{k=1}^{\infty} a_k(A) \cos k\theta \quad (4.9)$$

where:

$$a_k(A) = \frac{2}{\pi} \int_0^\pi y(A \cos \theta) \cos k\theta d\theta \quad (4.10)$$

for $k = 0, 1, \dots, \infty$.

The term $a_1 [A(t)] \cos[2\pi f_c t + \alpha(t)]$ represents the output spectrum concentrated around the carrier frequency f_c and is the only observable output in a band-pass nonlinearity, for example an RF PA.

By the change in variable in (4.7), the relationship between θ and x is given by:

$$\theta = \arccos(x/A) \quad (4.11)$$

Using (4.11), for any $A \geq |x|$, (4.9) can be rewritten as [84]:

$$y(x) = \frac{1}{2}a_0(A) + \sum_{k=1}^{\infty} a_k(A)T_k(x/A) \quad (4.12)$$

where:

$$a_k(A) = \frac{2}{\pi} \int_{-A}^A \frac{y(x)T_k(x/A)}{\sqrt{A^2 - x^2}} dx \quad (4.13)$$

for $k = 0, 1, \dots, \infty$ and:

$$T_k(u) = \cos(k\theta) = \cos[k \arccos(u)] \quad (4.14)$$

is the first-kind Chebyshev polynomial of order k .

¹From now on, the suffice t will be sometimes omitted to simplify the notation.

If the trigonometric identity:

$$\cos(k\theta) + \cos(k-2)\theta = 2 \cos(\theta) \cos(k-1)\theta \quad (4.15)$$

is substituted in (4.14), the recurrence relation:

$$T_k(u) = 2uT_{k-1}(u) - T_{k-2}(u) \quad (4.16)$$

for $k = 2, 3, \dots, \infty$ and with the initial conditions $T_0(u) = 1$ and $T_1(u) = u$ is obtained. Using (4.16) together with the given initial conditions for $T_0(u)$ and $T_1(u)$, it can be shown by induction [83] that $T_k(u)$ is an even or odd function of u according as k is even or odd.

Looking back to (4.13), the Chebyshev coefficients are given by the definite integral on the variable x over the interval $[-A, A]$ of the integrand:

$$\frac{y(x)T_k(x/A)}{\sqrt{A^2 - x^2}} \quad (4.17)$$

Since $\sqrt{A^2 - x^2}$ is always an even function of x , if the nonlinearity $y(x) = F(x)$ is an even function of x and k is odd which implies that $T_k(x/A)$ is an odd function of x , then the integrand, as a function of the integration variable x , is given by the product of an even function and an odd function, divided by an even function. Applying basic parity properties of real-valued functions, it is easy to show that this particular integrand is an odd function of x . Additionally, the definite integral of an odd function of the integration variable over a symmetric interval $[-A, A]$ is identically zero if A is bounded and the integrand has no vertical asymptotes between $-A$ and A . Hence, if the nonlinearity $y(x) = F(x)$ is an even function of x and for odd values of k , the coefficients a_k of the Chebyshev series are identically zero. This completes the proof that the narrow-band first-zonal signal at the output will be null if the nonlinearity $F(.)$ has even symmetry.

On the other hand, if the nonlinearity $F(.)$ is an odd function of x and k is odd which implies that $T_k(x/A)$ is an odd function of x , then the integrand, as a function of the integration variable x , is given by the product of two odd functions, divided by an even function. Applying basic parity properties of real-valued functions, it is easy to show that this particular integrand is an even function of x . Additionally, the definite integral of an even function of the integration variable over a symmetric interval $[-A, A]$ is twice the integral from $[0, A]$ if A is bounded and the integrand has no vertical asymptotes between

$-A$ and A . Hence, if the nonlinearity $y(x) = F(x)$ is an odd function of x and for odd values of k , the coefficients a_k of the Chebyshev series are different from zero if the input is different from zero. Now, if the first-zonal signal at the output is of interest, only the term with $k = 1$ in (4.9) is retained and the output is given by:

$$y(t) = a_1[A(t)] \cos \theta(t) = a_1[A(t)] \cos[2\pi f_c t + \alpha(t)] \quad (4.18)$$

$F(x)$ being an odd function of x does not imply any parity for $a_1[A(t)]$ as a function of the argument $A(t)$. This statement is a key point. To confirm its validity, two different odd functions that produce different parities for $a_1[A(t)]$ will be presented. Remember that $T_1(u) = u$ was the initial condition for the recurrence equation in (4.16). Suppose the odd function $F_1(x) = x$. Substituting $F_1(x)$ in (4.13) for $k = 1$:

$$\begin{aligned} a_1(A) &= \frac{2}{\pi} \int_{-A}^A x \frac{x}{A} \frac{1}{\sqrt{A^2 - x^2}} dx \\ &= \frac{4}{\pi A} \int_0^A \frac{x^2}{\sqrt{A^2 - x^2}} dx \\ &= \frac{4}{\pi A} \left\{ \frac{1}{2} \left[-x\sqrt{A^2 - x^2} + A^2 \arcsin\left(\frac{x}{A}\right) \right]_{x=0}^{x=A} \right\} = A \end{aligned} \quad (4.19)$$

e.g. $a_1(A)$ is an odd function of the amplitude A if the odd nonlinearity is given by $F_1(x)$. This was a trivial case since $F_1(x)$ was a linear function.

Suppose the odd function $F_2(x) = x/|x|$. Substituting $F_2(x)$ in (4.13) for $k = 1$:

$$\begin{aligned} a_1(A) &= \frac{2}{\pi} \int_{-A}^A \frac{x}{|x|} \frac{x}{A} \frac{1}{\sqrt{A^2 - x^2}} dx \\ &= \frac{4}{\pi A} \int_0^A \frac{x}{\sqrt{A^2 - x^2}} dx \\ &= \frac{4}{\pi A} \left[-\sqrt{A^2 - x^2} \right]_{x=0}^{x=A} = \frac{4}{\pi} \end{aligned} \quad (4.20)$$

e.g. $a_1(A)$ is an even function of the amplitude A if the odd nonlinearity is given by $F_2(x)$. The signal at the output of the nonlinearity $F_2(x)$ is a square wave of amplitude 1 (the fundamental amplitude is $4/\pi$).

If the real-valued input $x(t) = A(t) \cos[2\pi f_c t + \alpha(t)]$ and output $y(t)$ signals are represented by their respective complex-valued envelopes $\tilde{x}(t) = A(t)e^{j\alpha(t)}$ and $\tilde{y}(t)$, then the low-pass equivalent representation for a band-pass nonlinearity is obtained:

$$\tilde{y}(t) = a_1[A(t)]e^{j\alpha(t)} = \frac{a_1[A(t)]}{A(t)} \tilde{x}(t) \quad (4.21)$$

Based on the parity definitions for complex-valued functions, $\tilde{y}(t)$ is an odd function of the argument $\tilde{x}(t)$, independently of the parity of $a_1[A(t)]$ as a function of the argument $A(t)$.

4.3 Theoretical development

In this section, theoretical analysis are provided first to show that a polynomial approximation at RF level imposes an additional constraint on low-pass equivalent PA behavioral models, by no means associated to the odd parity constraint imposed by the band-pass nature of RF devices excited by narrow-band signals, and then to justify the use of new odd-order terms in the proposed base-band derived extensions of Volterra-based models.

The discussion initially presented in Subsection 4.3.1 is limited to the polynomial memoryless case. Then, the concepts are extended to include models with memory, starting in Subsection 4.3.2 by the particular case of the MP model that estimates the output by the sum of one-dimensional, 1D, functions driven by distinct delayed input samples, followed by a general Volterra series analysis in Subsection 4.3.3 and concluded in Subsection 4.3.4 with the considerations for the extension of the particular dynamic deviation (DD) approach to the reduction of the number of parameters in a general Volterra series.

4.3.1 Memoryless polynomial models

Memoryless polynomial PA behavioral models, as well as some non polynomial models like the Saleh model [15], intended to model both AM-AM and AM-PM conversions observed in RF PAs, can be represented by the block diagram shown in Figure 4.1.

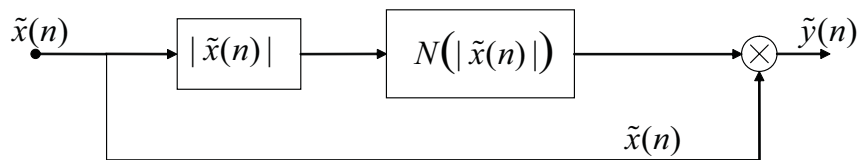


Figure 4.1: Memoryless PA behavioral model

The relationship between the complex-valued envelopes at the PA input and output,

represented by $\tilde{x}(n)$ and $\tilde{y}(n)$, respectively, is given by:

$$\tilde{y}(n) = \tilde{x}(n)N(|\tilde{x}(n)|) \quad (4.22)$$

where $N(|\tilde{x}(n)|)$ is a complex-valued nonlinear operator on the real-valued variable $|\tilde{x}(n)|$.

In Section 2.2, two equivalent representations for a PA memoryless behavioral model were presented, namely the series or polar representation and the quadrature or parallel representation. Both representations can have an equivalent description by the block diagram shown in Figure 4.1. Specifically, in the polar representation, $N(|\tilde{x}(n)|)$ is related to the AM-AM, $G(|\tilde{x}(n)|)$, and AM-PM, $\Psi(|\tilde{x}(n)|)$, conversions by:

$$N(|\tilde{x}(n)|) = \frac{G(|\tilde{x}(n)|)}{|\tilde{x}(n)|} e^{j\Psi(|\tilde{x}(n)|)} \quad (4.23)$$

while, in the quadrature representation, $N(|\tilde{x}(n)|)$ is related to the $S_I(|\tilde{x}(n)|)$ and $S_Q(|\tilde{x}(n)|)$ nonlinearities by:

$$N(|\tilde{x}(n)|) = \frac{S_I(|\tilde{x}(n)|)}{|\tilde{x}(n)|} + j \frac{S_Q(|\tilde{x}(n)|)}{|\tilde{x}(n)|} \quad (4.24)$$

According to (4.22), the complex-valued envelope $\tilde{y}(n)$ at the PA output can be seen as the product of two functions:

$$\begin{aligned} \tilde{y}(n) &= g_1[\tilde{x}(n)] \times g_2[\tilde{x}(n)] \\ \tilde{y}[I_x(n), Q_x(n)] &= g_1[I_x(n), Q_x(n)] \times g_2[I_x(n), Q_x(n)] \end{aligned} \quad (4.25)$$

where $g_1[\tilde{x}(n)] = \tilde{x}(n)$ and $g_2[\tilde{x}(n)] = N(|\tilde{x}(n)|)$. Applying the previous parity definitions for complex-valued functions, it is found that $g_1[\tilde{x}(n)]$:

$$\begin{aligned} g_1[I_x(n), Q_x(n)] &= I_x(n) + jQ_x(n) \\ g_1[-I_x(n), -Q_x(n)] &= -I_x(n) - jQ_x(n) = -[I_x(n) + jQ_x(n)] \\ g_1[-I_x(n), Q_x(n)] &= -g_1[I_x(n), Q_x(n)] \end{aligned} \quad (4.26)$$

is an odd function, while $g_2[\tilde{x}(n)]$:

$$\begin{aligned}
g_2[I_x(n), Q_x(n)] &= N(|I_x(n) + jQ_x(n)|) \\
g_2[I_x(n), Q_x(n)] &= N\left(\sqrt{I_x^2(n) + Q_x^2(n)}\right) \\
g_2[-I_x(n), -Q_x(n)] &= N(|-I_x(n) - jQ_x(n)|) \\
g_2[-I_x(n), -Q_x(n)] &= N\left(\sqrt{[-I_x(n)]^2 + [-Q_x(n)]^2}\right) \\
g_2[-I_x(n), -Q_x(n)] &= N\left(\sqrt{I_x^2(n) + Q_x^2(n)}\right) \\
g_2[-I_x(n), -Q_x(n)] &= g_2[I_x(n), Q_x(n)]
\end{aligned} \tag{4.27}$$

is an even function, independently of the particular expression for $N(.)$. In fact, the composition of any function with an even function is an even function and (4.27) is a particular example of this property.

Therefore, the complex-valued envelope $\tilde{y}(n)$ at the PA output can be seen as the product of an odd and an even function of the arguments $I_x(n)$ and $Q_x(n)$. As previously shown by (4.3), the product of an even function by an odd function results in an odd function. Hence, the complex-valued envelope $\tilde{y}(n) = \tilde{y}[I_x(n), Q_x(n)] = I_y(n) + jQ_y(n)$ at the PA output is an odd function of the complex-valued envelope $\tilde{x}(n) = I_x(n) + jQ_x(n)$ at the PA input, independently of the particular characteristic of the nonlinear operator $N(.)$. In other words, the odd parity constraint imposed by the band-pass nature of RF devices excited by narrow-band signals, shown in Section 4.2, is satisfied independently of the characteristic of the nonlinear operator $N(.)$.

The methodology followed in Chapters 2 and 3 begins with the expansion in a Volterra series of the system at RF level. For the particular memoryless case, it is possible to show [12] that the relationship between the complex-valued envelopes at the PA input and output, represented by $\tilde{x}(n)$ and $\tilde{y}(n)$, respectively, is given by:

$$\begin{aligned}
\tilde{y}(n) &= \sum_{p=1}^P \tilde{b}_{2p-1} |\tilde{x}(n)|^{2p-2} \tilde{x}(n) \\
&= \tilde{x}(n) N(|\tilde{x}(n)|)
\end{aligned} \tag{4.28}$$

where \tilde{b}_{2p-1} are complex-valued coefficients and the nonlinear operator $N(|\tilde{x}(n)|)$ is now given by:

$$N(|\tilde{x}(n)|) = \sum_{p=1}^P \tilde{b}_{2p-1} |\tilde{x}(n)|^{2p-2} \tag{4.29}$$

The polynomial approximation at RF level not only guarantees the necessary condition that the output must be an odd function of the input, but also assumes that $N(|\tilde{x}(n)|)$ is an even function of the argument $|\tilde{x}(n)|$, since it includes only even powers. However, there is not a physical justification for this additional constraint. If this additional non physical requirement is removed, then the polynomial expansion of $N(|\tilde{x}(n)|)$ in its argument $|\tilde{x}(n)|$ is complete and given by:

$$N(|\tilde{x}(n)|) = \sum_{p=0}^{P_0-1} \tilde{b}_{p+1} |\tilde{x}(n)|^p \quad (4.30)$$

where $P_0 = 2P - 1$ is the polynomial order truncation. Using this nonlinear operator $N(|\tilde{x}(n)|)$, (4.28) is extended to:

$$\begin{aligned} \tilde{y}(n) &= \sum_{p=1}^{P_0} \tilde{b}_p |\tilde{x}(n)|^{p-1} \tilde{x}(n) \\ &= \tilde{x}(n) N(|\tilde{x}(n)|) \end{aligned} \quad (4.31)$$

Since $|\tilde{x}(n)|$ can only assume positive values, the assumption that $N(|\tilde{x}(n)|)$ is an even function of $|\tilde{x}(n)|$ does not imply, analytically, any loss in modeling capability. For instance, the same reasoning would justify a model in which the nonlinear operator $N(|\tilde{x}(n)|)$ is assumed to be an odd function of $|\tilde{x}(n)|$ and, therefore, its polynomial expansion would include only odd powers. However, in practice, different behaviors are expected for the different choices of the nonlinear operator $N(|\tilde{x}(n)|)$, once these models are implemented in finite precision hardware. In Chapter 5, memoryless PA behavioral models using both $N(|\tilde{x}(n)|)$ given by (4.29) and (4.30) are used to fit measured input-output complex-valued envelopes in an RF PA and their accuracy are compared. If (4.28) is used, the model will be referred to as RF polynomial (RF Poly) memoryless model. If (4.31) is used, the model will be referred to as base-band polynomial (BB Poly) memoryless model.

A comparison between the BB Poly and RF Poly memoryless models was already performed in [80] and [81]. However, in [80] and [81] the additional terms of (4.31) with respect to (4.28) were misunderstood as even-order terms and the justification for their usage was that the polynomial approximation was not precise. In fact, despite the presented results show superior modeling accuracy for the BB Poly memoryless model

than for the RF Poly memoryless model, very few posterior works in PA behavioral modeling have adopted the Poly BB model. The majority of the posterior works in this field still neglect the additional terms of the BB Poly with respect to the RF Poly probably because of the improper use of the terminology even-order terms, combined to the very general and informal, from a mathematical point of view, justification for their usage. The purposes of the rigorous mathematical analysis just presented for memoryless polynomial models are threefold. First, to clarify that the additional terms in the BB Poly are actually odd-order terms. For instance, second-degree even-order terms are $|x|^2$ and x^2 . The term $x|x|$, by the reasons just presented, is an odd-order term. Besides, as shown earlier, even-order terms can not improve, even numerically, PA behavioral modeling. Second, to reinforce the possible improvements by the use of the BB Poly with respect to the RF Poly, in this way encouraging their usage by the microwave community. Third, the concepts presented for the memoryless model will be used in the extension of Volterra-based models in next subsections.

In the Saleh polar model [15], the AM-AM conversion is modeled by a rational odd function of the amplitude of the input signal $|\tilde{x}(n)|$, while the AM-PM conversion is modeled by a rational even function of the amplitude of the input signal. Additionally, in the Saleh quadrature model [15], both in-phase $S_I(|\tilde{x}(n)|)$ and quadrature $S_Q(|\tilde{x}(n)|)$ nonlinearities are modeled by rational odd functions of the amplitude of the input signal. Since $\Psi(|\tilde{x}(n)|)$ is an even function of $|\tilde{x}(n)|$, both $\cos \Psi(|\tilde{x}(n)|)$ and $\sin \Psi(|\tilde{x}(n)|)$ are also even functions of $|\tilde{x}(n)|$. Being $G(|\tilde{x}(n)|)$ an odd function of $|\tilde{x}(n)|$, then both $G(|\tilde{x}(n)|) \cos \Psi(|\tilde{x}(n)|)$ and $G(|\tilde{x}(n)|) \sin \Psi(|\tilde{x}(n)|)$ nonlinearities of the polar model are odd functions of the argument $|\tilde{x}(n)|$. Hence, the Saleh polar and quadrature models share the same parity with respect to the argument $|\tilde{x}(n)|$. More specifically, the function $N(.)$ of the Saleh model in both polar and quadrature representations are even functions not only of the argument $\tilde{x}(n)$, as required, but also even (division between two odd functions) functions of the argument $|\tilde{x}(n)|$, not necessary. In conclusion, both the polynomial approximation at RF level and the Saleh model imposes the non physical constraint that $N(|\tilde{x}(n)|)$ is an even function of the argument $|\tilde{x}(n)|$.

4.3.2 One-dimensional polynomial approximations

At this point, the concepts are extended to include models with memory. First of all, the particular case of 1D polynomial approximations is discussed. The extension of the concepts from the memoryless case to the memory polynomial (MP) model is straightforward. In fact, the complex-valued envelope at the PA output is given by the sum of memoryless models driven by distinct delayed input samples, as shown in Figure 4.2.

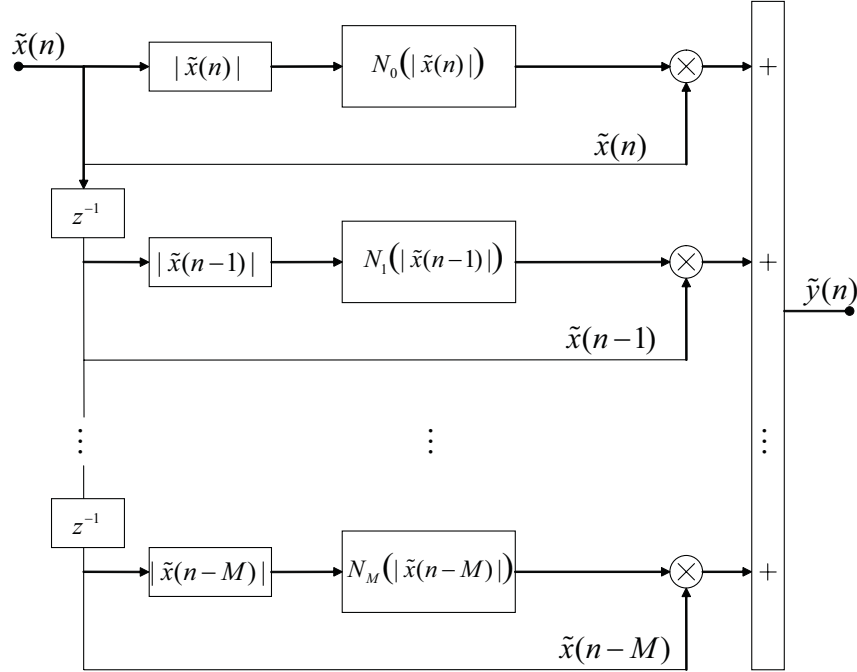


Figure 4.2: Memory polynomial (MP) PA behavioral model

The relationship between the complex-valued envelopes at the PA input and output, represented by $\tilde{x}(n)$ and $\tilde{y}(n)$, respectively, is given by:

$$\begin{aligned}
 \tilde{y}(n) &= \sum_{p=1}^P \sum_{m=0}^M \tilde{b}_{2p-1,m} |\tilde{x}(n-m)|^{2p-2} \tilde{x}(n-m) \\
 &= \sum_{m=0}^M \tilde{x}(n-m) N_m (|\tilde{x}(n-m)|)
 \end{aligned} \tag{4.32}$$

where each of the $(M + 1)$ nonlinear operators $N_m (|\tilde{x}(n - m)|)$, for $m = 0, \dots, M$, are given by:

$$N_m (|\tilde{x}(n - m)|) = \sum_{p=1}^P \tilde{b}_{2p-1,m} |\tilde{x}(n - m)|^{2p-2} \tag{4.33}$$

Each one-dimensional nonlinear operator $N_m(\cdot)$ in the MP model is assumed to be an even function of its argument $|\tilde{x}(n - m)|$. If, as was done in the memoryless case, this assumption is removed, then each $N_m(\cdot)$ is changed to:

$$N_m(|\tilde{x}(n - m)|) = \sum_{p=0}^{P_0-1} \tilde{b}_{p+1,m} |\tilde{x}(n - m)|^p \quad (4.34)$$

where $P_0 = 2P - 1$ is the polynomial order truncation. Using the nonlinear operators in (4.34), (4.32) is extended to:

$$\begin{aligned} \tilde{y}(n) &= \sum_{p=1}^{P_0} \sum_{m=0}^M \tilde{b}_{p,m} |\tilde{x}(n - m)|^{p-1} \tilde{x}(n - m) \\ &= \sum_{m=0}^M \tilde{x}(n - m) N_m(|\tilde{x}(n - m)|) \end{aligned} \quad (4.35)$$

In the MP model, the statement that the output is an odd function of the input has the following interpretation. The output is given by the sum of 1D functions of distinct delayed input samples. Each 1D contribution is an odd function of its own delayed input sample since it comes from the product of an odd function by an even function of the same argument. This is guaranteed individually by each 1D contribution and independently of the other contributions. Indeed, linear systems can only change the magnitude and phase of a spectral line applied to its input, but can not create spectral lines at its output. Since just nonlinear terms can change spectral content, in this particular inspection of which terms can be presented at the output pass-band, linear filters can be considered, without any loss, as constant gains.

In Chapter 5, PA MP behavioral models using both nonlinear functions $N_m(\cdot)$ given by (4.33) and (4.34) are used to fit measured input-output complex-valued envelopes in an RF PA and their accuracy are compared. If (4.32) is used, the model will be referred to as RF polynomial (RF Poly) MP model. If (4.35) is used, the model will be referred to as base-band polynomial (BB Poly) MP model.

Again, comparison between the BB Poly and RF Poly MP models was already performed in [80] and [81]. However, in [80] and [81] the additional terms of (4.35) respect to (4.32) were misunderstood as even-order terms, and the previous comments on this work reported in the memoryless case also apply for the MP case.

4.3.3 Volterra series

Now, the concepts are extended to include a general Volterra series. In this case, the extension of the concepts from the memoryless case is not straightforward, since each nonlinear operator $N_m(\cdot)$ is now a $(2M+2)$ -dimensional function, as shown in the equivalent representation of a Volterra series model in Figure 4.3.

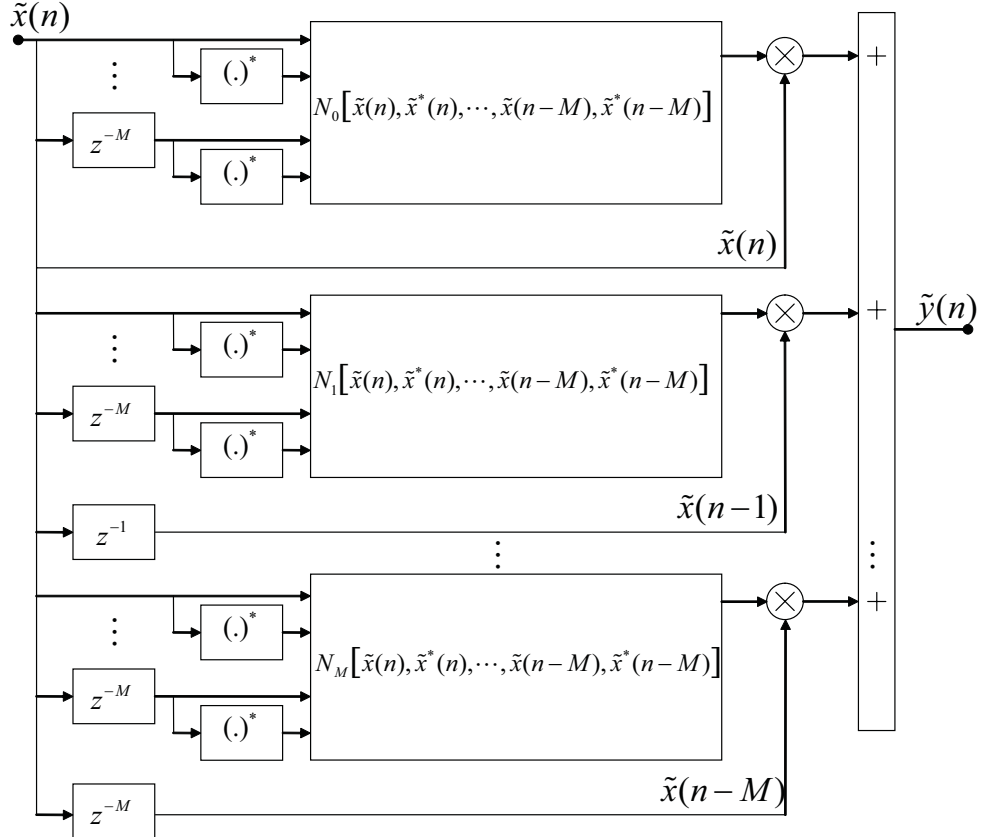


Figure 4.3: Volterra series PA behavioral model

The relationship between the complex-valued envelopes at the PA input and output, represented by $\tilde{x}(n)$ and $\tilde{y}(n)$, respectively, is given by:

$$\begin{aligned}
\tilde{y}(n) &= \sum_{p=1}^P \sum_{q_1=0}^M \sum_{q_2=q_1}^M \cdots \sum_{q_p=q_{p-1}}^M \sum_{q_{p+1}=0}^M \sum_{q_{p+2}=q_{p+1}}^M \cdots \sum_{q_{2p-1}=q_{2p-2}}^M \\
&\quad \times \tilde{h}_{2p-1}(q_1, q_2, \dots, q_{2p-1}) \prod_{j_1=1}^p \tilde{x}(n - q_{j_1}) \prod_{j_2=p+1}^{2p-1} \tilde{x}^*(n - q_{j_2}) \\
&= \sum_{m=0}^M \tilde{x}(n-m) N_m [\tilde{x}(n), \tilde{x}^*(n), \dots, \tilde{x}(n-M), \tilde{x}^*(n-M)] \tag{4.36}
\end{aligned}$$

where each of the $(M+1)$ nonlinear operators $N_m [\tilde{x}(n), \tilde{x}^*(n), \dots, \tilde{x}(n-M), \tilde{x}^*(n-M)]$, for $m = 0, \dots, M$, are $(2M+2)$ -dimensional functions given by:

$$N_m = \sum_{p=1}^P \sum_{q_2=m}^M \dots \sum_{q_p=q_{p-1}}^M \sum_{q_{p+1}=0}^M \sum_{q_{p+2}=q_{p+1}}^M \dots \sum_{q_{2p-1}=q_{2p-2}}^M \\ \times \tilde{h}_{2p-1}(m, q_2, \dots, q_{2p-1}) \prod_{j_1=2}^p \tilde{x}(n - q_{j_1}) \prod_{j_2=p+1}^{2p-1} \tilde{x}^*(n - q_{j_2}) \quad (4.37)$$

In the discrete-time models with memory, the statement that the output is an odd function of the input is not a precise mathematical definition. In fact, it makes reference for just one input and one output. However, in discrete-time models with memory and without feedback, the instantaneous output sample is modeled as a function of the instantaneous and previous input samples over the system memory span M . If the definitions given in (4.1) and (4.2) for even and odd two-dimensional complex-valued functions were extended to $(2M+2)$ -dimensional functions, and then the parity properties were applied to the $(2M+2)$ -dimensional nonlinear operators $N_m(\cdot)$, a too strong requirement, surely not satisfied by the Volterra series nonlinear operators in (4.37), would be necessary for the satisfaction of the statement that the output is an odd function of the inputs. A more viable, but less formal from a mathematical viewpoint, approach to guarantee that the output is an odd function of the input, is first map the $(2M+2)$ -dimensional nonlinear operators $N_m(\cdot)$ into one-dimensional functions whose argument is an equivalent complex-valued input, and then the previous definitions for even and odd complex-valued functions dependent on two real-valued variables are used to assess the parity properties. A simple way to do this is to consider that the same input sample, say \tilde{x} , is applied over the memory span M . Indeed, linear systems can only change the magnitude and phase of a spectral line applied to its input, but can not create new spectral lines at its output. Since just nonlinear terms can change spectral content, in this particular inspection of which terms can be present at the pass-band output, linear filters can be considered, without any loss, as constant gains. In that case, all the nonlinear functions $N_m(\cdot)$ in (4.37) will be even functions of the argument $|\tilde{x}|$, since only one time sample is involved and the number of non conjugate and conjugate input samples in the nonlinear functions $N_m(\cdot)$ is always the same. As a consequence, all the nonlinear operators $N_m(\cdot)$ will also be even functions of the argument \tilde{x} . Once again, the requirement that the $N_m(\cdot)$ are even

functions of the argument $|\tilde{x}|$ can be removed in (4.37) and then each nonlinear operator $N_m(\cdot)$ is given by:

$$N_m [|\tilde{x}(n)|, \dots, |\tilde{x}(n-m)|] = \sum_{p=1}^{P_0} \sum_{q_2=0}^M \sum_{q_3=q_2}^M \dots \sum_{q_p=q_{p-1}}^M \times \tilde{h}_p(m, q_2, \dots, q_p) \prod_{j=2}^p |\tilde{x}(n-q_j)| \quad (4.38)$$

where $P_0 = 2P - 1$ is the polynomial order truncation. Using the nonlinear operators $N_m(\cdot)$ in (4.38), (4.36) is extended to:

$$\tilde{y}(n) = \sum_{p=1}^{P_0} \sum_{q_1=0}^M \sum_{q_2=0}^M \sum_{q_3=q_2}^M \dots \sum_{q_p=q_{p-1}}^M \times \tilde{h}_p(q_1, q_2, \dots, q_p) \tilde{x}(n-q_1) \prod_{j=2}^p |\tilde{x}(n-q_j)| \quad (4.39)$$

Actually, (4.38) is an exact extension of (4.37) just in the memoryless case. The even-order terms in (4.37) are given by the product of an equal number of non conjugate and conjugate input samples (present or past), while in (4.38) all the terms are given by the product of magnitudes of present or past input samples.

To my knowledge, no previous work in PA behavioral modeling has used (4.38). In Chapter 5, Volterra series using both nonlinear operators $N_m(\cdot)$ given by (4.37) and (4.38) are used to fit measured input-output complex-valued envelopes in an RF PA and their accuracy are compared. If (4.36) is used, the model will be referred to as RF polynomial (RF Poly) Volterra series. If (4.39) is used, the model will be referred to as base-band polynomial (BB Poly) Volterra series.

4.3.4 Dynamic deviation reduction of Volterra series

Pruning approaches usually adopted in the complete Volterra series given by (4.36) can be performed, in the same way, in the base-band polynomial (BB Poly) Volterra series given by (4.39). For instance, the same reasoning done for the Volterra series could be applied to the dynamic deviation (DD) model proposed in [49] and described in Chapter 2, whose relationship between the complex-valued envelopes at the PA input and output, represented by $\tilde{x}(n)$ and $\tilde{y}(n)$ respectively, was given by (2.32). Here, just the final results

are presented. The extended DD model is given by:

$$\begin{aligned}
\tilde{y}(n) = & \sum_{p=1}^{P_0} \tilde{h}_p(0, \dots, 0) \tilde{x}(n) |\tilde{x}(n)|^{p-1} \\
& + \sum_{p=1}^{P_0} \sum_{r=1}^{\min\{p-1, R\}} \tilde{x}(n) |\tilde{x}(n)|^{p-1-r} \sum_{q_1=1}^M \dots \sum_{q_r=q_{r-1}}^M \\
& \quad \times \tilde{h}_p(0, \dots, 0, q_1, \dots, q_r) \prod_{j=1}^r |\tilde{x}(n - q_j)| \\
& + \sum_{p=1}^{P_0} \sum_{r=1}^{\min\{p, R\}} \sum_{q_1=1}^M \tilde{x}(n - q_1) |\tilde{x}(n)|^{p-r} \sum_{q_2=1}^M \dots \sum_{q_r=q_{r-1}}^M \\
& \quad \times \tilde{h}_p(q_1, 0, \dots, 0, q_2, \dots, q_r) \prod_{j=2}^r |\tilde{x}(n - q_j)| \tag{4.40}
\end{aligned}$$

where $P_0 = 2P - 1$ is the polynomial order truncation and $R \leq P_0$ is the dynamic order truncation.

To my knowledge, no previous work in PA behavioral modeling has used (4.40). In Chapter 5, dynamic deviation (DD) behavioral models given by (2.32) and (4.40) are used to fit measured input-output complex-valued envelopes in an RF PA and their accuracy are compared. If (2.32) is used, the model will be referred to as RF polynomial (RF Poly) dynamic deviation model. If (4.40) is used, the model will be referred to as base-band polynomial (BB Poly) dynamic deviation model.

4.4 Possible improvements in PA behavioral model performances

This section points out some possible improvements in PA behavioral modeling by the adoption of the proposed base-band approach in deriving a PA behavioral model.

The polynomial approximation at RF level excludes terms that in principle could be useful for efficient and parsimonious modeling of the relationship between the base-band complex-valued envelopes at the PA input and output. As an example, for narrow-band input signals $x(n)$, the pass-band output of $x(n)|x(n)|^p$, where p is even, is band-limited to $p + 1$ times the bandwidth of the input signal. On the other hand, the output of $x(n)|x(n)|$ is not band-limited. In particular cases, the proposed BB Poly models with a

second-degree polynomial truncation ($P_0 = 2$) could already be a good approximation for the whole measured PA pass-band spectrum.

Moreover, with similar number of parameters, the nonlinear operators $N[.]$ with only even-order terms of the RF Poly models require higher powers of the input signal than the nonlinear operators $N[.]$ with a complete polynomial approximation of the BB Poly models. As pointed out in [80] and [81], higher powers of the input make the numerical algorithms for parameter identification more ill-conditioned and the extrapolation is more catastrophic.

Chapter 5

Simulation and experimental results for PA behavioral modeling

In this chapter, the theoretical analysis of PA behavioral modeling presented in Chapters 2, 3 and 4 are validated using input-output data measured in a real RF PA.

In system identification terminology, the whole process of identification and validation of a model is called design of a experiment [85].

The first step in the design includes the choice of the input signal and the experimental measurement of the output signal. A general requirement common to all models is that the input signal must have a frequency content large enough to excite all the relevant system dynamics. A band-limited white noise input signal is the best choice to fulfill this requirement. In the specific case of RF PAs, two commonly performed measurements are multi-tone power sweep measurements using a vector network analyzer (VNA) and base-band time-domain measurements using a vector signal analyzer (VSA). A power meter must be present if absolute power levels are desired. In the first measurement, the voltage phasors at RF frequencies are measured. Similar input-output data could also be obtained by power sweep Harmonic Balance (HB) simulations in a circuit-equivalent model of a PA. If two or more tones are used as input, the input envelope is non constant, and the measurements at the output can be seen as time-averaged stationary envelope responses. If one-tone is used as input, the input envelope is constant and the measured output envelope is also constant. In the second measurement, an input signal with arbitrary amplitude and phase modulation is applied to the PA input and the complex-valued

envelope at the PA output is sampled at time instants taken at constant time interval. So, it is a transient time-domain base-band measurement. Similar input-output data could also be obtained by circuit-envelope simulations in a circuit-equivalent model of a PA.

The PA behavioral models investigated in this chapter relate the complex-valued envelopes at the PA input and output. Their particular application is in the real-time processing of the instantaneous envelope (voltage) signal. Only time-domain input-output base-band data is used. Its advantages over steady-state frequency-domain measurements include the arbitrary choice of amplitude and phase modulation and its direct application in the discrete-time constitutive equations describing the PA behavioral models, both for identification and validation purposes.

The schematic diagram of the experimental setup used for the input-output data collection is shown in Figure 5.1. The in-phase $x_I(t)$ and quadrature $x_Q(t)$ components of a complex-valued base-band signal $\tilde{x}(t) = x_I(t) + jx_Q(t)$ are applied to the arbitrary waveform generator (AWG) of a Rohde & Schwarz SMU200A vector signal generator (VSG). In the VSG, an IQ modulator up-converts the base-band signals $x_I(t)$ and $x_Q(t)$ to RF. The RF signal passes through the cascade of a driver followed by the PA. A Rohde & Schwarz FSQ vector signal analyzer (VSA) down-converts the RF signal at the PA output and stores the $y_I(t)$ and $y_Q(t)$ components of the complex-valued base-band output signal $\tilde{y}(t) = y_I(t) + jy_Q(t)$. The input signal is created in a personal computer, using the MATLAB software from the MathWorks, Inc. and stored in the VSG memory. No direct measurements of the input signal are performed. Hence, the considered device-under-test (DUT) is the complete cascade from the VSG to the VSA channel.

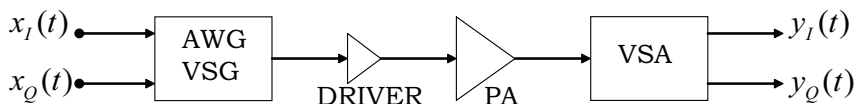


Figure 5.1: Schematic diagram of the experimental setup

The measured $y_I(t)$ and $y_Q(t)$ must be aligned with the applied input signal. This can be controlled by hardware and/or by software. By hardware, the VSG puts a marker in the first sample of the stored input sequence and then sends a trigger signal for the

VSA to synchronize the data acquisition. By software, a crosscorrelation between the amplitudes of the applied and measured envelopes is performed and the signals are aligned to maximize their crosscorrelation. After the alignment, a phase correction must be performed in the measured output sequence. The local oscillators (LOs) in the VGS and VSA used for up- and down-conversion, respectively, are synchronized in frequency by a 10MHz reference signal. However, a random phase difference between the LOs is still present and, at each data acquisition, all the complex-valued time-domain measured samples must be shifted in phase by a constant value.

The input signals used in the experimental results presented in this chapter are a single-carrier WCDMA-3GPP signal with a bandwidth of approximately 3.84MHz and a double-carrier WCDMA-3GPP signal with carrier frequency separation of 5MHz. The WCDMA signals [1] are pseudo-random signals that satisfy the above requirement of having a spectral content large enough to excite all the relevant PA dynamic effects.

The second step in the design is the choice of the model structure. This involves not only the selection of the particular topology, e.g. neural networks, Volterra series, block-oriented, among others, but also the selection of the truncation factors, namely the polynomial order P and memory length M for the Volterra series, and the number of hidden neurons R and memory length M for the neural networks. The justifications, guidance, proposition and validation of the particular topology for PA behavioral model is the main scope of this thesis. Regarding the truncation factor selection, it is done empirically and the details will be soon presented. In fact, statistical indicators such as Akaike's information criterion (AIC), Akaike's final prediction error (FPE) and Bayesian information criterion (BIC) are frequently used in literature for this purpose. However, their applicability are limited to the modeling of linear systems and no such equivalent indicators for the modeling of nonlinear systems are found in literature.

The final step in the design concerns the choice of the indicators for model performance assessment, the so-called figure of merits (FoMs), as well as the selection of the input-output data in which the FoMs are evaluated. A fundamental requirement is that the data used for the model extraction must be different from the data used for the model validation. This is because the noise present in the measurements combined with model topology mismatch can result in overfitting, e.g. increasing the number of parameters

can reduce the model error in the data sequence used for parameter extraction even if the new parameters are not present in the physical system, but due to noise or topology mismatch. Additionally, the numerical algorithms used for parameter extraction could be ill-conditioned, specially in the presence of overfitting, and the poor parameter identification could be masked if not validated with an input-output data sequence different from the one used in the identification process. For these reasons, a single measured input-output sequence is divided into two subsets: one subset is used for model extraction and the other one, for model validation. In others words, the models are not validated by their capability of predicting the envelope at the PA output when the PA is driven by significantly different input signals, but only to validate their capability of prediction within a same input class, particularly represented by WDCMA signals.

A commonly used FoM for the validation of PA behavioral models is the normalized mean square error (NMSE) [54], defined by:

$$NMSE = 10 \log_{10} \left[\frac{\sum_{n=1}^N |e(n)|^2}{\sum_{n=1}^N |y_{ref}(n)|^2} \right] \quad (5.1)$$

where $y_{ref}(n)$ is the reference complex-envelope signal at time instant n and $e(n) = y_{ref}(n) - y_{test}(n)$ is the error signal at time instant n defined as the difference between the reference $y_{ref}(n)$ and test $y_{test}(n)$ signals at time instant n . For the validation of PA behavioral models, the reference signal is the measured signal at the PA output and the test signal is the estimated signal at the PA behavioral model output when driven by the same input signal applied to the PA input. Just a remark, the NMSE calculated over the extraction input-output data subset is the cost function in the optimization processes for model identification, in both linear and nonlinear cases.

All the NMSE values reported in this chapter are calculated over the validation input-output data subset. These NMSE values are also used for the empirical selection of the truncation factors mentioned above. Specifically, for each particular chosen topology, several models with varying truncation factors are extracted and the corresponding NMSE values over the validation data subset are calculated. This process continues until an increasing in the truncation orders results in negligible improvements or degradation in

terms of NMSE.

The NMSE by itself can not provide a complete and rigorous validation for a PA behavioral model, mainly because it is strongly affected by the modeling errors in the in-band channel. A better FoM for the assessment of a PA behavioral model accuracy in the modeling of the spectral regrowth is the adjacent channel error power ratio (ACEPR) [17]:

$$ACEPR = 10 \log_{10} \left[\frac{\int_{adj} |E(f)|^2 df}{\int_{ch} |Y_{ref}(f)|^2 df} \right] \quad (5.2)$$

where $E(f)$ is the discrete Fourier transform of the error signal and $Y_{ref}(f)$ is the discrete Fourier transform of the reference signal. The integral in the denominator is over the main channel, while the integral in the numerator is over an upper or lower adjacent channel of same bandwidth as the main channel. Two additional specifications, namely the channel bandwidth BW and the frequency separation Δ_f between the center frequencies of the main and adjacent channels, must be stated for a unique evaluation.

Additionally to these two scalar FoMs, graphical representations are also presented for a better illustration of the model fidelity. Among them, the instantaneous output power as a function of the instantaneous input power (the instantaneous AM-AM conversion), the power spectral density (PSD), and the in-phase and quadrature time-domain waveforms are presented.

A discussion on the sampling frequency is now presented. Concerning the parameter identification of the Volterra-based structures, it is enough to sample the input and output signals at a sampling frequency that satisfies the Nyquist requirement for the input signal [86] and [87]. In other words, if the input and output signals are sampled at this minimum required frequency, then the aliased output signal could be used, without any loss, to the parameter identification. However, the same statement is not true for the three-layer perceptron training. Furthermore, to calculate the ACEPR FoM and to visualize the spectral regrowth prediction by the models, the sampling frequency of the input-output validation subset must satisfy the Nyquist requirement also at the PA output. In practice, some aliasing will occur at the PA output since the nonlinearity order is not known *a priori*. In conclusion, even if it would be possible to use, for the Volterra-based structures, an input-output extraction subset measured at a lower sampling frequency

and then applying interpolation techniques to implement and validate the model at a higher sampling frequency, it was preferred to use the same sampling frequency for both extraction and validation purposes. The chosen sampling frequency satisfies the Nyquist requirement at both input and output.

The obtained results are now presented in the following sequence: Section 5.1 presents the results of a comparative analysis of most PA behavioral models described in Chapter 2, then Section 5.2 presents the results for the validation of the low-pass equivalent PA behavioral model with feedback topology presented in Chapter 3 and finally Section 5.3 presents the improvements in PA behavioral modeling by the inclusion of the new terms proposed in Chapter 4. All the models were extracted and validated in the MATLAB software from The MathWorks, Inc. using a double-precision floating-point processor.

5.1 Comparative results of state-of-the-art PA behavioral models

This section uses input-output experimental data measured in an RF PA to make a comparative analysis of most of the PA behavioral models described in Chapter 2.

The low-pass equivalent representation of the Volterra series given by (2.17) is compared in terms of number of parameters and model accuracy with its simplified implementations:

- dynamic deviation (DD) model, given by (2.32);
- Wiener cascade, given by (2.33);
- Hammerstein cascade, given by (2.34);
- Wiener-Hammerstein or three-box cascade, given by (2.35);
- memory polynomial (MP) model , given by (2.41);
- physical pruning (PP), assuming that the only dynamic effects are due to base-band frequencies, given by (2.44);

- physical pruning (PP), assuming that the dynamic effects are due to base-band and second-band frequencies, given by (2.45).

These models have already been reported in PA behavioral modeling literature, but no comparative analysis within such framework have been previously reported. All the cited simplified implementations are low-pass equivalent versions in which the kernel symmetry was assumed. According to [12], only odd-order terms are present and the number of conjugate input samples (instantaneous or past samples) is always one less than the number of non conjugate input samples. The simplified implementations will be sometimes referred to as Volterra-based models.

Additionally, a three-layer perceptron (TLP), described in Section 2.3.1, is implemented and included in the comparative analysis. The complex-valued PA input signal is decomposed into its real-valued in-phase $x_I(t)$ and quadrature $x_Q(t)$ components. Both $x_I(t)$ and $x_Q(t)$ components, together with their delayed samples, are applied as inputs to a real-valued TLP having two outputs that estimate the in-phase $y_I(t)$ and quadrature $y_Q(t)$ components of the complex-valued signal at the PA output.

The comparative analysis is presented in two distinct case studies.

5.1.1 Case study 1: one carrier WCDMA input signal

In the first case study, time-domain measurements were performed in a class AB PA with GaN based technology, driven by a WCDMA 3GPP signal of bandwidth 3.84 MHz and peak-to-average power ratio (PAPR) of 11.6 dB, for an average output power of 26 dBm. The sampling frequency was set to 61.44 MHz. The measured instantaneous AM-AM conversion is shown in Figure 5.2. The ACEPR results presented in this subsection use a bandwidth of $BW = 3.84$ MHz for both main and adjacent channels.

Attention was paid to avoid extrapolation. Specifically, the minimum and maximum instantaneous values of both in-phase I_x and quadrature Q_x components of the input signal as well as the maximum instantaneous magnitude of the input signal in the validation subset were guaranteed to be inside their respective ranges in the extraction subset, as shown in Table 5.1.

Initially, several Volterra models with different P and M were extracted to model the

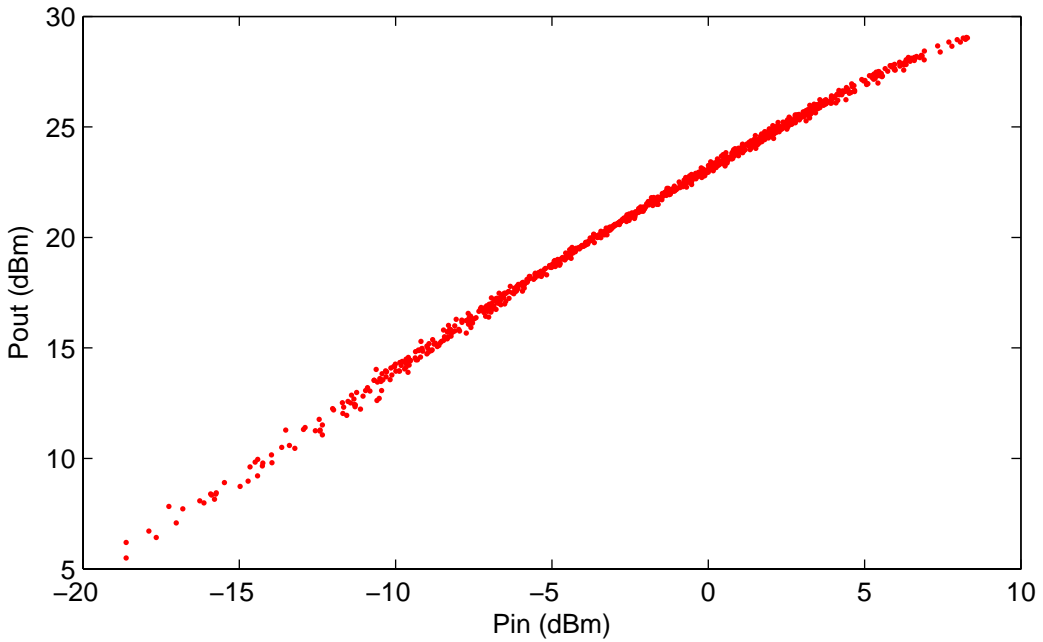


Figure 5.2: Measured instantaneous AM-AM conversion

Table 5.1: Range of the input signals in the extraction and validation subsets

Input-output data subset	minimum of I_x	maximum of I_x	minimum of Q_x	maximum of Q_x	maximum of $ \tilde{x}(t) $
Extraction	-0.8915	0.9558	-0.8955	0.7862	1.0477
Validation	-0.7545	0.7045	-0.6670	0.6741	0.8213

relationship between the measured complex-valued envelopes at the PA input and output. Table 5.2 shows the NMSE and ACEPR results, as well as the number of complex-valued parameters N in each case. The number of complex-valued parameters was limited to 300 due to hardware, specifically physical memory, limitations.

Using the empirical procedure described earlier and based on NMSE results, the best Volterra model in Table 5.2 was chosen as the one with $P = 7$ and $M = 1$. With respect to the best selected model, 0.2 dB improvements in NMSE were obtained with $P = 8$ and $M = 1$ by the addition of 72 complex-valued coefficients. However, the trade-off between improvements in accuracy and increasing in the number of parameters was considered worse in the latter case. The Volterra models with $P = 4$ and $M = 3$, and with $P = 5$ and $M = 2$, were not extracted because they would require 944 and 546 complex-valued

Table 5.2: NMSE and ACEPR results for the Volterra series with different P and M

P	M	N	NMSE (dB)	ACEPR _{LW} (dB) $\Delta_f =$ 10 MHz	ACEPR _{LW} (dB) $\Delta_f =$ 5 MHz	ACEPR _{UP} (dB) $\Delta_f =$ 5 MHz	ACEPR _{UP} (dB) $\Delta_f =$ 10 MHz
3	2	81	-40.02	-60.47	-48.81	-49.65	-60.84
3	3	244	-40.03	-60.41	-49.04	-49.36	-60.88
4	1	40	-42.95	-61.36	-51.27	-52.16	-62.04
4	2	231	-43.20	-61.26	-51.28	-50.83	-62.24
5	1	70	-45.25	-62.22	-53.50	-55.59	-63.68
6	1	112	-47.59	-63.53	-56.06	-58.04	-64.51
7	0	7	-36.03	-65.12	-45.19	-45.30	-65.66
7	1	168	-49.16	-65.81	-59.86	-60.04	-66.46
8	1	240	-49.40	-66.26	-61.08	-60.23	-66.80

parameters, respectively. The model with $P = 7$ and $M = 0$ is a memoryless model. It was included in Table 5.2 to show the improvements in model fidelity by the inclusion of memory. Specifically, the difference in NMSE between the memoryless model and the best Volterra is 13.1 dB, while the improvements in ACEPR for a 5 MHz separation between the adjacent and main channels are 14.7 dB for both upper and lower adjacent channels. On the other hand, improvements in ACEPR for a 10 MHz separation between the adjacent and main channels of just 0.7 dB and 0.8 dB were observed for the lower and upper adjacent channels, respectively. For the best Volterra model, the measured and modeled instantaneous AM-AM conversions are shown in Figure 5.3, while the power spectral densities (PSDs) of the measured and modeled output signals, and also of the error signal between them, are shown in Figure 5.4.

As a first comparison, the simplified implementations of the Volterra model were extracted for the previously chosen $P = 7$ and $M = 1$. The NMSE and ACEPR results obtained for the Volterra-based models, as well as the number of complex-valued parameters N in each case are reported in Table 5.3. The Volterra, dynamic deviation (DD) and memory polynomial (MP) models were extracted using least squares (LS), specifically QR factorization. In the case of the physical pruning (PP) model, an additional linear finite-

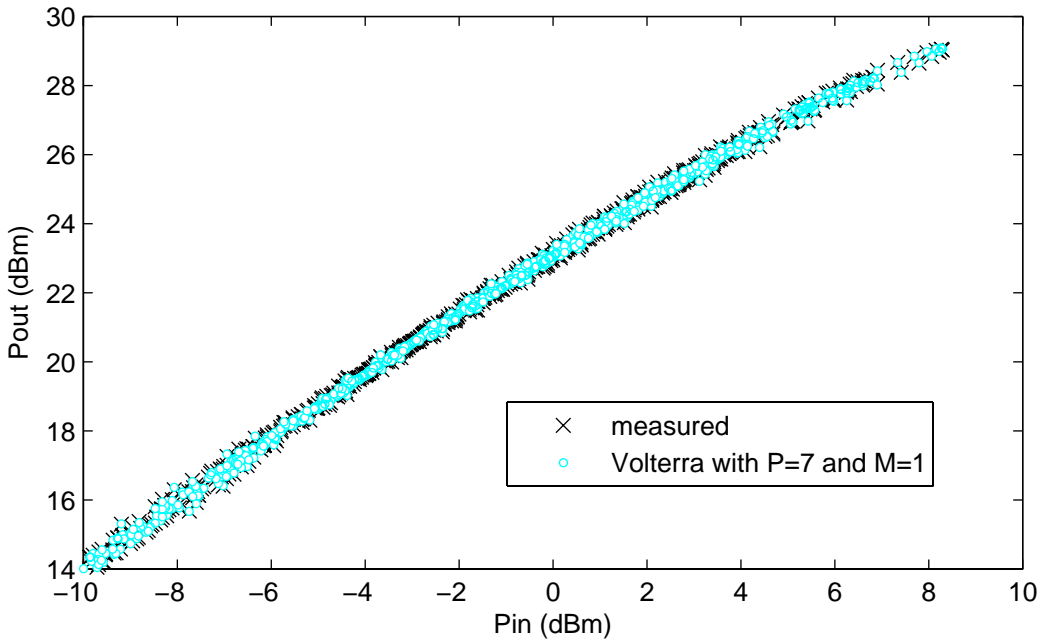


Figure 5.3: Instantaneous AM-AM conversions: measured and estimated by a Volterra series with $P = 7$ and $M = 1$

impulse response (FIR) filter with three complex-valued taps was put in front of the PP model to account for the memory effects observed in small-signal operation. The physical justification is that the driver used in the experimental setup does not have a flat response within the bandwidth of operation. These three additional complex-valued parameters were included in the total number of parameters presented in Table 5.3. The PP model plus input filter parameter extraction was done using a separable least squares (SLS). Just the input filter taps were optimized by a nonlinear algorithm, since once the input filter is known the model is linear in the remaining parameters. Concerning the block-oriented Wiener, Hammerstein and three-box structures, the parameters identification were done using SLS.

The best result in NMSE shown in Table 5.3 is -49.18 dB for the dynamic deviation (DD) model with $R = 4$. If the particular Volterra series with $P = 7$ and $M = 1$ was not overfitted and also its parameter extraction was not affected by numerical ill-conditioning problems, then the Volterra series would present the best result in NMSE, since all the other models reported in Table 5.3 are simplifications of it. Indeed, the NMSE result for the Volterra series is only slightly (a difference of 0.02 dB) worse than the one for the

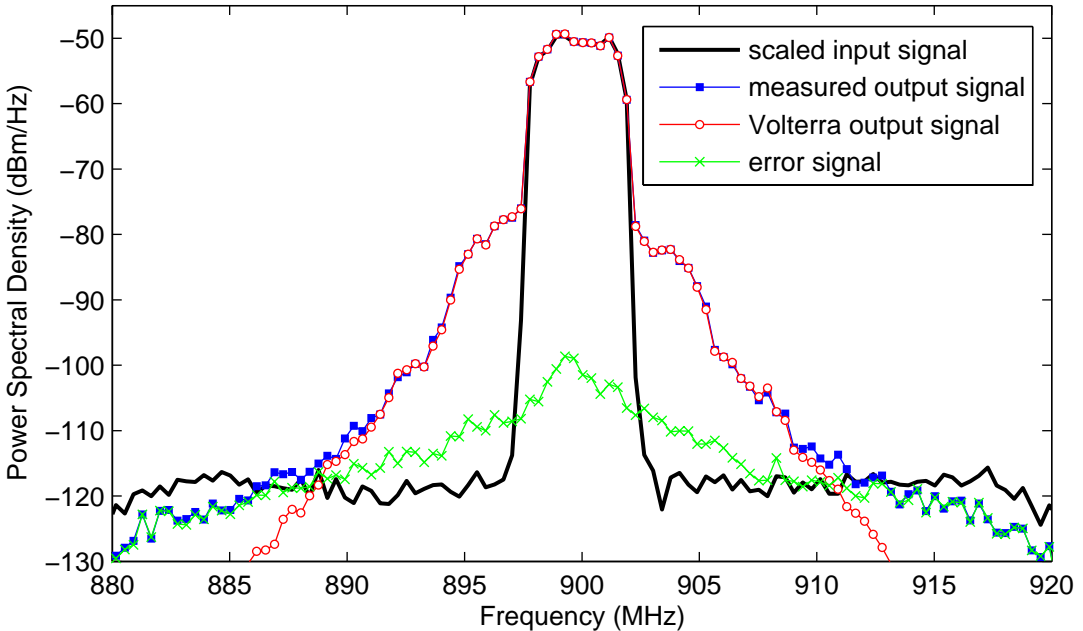


Figure 5.4: Power spectral densities of the measured output signal, modeled output signal by a Volterra series ($P = 7$ and $M = 1$) and error signal

DD model with $R = 4$. However, the DD model uses only 78 complex-valued coefficients from the total 168 complex-valued coefficients of the Volterra series. This means that this particular Volterra series is clearly overfitted, but the overfitting has almost negligible influence on the numerical algorithm used for the Volterra parameter identification.

The worst results both in NMSE and ACEPR shown in Table 5.3 are for the block-oriented structures. Differences of about 10.6 dB in NMSE and 14.8 dB in ACEPR_{LW} for $\Delta_f = 5$ MHz are observed between the Wiener model and the DD model with $R = 4$. The three-box structure only improves the Wiener results in NMSE by 1.2 dB and in ACEPR_{LW} for $\Delta_f = 5$ MHz by 1.3 dB, while the Hammerstein cascade has a performance in between the Wiener and the three-box structures. This is expected since the block-oriented models have the simplest topologies and their accuracy for the modeling of the PA nonlinear dynamic effects is limited. Figure 5.5 shows the measured and modeled instantaneous AM-AM conversions. Whereas the measured and Volterra modeled AM-AM conversions are almost indistinguishable, the Wiener and three-box modeled AM-AM conversions are visibly different at moderate and high input power.

Even if the memory polynomial (MP) model has a NMSE of about 5.9 dB worse than

Table 5.3: NMSE and ACEPR results with $P = 7$ and $M = 1$

Model	N	NMSE (dB)	ACEPR _{LW} (dB) $\Delta_f =$ 10 MHz	ACEPR _{LW} (dB) $\Delta_f =$ 5 MHz	ACEPR _{UP} (dB) $\Delta_f =$ 5 MHz	ACEPR _{UP} (dB) $\Delta_f =$ 10 MHz
Volterra	168	-49.16	-65.81	-59.86	-60.04	-66.46
MP	14	-43.31	-65.38	-54.62	-54.24	-66.41
DD ($R = 1$)	20	-48.59	-65.44	-58.96	-58.90	-66.58
DD ($R = 2$)	37	-49.14	-65.82	-60.04	-60.35	-66.73
DD ($R = 3$)	57	-49.15	-65.93	-59.87	-60.44	-66.89
DD ($R = 4$)	78	-49.18	-65.89	-59.93	-59.97	-66.18
DD ($R = 5$)	99	-49.17	-65.75	-59.88	-60.01	-66.18
DD ($R = 6$)	118	-49.17	-65.69	-59.88	-60.21	-66.46
PP (Δ_f)	31	-48.27	-64.73	-58.92	-59.51	-66.58
Wiener	9	-38.63	-65.10	-45.18	-45.41	-65.72
Hammerstein	9	-39.26	-65.21	-45.72	-46.06	-65.84
three-box	11	-39.80	-64.90	-46.51	-46.92	-65.21

the Volterra series, their instantaneous AM-AM conversions shown in Figure 5.5 are very similar. However, the differences between the MP model and the Volterra series are clearly observed in the PSDs of the error signals between the measured and modeled outputs, as shown in Figure 5.6. The 5.2 dB and 5.8 dB differences in ACEPR_{LW} and ACEPR_{UP} for $\Delta_f = 5$ MHz between the MP model and the Volterra series are in accordance with Figure 5.6. The instantaneous AM-AM conversions modeled by the PP model and DD model with $R = 4$ are indistinguishable from the Volterra series modeled AM-AM conversion. Besides, as shown in Figure 5.6, the PSDs of the error signals for the PP, DD and Volterra models are very close. The largest difference among them, in Table 5.3, is 0.9 dB in NMSE and 1.0 dB in ACEPR for $\Delta_f = 5$ MHz.

Two advantages of the simplified implementations of the Volterra series were proved in Table 5.3. First, a reduction in the number of parameters without compromising the accuracy of the complete Volterra model. As examples, the DD model with $R = 2$ reduced the number of parameters from 168 to 37 with a deterioration of less than 0.1 dB in NMSE

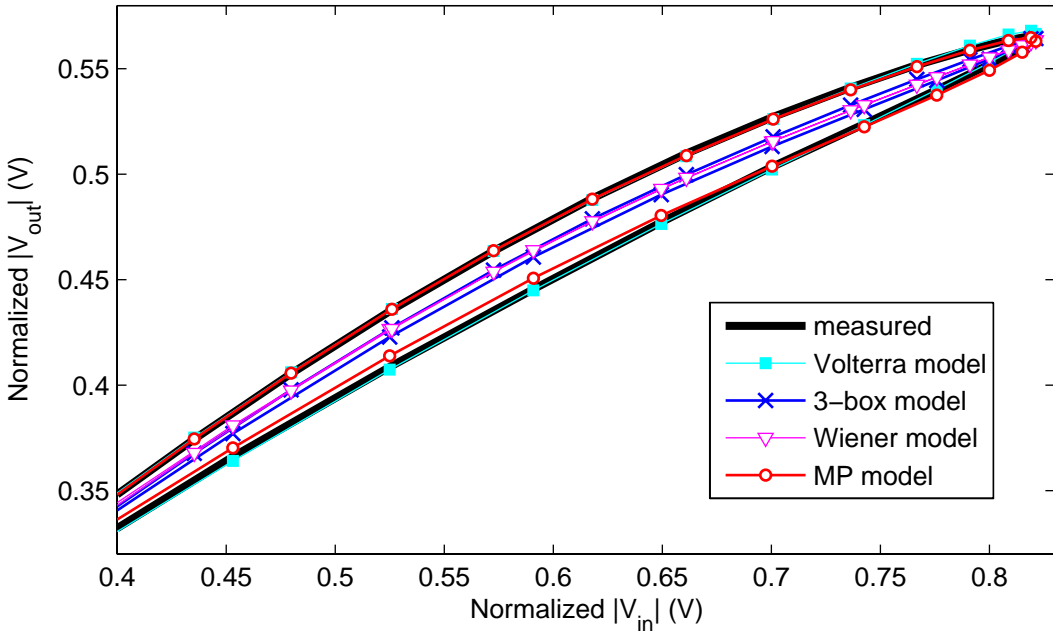


Figure 5.5: Samples of instantaneous AM-AM conversions: measured and estimated by different PA behavioral models with $P = 7$ and $M = 1$

but an amelioration of 0.3 dB in ACEPR_{UP} for $\Delta_f = 5$ MHz, while the PP model reduced the number of parameters to 31 with an increasing of only 0.9 dB in NMSE, 0.9 dB in ACEPR_{LW} and 0.5 dB in ACEPR_{UP} for $\Delta_f = 5$ MHz. Second, a finer checking on model overfitting and numerical problems was possible by the simplified implementations of the Volterra series. In fact, based on the results for the DD model with $R = 4$ in Table 5.3, it was possible to confirm the overfitting in the Volterra series and DD models with $R \geq 5$.

Another advantage of using simplified Volterra models is that the reduced number of parameters allows to the extraction of models with higher polynomial order and longer memory length, which is not possible for the complete Volterra model due to the huge number of parameters. In other words, simplified Volterra models can produce better results than the complete Volterra series if their number of parameters are similar. The NMSE and ACEPR results for the best simplified Volterra models, based on the empirical truncation factors procedure using the NMSE results detailed earlier and for a number of complex-valued parameters limited to 300, are shown in Table 5.4, as well as the respective number of complex-valued parameters N . In the input-output data for model extraction and validation used in this case study , the nonlinear effects are dominant over

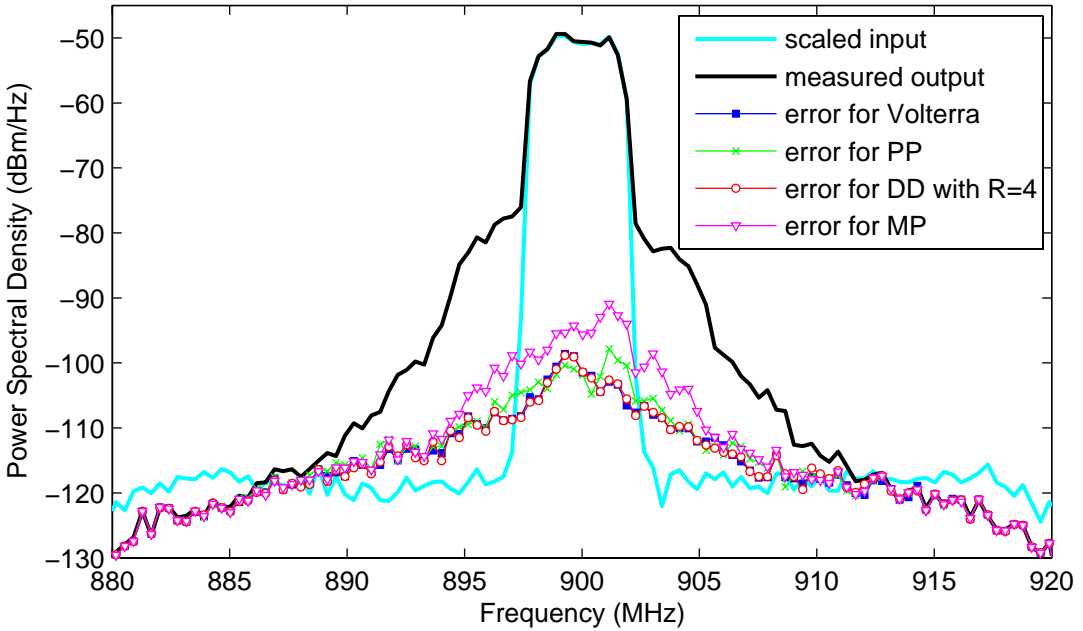


Figure 5.6: PSDs of the error signals for different PA behavioral models with $P = 7$ and $M = 1$

the dynamic ones. The polynomial order $2P - 1 = 13$ of the extracted Volterra model was already accurate enough for the modeling of this dominant nonlinear behavior, since the best results for all the simplified implementations have $P = 7$. On the other hand, the maximum memory length $M = 1$ that could be extracted for a Volterra series with $P = 7$, considering that the number of parameters is limited to 300, was not accurate enough for the modeling of the system dynamics, since the best results in NMSE and ACEPR_{UP} for $\Delta_f = 5$ MHz in Table 5.4 were 1.7 dB and 2.2 dB better than the respective results in Table 5.3 for the Volterra series with $P = 7$ and $M = 1$. For instance, a Volterra series with $P = 7$ and $M = 2$ or $M = 3$ would require 2142 or 17688 complex-valued parameters, respectively. As a conclusion, in this case study, and for a number of parameters limited to 300, it was possible to obtain best absolute results in both NMSE and ACEPR FoMs for the DD and PP models than for the Volterra series.

At this point, the improvements in the single models by changing the memory length are investigated. The improvements in the DD model with $R = 2$ by increasing M from 1 to 3 were 1.7 dB in NMSE, 1.3 dB in ACEPR_{LW} and 1.8 dB in ACEPR_{UP} for $\Delta_f = 5$ MHz, while the improvements for the PP model by the same change in M were 1.4 dB in NMSE, 1.9 dB in ACEPR_{LW} and 2.7 dB in ACEPR_{UP} for $\Delta_f = 5$ MHz, and finally the

Table 5.4: NMSE and ACEPR results for the best choices of P and M

Model	P	M	N	NMSE (dB)	ACEPR _{LW} (dB) $\Delta_f =$ 10 MHz	ACEPR _{LW} (dB) $\Delta_f =$ 5 MHz	ACEPR _{UP} (dB) $\Delta_f =$ 5 MHz	ACEPR _{UP} (dB) $\Delta_f =$ 10 MHz
MP	7	3	28	-43.83	-65.64	-56.76	-55.41	-66.79
DD ($R = 2$)	7	3	166	-50.85	-66.30	-61.35	-62.12	-67.23
PP (Δ_f)	7	3	213	-49.62	-65.45	-60.83	-62.23	-66.95
Wiener	7	2	10	-38.66	-65.11	-45.16	-45.44	-65.72
Hammerstein	7	3	11	-40.30	-61.91	-48.96	-49.19	-62.90
three-box	7	4	17	-41.47	-60.73	-53.08	-51.46	-62.54

improvements for the MP model by the same change in M were 0.5 dB in NMSE, 2.1 dB in ACEPR_{LW} and 1.2 dB in ACEPR_{UP} for $\Delta_f = 5$ MHz. The Wiener cascade improvements from $M = 1$ to $M = 2$ are negligible and differences always lower than 0.1 dB for the used FoMs were observed. The larger improvements were observed for the three-box model, specifically 1.7 dB in NMSE, 6.6 dB in ACEPR_{LW} and 4.5 dB in ACEPR_{UP} for $\Delta_f = 5$ MHz. Considerable improvements for the Hammerstein cascade were also reported, including 1.0 dB in NMSE, 3.2 dB in ACEPR_{LW} and 3.1 dB in ACEPR_{UP} for $\Delta_f = 5$ MHz.

In Figure 5.7 is shown the measured and modeled instantaneous AM-AM conversions, according to several approaches, using the best choices for P and M presented in Table 5.4. The AM-AM conversions modeled by the DD and MP models are very close to the measured one, while the block-oriented modeled AM-AM conversions are visibly different from the measured one. However, the improvements of the three-box model over the Wiener cascade are considerable.

In Figure 5.8 is shown the PSDs of the measured output signal and of the error signals for some of the simplified implementations with M and P according to Table 5.4. Also included is the error signal for the memoryless model with $P = 7$. The spectrum of the error signals for the Wiener and memoryless models differs only at the in-band frequencies. If their FoMs are compared, the Wiener model improves the NMSE in 2.6 dB, while differences lower than 0.2 dB are observed in the ACEPR. This proves the previous mentioned in-band influence on the NMSE FoM. Additionally, the similar behavior of the

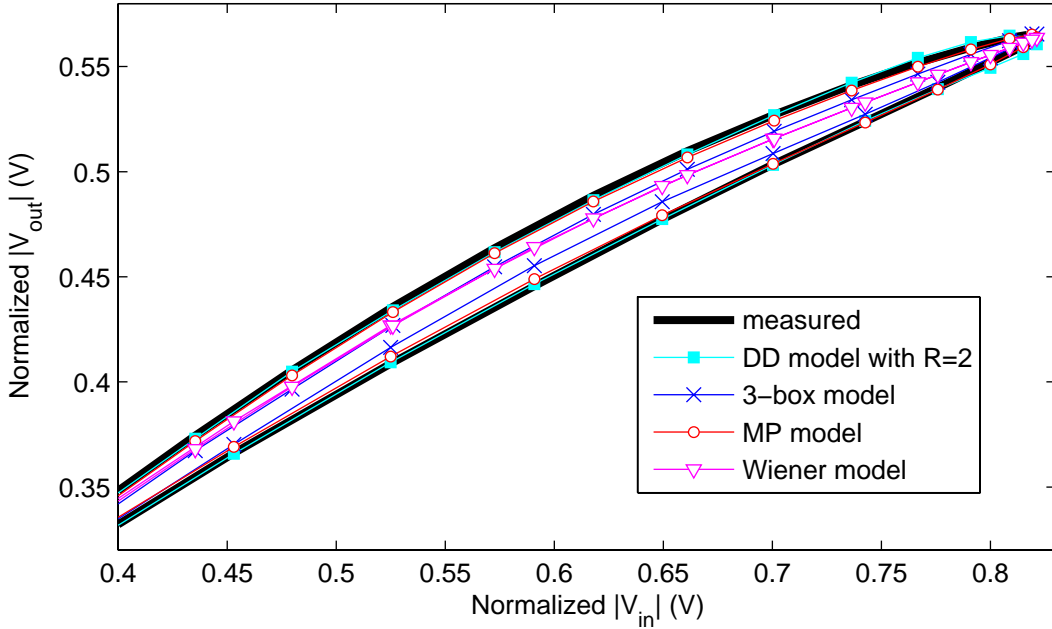


Figure 5.7: Samples of instantaneous AM-AM conversions: measured and estimated by different PA behavioral models with M and P given by Table 5.4

Wiener and memoryless models at the adjacent channels could also be inferred by the very thin AM-AM conversion of the Wiener cascade at high input power, shown in Figure 5.5. Furthermore, in Figure 5.8 the three-box error spectrum is considerably better than the Wiener one and the DD model with $R = 2$ clearly has the lower error.

As another possible comparison, Table 5.5 shows the NMSE and ACEPR results obtained with the MP, DD and PP models for a particular case in which they have a similar number of complex-valued parameters.

Table 5.5: NMSE and ACEPR results for the Volterra-based models with similar number of parameters

Model	P	M	N	NMSE (dB)	ACEPR _{LW} (dB) $\Delta_f =$ 10 MHz	ACEPR _{LW} (dB) $\Delta_f =$ 5 MHz	ACEPR _{UP} (dB) $\Delta_f =$ 5 MHz	ACEPR _{UP} (dB) $\Delta_f =$ 10 MHz
MP	7	3	28	-43.83	-65.64	-56.76	-55.41	-66.79
DD ($R = 1$)	7	2	33	-49.05	-65.57	-59.47	-60.00	-66.65
PP (Δ_f)	7	1	31	-48.27	-64.73	-58.92	-59.51	-66.58

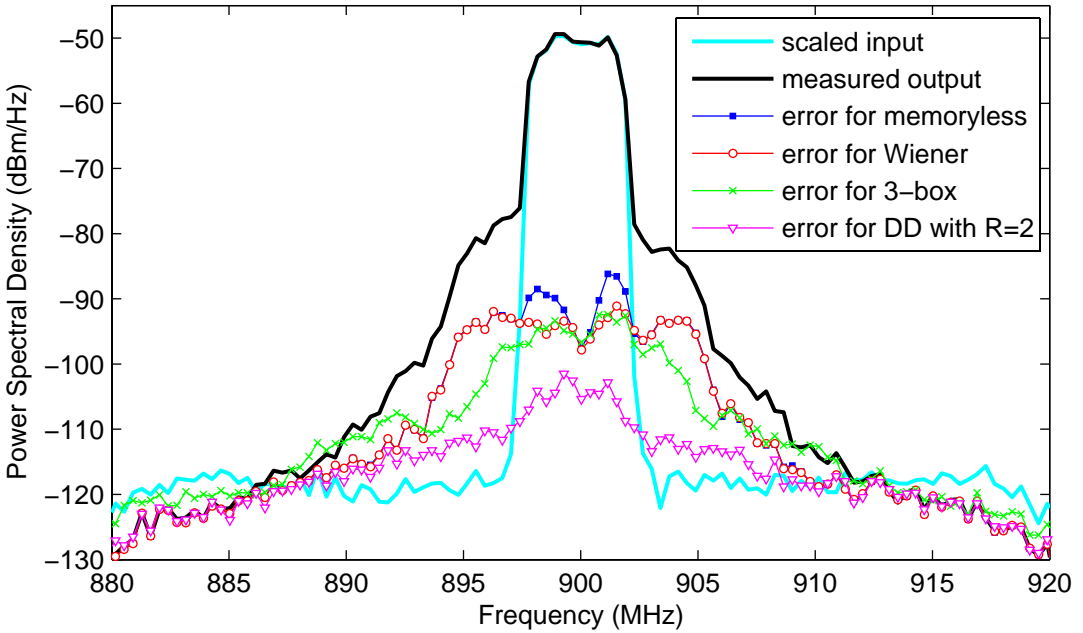


Figure 5.8: PSDs of the error signals for different PA behavioral models with M and P given by Table 5.4

In Figure 5.9 is shown that the measured and modeled instantaneous AM-AM conversions by the MP, DD and PP using the P and M values presented in Table 5.5 are very close to each other. Moreover, using about 30 complex-valued parameters it was possible to accurately model the measured instantaneous AM-AM conversion.

In Figure 5.10 is shown that the PSD of the error signal for the MP model is clearly larger than the PSDs of the error signals for the DD and PP models using for P and M the values presented in Table 5.5, specially at the in-band and adjacent channels. This is in accordance with the ACEPR results presented in Table 5.5.

The in-phase and quadrature time-domain waveforms measured and estimated by the PP model with $P = 7$ and $M = 1$ at the PA output are shown in Figure 5.11. An excellent agreement is observed in both in-phase and quadrature components.

At this moment, the parameter extraction of the Wiener and Hammerstein cascades are investigated. In SubSection 2.4.2, an alternative approach for the nonlinear optimization, based on time-domain input-output data and previously proposed in [41] and [50], was described as a sub-optimal procedure for the parameter extraction. Tables 5.6 and 5.7 show the NMSE results for the Wiener and Hammerstein cascades, respectively, in which

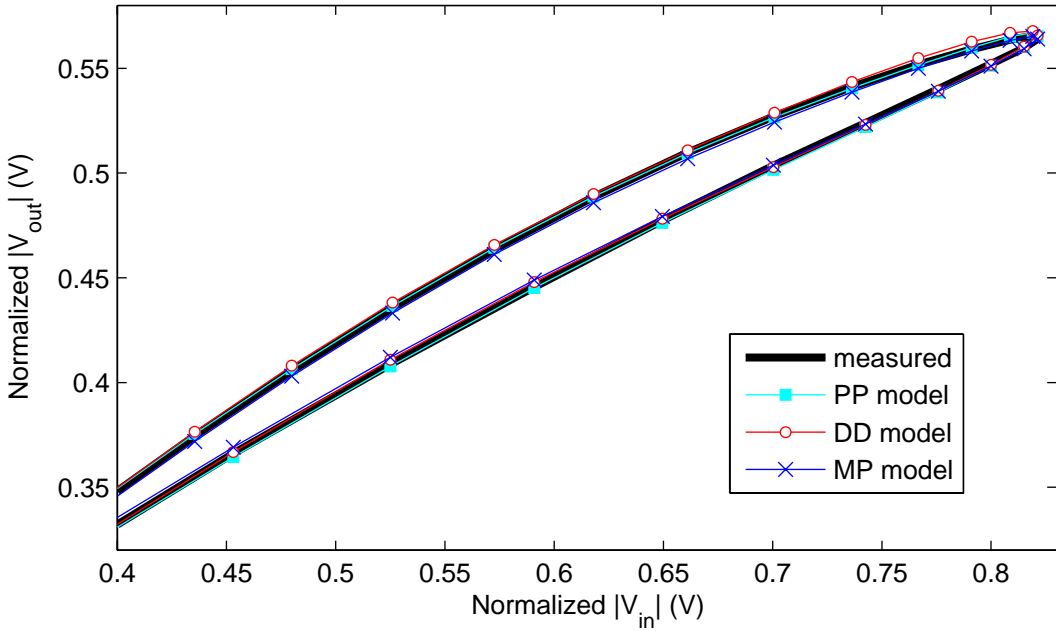


Figure 5.9: Samples of instantaneous AM-AM conversions: measured and estimated by different PA behavioral models with M and P given by Table 5.5

the parameters were extracted both by the nonlinear separable least square (SLS) optimization, and by the alternative iterative procedure. The largest differences in terms of NMSE between the two extraction strategies were lower than 0.6 dB in the Wiener case, and lower than 0.1 dB in the Hammerstein one. This shows that the loss in modeling accuracy by the use of a sub-optimal parameter extraction instead of a more computationally demanding optimal nonlinear procedure is much lower than the inevitable loss in accuracy by the choice of block-oriented topologies, and this encourages the use of the iterative procedure for block-oriented Wiener and Hammerstein cascades.

At this point, a TLP PA behavioral model is included in the comparison. Table 5.8 shows the NMSE and ACEPR results obtained by a PA modeled by a TLP with $M = 1$, and varying number of hidden neurons R , as well as the number of real-valued parameters in each case. The TLP training is a nonlinear process and the estimated parameters can be different if the initial conditions are changed. The best NMSE and ACEPR results are for the TLP with $R = 18$. This TLP, compared to the DD model with $R = 4$, $P = 7$ and $M = 1$, deteriorates 2.2 dB in NMSE, and 5.7 dB in ACEPR_{LW} and 3.6 dB in ACEPR_{UP} for $\Delta_f = 5 \text{ MHz}$.

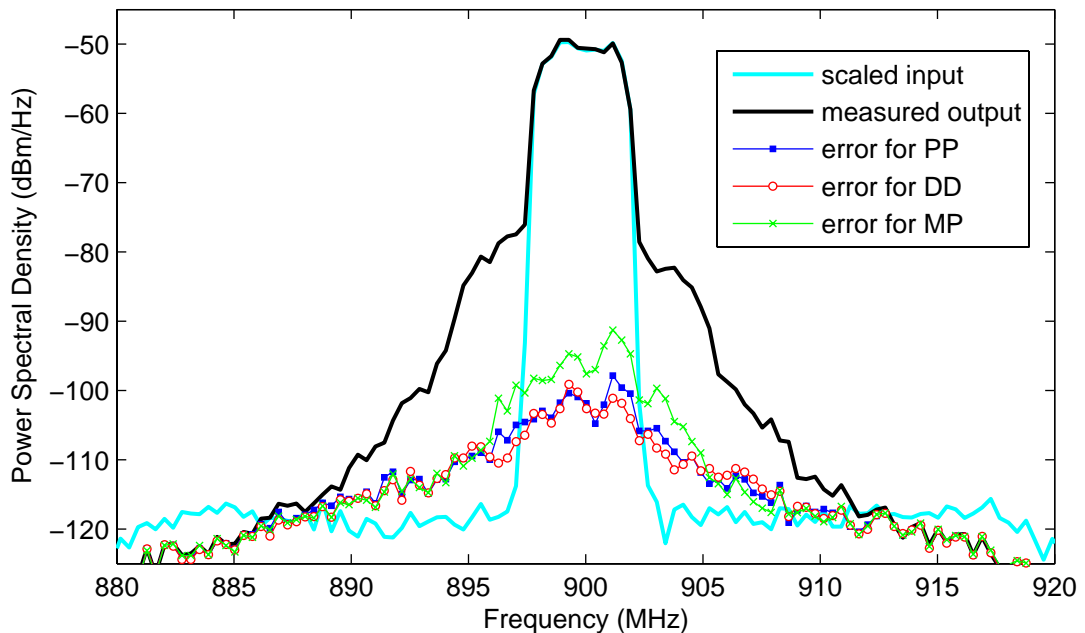


Figure 5.10: PSDs of the error signals for different PA behavioral models with M and P given by Table 5.5

Table 5.6: NMSE results for a Wiener PA behavioral model

P	M	N	NMSE (SLS)	NMSE (iterative procedure)
4	1	6	-37.17	-37.57
4	2	7	-37.18	-37.59
5	1	7	-37.68	-38.13
5	2	8	-37.68	-38.15
6	1	8	-37.95	-38.45
6	2	9	-37.96	-38.47
7	1	9	-38.12	-38.63
7	2	10	-38.13	-38.66
7	3	11	-38.10	-38.64

In Figure 5.12 is shown that the instantaneous AM-AM conversion modeled by the TLP with $R = 18$ and $M = 1$ differs from the one modeled by the DD with $R = 4$, $P = 7$ and $M = 1$ at high input power. Hence, the DD model estimates more accurately the

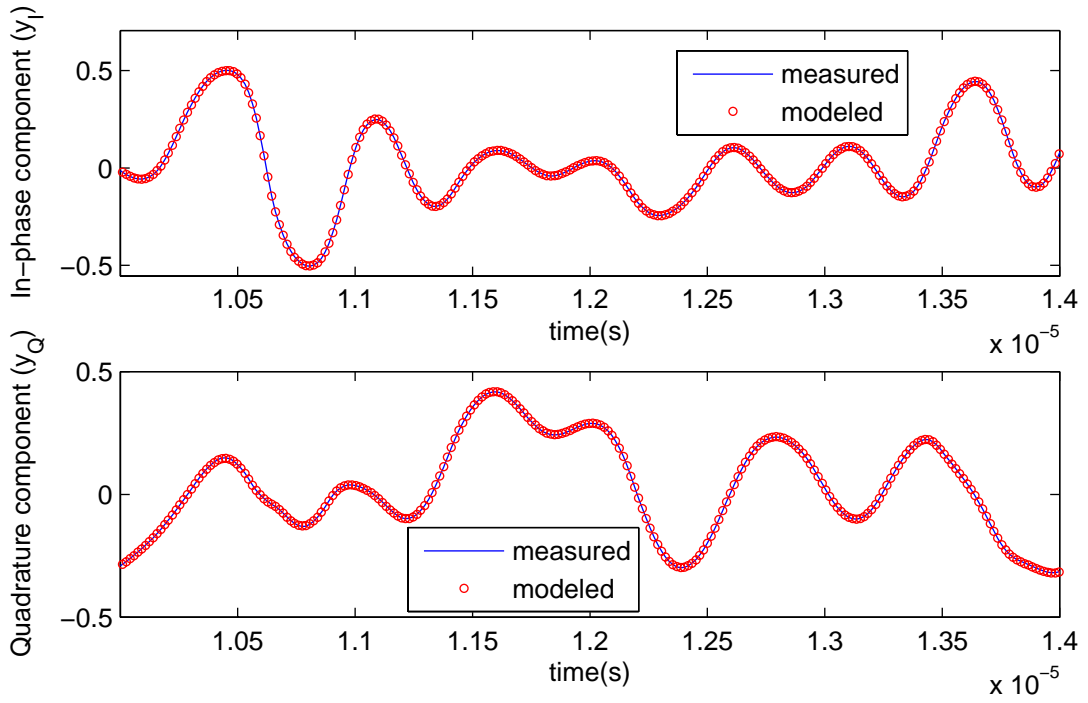


Figure 5.11: Time-domain waveforms of the in-phase and quadrature components of the output signal, measured and estimated by the PP model with $P = 7$ and $M = 1$

Table 5.7: NMSE results for a Hammerstein PA behavioral model

P	M	N	NMSE (SLS)	NMSE (iterative procedure)
4	1	6	-38.08	-38.08
4	2	7	-38.19	-38.19
5	1	7	-38.70	-38.70
5	2	8	-38.82	-38.83
6	1	8	-39.04	-39.04
6	2	9	-39.17	-39.18
7	1	9	-39.25	-39.26
7	2	10	-39.39	-39.40
7	3	11	-40.28	-40.30

measured instantaneous AM-AM conversion at high input power.

In Figure 5.13 is shown that the PSD of the error signal for the TLP model is clearly

Table 5.8: NMSE and ACEPR results for a TLP PA behavioral model with $M = 1$

R	N	NMSE (dB)	ACEPR _{LW} (dB) $\Delta_f =$ 10 MHz	ACEPR _{LW} (dB) $\Delta_f =$ 5 MHz	ACEPR _{UP} (dB) $\Delta_f =$ 5 MHz	ACEPR _{UP} (dB) $\Delta_f =$ 10 MHz
13	93	-43.31	-61.28	-50.36	-52.53	-62.57
14	100	-43.94	-61.05	-52.09	-52.67	-62.04
15	107	-45.41	-61.12	-53.21	-55.22	-64.33
16	114	-46.50	-61.40	-55.27	-55.18	-63.95
17	121	-45.24	-61.55	-53.72	-53.73	-63.22
18	128	-46.96	-62.55	-54.28	-56.42	-63.41
19	135	-46.24	-62.62	-54.90	-54.83	-64.85
20	142	-46.36	-63.12	-54.12	-54.68	-63.65

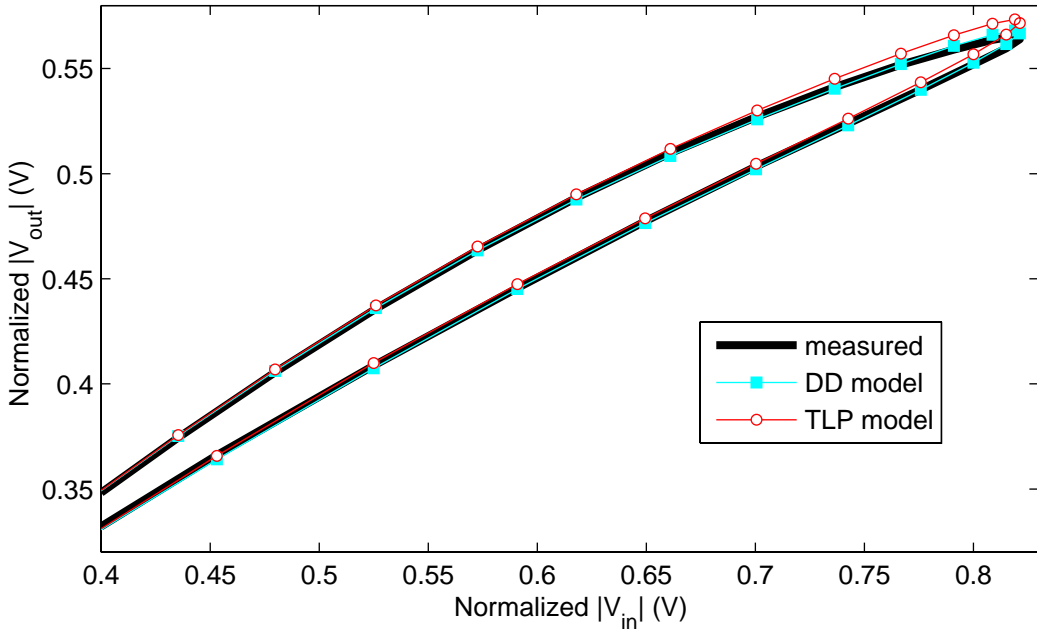


Figure 5.12: Samples of instantaneous AM-AM conversions: measured, estimated by a DD model ($R = 4$, $P = 7$ and $M = 1$) and estimated by a TLP model ($M = 1$ and $R = 18$)

larger than the error signal for the DD with $R = 4$, $P = 7$ and $M = 1$, specially in the in-band and adjacent channels. This is in accordance with the presented ACEPR results.

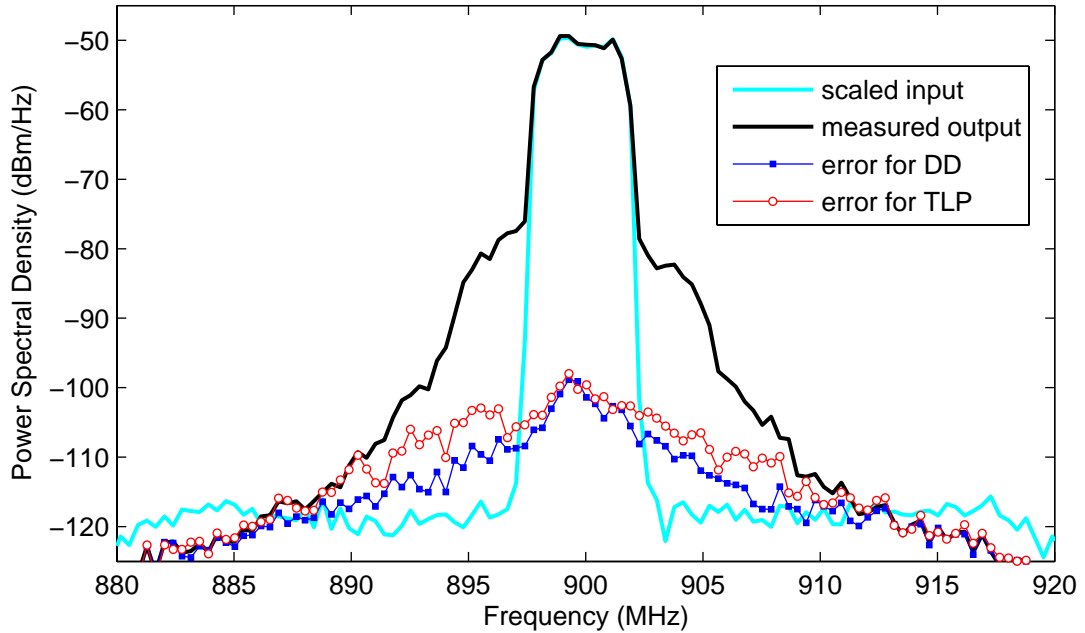


Figure 5.13: PSDs of the error signals for a DD model ($R = 4$, $P = 7$ and $M = 1$) and a TLP model ($M = 1$ and $R = 18$)

5.1.2 Case study 2: two carrier WCDMA input signal

In this second case study, time-domain measurements were performed in the same class AB PA with GaN based technology used in the case study 1, but now driven by a two carrier WCDMA 3GPP signal of bandwidth 3.84 MHz each carrier, with carrier frequency separation of 5MHz and PAPR of 11 dB, for an average output power of 26 dBm. The sampling frequency was set to 61.44 MHz. In this case, the memory effects are more evident in the measured instantaneous AM-AM conversion, as shown in Figure 5.14. The ACEPR results also use a bandwidth of $BW = 3.84$ MHz for both main and adjacent channels. The center frequency of the main channel coincides with the center frequency of one of the two carriers.

Attention was paid to avoid extrapolation. Specifically, the minimum and maximum instantaneous values of both in-phase I_x and quadrature Q_x components of the input signal as well as the maximum instantaneous magnitude of the input signal in the validation subset were forced to be inside their respective ranges in the extraction subset, as shown in Table 5.9.

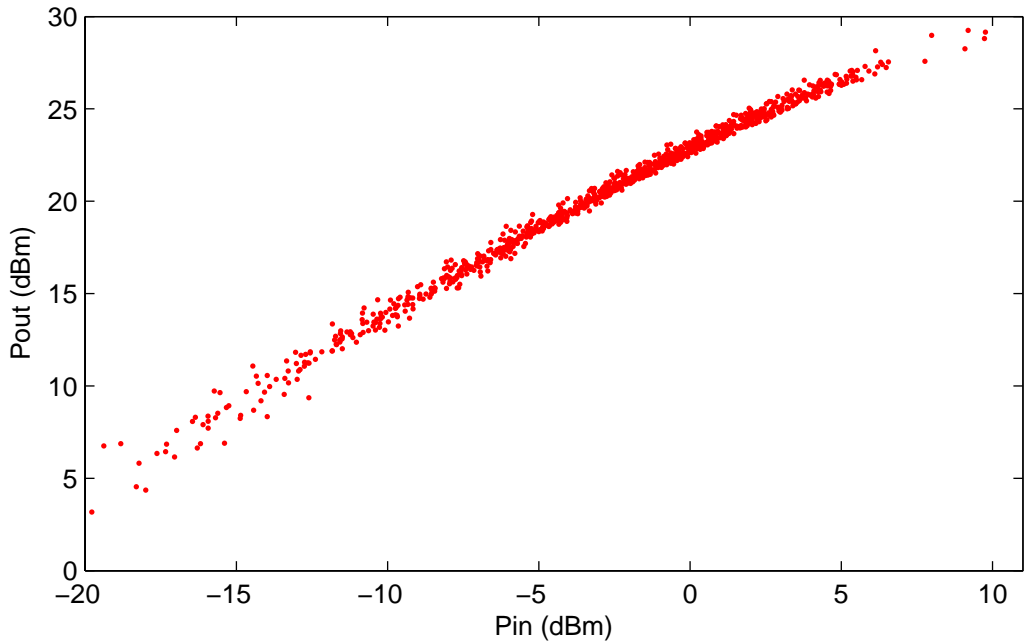


Figure 5.14: Measured instantaneous AM-AM conversion

Table 5.9: Range of the input signals in the extraction and validation subsets

Input-output data subset	minimum of I_x	maximum of I_x	minimum of Q_x	maximum of Q_x	maximum of $ \tilde{x}(t) $
Extraction	-0.9209	0.9638	-0.8689	0.8264	0.9908
Validation	-0.8421	0.7486	-0.7905	0.8100	0.9731

Again, several Volterra models with varying P and M were preliminary extracted to model the relationship between the complex-valued envelopes measured at the PA input and output. Table 5.10 shows the NMSE and ACEPR results, as well as the number of complex-valued parameters N in each case. The number of complex-valued parameters was limited to 300.

The best Volterra model in Table 5.10 was chosen as the one with $P = 4$ and $M = 2$, since its NMSE results are at least 2.3 dB better than the NMSE for the other P and M choices. The difference in NMSE between the memoryless model, with $P = 4$ and $M = 0$, and the best Volterra model is 14.5 dB, while the improvements in ACEPR are, for a 5 MHz separation between the adjacent and main channels, 13.6 dB for the upper and 14.3 dB for the lower adjacent channels and, for a 10 MHz separation, 6.4 dB for

Table 5.10: NMSE and ACEPR results for the Volterra model with different P and M

P	M	N	NMSE (dB)	ACEPR _{LW} (dB) $\Delta_f =$ 10 MHz	ACEPR _{LW} (dB) $\Delta_f =$ 5 MHz	ACEPR _{UP} (dB) $\Delta_f =$ 5 MHz	ACEPR _{UP} (dB) $\Delta_f =$ 10 MHz
3	2	81	-39.72	-50.44	-46.33	-45.90	-48.86
3	3	244	-40.28	-51.13	-47.05	-46.47	-49.31
4	0	4	-28.13	-43.09	-35.27	-35.67	-47.39
4	1	40	-39.24	-49.87	-46.21	-46.99	-50.62
4	2	231	-42.61	-53.88	-49.59	-49.27	-53.78
5	1	70	-39.59	-50.02	-46.67	-47.30	-51.47
6	1	112	-39.82	-50.56	-46.92	-47.44	-51.62

the upper and 10.8 dB for the lower adjacent channels. For the best Volterra model, the measured and modeled instantaneous AM-AM conversions are shown in Figure 5.15, while the PSDs of the measured and modeled output signals, and also of the error signal, are shown in Figure 5.16.

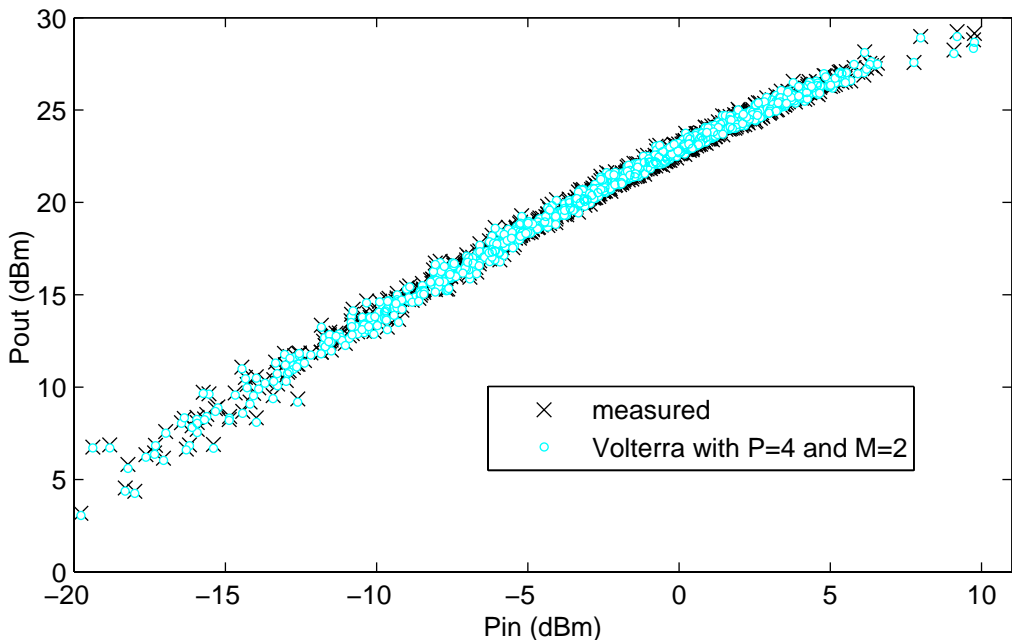


Figure 5.15: Instantaneous AM-AM conversions: measured and estimated by a Volterra series with $P = 4$ and $M = 2$

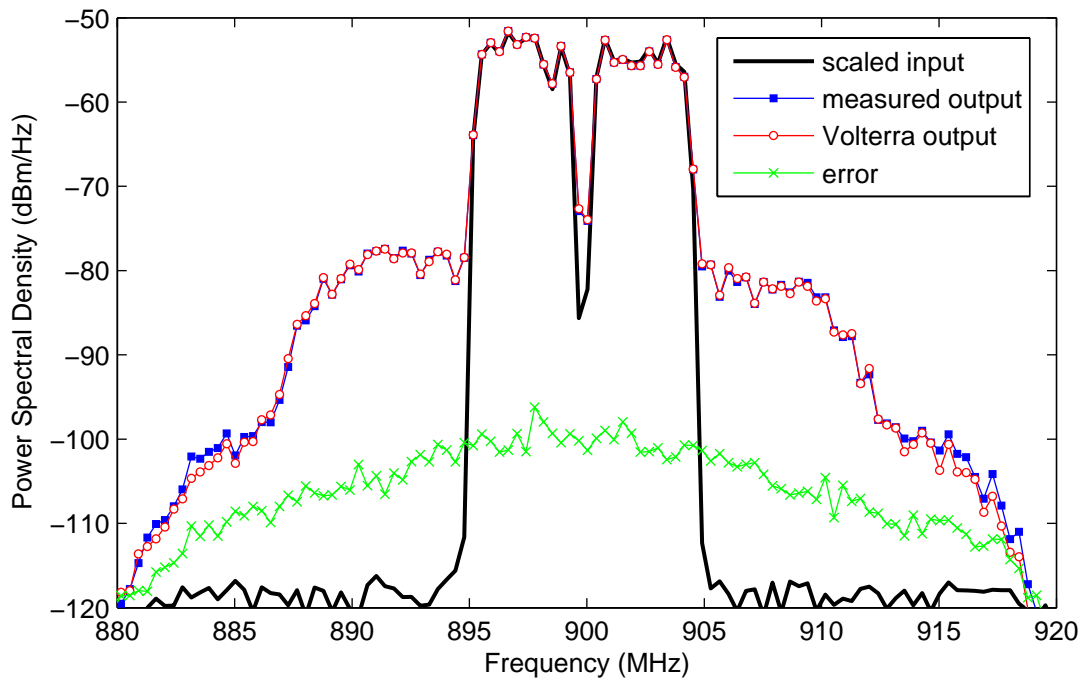


Figure 5.16: Power spectral densities of the measured output signal, modeled output signal by a Volterra series ($P = 4$ and $M = 2$) and error signal

Repeating the procedure followed in the case study 1, the simplified implementations of the Volterra model were extracted for the truncation factors, $P = 4$ and $M = 2$, of the selected best Volterra model. The NMSE and ACEPR results obtained for the Volterra-based models, as well as the number of complex-valued parameters N in each case are reported in Table 5.11. Again, in the case of the PP models, with the assumption of only base-band dynamics, PP (Δ_f), and also with the assumption of base-band and second harmonic dynamics, PP ($\Delta_f, 2f$), an additional linear FIR filter with three complex-valued taps was put prior to the model to account for the memory effects observed in small-signal operation. All the models were extracted using the same algorithms implemented in the case study 1. Concerning the block-oriented Wiener, Hammerstein and three-box structures, the parameter identification was done using SLS.

The best result in NMSE, as shown in Table 5.11, is -42.76 dB for the PP model with base-band and second harmonic dynamics. In fact, since an input filter was put before the PP model, its Volterra kernels do not exactly match those of the complete Volterra series. Additionally, the NMSE result for the Volterra series is slightly (a difference of 0.01 dB)

Table 5.11: NMSE and ACEPR results with $P = 4$ and $M = 2$

Model	N	NMSE (dB)	ACEPR _{LW} (dB) $\Delta_f =$ 10 MHz	ACEPR _{LW} (dB) $\Delta_f =$ 5 MHz	ACEPR _{UP} (dB) $\Delta_f =$ 5 MHz	ACEPR _{UP} (dB) $\Delta_f =$ 10 MHz
Volterra	231	-42.61	-53.88	-49.59	-49.27	-53.78
MP	12	-35.64	-53.27	-44.25	-44.16	-53.57
DD ($R = 1$)	18	-36.58	-47.23	-42.22	-43.31	-48.80
DD ($R = 2$)	45	-42.07	-53.09	-48.18	-48.40	-52.70
DD ($R = 3$)	87	-42.57	-53.79	-49.52	-49.34	-53.52
DD ($R = 4$)	134	-42.62	-53.73	-49.68	-49.34	-53.69
DD ($R = 5$)	180	-42.61	-53.80	-49.60	-49.31	-53.75
DD ($R = 6$)	211	-42.61	-53.87	-49.61	-49.26	-53.79
DD ($R = 7$)	231	-42.61	-53.88	-49.59	-49.27	-53.78
PP (Δ_f)	24	-41.82	-51.52	-49.13	-49.23	-51.96
PP ($\Delta_f, 2f$)	84	-42.76	-53.15	-49.15	-48.97	-52.92
Wiener	7	-31.23	-43.15	-35.05	-35.28	-46.16
Hammerstein	7	-31.96	-45.16	-36.50	-35.90	-45.82
three-box	10	-33.58	-49.83	-40.07	-39.43	-50.59

worse than the NMSE result for the DD model with $R = 4$. However, the DD model uses only 134 complex-valued coefficients from the total 231 complex-valued coefficients of the Volterra series. As seen in the case study 1, the chosen best Volterra series is overfitted, but the overfitting has almost negligible influence on the numerical algorithm performing the Volterra series parameter identification. The worst results both in NMSE and ACEPR shown in Table 5.11 are for the block-oriented structures. Differences of 11.4 dB in NMSE, 14.6 dB in ACEPR_{LW} and 14.1 dB in ACEPR_{UP} for $\Delta_f = 5$ MHz and 10.6 dB in ACEPR_{LW} and 7.5 dB in ACEPR_{UP} for $\Delta_f = 10$ MHz are observed between the Wiener model and the DD model with $R = 4$. The three-box structure improves the Wiener results in NMSE by 2.4 dB and in ACEPR_{LW} for $\Delta_f = 5$ MHz by 5.0 dB and for $\Delta_f = 10$ MHz by 6.7 dB, while the Hammerstein cascade has a performance in between the Wiener and three-box structures, but closer to the Wiener cascade. Figure 5.17 shows the

measured and modeled instantaneous AM-AM conversions. The Volterra modeled AM-AM conversion is the closest to the measured AM-AM conversion and they differ only at high input power. On the other hand, the block-oriented modeled AM-AM conversions are visibly different from the measured AM-AM conversion for the whole input power range displayed. Specifically, the Wiener AM-AM conversion is practically a line at moderate and high input power, indicating that the modeled memory effects are limited to the linear operation and so concentrated at the in-band frequencies. This behavior is confirmed in Figure 5.18 by the PSDs of the error signals for the Wiener and memoryless model and in accordance with the similar results in ACEPR (differences not higher than 1.2 dB) reported in Table 5.10 for the memoryless model, and in Table 5.11 for the Wiener cascade. The improvements of the Wiener model at the in-band frequencies over the memoryless model is sensed by the 3.1 dB improvements in NMSE.

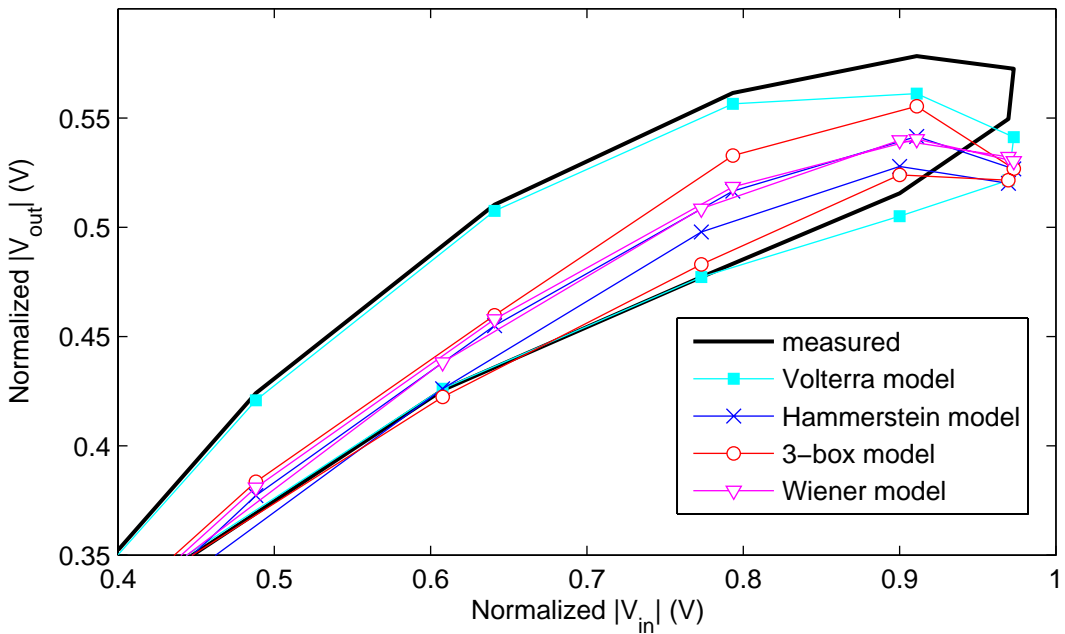


Figure 5.17: Samples of instantaneous AM-AM conversions: measured and estimated by different PA behavioral models with $P = 4$ and $M = 2$

The differences between the MP model and the DD model with $R = 3$ are clearly observed by the PSDs of their error signals shown in Figure 5.19. The 5.3 dB and 5.2 dB differences in ACEPR_{LW} and ACEPR_{UP} for $\Delta_f = 5$ MHz between the MP model and the DD model with $R = 3$ are in accordance with Figure 5.19. Besides, the PSDs of the error

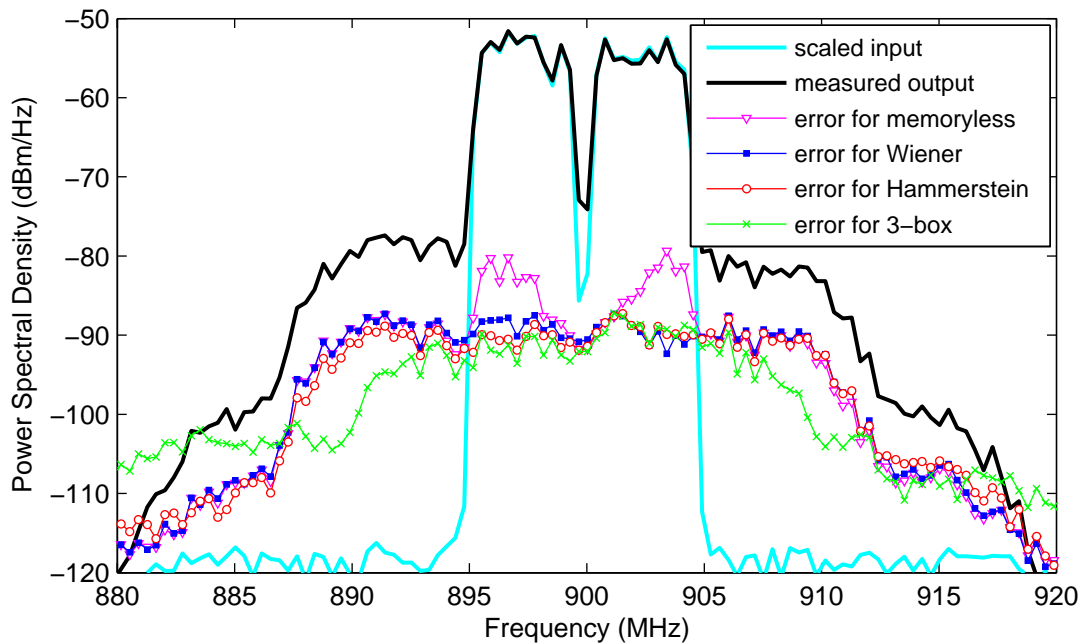


Figure 5.18: PSDs of the error signals for different PA behavioral models with $P = 4$ and $M = 2$

signals for the PP ($\Delta_f, 2f$), DD with $R = 3$ and Volterra models are very close.

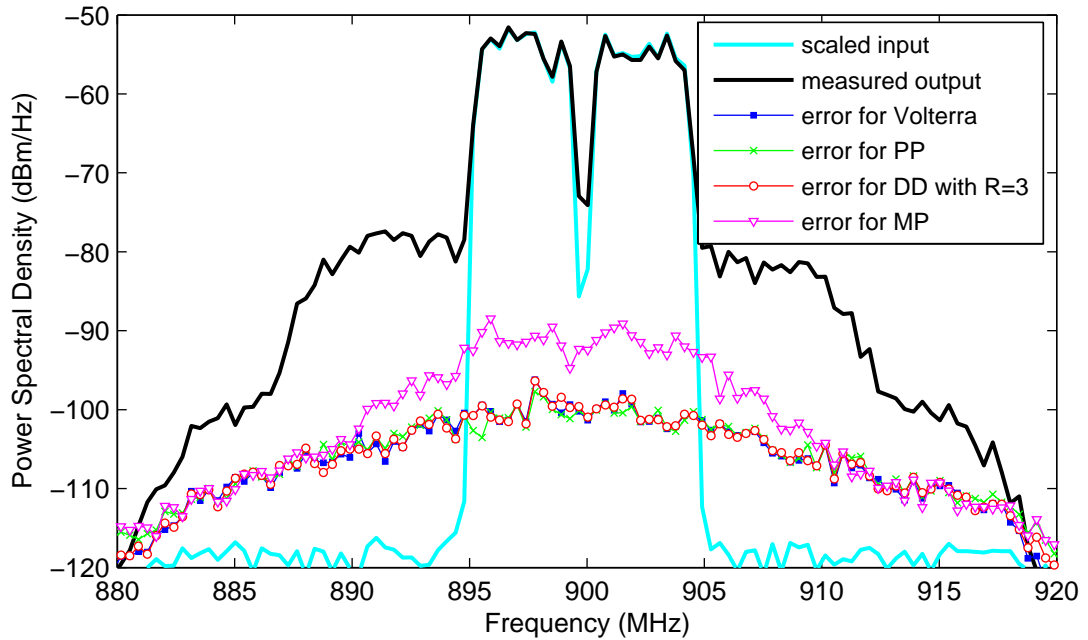


Figure 5.19: PSDs of the error signals for different PA behavioral models with $P = 4$ and $M = 2$

As a conclusion of the first comparison framework, the two advantages of the simplified implementations of the Volterra series, namely a reduction in the number of parameters without compromising the accuracy of the complete Volterra model and a finer checking on model overfitting and numerical problems, were again proved in the case study 2.

Already in the second comparison framework, the NMSE and ACEPR results for the best simplified Volterra models, based on the empirical truncation factors selection procedure using the NMSE results detailed earlier are shown in Table 5.12, as well as the respective number of complex-valued parameters N .

Table 5.12: NMSE and ACEPR results for the best choices of P and M

Model	P	M	N	NMSE (dB)	ACEPR _{LW} (dB) $\Delta_f =$ 10 MHz	ACEPR _{LW} (dB) $\Delta_f =$ 5 MHz	ACEPR _{UP} (dB) $\Delta_f =$ 5 MHz	ACEPR _{UP} (dB) $\Delta_f =$ 10 MHz
MP	7	5	42	-36.20	-58.68	-45.84	-45.20	-57.78
DD ($R = 2$)	6	4	220	-46.63	-56.76	-54.07	-54.57	-56.57
PP (Δ_f)	6	3	130	-44.09	-56.10	-51.59	-53.24	-56.09
Wiener	7	3	11	-31.35	-43.36	-35.10	-35.26	-46.35
Hammerstein	7	4	12	-33.40	-50.35	-39.45	-38.61	-53.13
three-box	7	3	15	-34.32	-48.73	-41.67	-40.84	-50.54

In the input-output data for model extraction and validation used in the case study 2, the dynamic effects are more relevant with respect to the case study 1. As a consequence, a Volterra model with $M = 2$ provides a much more accurate modeling than with $M = 1$, even if a lower polynomial order is used, as reported in Table 5.10. On the other hand, the highest polynomial order that could be extracted for a Volterra model with $M = 2$, considering that the number of parameters is limited to 300, was $(2P - 1 = 7)$. Since the average PA output power and the input signal PAPR are similar in both case studies, this polynomial order is not as accurate for the modeling of the nonlinear behavior as the polynomial order used in the case study 1 ($2P - 1 = 13$) and, hence, best results for the simplified implementations with $P > 4$ and $M \geq 2$ are expected. This expected behavior was confirmed by the improvements of 4.0 dB in NMSE and 5.3 dB in ACEPR_{UP} for $\Delta_f = 5$ MHz of the DD model with $P = 6$, $M = 4$ and $R = 2$ reported in Table 5.12

over the Volterra series with $P = 4$ and $M = 2$ reported in Table 5.11. Additionally, the PP model with only base-band dynamics having $P = 6$ and $M = 3$ also improves the Volterra series model with $P = 4$ and $M = 2$, specifically in 1.5 dB in NMSE, 2.0 dB in ACEPR_{LW} and 4.0 dB in ACEPR_{UP} for $\Delta_f = 5$ MHz. As a conclusion, simplified Volterra models have produced better results than the complete Volterra series when their number of parameters were similar.

In Figures 5.20 and 5.21 are shown the measured and modeled instantaneous AM-AM conversions using the best choices for P and M presented in Table 5.12. The PP modeled AM-AM conversion is the closest to the measured one, while the block-oriented modeled AM-AM conversions are clearly different from the measured AM-AM conversion, specially for the Wiener and Hammerstein cascades. This is expected since they have only one filter to account for different dynamic effects observed in the measured PA: nonlinear dynamic effects originated outside the pass-band and the non flatness response of the PA driver at fundamental band. In fact, the Wiener cascade could accurately model the latter dynamic behavior. However, to model these two different behaviors by just one filter, the Hammerstein cascade presented superior results than the Wiener cascade according to the used FoMs.

In Figure 5.22 is shown the PSDs of the measured output signal and of the error signals for some of the simplified implementations with M and P according to Table 5.12. The three-box error spectrum is better than the Hammerstein one in the adjacent channels. The PP model clearly has the lower error in the main and adjacent channels, however the MP model shows the best performance for frequencies far away from the in-band channels.

In the third comparison framework, Table 5.13 shows the NMSE and ACEPR results obtained with the MP, DD and PP models for a particular case in which they have a similar number of complex-valued parameters.

In Figure 5.23 is shown that the measured and modeled instantaneous AM-AM conversions by the MP, DD and PP models, using P and M values presented in Table 5.13, are close to each other. Hence, using about 40 complex-valued parameters it was possible to accurately model the measured instantaneous AM-AM conversion.

In Figure 5.24 is shown that the PSD of the error signal for the MP model is clearly larger, at the in-band and adjacent channels, than the PSDs of the error signals for the

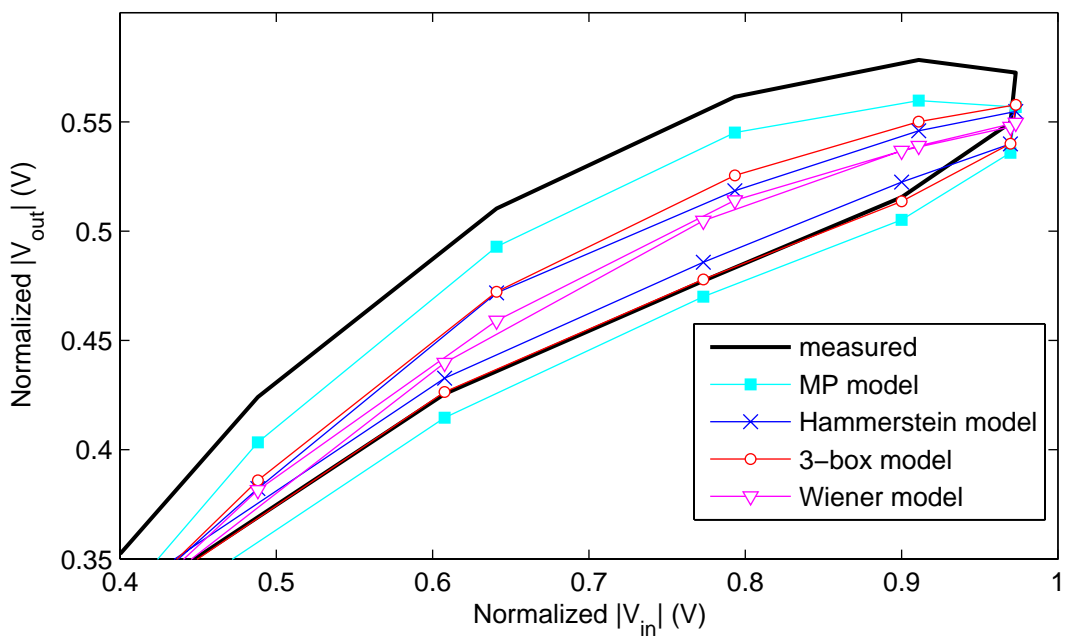


Figure 5.20: Samples of instantaneous AM-AM conversions: measured and estimated by different PA behavioral models with M and P given by Table 5.12

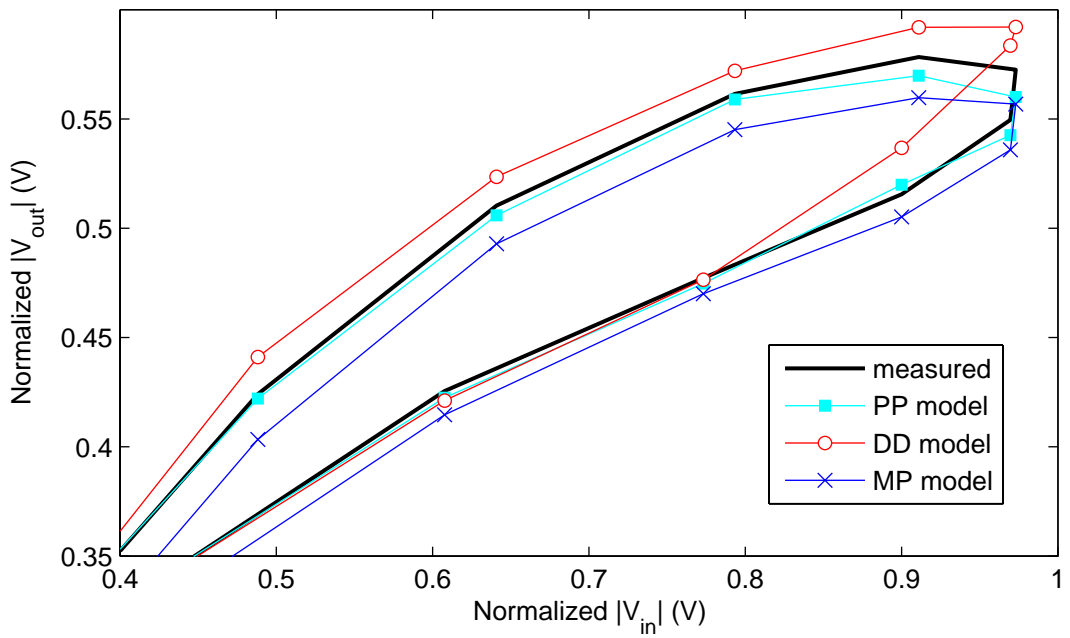


Figure 5.21: Samples of instantaneous AM-AM conversions: measured and estimated by different PA behavioral models with M and P given by Table 5.12

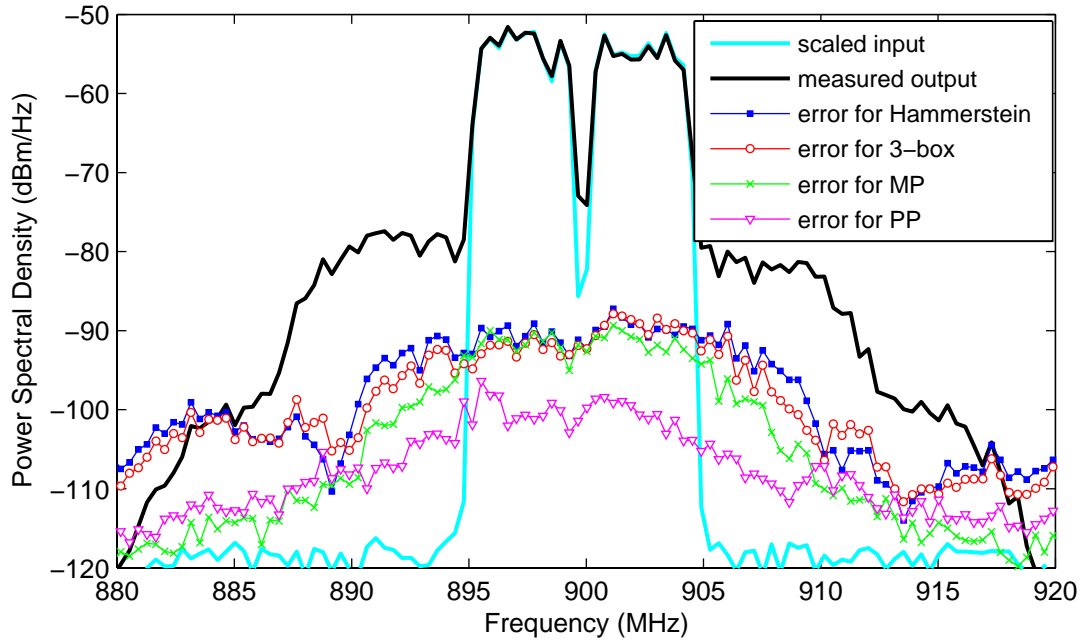


Figure 5.22: PSDs of the error signals for different PA behavioral models with M and P given by Table 5.12

Table 5.13: NMSE and ACEPR results for the Volterra-based models with similar number of parameters

Model	P	M	N	NMSE (dB)	ACEPR _{LW} (dB) $\Delta_f = 10$ MHz	ACEPR _{LW} (dB) $\Delta_f = 5$ MHz	ACEPR _{UP} (dB) $\Delta_f = 5$ MHz	ACEPR _{UP} (dB) $\Delta_f = 10$ MHz
MP	7	5	42	-36.20	-58.68	-45.84	-45.20	-57.78
DD ($R = 2$)	4	2	45	-42.07	-53.09	-48.18	-48.40	-52.70
PP (Δ_f)	4	3	39	-42.10	-53.08	-49.39	-50.13	-52.80

DD and PP models, using the P and M values presented in Table 5.13. However, the situation changes for frequencies far away from the in-band channels. This is in accordance with the ACEPR results presented in Table 5.13.

The in-phase and quadrature time-domain waveforms measured and estimated, by the DD model with $P = 4$, $M = 2$ and $R = 2$, at the PA output are shown in Figure 5.25. An excellent agreement is observed in both in-phase and quadrature components.

At this moment, the parameter extraction of the Wiener and Hammerstein cascades are

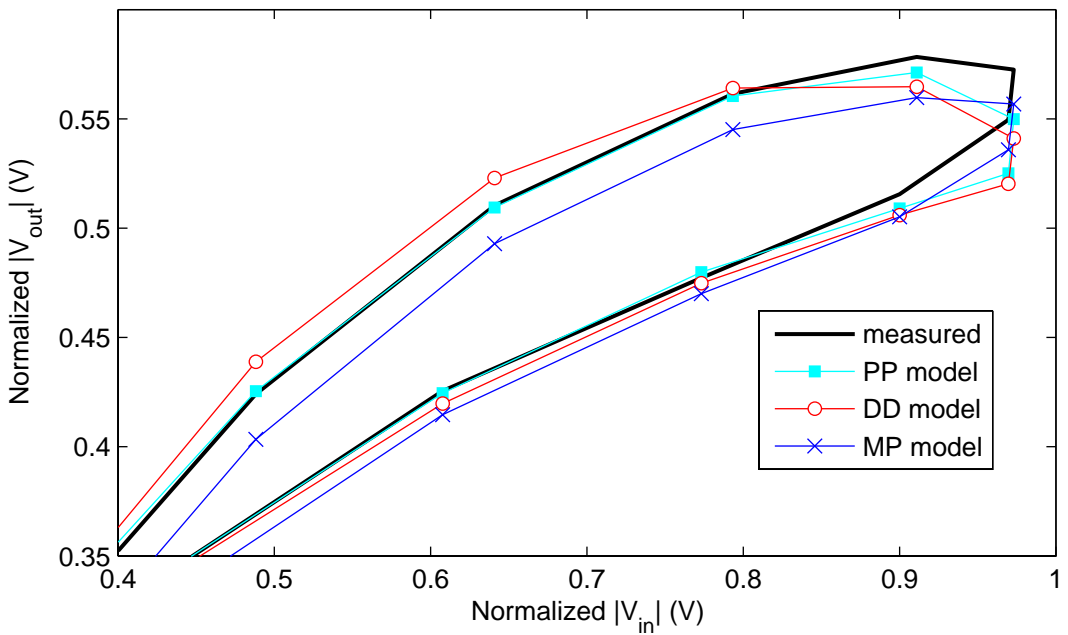


Figure 5.23: Samples of instantaneous AM-AM conversions: measured and estimated by different PA behavioral models with M and P given by Table 5.13

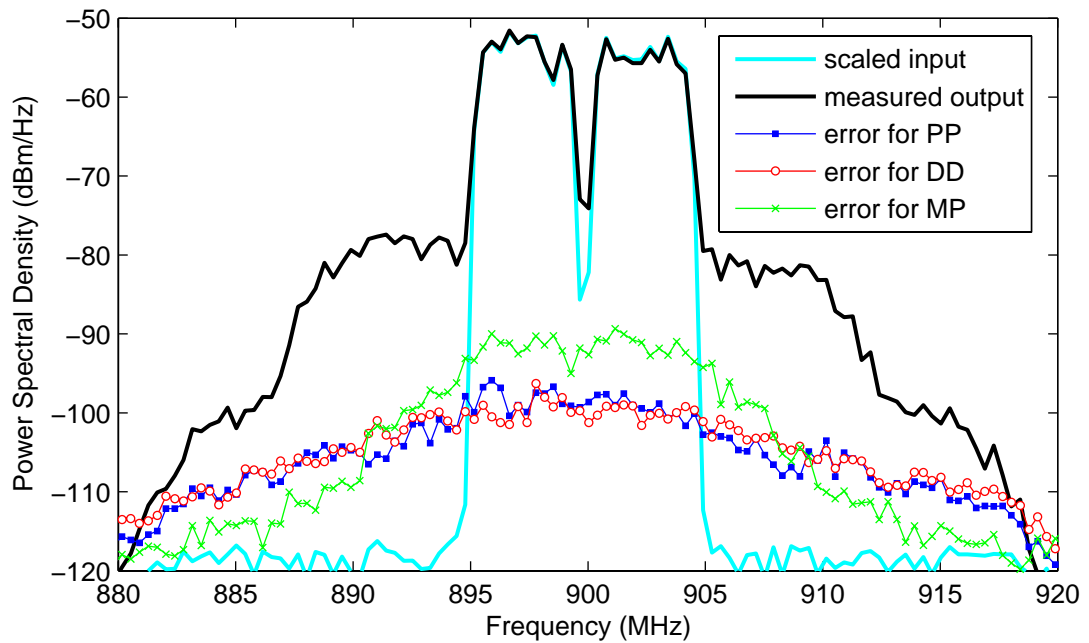


Figure 5.24: PSDs of the error signals for different PA behavioral models with M and P given by Table 5.13

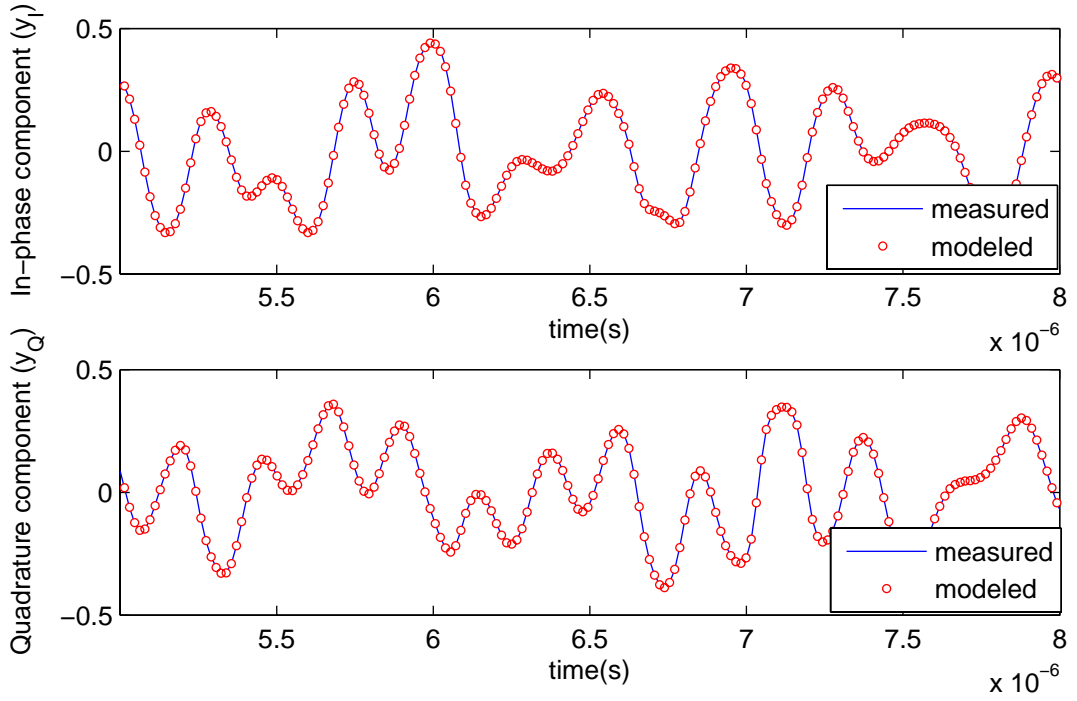


Figure 5.25: Time-domain waveforms of the in-phase and quadrature components of the output signal, measured and estimated by the DD model with $P = 4$, $M = 2$ and $R = 2$

under investigation. The largest differences in terms of NMSE between the two extraction strategies described in the case study 1 were less than 0.7 dB in the Wiener case and less than 0.2 dB in the Hammerstein one. Again, the loss in modeling accuracy by the use of a sub-optimal parameter extraction instead of a more computationally demanding optimal nonlinear procedure is much lower than the loss in accuracy by the choice of block-oriented topologies.

Finally, a TLP PA behavioral model is included in the comparison. Table 5.14 shows the NMSE and ACEPR results obtained by a PA modeled by a TLP with $M = 2$ and varying the number of hidden neurons R , as well as the number of real-valued parameters in each case. The best NMSE and ACEPR results are for the TLP with $R = 17$. This TLP compared to the DD model with $R = 4$, $P = 4$ and $M = 2$ deteriorates 0.3 dB in NMSE, 0.6 dB and 0.7 dB in ACEPR_{LW} for $\Delta_f = 5$ MHz and $\Delta_f = 10$ MHz, respectively and 2.5 dB in ACEPR_{UP} for $\Delta_f = 10$ MHz.

In Figure 5.26 is shown that the measured and modeled instantaneous AM-AM conversions by the DD model with $R = 4$, $P = 4$ and $M = 2$ and the TLP model with

Table 5.14: NMSE and ACEPR results for a TLP PA behavioral model with $M = 2$

R	N	NMSE (dB)	ACEPR _{LW} (dB) $\Delta_f =$ 10 MHz	ACEPR _{LW} (dB) $\Delta_f =$ 5 MHz	ACEPR _{UP} (dB) $\Delta_f =$ 5 MHz	ACEPR _{UP} (dB) $\Delta_f =$ 10 MHz
12	110	-38.08	-50.16	-43.03	-43.07	-46.52
13	119	-40.09	-51.11	-46.05	-44.83	-50.47
14	128	-39.28	-51.02	-45.49	-44.25	-45.21
15	137	-40.59	-51.91	-46.08	-45.84	-50.40
16	146	-41.59	-53.45	-47.10	-46.85	-51.66
17	155	-42.30	-53.00	-49.04	-47.88	-51.23
18	164	-42.24	-52.63	-48.69	-49.14	-52.64

$R = 17$ are very close to each other and both models accurately estimate the measured instantaneous AM-AM conversion.

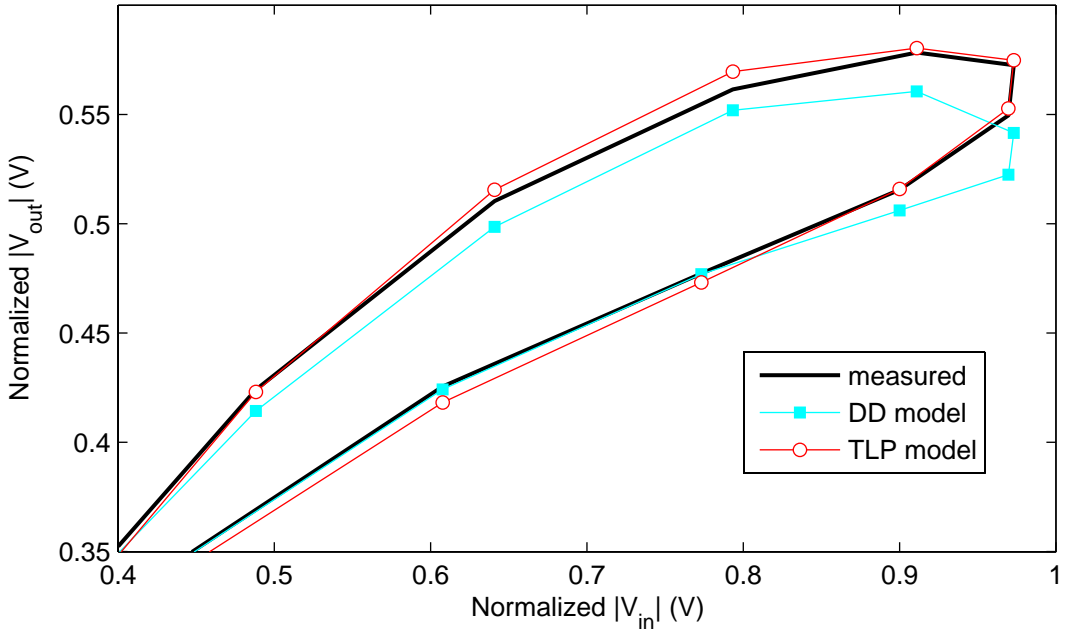


Figure 5.26: Samples of instantaneous AM-AM conversions: measured, estimated by a DD model ($R = 4$, $P = 4$ and $M = 2$) and estimated by a TLP model ($M = 2$ and $R = 17$)

In Figure 5.27 is shown that the PSD of the error signal for the TLP with $R = 17$ is slightly larger than the PSD of the error signal for the DD model with $R = 4$, $P = 4$ and

$M = 2$. This is in accordance with the presented ACEPR results.

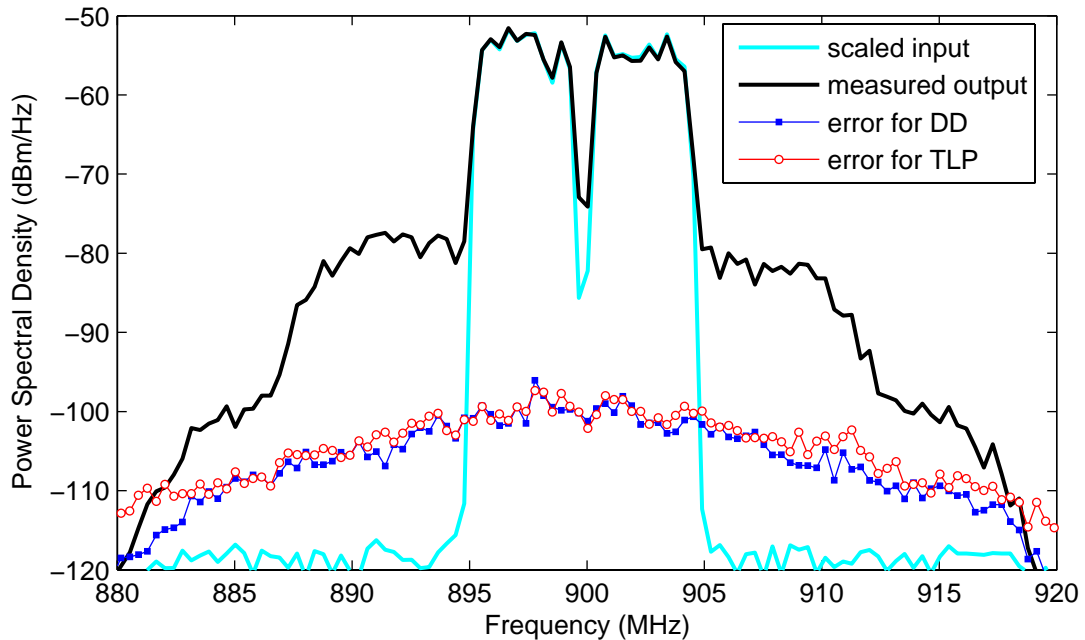


Figure 5.27: PSDs of the error signals for a DD model ($R = 4$, $P = 4$ and $M = 2$) and a TLP model($M = 2$ and $R = 17$)

As final conclusions of both case studies, the PP and DD models have shown the best trade-off between accuracy and complexity (in terms of number of fitting parameters). Their accuracies were even better than the accuracy of a TLP model. This means that, although a TLP has a modeling capability superior than or at least equivalent to the PP and DD models, its nonlinear parameter extraction procedure not always guarantee a full exploitation of its modeling capability. The MP model has shown an intermediate trade-off between accuracy and complexity. It is not as good as the PP and DD models, but it is clearly superior to the block-oriented models. Concerning the block-oriented Wiener and Hammerstein cascades, the cumbersome nonlinear parameter identification can be substituted by an iterative algorithm much less computational demanding without compromising the accuracy. However, their capability to model the PA behaviors are limited. Specifically, the Wiener cascade has shown improvements with respect to the memoryless polynomial just in the in-band spectrum of the estimated output signal.

5.2 Validation of the low-pass equivalent PA behavioral model with feedback topology described in Chapter 3

This section validates the low-pass equivalent PA behavioral model with feedback topology described in Chapter 3 in two different scenarios. In the first, the LPE feedback model accuracy will be compared with its third-order feed-forward approximation, 3rd FF model, in order to represent the relationship between the simulated complex-valued envelopes at the input and output of a known model. In the second, the LPE feedback model will be used to fit experimental data measured in a physical PA and its modeling performance will be compared to the previously studied Volterra series and three-layer-perceptron PA behavioral models.

5.2.1 Case study 1: input-output data simulated in a known RF feedback model

In the case study 1, the LPE feedback model is used to fit simulated circuit-envelope data performed in a known RF feedback model, whose block diagram was shown in Figure 3.1. The polynomial in the feed-forward path was truncated to $P_0 = 3$. The RF feedback model was driven by a three carrier (of bandwidth 1.25 MHz each) IS-95 CDMA signal, with carrier frequency separation of 1.875 MHz and PAPR of 15.4 dB. The sampling frequency was set to 30.72 MHz.

Since the LPE feedback model parameters are related to the RF feedback model parameters by simple closed-form expressions, no parameter identification is required.

The NMSE results obtained for the LPE feedback model, as well as for its third-order feed-forward approximation, 3rd FF, are reported in Table 5.15 for different average output power levels.

As expected, for low average output power levels Table 5.15 shows that the 3rd FF model and the LPE feedback model are indistinguishable and can model very accurately the relationship between the complex-valued envelopes at the input and output of the RF feedback system. As the average output power level increases, the contribution of

Table 5.15: NMSE results in dB for a three carrier IS-95 CDMA input signal

Average P_{OUT} (dBm)	11.0	22.3	26.4	28.1	29	30	31.1
LPE feedback model	-38.58	-37.97	-36.50	-35.09	-33.84	-31.94	-28.81
3 rd FF model	-38.58	-37.92	-34.02	-29.16	-25.85	-22.05	-17.45

higher order nonlinear terms to the complex-valued envelope at the output of the RF feedback system becomes no more negligible, and the 3rd FF model rapidly degrades its performances. On the other hand, the presence of the fed-back filter $\tilde{F}_1(\Omega)$ allowed the LPE feedback model to maintain a good accuracy in the estimation of the signal at the output even for high average output power levels. This proves that, in the idealized case where the original system is exactly given by an RF feedback model without any topology mismatch, the higher order Volterra kernels produced by the LPE feedback model are a significant representative subset of the kernels produced by the original RF feedback system.

Figure 5.28 shows the instantaneous AM-AM conversions simulated by the RF feedback, LPE feedback and 3rd FF models for an average output power of 29 dBm. Whereas the 3rd FF AM-AM conversion is visibly different from the RF feedback one, the AM-AM conversions of both RF and LPE feedback models are very close to each other.

Figure 5.29 shows the PSDs of the simulated output signals by the RF feedback, LPE feedback and 3rd FF models for an average output power of 29 dBm. Only the LPE feedback could accurately estimate the distortion generated by the RF feedback at the adjacent channel.

5.2.2 Case study 2: input-output data measured in a PA with GaN based technology

In the case study 2, the LPE feedback model is used to fit experimental time-domain measurements performed in a class AB PA with GaN based technology – same PA used in Section 5.1 – driven by a two carrier (of bandwidth 3.84 MHz each) WCDMA 3GPP signal, with carrier frequency separation of 5 MHz and PAPR of 11 dB, for an average output power of 26 dBm. The sampling frequency was set to 61.44 MHz. The ACEPR

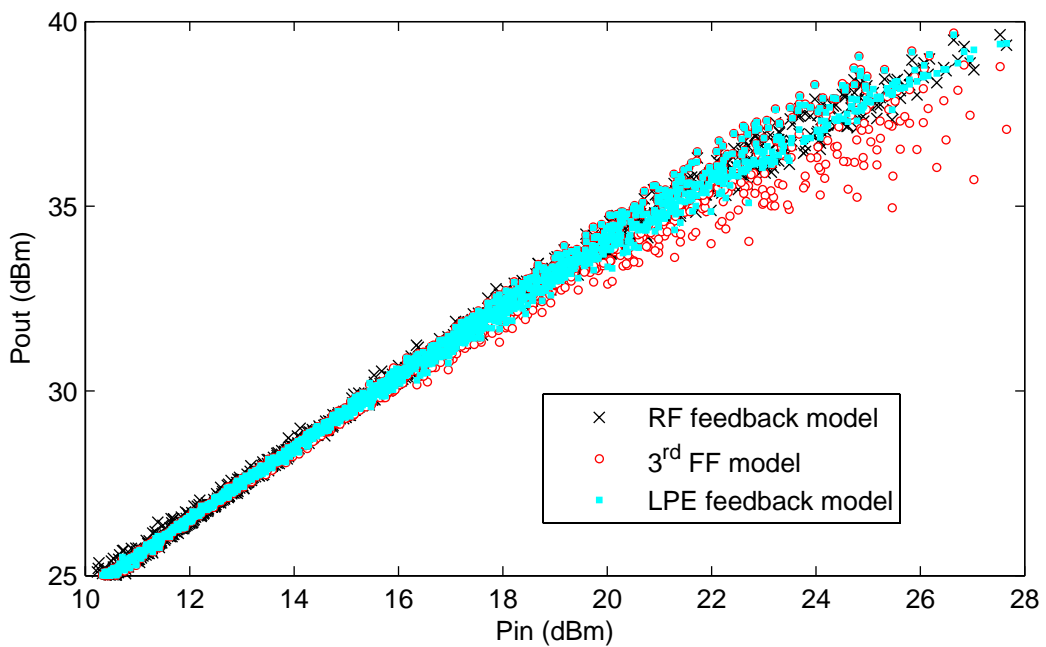


Figure 5.28: Simulated AM-AM conversions by the different models for an average output power of 29 dBm

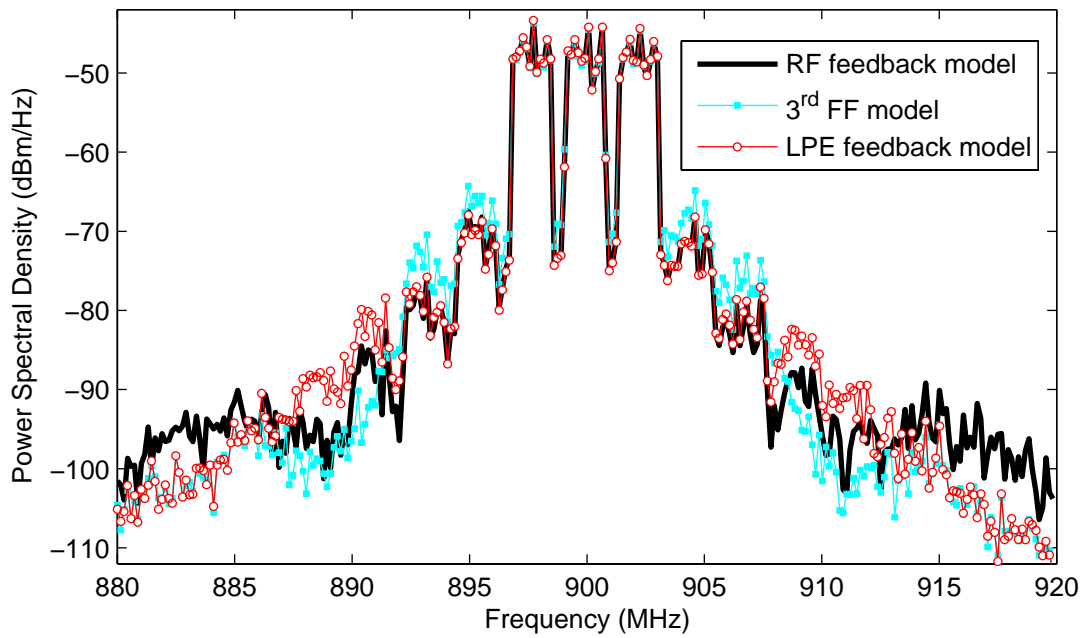


Figure 5.29: PSDs of the simulated output signals by the different models for an average output power of 29 dBm

results presented here use a bandwidth of 3.84 MHz for both main and adjacent channels. The center frequency of the main channel coincides with the center frequency of one of the two carriers.

Attention was paid to avoid extrapolation. Specifically, the minimum and maximum instantaneous values of both in-phase I_x and quadrature Q_x components of the input signal as well as the maximum instantaneous magnitude of the input signal in the validation subset were guaranteed to be inside their respective ranges in the extraction subset. See Table 5.9 for the numerical values.

The NMSE and ACEPR results obtained for the LPE feedback model, as well as its number of real-valued parameters N , are reported in Table 5.16. In the extracted LPE feedback model, according to Figure 3.2, the static nonlinear branch was truncated to $P_0 = 7$ and the linear filter in the feed-back path, $\tilde{F}_1(\Omega)$, was assumed flat and so modeled by a complex-valued gain \tilde{f}_0 . While the output linear filter $\tilde{O}(\Omega)$ was neglected, the input linear filter $\tilde{H}(\Omega)$ was included to account for the memory effects observed in small-signal operation and attributed both to the PA driver used in the experimental setup and the PA input matching network. Each linear filter was modeled by a finite-impulse response (FIR) digital filter with four taps. The real-valued parameters a_2 and a_3 were not explicitly extracted, but just included in the $\tilde{G}_2(\Omega)$ and $G_0(\Omega)$ filters according to (3.6) and (3.7). The coefficients of the LPE feedback model were all extracted at once via a nonlinear optimization procedure, specifically the minimization of the 2-norm of the error signal defined as the difference between the measured and modeled time-domain base-band output signals.

Additionally, the third-order feed-forward approximation, 3rd FF, of the LPE feedback model, obtained by imposing $\tilde{f}_0 = 0$ and truncating the static nonlinear branch to $P_0 = 3$, was also extracted and its NMSE and ACEPR results, as well as its number of real-valued parameters N , are reported in Table 5.16. The 3rd FF parameter extraction was done using a Separable Least Squares (SLS) in which just the input filter $\tilde{H}(\Omega)$ taps were optimized by a nonlinear algorithm since, once the input filter parameters are known, the model is linear in the remaining parameters and so a least-squares (LS) approach can be used to the extraction of the remaining parameters.

Also reported in Table 5.16 are the respective NMSE and ACEPR results, as well

as their number of real-valued parameters N , for Volterra series and TLP PA behavioral models with $M = 2$, previously obtained and reported in SubSection 5.1.2.

Table 5.16: NMSE and ACEPR results for a two carrier WCDMA input signal

Model	N	NMSE (dB)	ACEPR _{LW} (dB) $\Delta_f =$ 10 MHz	ACEPR _{LW} (dB) $\Delta_f =$ 5 MHz	ACEPR _{UP} (dB) $\Delta_f =$ 5 MHz	ACEPR _{UP} (dB) $\Delta_f =$ 10 MHz
LPE feedback	25	-42.24	-53.03	-47.34	-49.05	-54.73
3 rd FF	21	-32.50	-43.58	-37.63	-39.98	-43.35
Volterra, P=2	21	-32.87	-44.17	-38.55	-39.54	-43.31
Volterra, P=4	462	-42.61	-53.88	-49.59	-49.27	-53.78
TLP, R=17	155	-42.30	-53.00	-49.04	-47.88	-51.23

As shown in Table 5.16, third-order models are not accurate enough to represent the measured experimental data. Particularly, both the third-order Volterra model ($P = 2$) and the 3rd FF model deteriorates the model performance, with respect to the other models reported in Table 5.16, by approximated 10 dB in NMSE and ACEPR for both $\Delta_f = 5$ MHz and $\Delta_f = 10$ MHz. By the inclusion of only four additional real-valued coefficients in the 3rd FF model, the LPE feedback model not only shows improvements in the order of 10 dB in NMSE and ACEPR, but also presents similar modeling performance results (NMSE and ACEPR FoMs) with respect to the Volterra series with $P = 4$ and to the TLP with $R = 17$ using a much lower number of real-valued parameters. Specifically, the LPE feedback model required approximately 5% of the number of real-valued coefficients of the Volterra series and about 15% of the number of real-valued coefficients of the TLP model to show similar modeling performance results.

In Figure 5.30 is shown the measured and modeled instantaneous AM-AM conversions by the PA behavioral models presented in Table 5.16. The Volterra series AM-AM conversion shown uses $P = 4$. While the 3rd FF modeled AM-AM conversion is visibly different from the measured one, the instantaneous AM-AM conversions modeled by the LPE feedback, Volterra series with $P = 4$ and TLP are very close to the measured one. A better matching between measured and modeled AM-AM conversions at high input power levels was observed for the TLP model.

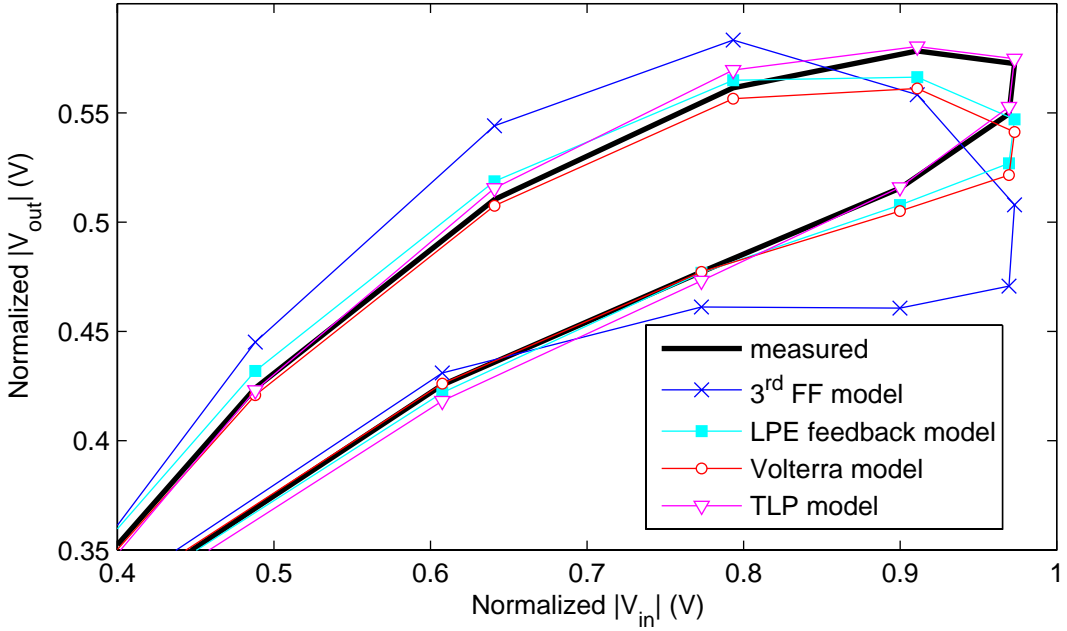


Figure 5.30: Samples of instantaneous AM-AM conversions: measured and estimated by the PA behavioral models reported in Table 5.16

In Figure 5.31 is shown the PSDs of the measured output signal and of the error signals for the PA behavioral models presented in Table 5.16. The Volterra series PSD shown uses $P = 4$. The error signal for the 3rd FF model is clearly larger at the whole measured spectrum, whereas the PSD of the error signals for the LPE feedback, Volterra series with $P = 4$ and TLP models are very similar.

Now, the parameters of the LPE feedback, Volterra series and TLP models are extracted again, using the same identification algorithms, to fit input-output measured data from another realization of a two carrier WCDMA 3GPP signal having bandwidth, carrier frequency separation and PAPR similar to the ones previously reported in this subsection, also for an average output power of 26 dBm. However, in this case, the maximum instantaneous magnitude of the input signal in the validation and extraction subsets were chosen to be equals. As a consequence, some extrapolation is present, as shown in Table 5.17, since the minimum and maximum instantaneous values of the in-phase I_x signal and maximum instantaneous value of the quadrature Q_x signal in the validation subset are not inside their respective ranges in the extraction subset.

The NMSE and ACEPR results obtained for the LPE feedback (same truncations as

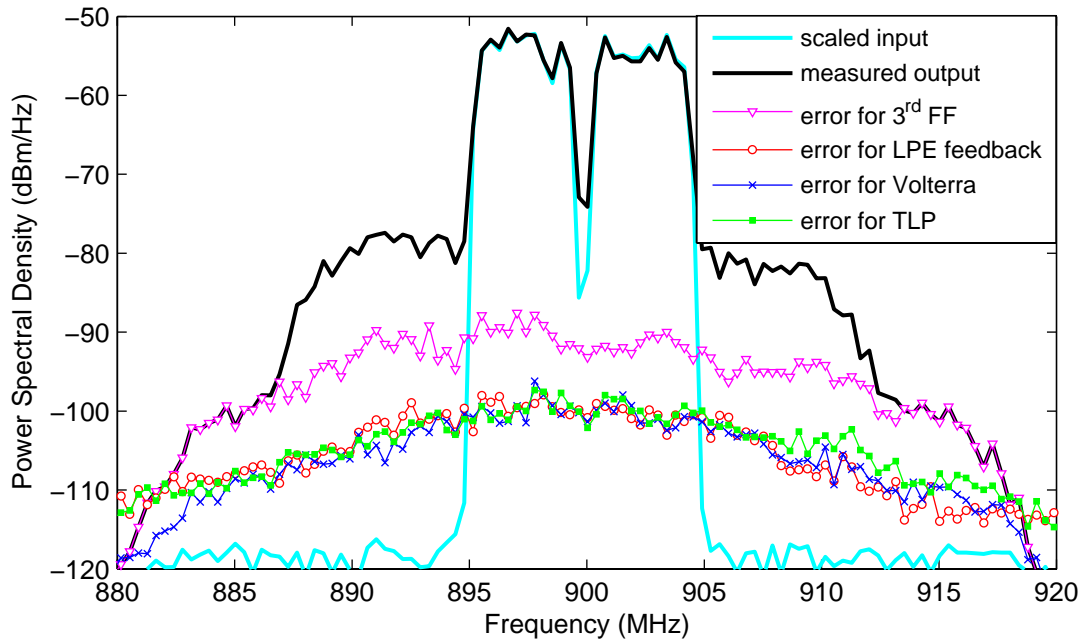


Figure 5.31: PSDs of the error signals for the PA behavioral models reported in Table 5.16

Table 5.17: Range of the input signals in the extraction and validation subsets

Input-output data subset	minimum of I_x	maximum of I_x	minimum of Q_x	maximum of Q_x	maximum of $ \tilde{x}(t) $
Extraction	-0.7720	0.8319	-0.9477	0.7451	1.0000
Validation	-0.9547	0.8677	-0.8021	0.8951	1.0000

before), Volterra series (with $P = 4$ and $M=2$) and TLP (with $R = 17$ and $M = 2$) models, as well as their number of real-valued parameters N , using the new validation subset, are reported in Table 5.18.

Table 5.18: NMSE and ACEPR results for a two carrier WCDMA input signal

Model	N	NMSE (dB)	ACEPR _{LW} (dB) $\Delta_f = 10$ MHz	ACEPR _{LW} (dB) $\Delta_f = 5$ MHz	ACEPR _{UP} (dB) $\Delta_f = 5$ MHz	ACEPR _{UP} (dB) $\Delta_f = 10$ MHz
LPE feedback	25	-41.79	-52.69	-48.04	-49.51	-54.86
Volterra, P=4	462	-38.07	-51.27	-46.49	-45.73	-51.81
TLP, R=17	155	-41.53	-53.03	-48.69	-48.62	-52.72

A comparison between the results reported in Tables 5.16 and 5.18 confirms that the modeling accuracy of the Volterra series with $P = 4$ was considerably affected by the presence of extrapolation in the validation dataset. Indeed, differences of 4.5 dB in NMSE and in between 2.0 dB and 3.5 dB in ACEPR were observed in the two different extracted Volterra series with $P = 4$ and $M = 2$, being the worst results always observed when extrapolation was present in the validation dataset. On the other hand, the LPE and TLP modeling performances were slightly affected by the presence of some extrapolation in the validation dataset. Specifically, in presence of extrapolation in the validation dataset with respect to the guaranteed absence of extrapolation, a deterioration of 0.5 dB and 0.8 dB in NMSE results were observed for the LPE and TLP models, respectively, whereas in terms of ACEPR, deterioration not higher than 0.4 dB were observed for the lower adjacent channels and improvements between 0.1 dB and 1.5 dB were observed for the upper adjacent channels.

In Figure 5.32 is shown the measured and modeled instantaneous AM-AM conversions by the PA behavioral models presented in Table 5.18, in which the maximum instantaneous value of the Q_x component in the validation subset was higher than its maximum value in the extraction subset. The degradation in the modeling accuracy of the Volterra series by the presence of extrapolation data is clearly observed by the completely wrong estimation of the measured instantaneous AM-AM conversion at high input levels. On the other hand, the instantaneous AM-AM conversions estimated by the LPE feedback and TLP models are still close to the measured one and could provide a good estimation in this context of weak extrapolation.

In Figure 5.33 is shown the PSDs of the measured output signal and of the error signals for the PA behavioral models presented in Table 5.18. The error signal for the Volterra model is clearly larger at the whole measured spectrum, while the spectrum of the error signal for the LPE feedback and TLP models are very similar. This further confirms the degraded behavior of the Volterra series in this context of weak extrapolation.

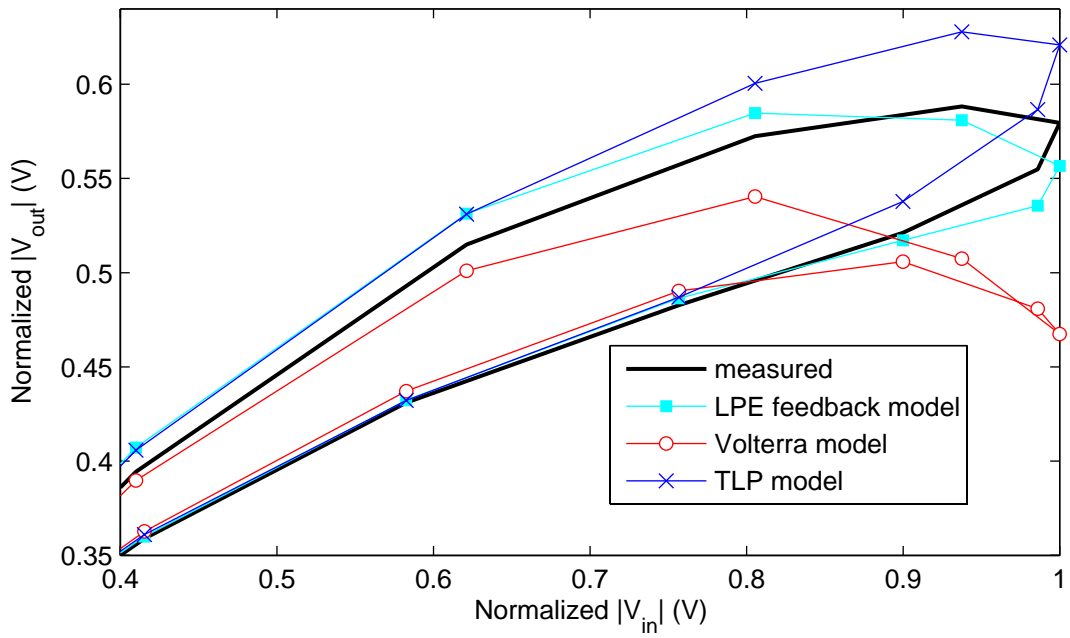


Figure 5.32: Samples of instantaneous AM-AM conversions: measured and estimated by the PA behavioral models reported in Table 5.18

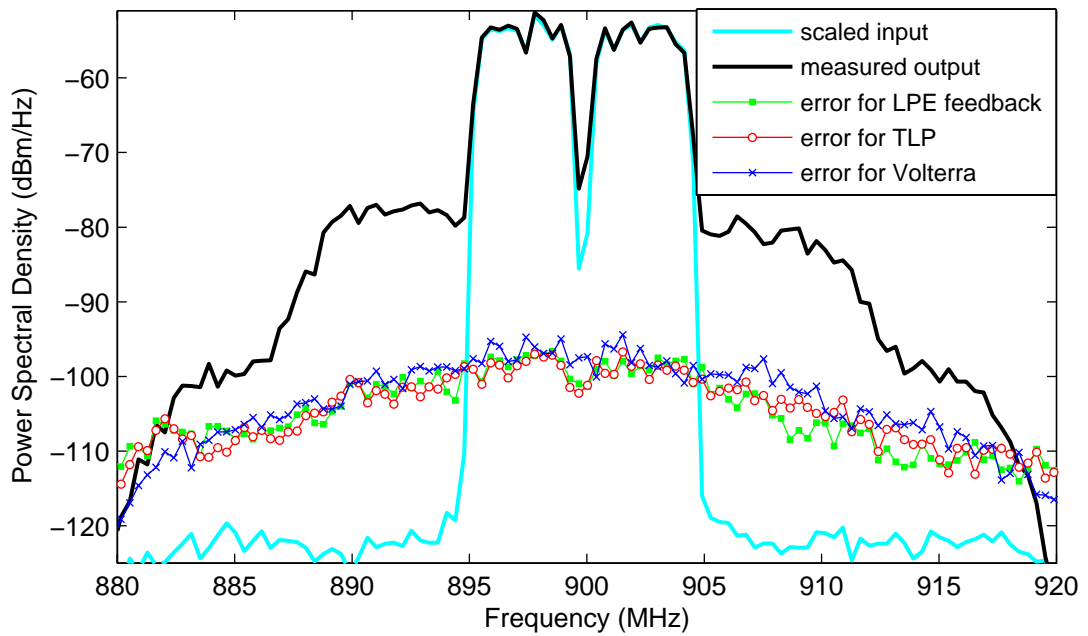


Figure 5.33: PSDs of the error signals for the PA behavioral models reported in Table 5.18

5.3 Validation of the new approach in deriving PA behavioral models presented in Chapter 4

In this section, it is investigated the differences in PA behavioral modeling by assuming a polynomial approximation at RF level or at baseband level. The theory behind these two approaches was presented in Chapter 4. The first approach, which was the methodology followed in Chapter 2, starts by the expansion in a Volterra series of the system at RF level, and then attention is paid to the terms at output that fall in the PA pass-band. On the other hand, the second approach directly derives a low-pass equivalent PA behavioral model in which a Volterra approximation is done at base-band level.

In this section, the models employing the polynomial approximation at RF level will be referred to as RF Poly, while the models employing the polynomial approximation at base-band level will be referred to as BB Poly. Four different models for both polynomial approximations are compared:

- memoryless model. The RF Poly is given by (4.28), while the BB Poly is given by (4.31);
- memory polynomial (MP) model. The RF Poly is given by (2.41) or (4.32), while the BB Poly is given by (4.35);
- Volterra series. The RF Poly is given by (2.17) or (4.39), while the BB Poly is given by (4.35);
- dynamic deviation (DD) model. The RF Poly is given by (2.32), while the BB Poly is given by (4.40).

In the results presented in this section, the BB Poly models use the truncation factor P_0 that is equal to the polynomial order truncation, while the RF Poly models use the truncation factor P that is related to the polynomial order truncation by $2P - 1 = P_0$.

The same experimental input-output data, and specifically the same subsets for extraction and validation purposes used in Section 5.1, is again used here.

5.3.1 Case study 1: one carrier WCDMA input signal

In the first case study, time-domain measurements were performed in a class AB PA with GaN based technology, driven by a WCDMA 3GPP signal of bandwidth 3.84 MHz and peak-to-average power ratio (PAPR) of 11.6 dB, for an average output power of 26 dBm. The sampling frequency was set to 61.44 MHz. Attention was paid to avoid extrapolation. Specifically, the minimum and maximum instantaneous values of both in-phase I_x and quadrature Q_x components of the input signal as well as the maximum instantaneous magnitude of the input signal in the validation subset were forced to be inside their respective ranges in the extraction subset. See Table 5.1 presented in SubSection 5.1.1 for the numerical values.

Initially, several memoryless models with different truncation factor P , for RF Poly models, and P_0 , for BB Poly models, were extracted to model the relationship between the complex-valued envelopes measured at the PA input and output. Table 5.19 shows the NMSE and ACEPR results, as well as the number of complex-valued parameters N in each case.

For the same number of complex-valued parameters and up to five parameters, Table 5.19 shows that the memoryless models with BB Poly have superior performance on both NMSE and ACEPR FoMs than the memoryless models with RF Poly. The largest differences, specifically 3.5 dB in NMSE and 3.5 dB and 2 dB in ACEPR_{LW} and ACEPR_{UP}, respectively, for $\Delta_f = 5$ MHz are observed in the case with two complex-valued parameters. As the number of parameters increases, the differences between the two polynomial approximations reduce. A similar performance for both RF Poly and BB Poly is observed for a number of parameters higher than five.

In Figure 5.34 is shown the measured instantaneous AM-AM conversion as well as the estimated instantaneous AM-AM conversions by the memoryless models with two complex-valued parameters for both RF Poly and BB Poly. The superior performance of the memoryless model with BB Poly is evident. Additionally, the AM-AM conversion of the memoryless model with RF Poly and three complex-valued coefficients was included in Figure 5.34 to show that the BB Poly still has superior performance, even with a lower number of parameters.

Table 5.19: NMSE and ACEPR results for memoryless models with different polynomial approximations

Model	P or P_0	N	NMSE (dB)	ACEPR _{LW} (dB) $\Delta_f =$ 10 MHz	ACEPR _{LW} (dB) $\Delta_f =$ 5 MHz	ACEPR _{UP} (dB) $\Delta_f =$ 5 MHz	ACEPR _{UP} (dB) $\Delta_f =$ 10 MHz
RF Poly	2	2	-32.07	-59.77	-40.89	-43.21	-59.85
BB Poly	2	2	-35.57	-60.70	-44.39	-45.20	-61.09
RF Poly	3	3	-34.54	-60.41	-43.57	-43.97	-60.71
BB Poly	3	3	-35.61	-60.95	-44.30	-45.35	-61.43
RF Poly	4	4	-35.39	-61.32	-44.24	-44.60	-61.70
BB Poly	4	4	-35.83	-62.24	-44.81	-45.26	-63.39
RF Poly	5	5	-35.73	-62.40	-44.61	-45.05	-63.04
BB Poly	5	5	-35.93	-62.99	-45.09	-45.26	-64.20
RF Poly	6	6	-35.93	-63.77	-44.94	-45.23	-64.76
BB Poly	6	6	-35.97	-63.59	-45.12	-45.31	-64.67
RF Poly	7	7	-36.03	-65.12	-45.19	-45.30	-65.66
BB Poly	7	7	-36.04	-65.48	-45.22	-45.34	-66.29
RF Poly	8	8	-36.06	-65.91	-45.29	-45.32	-66.15
BB Poly	8	8	-36.05	-66.02	-45.28	-45.37	-66.49
RF Poly	9	9	-36.05	-65.99	-45.29	-45.34	-66.33
BB Poly	9	9	-36.06	-66.47	-45.29	-45.36	-66.72

The power spectral densities (PSDs) of the measured output signal and modeled output signals by the memoryless models with two complex-valued parameters for both RF Poly and BB Poly are shown in Figure 5.35, as well as the PSDs of the error signals between measured and modeled outputs. Whereas the estimated output by the RF Poly memoryless model with $P = 2$ is band-limited to three times the bandwidth of the input signal, the estimated output by the BB Poly memoryless model with $P_0 = 2$ is not band-limited. The error signal for the BB Poly is clearly lower than the error signal for the RF Poly at the in-band and adjacent channels. This is in accordance with the FoMs reported in Table 5.19, since the error at the in-band channel is sensed by the NMSE FoM while

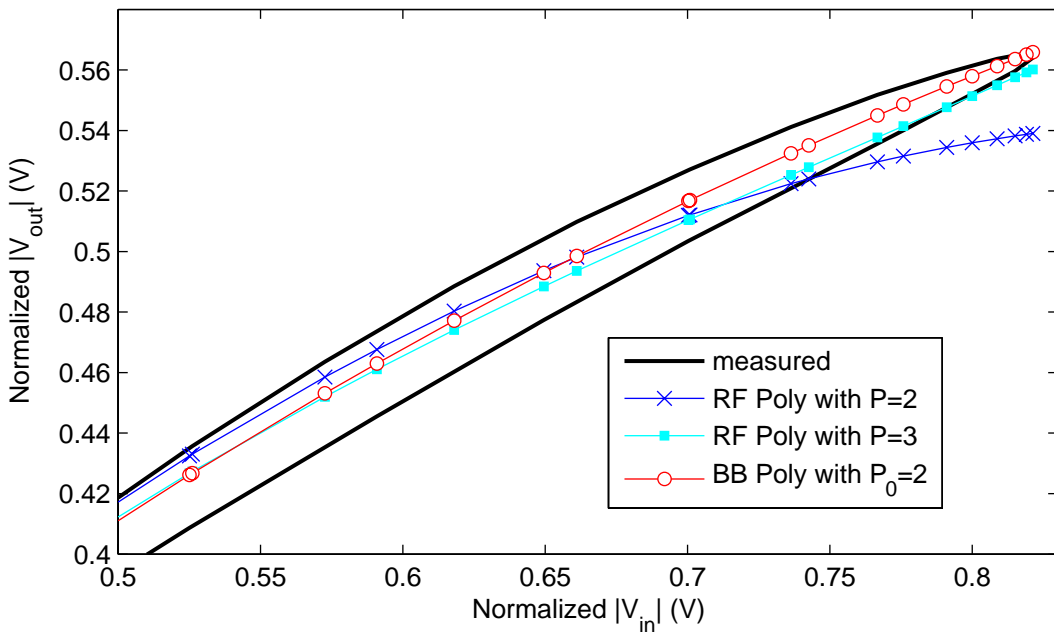


Figure 5.34: Samples of instantaneous AM-AM conversions: measured and estimated by memoryless models with different polynomial approximations

the errors at the adjacent channels are sensed by the ACEPR for $\Delta_f = 5$ MHz.

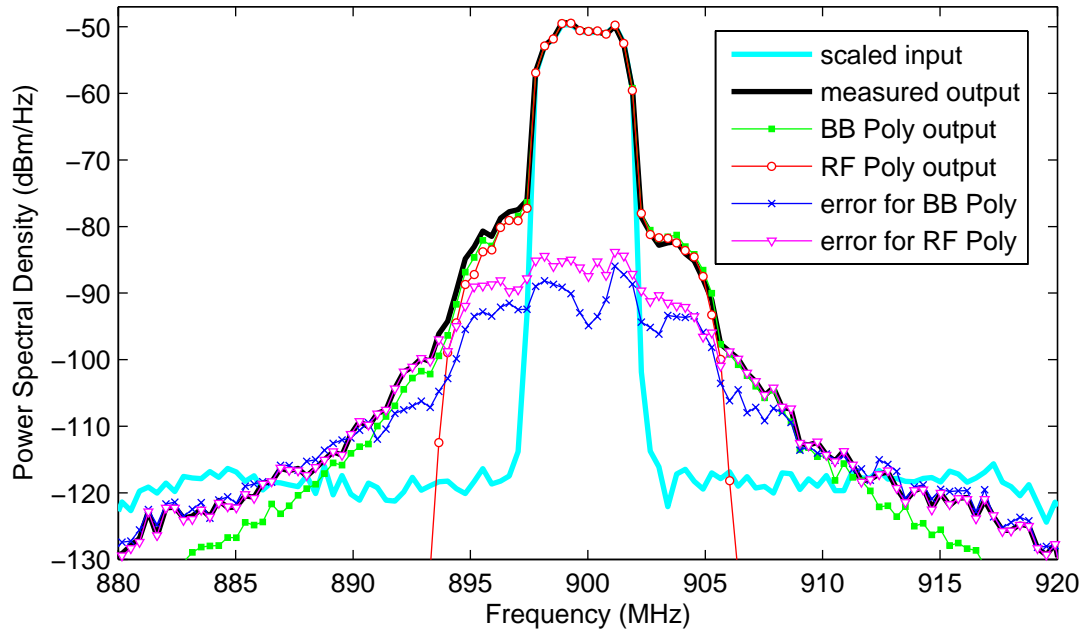


Figure 5.35: PSDs for memoryless models with $P = P_0 = 2$ and different polynomial approximations

In Figure 5.36 is shown the measured instantaneous AM-AM conversion as well as the estimated instantaneous AM-AM conversions by the memoryless models with eight complex-valued parameters for both RF Poly and BB Poly. In accordance with the FoMs reported in Table 5.19, no relevant differences between the two approaches are observed. This observation is reenforced by the similar PSDs of the error signals for both RF Poly and BB Poly memoryless models with eight complex-valued parameters shown in Figure 5.37. In fact, the unnecessary parity constraint imposed by the RF Poly models does not imply, analytically, any loss in modeling capability, since only positive absolute values are allowed. Hence, if the number of parameters is large enough and numerical problems associate with finite precision do not manifest at a considerable level, it is expected similar results for both polynomial approximations. Nevertheless, as already pointed out in [80], numerical algorithms tend to be more ill-conditioned in the presence of higher polynomial order. In the specific case studied here, the algorithms were implemented in a double-precision floating point hardware and numerical problems do not manifest until the desired polynomial order truncation. However, the situation could be diverse if the models were implemented in a DSP or FPGA having lower bits or fix-point.

For the same maximum polynomial order, Table 5.19 shows that the memoryless models with BB Poly have always superior performance (NMSE and ACEPR FoMs) than the memoryless models with RF Poly. The largest difference is observed for a maximum polynomial order equals to the third. Specifically, the BB Poly with $P_0 = 3$ improves 3.5 dB in NMSE and 3.4 dB and 2.1 dB in ACEPR_{LW} and ACEPR_{UP}, respectively, for $\Delta_f = 5$ MHz with respect to the RF Poly with $P = 2$. As the maximum polynomial order increases, the differences between the two polynomial approximations reduce. Particularly, the BB Poly with $P_0 = 9$ improves 0.3 dB in NMSE and 0.7 dB and 0.3 dB in ACEPR_{LW} and ACEPR_{UP}, respectively, for $\Delta_f = 5$ MHz with respect to the RF Poly with $P = 5$.

At this point, several memory polynomial (MP) models with different truncation factor P , for RF Poly models, and P_0 , for BB Poly models, and with fixed memory length $M = 3$ were extracted to model the relationship between the complex-valued envelopes measured at the PA input and output. Table 5.20 shows the NMSE and ACEPR results, as well as the number of complex-valued parameters N in each case.

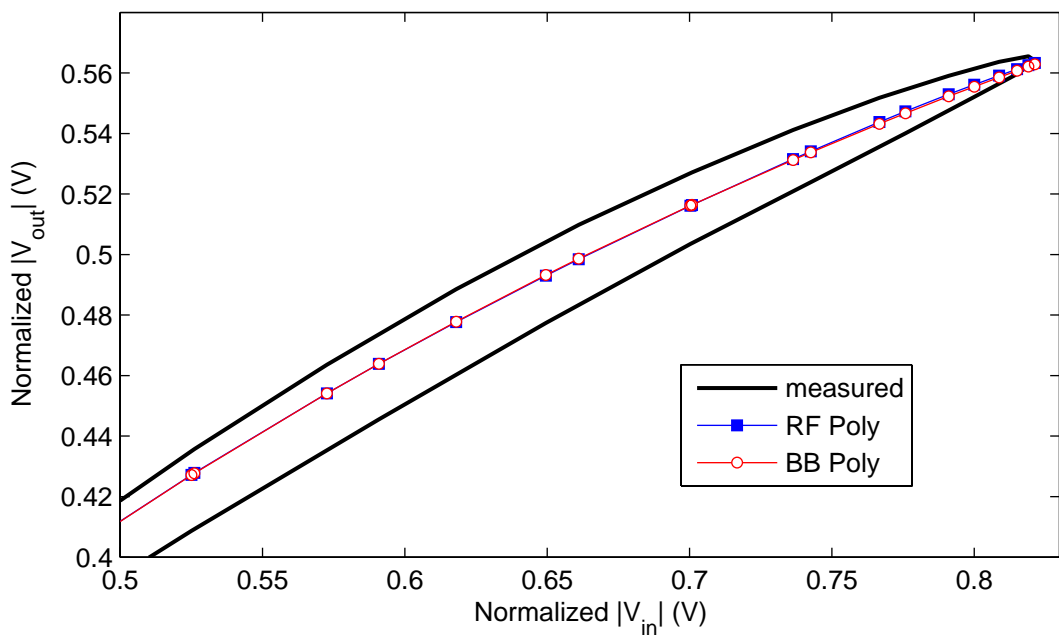


Figure 5.36: Samples of instantaneous AM-AM conversions: measured and estimated by memoryless models with $P = P_0 = 8$ and different polynomial approximations

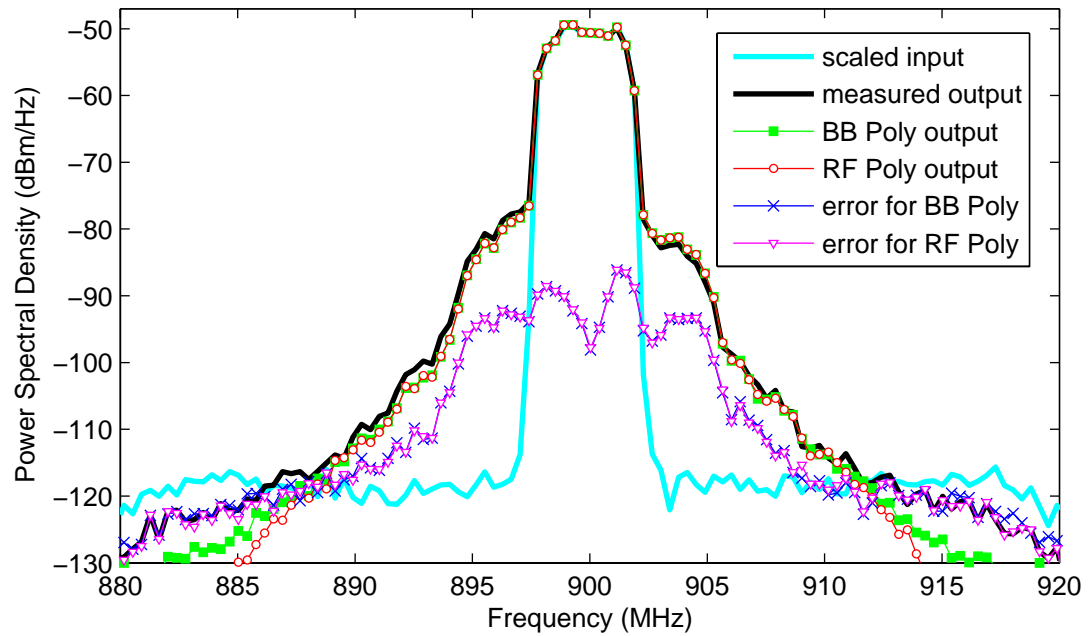


Figure 5.37: PSDs for memoryless models with 8 complex-valued parameters and different polynomial approximations

Table 5.20: NMSE and ACEPR results for MP models with different polynomial approximations

Model	P or P_0	M	N	NMSE (dB)	ACEPR _{LW} (dB) $\Delta_f =$ 10 MHz	ACEPR _{LW} (dB) $\Delta_f =$ 5 MHz	ACEPR _{UP} (dB) $\Delta_f =$ 5 MHz	ACEPR _{UP} (dB) $\Delta_f =$ 10 MHz
RF Poly	2	3	8	-33.77	-59.78	-42.98	-44.89	-59.85
BB Poly	2	3	8	-41.58	-58.05	-50.45	-53.47	-64.11
RF Poly	3	3	12	-38.53	-60.47	-48.20	-48.68	-60.84
BB Poly	3	3	12	-41.87	-60.22	-51.09	-53.82	-63.89
RF Poly	4	3	16	-41.17	-61.20	-50.86	-51.17	-61.99
BB Poly	4	3	16	-43.04	-62.64	-53.75	-54.54	-64.52
RF Poly	5	3	20	-42.52	-62.23	-52.79	-53.68	-63.33
BB Poly	5	3	20	-43.53	-63.39	-55.66	-54.82	-65.21
RF Poly	6	3	24	-43.31	-63.77	-54.74	-54.70	-65.04
BB Poly	6	3	24	-43.66	-63.89	-55.92	-55.25	-65.34
RF Poly	7	3	28	-43.83	-65.64	-56.76	-55.41	-66.79
BB Poly	7	3	28	-43.94	-65.90	-57.14	-55.60	-67.10
RF Poly	8	3	32	-44.12	-66.63	-58.00	-55.93	-67.45
BB Poly	8	3	32	-44.08	-66.28	-57.81	-55.98	-67.75
RF Poly	9	3	36	-44.13	-66.64	-58.01	-55.99	-67.47
BB Poly	9	3	36	-44.11	-66.90	-57.91	-56.13	-68.26

Again, for the same number of complex-valued parameters and up to $P = P_0 = 6$, in Table 5.20 is shown that the MP models with BB Poly have superior performance (NMSE and ACEPR FoMs) than the MP models with RF Poly. The largest differences, specifically 7.8 dB in NMSE, and 7.5 dB and 8.6 dB in ACEPR_{LW} and ACEPR_{UP}, respectively, for $\Delta_f = 5$ MHz are observed in the case with $P = P_0 = 2$ and $M = 3$. As the number of parameters increases, the differences between the two polynomial approximations reduce. A similar performance for the RF Poly and BB Poly is observed for $P = P_0 > 7$.

In Figure 5.38 is shown the measured instantaneous AM-AM conversion as well as the estimated instantaneous AM-AM conversions by the MP models with $P = P_0 = 2$ and $M = 3$ for both RF Poly and BB Poly. The superior performance of the MP model with

respect to the BB Poly is clearly observed.

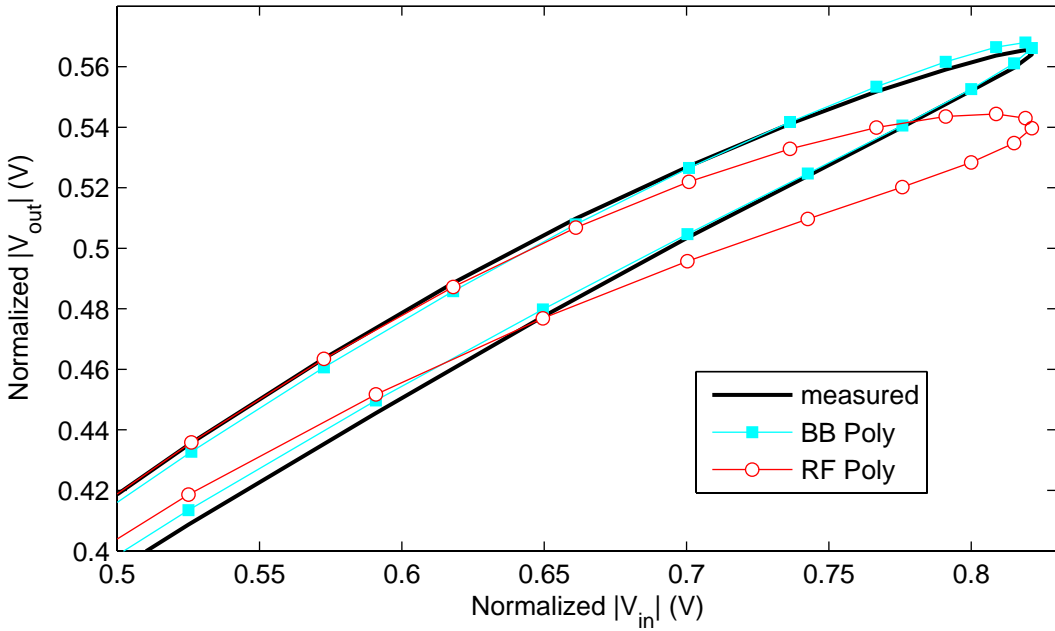


Figure 5.38: Samples of instantaneous AM-AM conversions: measured and estimated by MP models with $P = P_0 = 2$, $M = 3$ and different polynomial approximations

The power spectral densities (PSDs) of the measured output signal and simulated output signals by the MP models with $P = P_0 = 2$ and $M = 3$ for both RF Poly and BB Poly are shown in Figure 5.39, as well as the PSDs of the error signals between measured and modeled outputs. Whereas the estimated output by the RF Poly MP model with $P = 2$ and $M = 3$ is band-limited to three times the bandwidth of the input signal, the estimated output by the BB Poly MP model with $P_0 = 2$ and $M = 3$ is not band-limited. The error signal for the BB Poly is clearly lower than the error signal for the RF Poly at the in-band and adjacent channels. This is in accordance with the FoMs reported in Table 5.20. In fact, this particular BB Poly MP model with $P_0 = 2$ and $M = 3$ can model accurately the relationship between the complex-valued envelopes measured at the PA input and output with just eight complex-valued parameters.

In Figure 5.40 is shown the measured instantaneous AM-AM conversion as well as the estimated instantaneous AM-AM conversions by the MP models with $P = P_0 = 8$ and $M = 3$ for both RF Poly and BB Poly. In accordance with the FoMs reported in Table 5.20, no relevant differences between the two approaches are observed. This

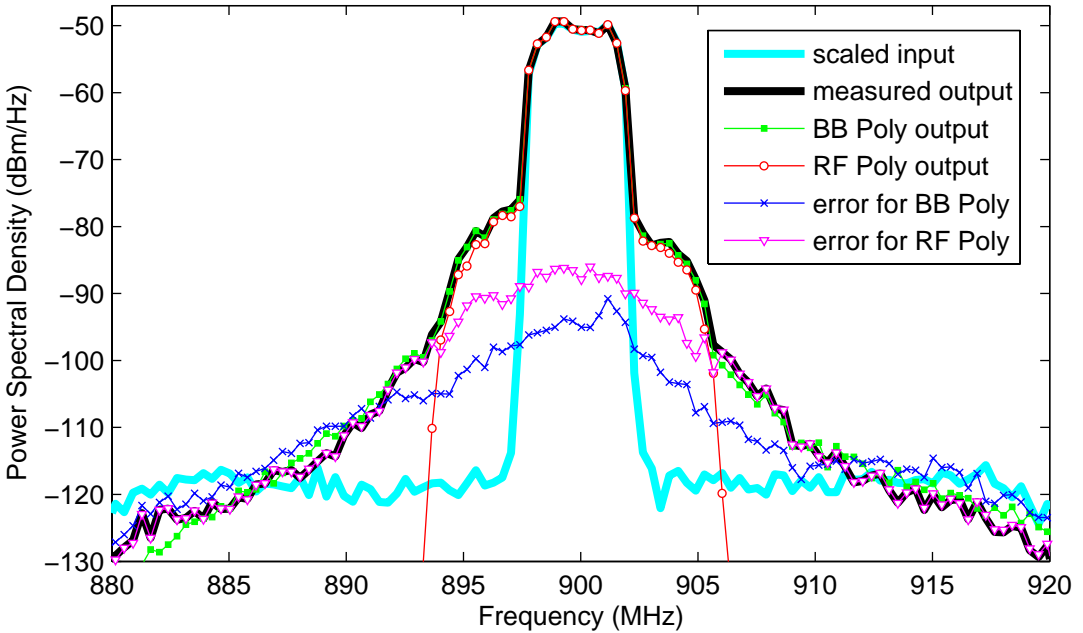


Figure 5.39: PSDs for MP models with $P = P_0 = 2$, $M = 3$ and different polynomial approximations

observation is reenforced by the similar PSDs of the error signals for both RF Poly and BB Poly MP models with $P = P_0 = 8$ and $M = 3$ shown in Figure 5.41. Again, since the number of parameters was large enough and the numerical problems associate with finite precision did not manifest at a considerable level, similar results for both polynomial approximations were expected.

For the same maximum polynomial order, Table 5.20 shows that the MP models with BB Poly have always superior performance (NMSE and ACEPR FoMs) than the MP models with RF Poly. The largest difference is observed for a maximum polynomial order equals to the third. Specifically, the BB Poly with $P_0 = 3$ and $M = 3$ improves 8.1 dB in NMSE and 8.1 dB and 8.9 dB in ACEPR_{LW} and ACEPR_{UP}, respectively, for $\Delta_f = 5$ MHz with respect to the RF Poly with $P = 2$ and $M = 3$. As the maximum polynomial order increases, the differences between the two polynomial approximations reduce. Particularly, the BB Poly with $P_0 = 9$ and $M = 3$ improves 1.6 dB in NMSE and 5.1 dB and 2.5 dB in ACEPR_{LW} and ACEPR_{UP}, respectively, for $\Delta_f = 5$ MHz with respect to the RF Poly with $P = 5$ and $M = 3$.

Now, several Volterra series with different memory length M and different truncation

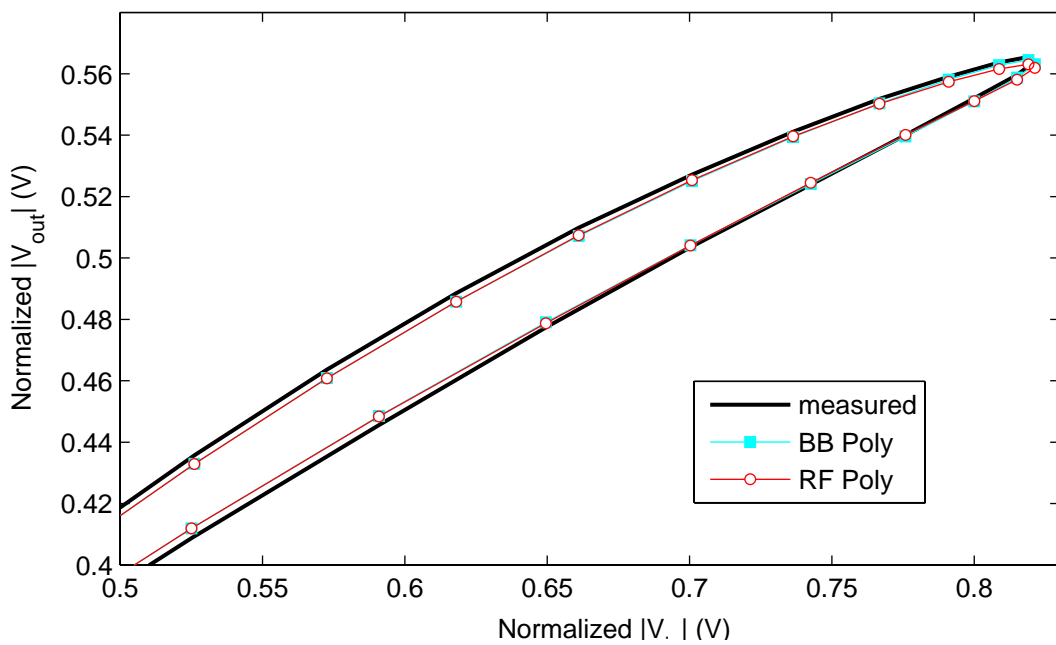


Figure 5.40: Samples of instantaneous AM-AM conversions: measured and estimated by MP models with $P = P_0 = 8$, $M = 3$ and different polynomial approximations

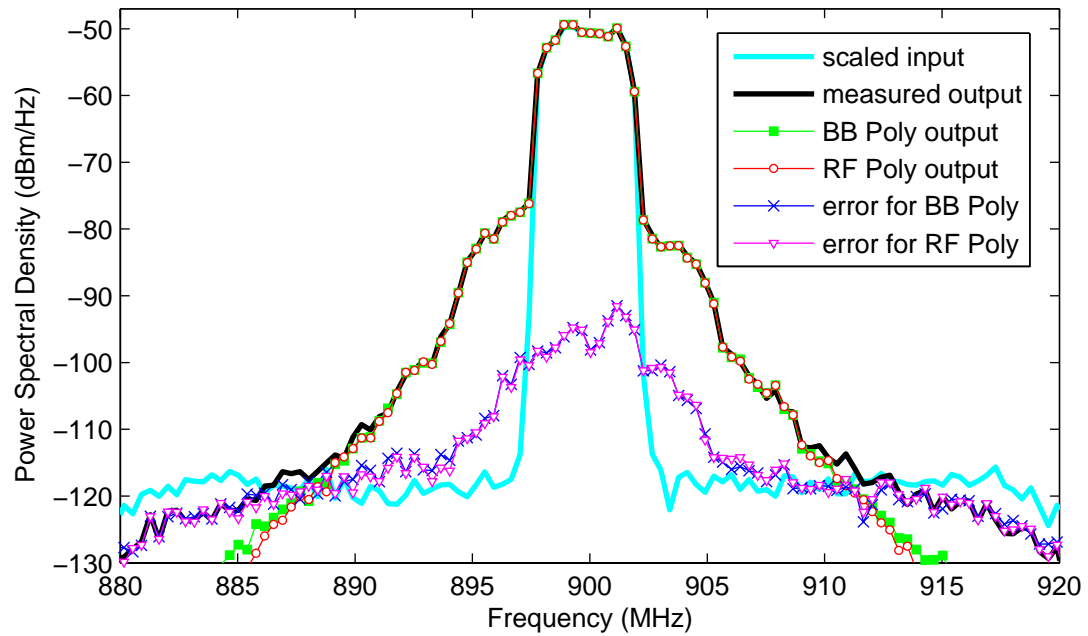


Figure 5.41: PSDs for MP models with $P = P_0 = 8$, $M = 3$ and different polynomial approximations

factor P , for RF Poly models, and P_0 , for BB Poly models, were extracted to model the relationship between the complex-valued envelopes measured at the PA input and output. In Table 5.21 is shown the NMSE and ACEPR results, as well as the number of complex-valued parameters N in each case.

Firstly, observe that the number of complex-valued parameters for fixed M and $P = P_0$ is different from the RF Poly and BB Poly Volterra series. Actually, their number of parameters coincides only if $M = 0$, e.g. just in the memoryless case, as explained in Chapter 4.

Once again, for the same truncation factor $P = P_0$ and up to $P = P_0 = 6$, Table 5.21 shows that the Volterra series with BB Poly have superior performance (NMSE and ACEPR FoMs) than the Volterra series with RF Poly. The largest differences, specifically 9.6 dB in NMSE and 7.7 dB and 9.9 dB in ACEPR_{LW} and ACEPR_{UP}, respectively, for $\Delta_f = 5$ MHz are observed in the case with $P = P_0 = 2$ and $M = 2$. As the truncation factor $P = P_0$ increases, the differences between the two polynomial approximations reduce. A similar performance for both RF Poly and BB Poly is observed for $P = P_0 > 7$ and $M = 1$.

In Figure 5.42 is shown the measured instantaneous AM-AM conversion as well as the estimated instantaneous AM-AM conversions by the Volterra series with $P = P_0 = 2$ and $M = 2$ for both RF Poly and BB Poly. The superior performance of the Volterra series with BB Poly is clearly observed.

The power spectral densities (PSDs) of the measured output signal and modeled output signals by the Volterra series with $P = P_0 = 2$ and $M = 2$ for both RF Poly and BB Poly are shown in Figure 5.43, as well as the PSDs of the error signals between measured and modeled outputs. Whereas the estimated output by the Volterra series with RF Poly ($P = 2$ and $M = 2$) is band-limited to three times the bandwidth of the input signal, the estimated output by the Volterra series with BB Poly ($P_0 = 2$ and $M = 2$) is not band-limited. The error signal for the BB Poly is clearly lower than the error signal for the RF Poly at the in-band and adjacent channels. This is in accordance with the FoMs reported in Table 5.21. Indeed, this particular BB Poly Volterra series with $P_0 = 2$ and $M = 2$ can model very accurately the relationship between the complex-valued envelopes measured at the PA input and output with just twelve complex-valued parameters.

Table 5.21: NMSE and ACEPR results for Volterra models with different polynomial approximations

Model	P or P_0	M	N	NMSE (dB)	ACEPR _{LW} (dB) $\Delta_f =$ 10 MHz	ACEPR _{LW} (dB) $\Delta_f =$ 5 MHz	ACEPR _{UP} (dB) $\Delta_f =$ 5 MHz	ACEPR _{UP} (dB) $\Delta_f =$ 10 MHz
RF Poly	2	1	8	-33.99	-59.78	-43.20	-45.06	-59.86
BB Poly	2	1	6	-43.38	-57.76	-50.83	-55.19	-64.34
RF Poly	2	2	21	-33.96	-59.78	-43.13	-45.22	-59.85
BB Poly	2	2	12	-43.52	-58.35	-50.87	-55.07	-64.36
RF Poly	3	1	20	-39.47	-60.65	-48.36	-49.63	-60.99
BB Poly	3	1	12	-43.99	-59.60	-51.47	-55.35	-63.88
RF Poly	3	2	81	-40.02	-60.47	-48.81	-49.65	-60.84
BB Poly	3	2	30	-44.29	-61.25	-51.46	-55.42	-64.79
RF Poly	4	1	40	-42.95	-61.36	-51.27	-52.16	-62.04
BB Poly	4	1	20	-46.00	-62.44	-54.49	-56.38	-64.46
RF Poly	4	2	231	-43.20	-61.26	-51.28	-50.83	-62.24
BB Poly	4	2	60	-46.49	-63.21	-54.46	-56.92	-64.96
RF Poly	5	1	70	-45.25	-62.22	-53.50	-55.59	-63.68
BB Poly	5	1	30	-47.51	-63.38	-57.07	-57.39	-65.07
BB Poly	5	2	105	-48.05	-64.11	-56.76	-58.39	-65.09
RF Poly	6	1	112	-47.59	-63.53	-56.06	-58.04	-64.51
BB Poly	6	1	42	-47.82	-63.86	-57.66	-58.30	-65.40
BB Poly	6	2	168	-48.56	-64.06	-57.44	-58.79	-65.36
RF Poly	7	1	168	-49.16	-65.81	-59.86	-60.04	-66.46
BB Poly	7	1	56	-49.05	-65.76	-59.78	-59.74	-66.89
BB Poly	7	2	252	-50.06	-66.07	-60.10	-61.20	-66.72
RF Poly	8	1	240	-49.40	-66.26	-61.08	-60.23	-66.80
BB Poly	8	1	72	-49.40	-66.28	-61.07	-60.54	-67.45

In Figure 5.44 is shown the measured instantaneous AM-AM conversion as well as the estimated instantaneous AM-AM conversions by the Volterra series with RF Poly (with

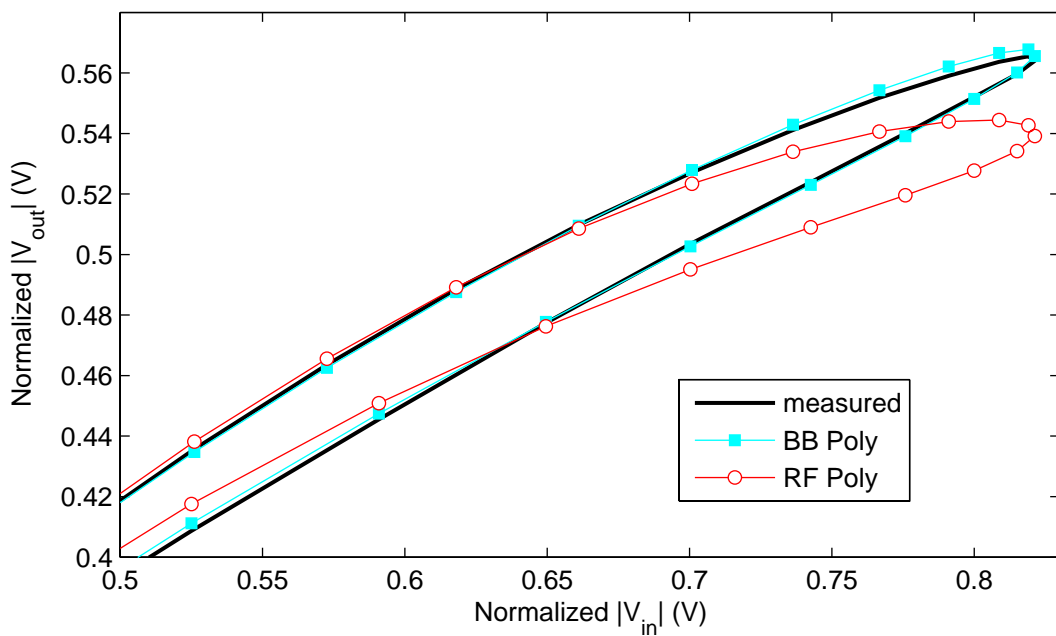


Figure 5.42: Samples of instantaneous AM-AM conversions: measured and estimated by Volterra series with $P = P_0 = 2$, $M = 2$ and different polynomial approximations

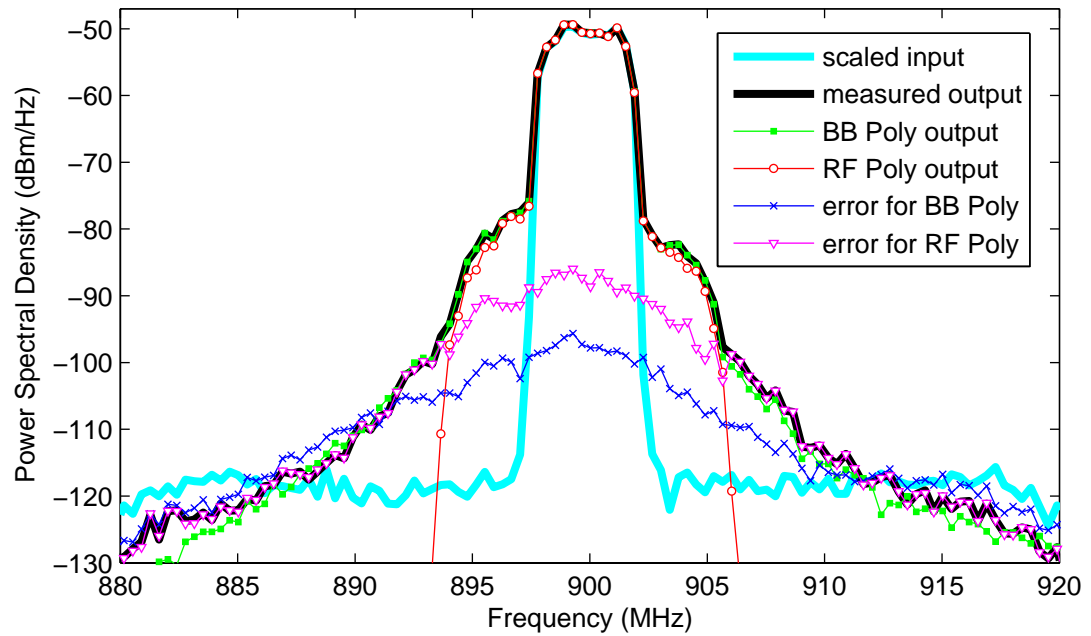


Figure 5.43: PSDs for Volterra series with $P = P_0 = 2$, $M = 2$ and different polynomial approximations

$P = 7$ and $M = 1$) and BB Poly (with $P_0 = 7$ and $M = 2$). Since now the RF Poly and BB Poly have different number of parameters, it was possible to extract a Volterra series with $P_0 = 7$ and $M = 2$ only for the BB Poly. A Volterra series with RF Poly and with $P = 7$ and $M = 2$ would require 2142 complex-valued parameters, which is much higher than the maximum allowed number of complex-valued parameters in this case study. A closer match between measured and modeled AM-AM conversions is observed for the BB Poly at high input powers. The PSDs of the error signals for these specific RF Poly and BB Poly Volterra models are shown in Figure 5.45. The error signal is slightly lower for the BB Poly at the in-band and adjacent channels.

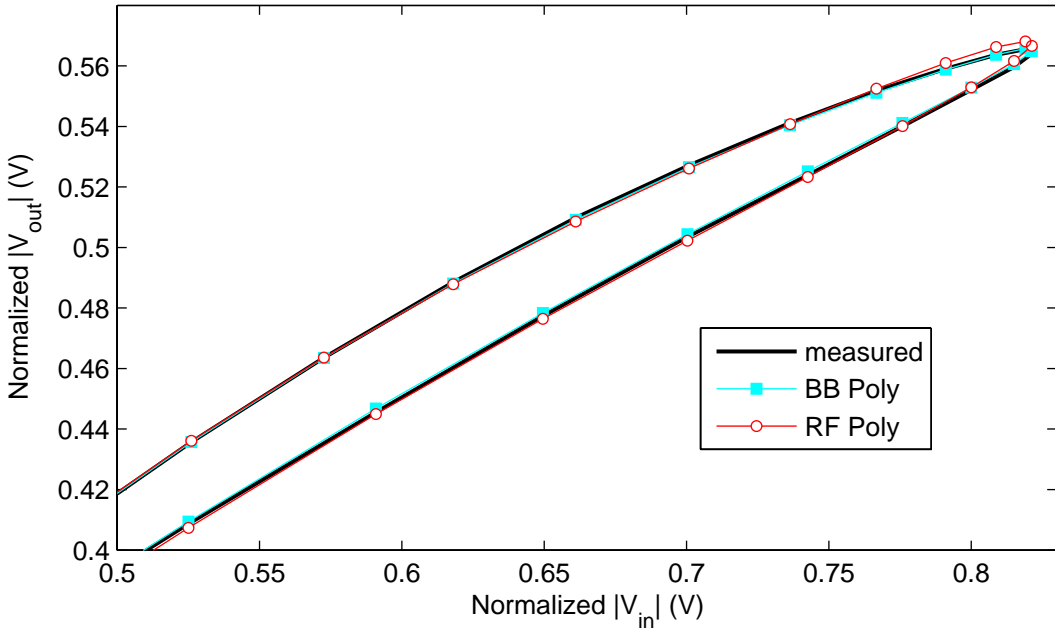


Figure 5.44: Samples of instantaneous AM-AM conversions: measured and estimated by Volterra series with different polynomial approximations: BB Poly with $P_0 = 7$ and $M = 2$; RF Poly with $P = 7$ and $M = 1$

For the same maximum polynomial order, Table 5.21 shows that the Volterra series with BB Poly have always superior performance (NMSE and ACEPR FoMs) than the Volterra series with RF Poly. The largest difference is observed for a maximum polynomial order equals to the third. Specifically, the BB Poly with $P_0 = 3$ and $M = 1$ improves 10.0 dB in NMSE and 8.3 dB and 10.3 dB in ACEPR_{LW} and ACEPR_{UP}, respectively, for $\Delta_f = 5$ MHz with respect to the RF Poly with $P = 2$ and $M = 1$. As the maximum

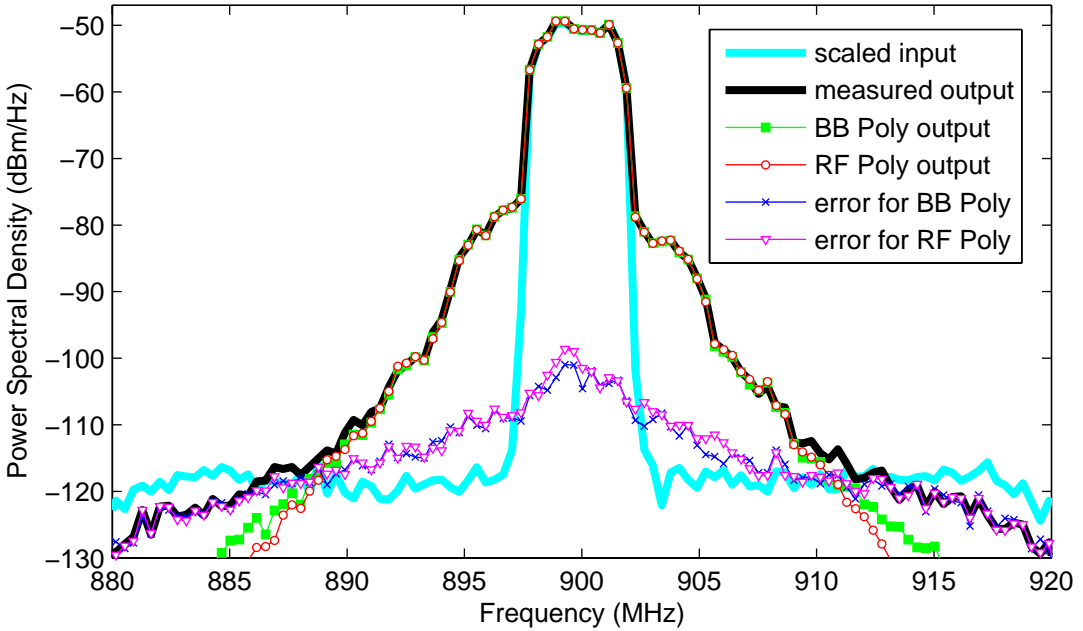


Figure 5.45: PSDs for Volterra series with different polynomial approximations: BB Poly with $P_0 = 7$ and $M = 2$; RF Poly with $P = 7$ and $M = 1$

polynomial order increases, the differences between the two polynomial approximations reduce. Particularly, the BB Poly with $P_0 = 7$ and $M = 1$ improves 6.1 dB in NMSE and 8.5 dB and 7.6 dB in ACEPR_{LW} and ACEPR_{UP}, respectively, for $\Delta_f = 5$ MHz with respect to the RF Poly with $P = 4$ and $M = 1$.

Finally, several dynamic deviation (DD) models with $R = 1$, different memory length M and different truncation factor P , for RF Poly models, and P_0 , for BB Poly models, were extracted to simulate the relationship between the complex-valued envelopes measured at the PA input and output. Table 5.22 shows the NMSE and ACEPR results, as well as the number of complex-valued parameters N in each case.

For the same number of complex-valued parameters, Table 5.22 shows that the DD models with BB Poly have superior performance (NMSE and ACEPR FOMs) than the DD models with RF Poly. The largest differences, specifically 9.6 dB in NMSE and 7.9 dB and 10.1 dB in ACEPR_{LW} and ACEPR_{UP}, respectively, for $\Delta_f = 5$ MHz are observed in the case with $P = P_0 = 2$ and $M = 3$. As the number of parameters increases, the differences between the two polynomial approximations reduce. A similar performance for both RF Poly and BB Poly is observed for $P = P_0 = 9$ and $M = 3$.

Table 5.22: NMSE and ACEPR results for DD models with $R = 1$ and different polynomial approximations

Model	P or P_0	M	N	NMSE (dB)	ACEPR _{LW} (dB) $\Delta_f =$ 10 MHz	ACEPR _{LW} (dB) $\Delta_f =$ 5 MHz	ACEPR _{UP} (dB) $\Delta_f =$ 5 MHz	ACEPR _{UP} (dB) $\Delta_f =$ 10 MHz
RF Poly	2	1	5	-34.00	-59.78	-43.18	-45.24	-59.86
BB Poly	2	1	5	-43.38	-57.78	-50.82	-55.10	-64.28
RF Poly	2	3	11	-33.95	-59.76	-42.94	-45.11	-59.85
BB Poly	2	3	11	-43.50	-58.43	-50.81	-55.19	-64.29
RF Poly	3	3	18	-39.85	-60.35	-48.59	-49.42	-60.72
BB Poly	3	3	18	-44.09	-59.81	-51.27	-55.81	-64.25
RF Poly	4	3	25	-43.09	-61.13	-51.55	-52.37	-61.93
BB Poly	4	3	25	-46.31	-62.33	-54.31	-57.23	-64.48
RF Poly	5	3	32	-45.65	-62.23	-53.98	-55.30	-63.91
BB Poly	5	3	32	-47.71	-63.32	-57.01	-58.10	-65.08
RF Poly	6	3	39	-47.86	-63.92	-57.10	-57.99	-65.59
BB Poly	6	3	39	-48.20	-63.65	-57.41	-58.78	-65.96
RF Poly	7	3	46	-49.13	-65.83	-59.84	-60.11	-66.71
BB Poly	7	3	46	-49.58	-66.05	-60.15	-61.05	-67.43
RF Poly	8	3	53	-49.39	-66.23	-60.75	-60.23	-67.23
BB Poly	8	3	53	-49.75	-66.22	-60.59	-61.62	-67.81
RF Poly	9	3	60	-49.49	-66.36	-60.77	-60.41	-67.29
BB Poly	9	3	60	-49.77	-66.29	-60.64	-61.66	-67.84

In Figure 5.46 is shown the measured instantaneous AM-AM conversion as well as the estimated instantaneous AM-AM conversions by the DD models with $P = P_0 = 2$ and $M = 3$ for both RF Poly and BB Poly. The superior performance of the DD model with BB Poly is clearly observed.

The power spectral densities (PSDs) of the measured output signal and modeled output signals by the DD models with $P = P_0 = 2$ and $M = 3$ for both RF Poly and BB Poly are shown in Figure 5.47, as well as the PSDs of the error signals between measured

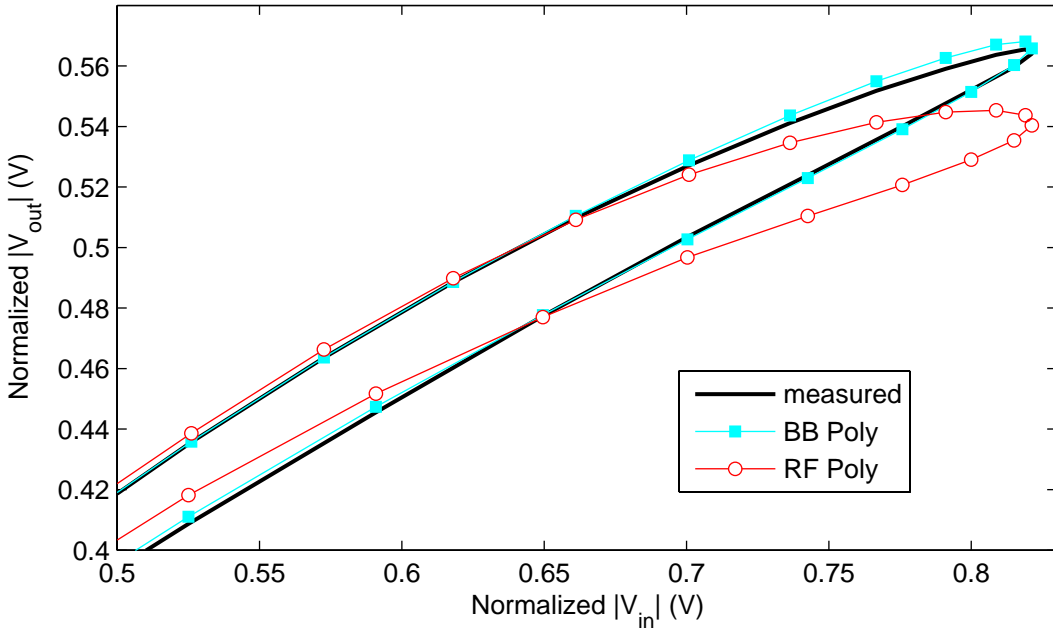


Figure 5.46: Samples of instantaneous AM-AM conversions: measured and estimated by DD models with $P = P_0 = 2$, $M = 3$, $R = 1$ and different polynomial approximations

and modeled outputs. Whereas the estimated output by the RF Poly DD model with $P = 2$ and $M = 3$ is band-limited to three times the bandwidth of the input signal, the estimated output by the BB Poly DD model with $P_0 = 2$ and $M = 3$ is not band-limited. The error signal for the BB Poly is clearly lower than the error signal for the RF Poly at the in-band and adjacent channels. This is in accordance with the FoMs reported in Table 5.22. Indeed, this particular BB Poly DD model with $P_0 = 2$, $M = 3$ and $R = 1$ can model very accurately the relationship between the complex-valued envelopes measured at the PA input and output with just 11 complex-valued parameters.

In Figure 5.48 is shown the measured instantaneous AM-AM conversion as well as the estimated instantaneous AM-AM conversions by the DD models with $P = P_0 = 8$ and $M = 3$ for both RF Poly and BB Poly. In accordance with the FoMs reported in Table 5.22, negligible differences between the two approaches are observed. This observation is reenforced by the similar PSDs of the error signals for both RF Poly and BB Poly MP models with $P = P_0 = 8$ and $M = 3$ shown in Figure 5.49. Again, since the number of parameters was large enough and numerical problems associate with finite precision did not manifest at a considerable level, the similar results for both polynomial

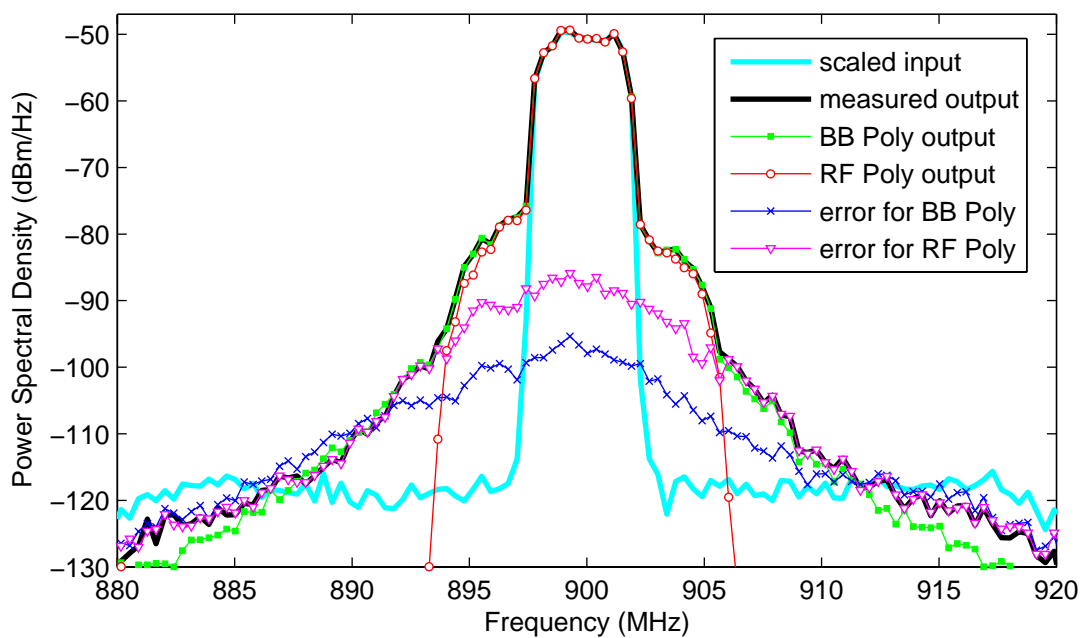


Figure 5.47: PSDs for DD models with $P = P_0 = 2$, $M = 3$, $R = 1$ and different polynomial approximations

approximations were expected.

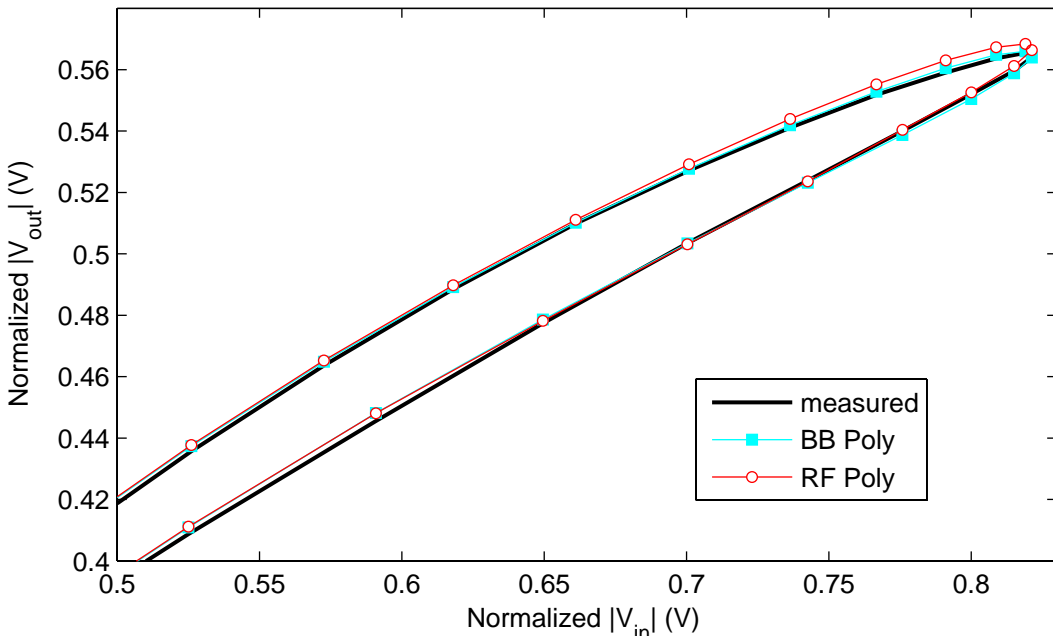


Figure 5.48: Samples of instantaneous AM-AM conversions: measured and estimated by DD models with $P = P_0 = 8$, $M = 3$, $R = 1$ and different polynomial approximations

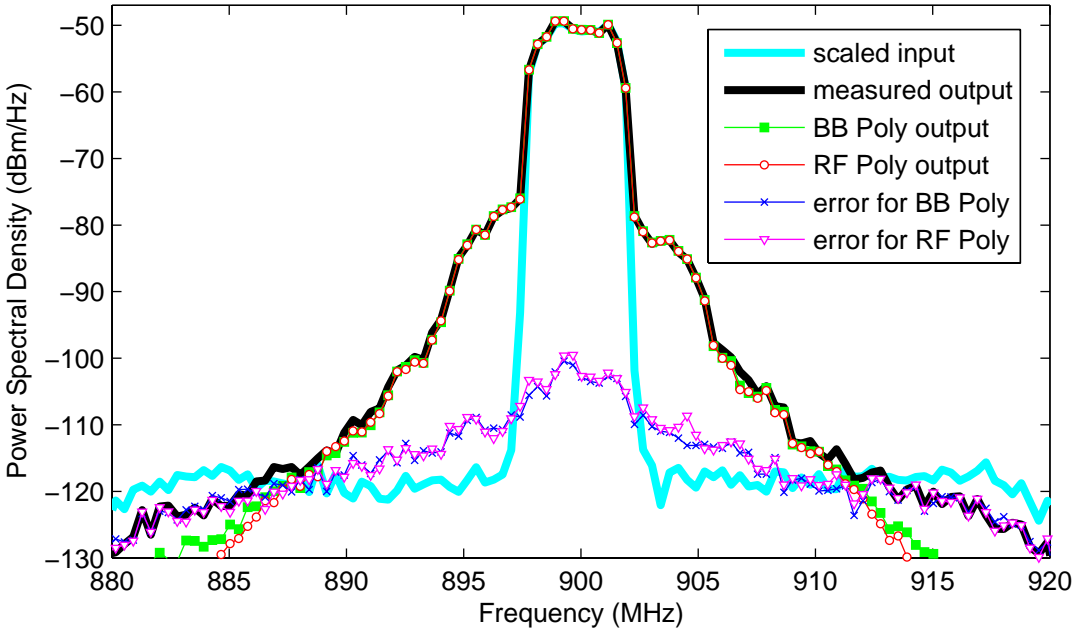


Figure 5.49: PSDs for DD models with $P = P_0 = 8$, $M = 3$, $R = 1$ and different polynomial approximations

For the same maximum polynomial order, Table 5.22 shows that the DD models with BB Poly have always superior performance (NMSE and ACEPR FoMs) than the DD models with RF Poly. The largest difference is observed for a maximum polynomial order equals to the third. Specifically, the BB Poly with $P_0 = 3$ and $M = 3$ improves 10.1 dB in NMSE and 8.3 dB and 10.7 dB in ACEPR_{LW} and ACEPR_{UP}, respectively, for $\Delta_f = 5$ MHz with respect to the RF Poly with $P = 2$ and $M = 3$. As the maximum polynomial order increases, the differences between the two polynomial approximations reduce. Particularly, the BB Poly with $P_0 = 9$ and $M = 3$ improves 4.1 dB in NMSE and 6.7 dB and 6.4 dB in ACEPR_{LW} and ACEPR_{UP}, respectively, for $\Delta_f = 5$ MHz with respect to the RF Poly with $P = 5$ and $M = 3$.

5.3.2 Case study 2: two carrier WCDMA input signal

In this second case study, time-domain measurements were performed in the same class AB PA with GaN based technology used in the case study 1, but now driven by a two carrier WCDMA 3GPP signal of bandwidth 3.84 MHz each carrier, with carrier frequency separation of 5MHz and PAPR of 11 dB, for an average output power of 26 dBm. The

sampling frequency was set to 61.44 MHz. Attention was paid to avoid extrapolation. Specifically, the minimum and maximum instantaneous values of both in-phase I_x and quadrature Q_x components of the input signal as well as the maximum instantaneous magnitude of the input signal in the validation subset were guaranteed to be inside their respective ranges in the extraction subset. See Table 5.9 presented in SubSection 5.1.2 for the numerical values.

Initially, several memoryless models with different truncation factor P , for RF Poly models, and P_0 , for BB Poly models, were extracted to model the relationship between the complex-valued envelopes measured at the PA input and output. Table 5.23 shows the NMSE and ACEPR results, as well as the number of complex-valued parameters N in each case.

Table 5.23: NMSE and ACEPR results for memoryless models with different polynomial approximations

Model	P or P_0	N	NMSE (dB)	ACEPR _{LW} (dB) $\Delta_f =$ 10 MHz	ACEPR _{LW} (dB) $\Delta_f =$ 5 MHz	ACEPR _{UP} (dB) $\Delta_f =$ 5 MHz	ACEPR _{UP} (dB) $\Delta_f =$ 10 MHz
RF Poly	2	2	-27.01	-40.16	-32.98	-35.01	-42.29
BB Poly	2	2	-28.10	-42.73	-35.04	-35.78	-46.82
RF Poly	3	3	-27.98	-42.86	-35.16	-35.44	-45.72
BB Poly	3	3	-28.12	-42.67	-34.95	-35.93	-47.10
RF Poly	4	4	-28.13	-43.09	-35.27	-35.67	-47.39
BB Poly	4	4	-28.16	-43.03	-35.28	-35.67	-47.39
RF Poly	5	5	-28.16	-43.03	-35.26	-35.66	-47.52
BB Poly	5	5	-28.18	-43.19	-35.31	-35.68	-47.50
RF Poly	6	6	-28.18	-43.13	-35.29	-35.67	-47.56
BB Poly	6	6	-28.18	-43.17	-35.31	-35.67	-47.51
RF Poly	7	7	-28.19	-43.23	-35.32	-35.69	-47.66
BB Poly	7	7	-28.18	-43.22	-35.31	-35.69	-47.64

For the same number of complex-valued parameters and up to four parameters, Table 5.23 shows that the memoryless models with BB Poly have superior performance

(NMSE and ACEPR FoMs) than the memoryless models with RF Poly. The largest differences, specifically 1.1 dB in NMSE, 2.1 dB and 0.8 dB in ACEPR_{LW} and ACEPR_{UP}, respectively, for $\Delta_f = 5$ MHz and 2.6 dB and 4.5 dB in ACEPR_{LW} and ACEPR_{UP}, respectively, for $\Delta_f = 10$ MHz are observed in the case with two complex-valued parameters. As the number of parameters increases, the differences between the two polynomial approximations reduce. A similar performance for both RF Poly and BB Poly is observed for a number of parameters higher than four.

In Figure 5.50 is shown the measured instantaneous AM-AM conversion as well as the estimated instantaneous AM-AM conversions by the memoryless models with two complex-valued parameters for both RF Poly and BB Poly. The superior performance of the memoryless model with BB Poly is evident. Additionally, the AM-AM conversion of the memoryless model with RF Poly having three complex-valued coefficients was included in Figure 5.50 to show that the BB Poly still has superior performance, even with a lower number of parameters.

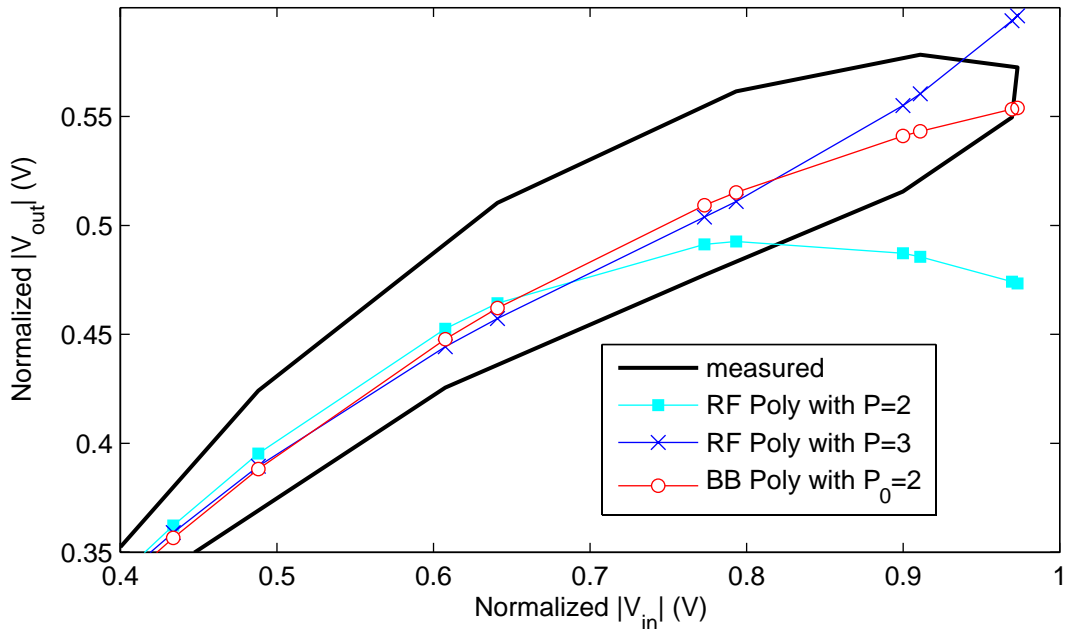


Figure 5.50: Samples of instantaneous AM-AM conversions: measured and estimated by memoryless models with different polynomial approximations

The power spectral densities (PSDs) of the measured output signal and modeled output signals by the memoryless models with two complex-valued parameters for both RF

Poly and BB Poly are shown in Figure 5.51, as well as the PSDs of the error signals between measured and modeled outputs. Whereas the estimated output by the RF Poly memoryless model with $P = 2$ is band-limited to three times the bandwidth of the input signal, the estimated output by the BB Poly memoryless model with $P_0 = 2$ is not band-limited. The error signal for the BB Poly is clearly lower than the error signal for the RF Poly at the whole measured spectrum. This is in accordance with the FoMs reported in Table 5.23, since the error at the in-band channel is sensed by the NMSE FoM while the errors at the adjacent channels are sensed by the ACEPR for $\Delta_f = 5$ MHz and $\Delta_f = 10$ MHz.

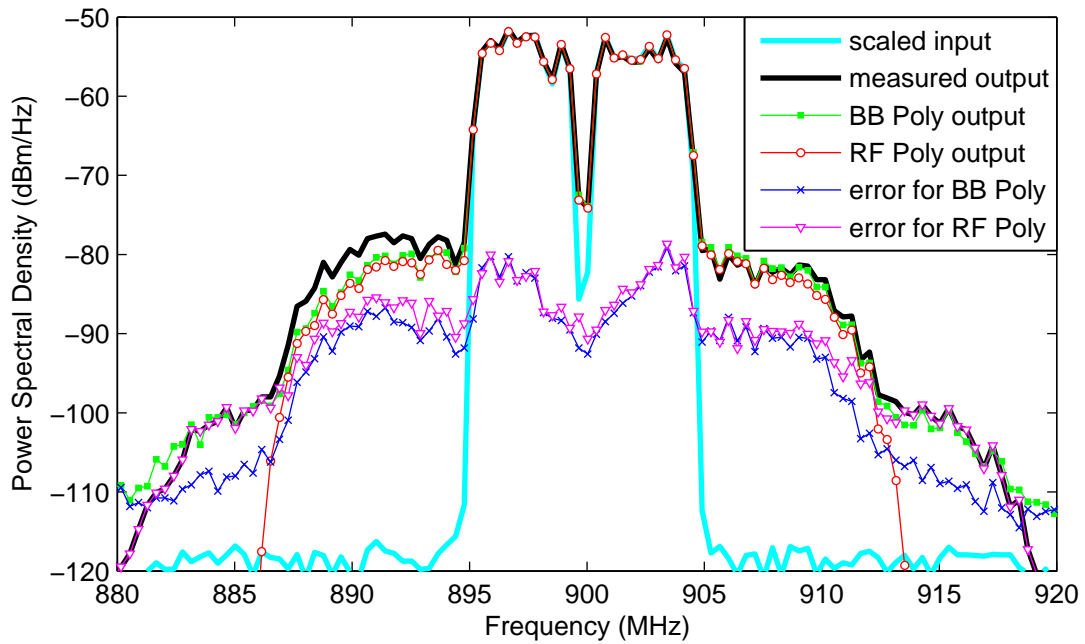


Figure 5.51: PSDs for memoryless models with $P = P_0 = 2$ and different polynomial approximations

In Figure 5.51 is shown the measured instantaneous AM-AM conversion as well as the estimated instantaneous AM-AM conversions by the memoryless models with six complex-valued parameters for both RF Poly ($P = 6$) and BB Poly ($P_0 = 6$). In accordance with the FoMs reported in Table 5.23, no relevant differences between the two approaches are observed. This observation is reenforced by the similar PSDs of the error signals for both RF Poly and BB Poly memoryless models with six complex-valued parameters shown in Figure 5.37.

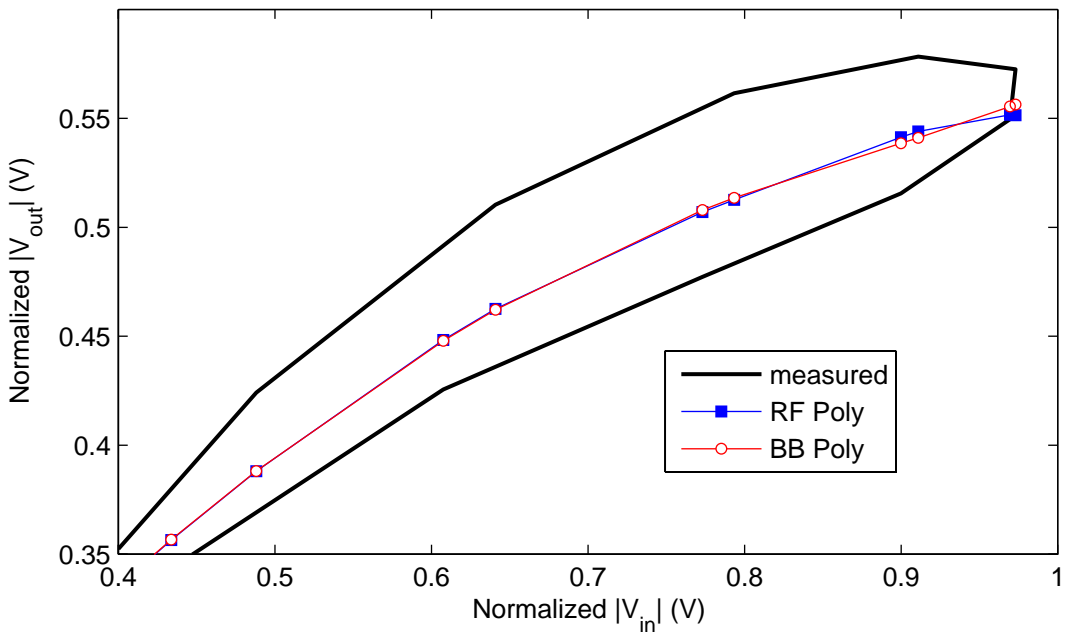


Figure 5.52: Samples of instantaneous AM-AM conversions: measured and estimated by memoryless models with $P = P_0 = 6$ and different polynomial approximations

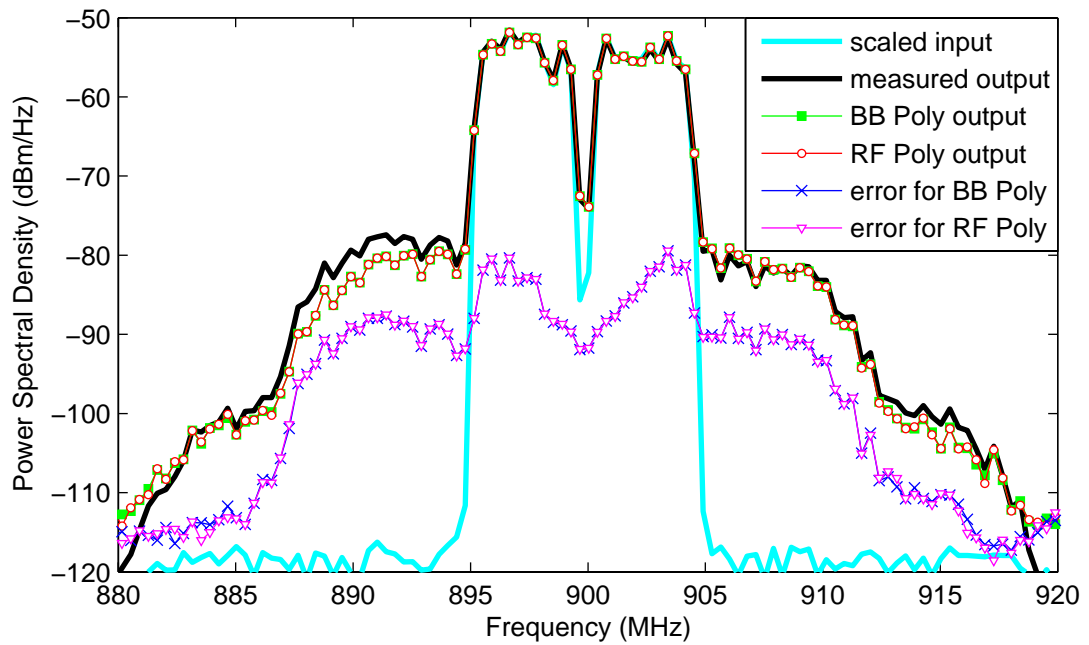


Figure 5.53: PSDs for memoryless models with $P = P_0 = 6$ and different polynomial approximations

For the same maximum polynomial order, Table 5.23 shows that the memoryless models with BB Poly have always superior performance (NMSE and ACEPR FoMs) than the memoryless models with RF Poly. The largest difference is observed for a maximum polynomial order equals to the third. Specifically, the BB Poly with $P_0 = 3$ improves 1.1 dB in NMSE, 2.0 dB and 0.9 dB in ACEPR_{LW} and ACEPR_{UP}, respectively, for $\Delta_f = 5$ MHz and 2.5 dB and 4.8 dB in ACEPR_{LW} and ACEPR_{UP}, respectively, for $\Delta_f = 10$ MHz with respect to the RF Poly with $P = 2$. As the maximum polynomial order increases, the differences between the two polynomial approximations reduce. Particularly, the BB Poly with $P_0 = 7$ improves 0.05 dB in NMSE, 0.04 dB and 0.02 dB in ACEPR_{LW} and ACEPR_{UP}, respectively, for $\Delta_f = 5$ MHz and 0.13 dB and 0.25 dB in ACEPR_{LW} and ACEPR_{UP}, respectively, for $\Delta_f = 10$ MHz with respect to the RF Poly with $P = 4$.

At this point, several memory polynomial (MP) models with different truncation factor P , for RF Poly models, and P_0 , for BB Poly models, and with different memory length M were extracted to model the relationship between the complex-valued envelopes measured at the PA input and output. Table 5.24 shows the NMSE and ACEPR results, as well as the number of complex-valued parameters N in each case.

Again, for the same number of complex-valued parameters and up to $P = P_0 = 5$, Table 5.24 shows that the MP models with BB Poly have superior performance (NMSE and ACEPR FoMs) than the MP models with RF Poly. The largest differences, specifically 4.0 dB in NMSE, 5.8 dB and 5.6 dB in ACEPR_{LW} and ACEPR_{UP}, respectively, for $\Delta_f = 5$ MHz and 5.2 dB and 9.4 dB in ACEPR_{LW} and ACEPR_{UP}, respectively, for $\Delta_f = 10$ MHz are observed in the case with $P = P_0 = 2$ and $M = 4$. As the number of parameters increases, the differences between the two polynomial approximations reduce. A similar performance for both RF Poly and BB Poly is observed for $P = P_0 > 5$ and $M = 3$.

In Figure 5.54 is shown the measured instantaneous AM-AM conversion as well as the estimated instantaneous AM-AM conversions by the MP models with $P = P_0 = 2$ and $M = 3$ for both RF Poly and BB Poly. The superior performance of the MP model with BB Poly is clearly observed.

The power spectral densities (PSDs) of the measured output signal and modeled output signals by the MP models with $P = P_0 = 2$ and $M = 3$ for both RF Poly and BB Poly are shown in Figure 5.55, as well as the PSDs of the error signals between measured and

Table 5.24: NMSE and ACEPR results for MP models with different polynomial approximations

Model	P or P_0	M	N	NMSE (dB)	ACEPR _{LW} (dB) $\Delta_f =$ 10 MHz	ACEPR _{LW} (dB) $\Delta_f =$ 5 MHz	ACEPR _{UP} (dB) $\Delta_f =$ 5 MHz	ACEPR _{UP} (dB) $\Delta_f =$ 10 MHz
RF Poly	2	2	6	-31.44	-43.74	-37.62	-39.13	-43.15
BB Poly	2	2	6	-35.29	-48.91	-42.95	-44.34	-52.54
RF Poly	2	3	8	-31.50	-44.00	-37.73	-39.26	-43.29
BB Poly	2	3	8	-35.36	-48.72	-43.21	-44.50	-52.15
RF Poly	2	4	10	-31.51	-44.02	-37.82	-39.29	-43.35
BB Poly	2	4	10	-35.46	-49.22	-43.57	-44.88	-52.70
RF Poly	3	3	12	-35.00	-49.70	-42.92	-43.40	-48.81
BB Poly	3	3	12	-35.68	-51.35	-43.62	-44.57	-52.45
RF Poly	4	3	16	-35.77	-52.51	-44.60	-44.28	-53.18
BB Poly	4	3	16	-36.02	-53.39	-44.93	-44.61	-54.06
RF Poly	5	3	20	-36.02	-53.70	-45.00	-44.44	-54.92
BB Poly	5	3	20	-36.14	-54.44	-45.30	-44.68	-55.42
RF Poly	6	3	24	-36.13	-54.82	-45.30	-44.66	-56.08
BB Poly	6	3	24	-36.15	-54.74	-45.28	-44.67	-55.80
RF Poly	7	3	28	-36.17	-55.67	-45.43	-44.81	-56.21
BB Poly	7	3	28	-36.18	-55.56	-45.44	-44.80	-56.49

modeled outputs. Whereas the estimated output by the RF Poly MP model with $P = 2$ and $M = 3$ is band-limited to three times the bandwidth of the input signal, the estimated output by the BB Poly MP model with $P_0 = 2$ and $M = 3$ is not band-limited. The error signal for the BB Poly is clearly lower than the error signal for the RF Poly at the whole measured spectrum. This is in accordance with the FoMs reported in Table 5.24. In fact, this particular BB Poly memory polynomial model with $P_0 = 2$ and $M = 3$ can model accurately the relationship between the complex-valued envelopes measured at the PA input and output with just eight complex-valued parameters.

In Figure 5.56 is shown the measured instantaneous AM-AM conversion as well as the estimated instantaneous AM-AM conversions by the MP models with $P = P_0 = 6$

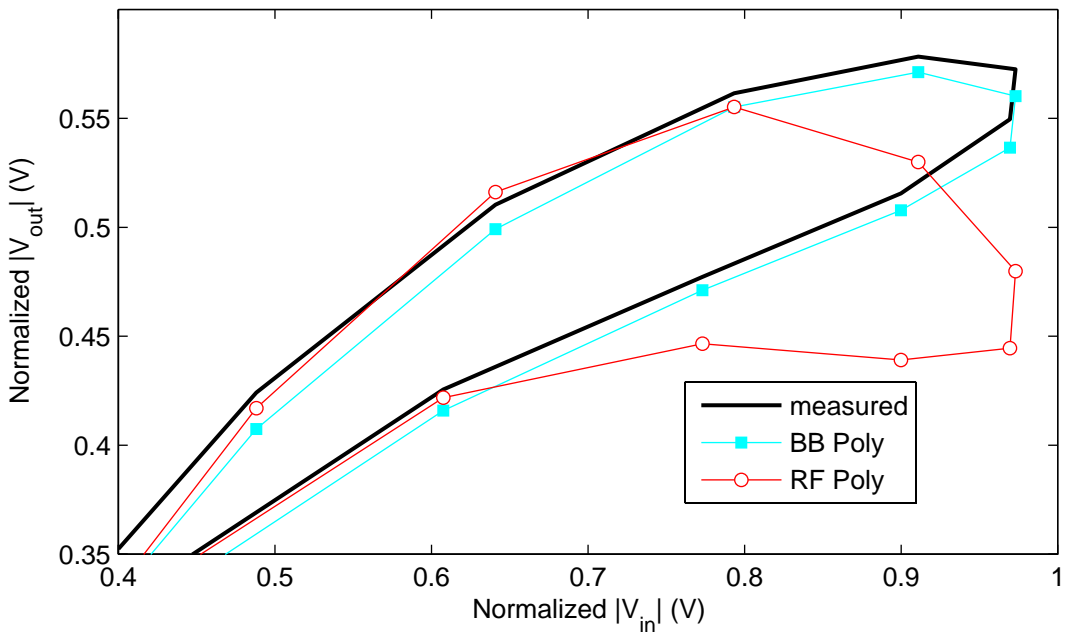


Figure 5.54: Samples of instantaneous AM-AM conversions: measured and estimated by MP models with $P = P_0 = 2$, $M = 3$ and different polynomial approximations

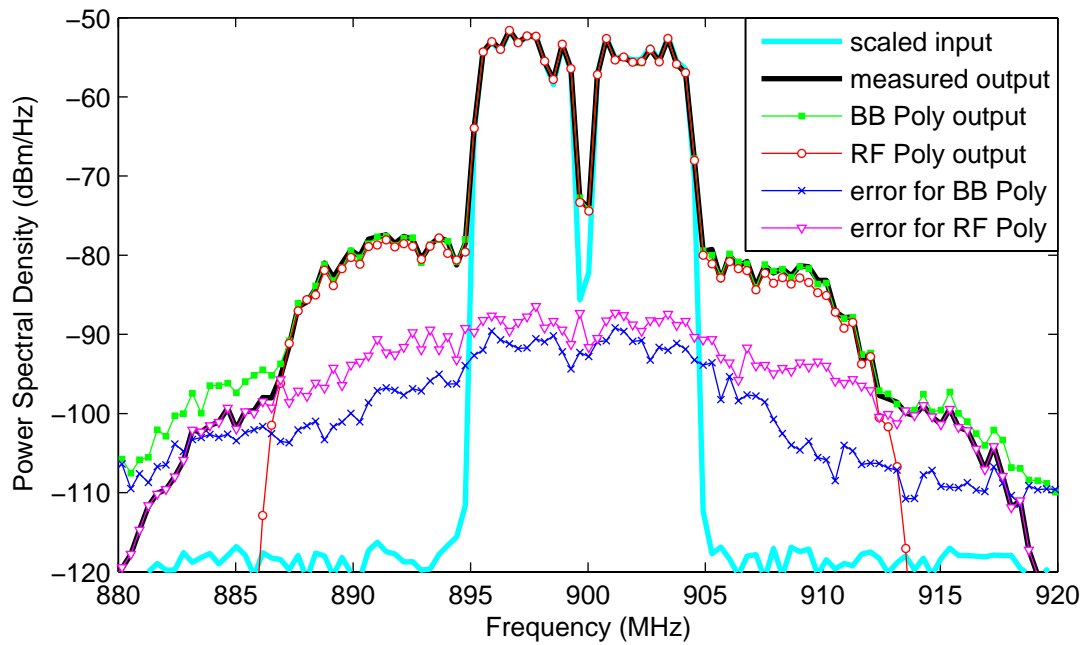


Figure 5.55: PSDs for MP models with $P = P_0 = 2$, $M = 3$ and different polynomial approximations

and $M = 3$ for both RF Poly and BB Poly. In accordance with the FoMs reported in Table 5.24, no relevant differences between the two approaches are observed. This observation is reenforced by the similar PSDs of the error signals for both RF Poly and BB Poly MP models with $P = P_0 = 6$ and $M = 3$ shown in Figure 5.57. Again, since the number of parameters was large enough and numerical problems associate with finite precision did not manifest at a considerable level, the similar results for both polynomial approximations were expected.

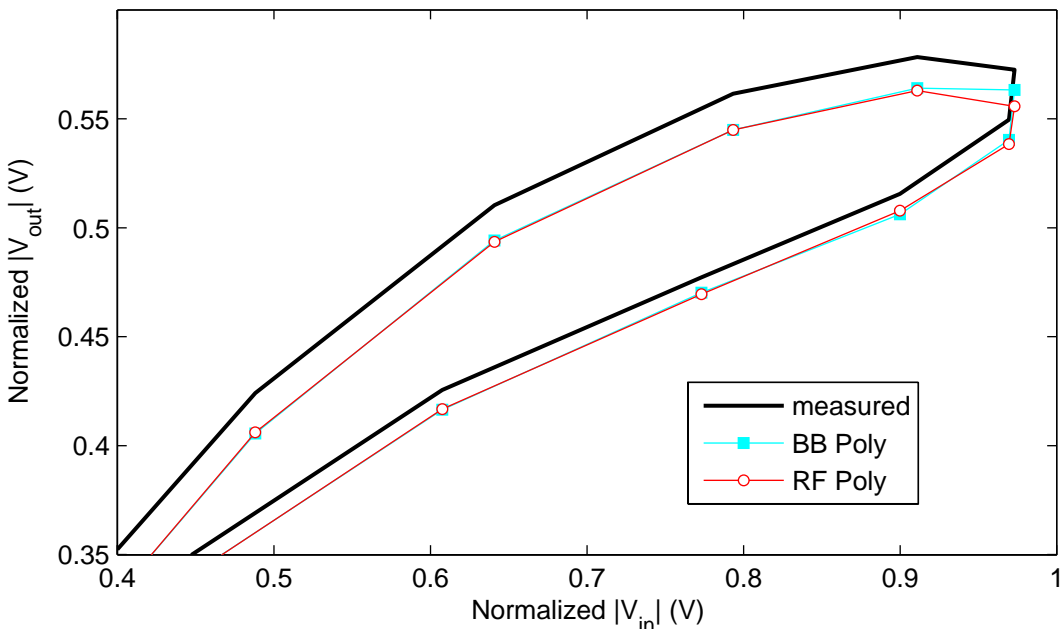


Figure 5.56: Samples of instantaneous AM-AM conversions: measured and estimated by MP models with $P = P_0 = 6$, $M = 3$ and different polynomial approximations

For the same maximum polynomial order, Table 5.24 shows that the MP models with BB Poly have always superior performance (NMSE and ACEPR FoMs) than the MP models with RF Poly. The largest difference is observed for a maximum polynomial order equals to the third. Specifically, the BB Poly with $P_0 = 3$ and $M = 3$ improves 4.2 dB in NMSE, 5.9 dB and 5.3 dB in ACEPR_{LW} and ACEPR_{UP}, respectively, for $\Delta_f = 5$ MHz and 7.4 dB and 9.2 dB in ACEPR_{LW} and ACEPR_{UP}, respectively, for $\Delta_f = 10$ MHz with respect to the RF Poly with $P = 2$ and $M = 3$. As the maximum polynomial order increases, the differences between the two polynomial approximations reduce. Particularly, the BB Poly with $P_0 = 7$ and $M = 3$ improves 0.4 dB in NMSE, 0.8 dB and 0.5 dB

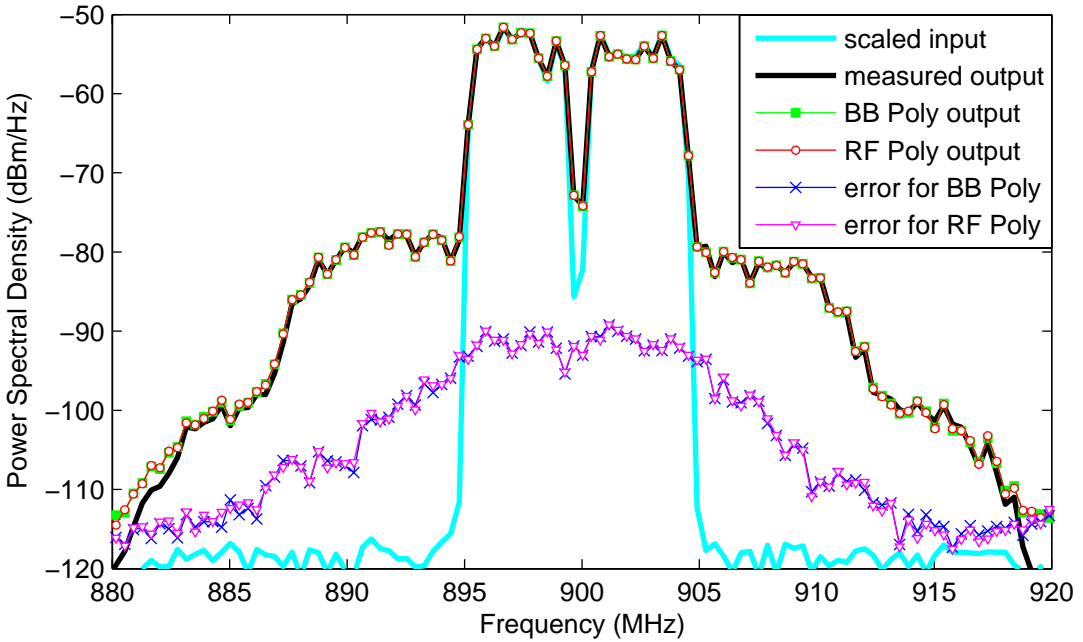


Figure 5.57: PSDs for MP models with $P = P_0 = 6$, $M = 3$ and different polynomial approximations

in ACEPR_{LW} and ACEPR_{UP}, respectively, for $\Delta_f = 5$ MHz and 3.1 dB and 3.3 dB in ACEPR_{LW} and ACEPR_{UP}, respectively, for $\Delta_f = 10$ MHz with respect to the RF Poly with $P = 4$ and $M = 3$.

Now, several Volterra series with different memory length M and different truncation factor P , for RF Poly models, and P_0 , for BB Poly models, were extracted to model the relationship between the complex-valued envelopes measured at the PA input and output. Table 5.25 shows the NMSE and ACEPR results, as well as the number of complex-valued parameters N in each case.

Firstly, observe that the number of complex-valued parameters for fixed M and $P = P_0$ are different from the RF Poly and BB Poly Volterra series. Actually, their number of parameters coincides only if $M = 0$, e.g., just in the memoryless case, as explained in Chapter 4.

For the same truncation factor $P = P_0$ and memory length M , Table 5.25 shows that the Volterra series with BB Poly have superior performance (NMSE and ACEPR FoMs) than the Volterra series with RF Poly. The largest differences, specifically 8.0 dB in NMSE, 7.0 dB and 10.1 dB in ACEPR_{LW} and ACEPR_{UP}, respectively, for $\Delta_f = 5$ MHz

Table 5.25: NMSE and ACEPR results for Volterra models with different polynomial approximations

Model	P or P_0	M	N	NMSE (dB)	ACEPR _{LW} (dB) $\Delta_f =$ 10 MHz	ACEPR _{LW} (dB) $\Delta_f =$ 5 MHz	ACEPR _{UP} (dB) $\Delta_f =$ 5 MHz	ACEPR _{UP} (dB) $\Delta_f =$ 10 MHz
RF Poly	2	2	21	-32.87	-44.17	-38.55	-39.54	-43.31
BB Poly	2	2	12	-40.05	-48.29	-44.57	-46.80	-50.50
RF Poly	2	3	44	-33.00	-44.07	-38.86	-39.46	-43.34
BB Poly	2	3	20	-40.96	-49.35	-45.80	-49.58	-52.22
RF Poly	2	4	80	-33.04	-43.98	-39.01	-39.62	-43.31
BB Poly	2	4	30	-41.02	-49.74	-45.96	-49.75	-52.10
RF Poly	3	2	81	-39.72	-50.44	-46.33	-45.90	-48.86
BB Poly	3	2	30	-42.00	-52.16	-46.64	-49.50	-53.14
RF Poly	3	3	244	-40.28	-51.13	-47.05	-46.47	-49.31
BB Poly	3	3	60	-42.51	-52.80	-47.42	-51.09	-53.90
RF Poly	4	2	231	-42.61	-53.88	-49.59	-49.27	-53.78
BB Poly	4	2	60	-44.07	-54.45	-50.49	-50.40	-55.12
BB Poly	4	3	140	-44.95	-56.02	-51.62	-52.36	-55.99
BB Poly	5	2	105	-44.79	-55.53	-51.32	-50.78	-56.51
BB Poly	5	3	280	-45.99	-57.57	-53.60	-53.00	-57.34
BB Poly	6	2	168	-44.94	-56.00	-51.63	-51.21	-57.01

and 5.8 dB and 8.8 dB in ACEPR_{LW} and ACEPR_{UP}, respectively, for $\Delta_f = 10$ MHz are observed in the case with $P = P_0 = 2$ and $M = 4$. As the truncation factor $P = P_0$ increases, the differences between the two polynomial approximations reduce. Particularly, the BB Poly with $P_0 = 4$ and $M = 2$ improves 1.5 dB in NMSE, 0.9 dB and 1.1 dB in ACEPR_{LW} and ACEPR_{UP}, respectively, for $\Delta_f = 5$ MHz and 0.6 dB and 1.3 dB in ACEPR_{LW} and ACEPR_{UP}, respectively, for $\Delta_f = 10$ MHz with respect to the RF Poly also with $P = 4$ and $M = 2$.

In Figure 5.58 is shown the measured instantaneous AM-AM conversion as well as the estimated instantaneous AM-AM conversions by the Volterra series with $P = P_0 = 2$ and

$M = 4$ for both RF Poly and BB Poly. The superior performance of the Volterra series with BB Poly is clearly observed.

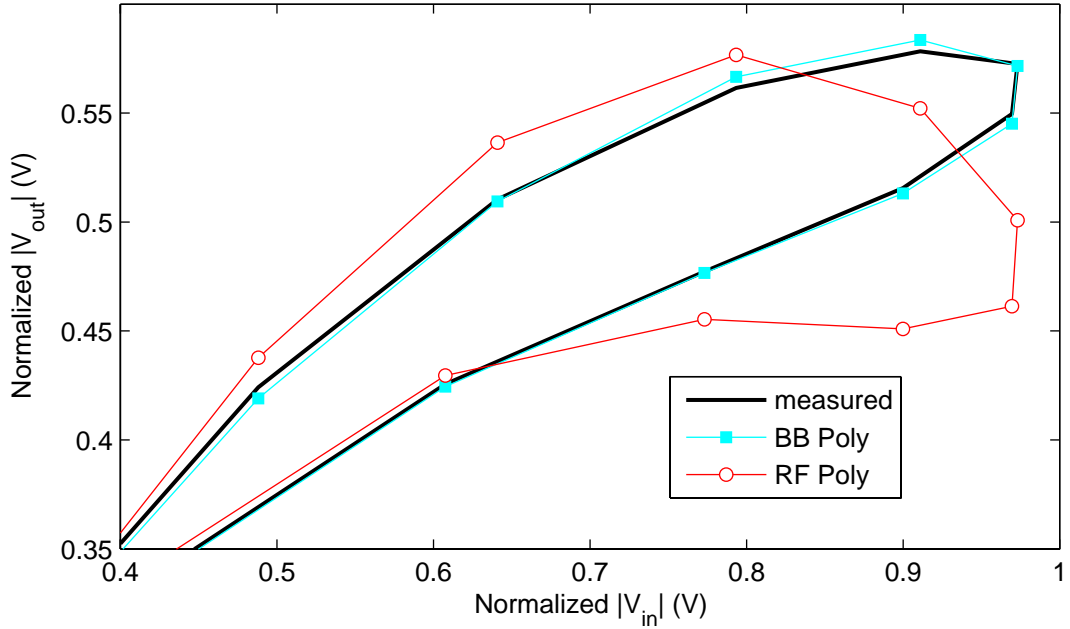


Figure 5.58: Samples of instantaneous AM-AM conversions: measured and estimated by Volterra series with $P = P_0 = 2$, $M = 4$ and different polynomial approximations

The power spectral densities (PSDs) of the measured output signal and modeled output signals by the Volterra series with $P = P_0 = 2$ and $M = 4$ for both RF Poly and BB Poly are shown in Figure 5.59, as well as the PSDs of the error signals between measured and modeled outputs. Whereas the estimated output by the Volterra series with RF Poly and with $P = 2$ and $M = 4$ is band-limited to three times the bandwidth of the input signal, the estimated output by the Volterra series with BB Poly and with $P_0 = 2$ and $M = 4$ is not band-limited. The error signal for the BB Poly is clearly lower than the error signal for the RF Poly at the whole measured spectrum. This is in accordance with the FoMs reported in Table 5.25. Indeed, this particular BB Poly Volterra series with $P_0 = 2$ and $M = 4$ can modeled very accurately the relationship between the complex-valued envelopes measured at the PA input and output with just thirty complex-valued parameters.

In Figure 5.60 is shown the measured instantaneous AM-AM conversion as well as the estimated instantaneous AM-AM conversions by the Volterra series with RF Poly (with

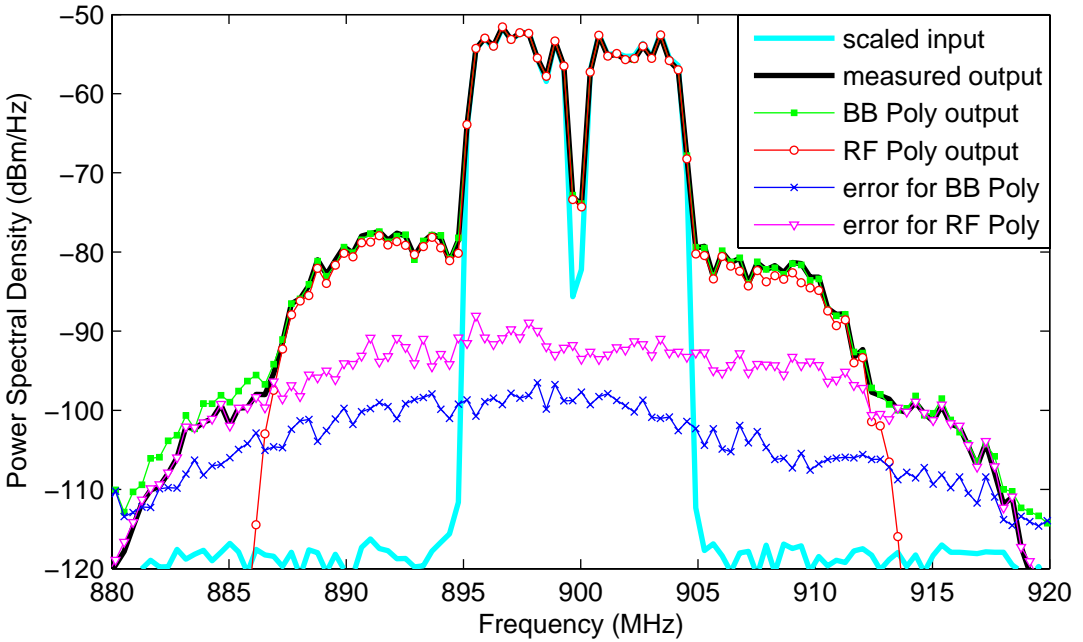


Figure 5.59: PSDs for Volterra series with $P = P_0 = 2$, $M = 4$ and different polynomial approximations

$P = 4$ and $M = 2$) and BB Poly (with $P_0 = 5$ and $M = 3$). Since now the RF Poly and BB Poly have different number of parameters, it was possible to extract a Volterra series with $P_0 = 5$ and $M = 3$ only for the BB Poly. A Volterra series with RF Poly and with $P = 5$ and $M = 3$ would require 2904 complex-valued parameters, which is much higher than the maximum allowed number of complex-valued parameters in this case study. A closer match between measured and modeled AM-AM conversions is observed for the BB Poly at high input powers. The PSDs of the error signals for these specific RF Poly and BB Poly Volterra models are shown in Figure 5.61. The error signal is visible lower for the BB Poly at the whole measured spectrum.

For the same maximum polynomial order, Table 5.25 shows that the Volterra series with BB Poly have always superior performance (NMSE and ACEPR FoMs) than the Volterra series with RF Poly. The largest difference is observed for a maximum polynomial order equals to the third. Specifically, the BB Poly with $P_0 = 3$ and $M = 3$ improves 9.5 dB in NMSE, 8.6 dB and 11.6 dB in ACEPR_{LW} and ACEPR_{UP}, respectively, for $\Delta_f = 5$ MHz and 8.7 dB and 10.6 dB in ACEPR_{LW} and ACEPR_{UP}, respectively, for $\Delta_f = 10$ MHz with respect to the RF Poly with $P = 2$ and $M = 3$. For a maximum

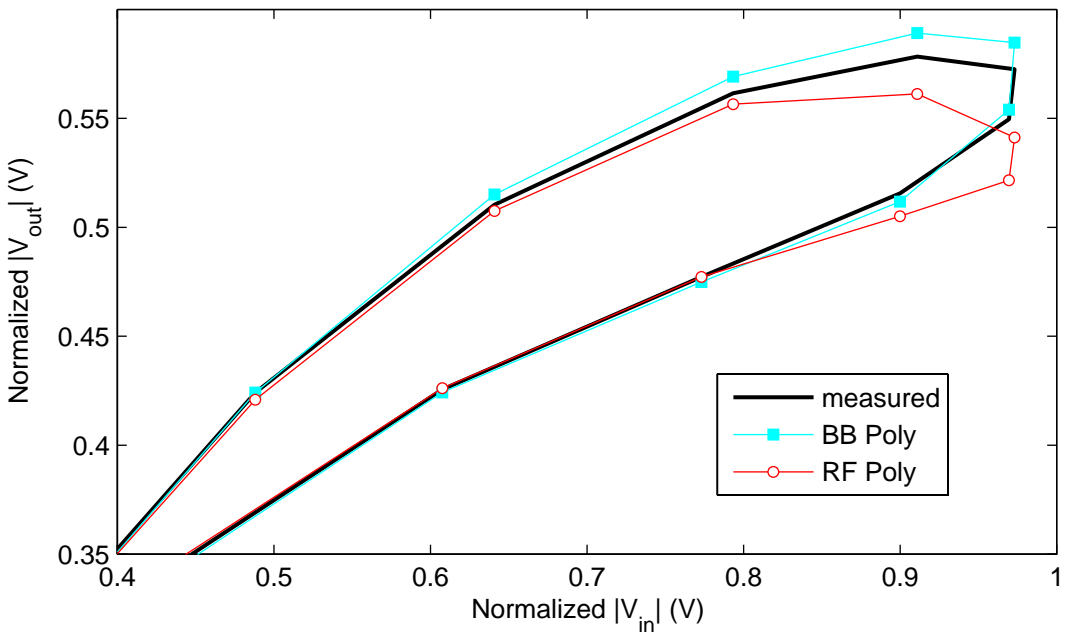


Figure 5.60: Samples of instantaneous AM-AM conversions: measured and estimated by Volterra series with different polynomial approximations: BB poly with $P_0 = 5$ and $M = 3$; RF Poly with $P = 4$ and $M = 2$

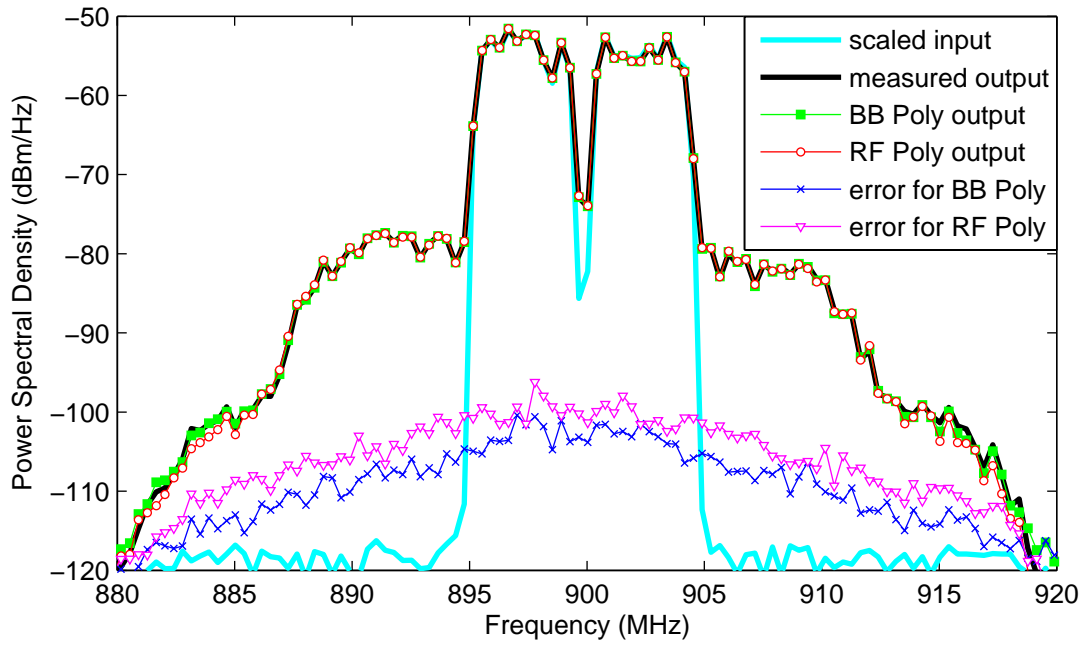


Figure 5.61: PSDs for Volterra series with different polynomial approximations: BB poly with $P_0 = 5$ and $M = 3$; RF Poly with $P = 4$ and $M = 2$

polynomial order equals to the fifth, the differences between the two polynomial approximations were reduced. Specifically, the BB Poly with $P_0 = 5$ and $M = 3$ improves 5.7 dB in NMSE, 6.6 dB and 6.5 dB in ACEPR_{LW} and ACEPR_{UP}, respectively, for $\Delta_f = 5$ MHz and 6.4 dB and 8.0 dB in ACEPR_{LW} and ACEPR_{UP}, respectively, for $\Delta_f = 10$ MHz with respect to the RF Poly with $P = 3$ and $M = 3$.

Finally, several dynamic deviation (DD) models with $R = 2$, different memory length M and different truncation factor P , for RF Poly models, and P_0 , for BB Poly models, were extracted to model the relationship between the complex-valued envelopes measured at the PA input and output. Table 5.26 shows the NMSE and ACEPR results, as well as the number of complex-valued parameters N in each case.

As happened in the Volterra series, the number of complex-valued parameters for $R = 2$, fixed M and $P = P_0$ are different from the RF Poly and BB Poly DD models. This is expected since the DD models are simplified versions of the Volterra series in which some coefficients are assumed zero.

For the same memory length M and truncation factor $P = P_0 < 6$, Table 5.26 shows that the DD models with BB Poly have superior performance (NMSE and ACEPR FoMs) than the DD models with RF Poly. The largest differences, specifically 8.0 dB in NMSE, 7.0 dB and 10.0 dB in ACEPR_{LW} and ACEPR_{UP}, respectively, for $\Delta_f = 5$ MHz and 5.4 dB and 8.9 dB in ACEPR_{LW} and ACEPR_{UP}, respectively, for $\Delta_f = 10$ MHz are observed in the case with $P = P_0 = 2$ and $M = 3$. As the number of parameters increases, the differences between the two polynomial approximations reduce. A slightly better performance in terms of NMSE, 0.3 dB to be precise, is observed for the RF Poly respect to the BB Poly when $P = P_0 = 6$ and $M = 4$ at the cost of 50 more complex-valued parameters.

In Figure 5.62 is shown the measured instantaneous AM-AM conversion as well as the estimated instantaneous AM-AM conversions by the DD models with $P = P_0 = 2$ and $M = 3$ for both RF Poly and BB Poly. The superior performance of the DD model with BB Poly is clearly observed.

The power spectral densities (PSDs) of the measured output signal and modeled output signals by the DD models with $P = P_0 = 2$ and $M = 3$ for both RF Poly and BB Poly are shown in Figure 5.63, as well as the PSDs of the error signals between measured

Table 5.26: NMSE and ACEPR results for DD models with $R = 2$ and different polynomial approximations

Model	P or P_0	M	N	NMSE (dB)	ACEPR _{LW} (dB) $\Delta_f =$ 10 MHz	ACEPR _{LW} (dB) $\Delta_f =$ 5 MHz	ACEPR _{UP} (dB) $\Delta_f =$ 5 MHz	ACEPR _{UP} (dB) $\Delta_f =$ 10 MHz
RF Poly	2	3	26	-33.01	-43.93	-38.76	-39.61	-43.35
BB Poly	2	3	20	-40.96	-49.35	-45.80	-49.58	-52.22
RF Poly	2	4	40	-33.05	-43.78	-38.94	-39.74	-43.35
BB Poly	2	4	30	-41.02	-49.74	-45.96	-49.75	-52.10
RF Poly	3	3	54	-39.90	-50.66	-46.08	-46.00	-48.45
BB Poly	3	3	42	-42.37	-52.57	-47.31	-51.09	-54.00
RF Poly	3	4	85	-40.03	-50.47	-46.21	-46.18	-48.52
BB Poly	3	4	65	-43.02	-52.43	-48.08	-52.08	-54.05
RF Poly	4	3	82	-43.22	-53.60	-49.59	-50.43	-52.92
BB Poly	4	3	64	-44.52	-56.05	-50.98	-51.47	-55.02
RF Poly	4	4	130	-43.22	-53.71	-50.01	-51.02	-53.23
BB Poly	4	4	100	-45.53	-56.12	-52.40	-52.89	-55.19
RF Poly	5	3	110	-43.07	-55.57	-51.70	-52.58	-55.04
BB Poly	5	3	86	-45.29	-57.57	-52.41	-51.78	-56.19
RF Poly	5	4	175	-45.68	-55.54	-52.46	-53.07	-55.60
BB Poly	5	4	135	-46.56	-57.17	-54.24	-53.50	-56.34
RF Poly	6	3	138	-43.51	-56.90	-52.95	-53.35	-56.34
BB Poly	6	3	108	-45.24	-58.22	-52.46	-52.10	-56.71
RF Poly	6	4	220	-46.63	-56.76	-54.07	-54.57	-56.57
BB Poly	6	4	170	-46.30	-57.89	-54.36	-53.79	-56.89

and modeled outputs. Whereas the RF Poly DD model with $P = 2$ and $M = 3$ is band limited to three times the bandwidth of the input signal, the BB Poly DD model with $P_0 = 2$ and $M = 3$ is not band limited. The error signal for the BB Poly is clearly lower than the error signal for the RF Poly at the whole measured spectrum. This is in accordance with the FoMs reported in Table 5.26. In fact, this particular BB Poly

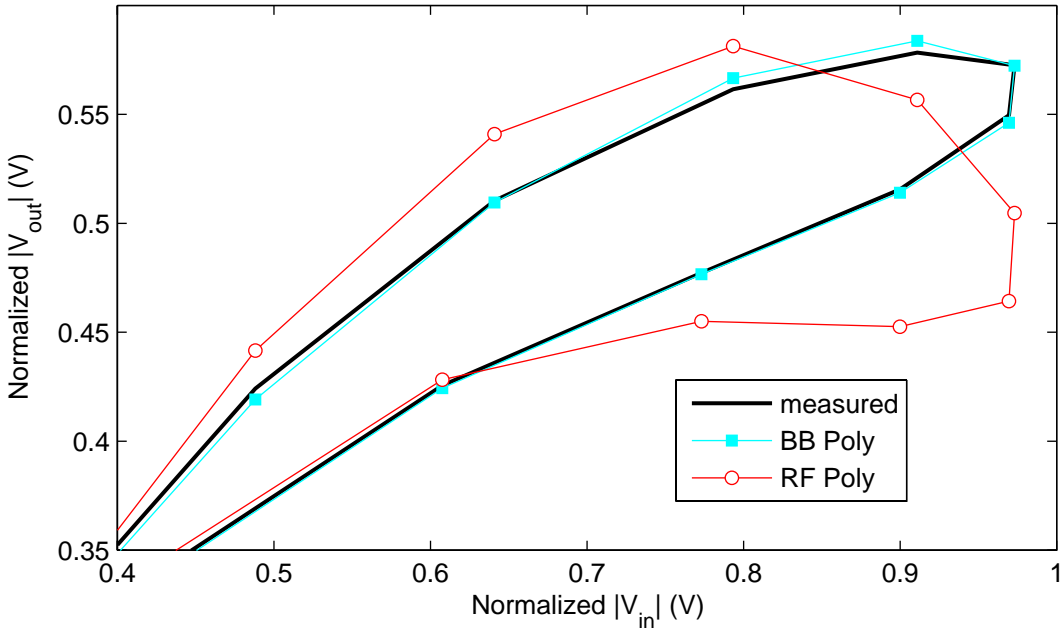


Figure 5.62: Samples of instantaneous AM-AM conversions: measured and estimated by DD models with $P = P_0 = 2$, $M = 3$, $R = 2$ and different polynomial approximations

dynamic deviation model with $P_0 = 2$, $M = 3$ and $R = 2$ can modeled very accurately the relationship between the complex-valued envelopes measured at the PA input and output with just 20 complex-valued parameters.

In Figure 5.64 is shown the measured instantaneous AM-AM conversion as well as the estimated instantaneous AM-AM conversions by the DD models with $P = P_0 = 6$ and $M = 4$ for both RF Poly and BB Poly. A slightly better match between measured and modeled AM-AM conversions is observed for the BB Poly at high input powers. The PSDs of the error signals for these specific RF Poly and BB Poly DD models are shown in Figure 5.65. The error signal is slightly lower for the RF Poly at the in-band and adjacent channels. However, the RF Poly requires 50 more complex-valued parameters than the BB Poly.

For the same maximum polynomial order, Table 5.26 shows that the DD models with BB Poly have always superior performance (NMSE and ACEPR FoMs) than the DD models with RF Poly. The largest difference is observed for a maximum polynomial order equals to the third. Specifically, the BB Poly with $P_0 = 3$ and $M = 4$ improves 10.0 dB in NMSE, 9.1 dB and 12.3 dB in ACEPR_{LW} and ACEPR_{UP}, respectively, for $\Delta_f = 5$ MHz

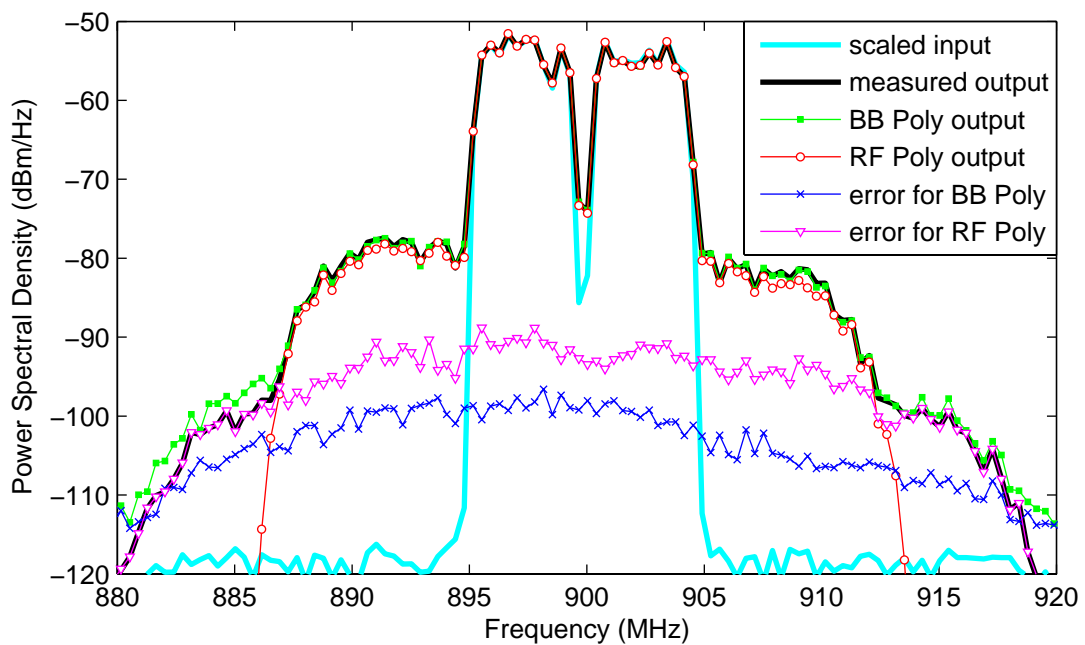


Figure 5.63: PSDs for DD models with $P = P_0 = 2$, $M = 3$, $R = 2$ and different polynomial approximations

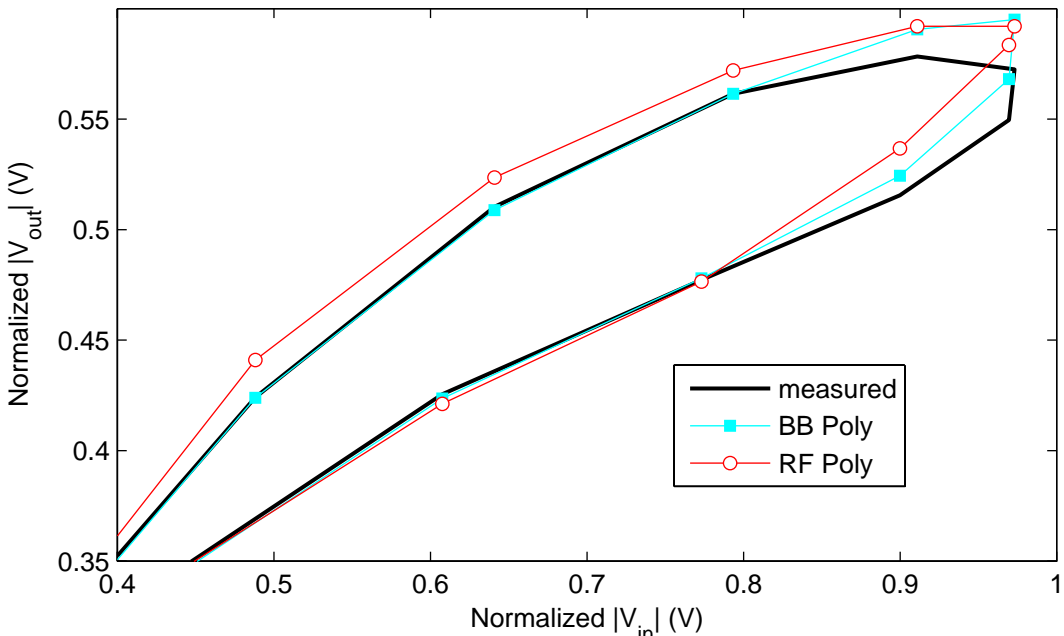


Figure 5.64: Samples of instantaneous AM-AM conversions: measured and estimated by DD models with $P = P_0 = 6$, $M = 4$, $R = 2$ and different polynomial approximations

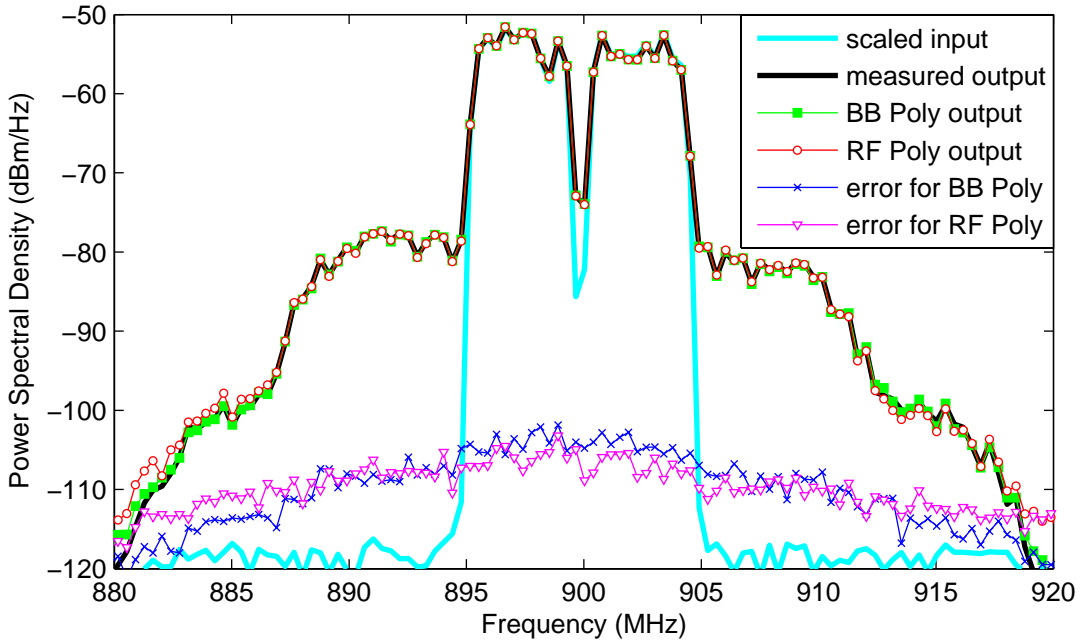


Figure 5.65: PSDs for DD models with $P = P_0 = 6$, $M = 4$, $R = 2$ and different polynomial approximations

and 8.7 dB and 10.7 dB in ACEPR_{LW} and ACEPR_{UP}, respectively, for $\Delta_f = 10$ MHz with respect to the RF Poly with $P = 2$ and $M = 4$. For a maximum polynomial order equals to the fifth, the differences between the two polynomial approximations were reduced. Specifically, the BB Poly with $P_0 = 5$ and $M = 4$ improves 6.5 dB in NMSE, 8 dB and 7.3 dB in ACEPR_{LW} and ACEPR_{UP}, respectively, for $\Delta_f = 5$ MHz and 6.7 dB and 7.8 dB in ACEPR_{LW} and ACEPR_{UP}, respectively, for $\Delta_f = 10$ MHz with respect to the RF Poly with $P = 3$ and $M = 4$.

5.3.3 Case Study 3: a (weak) extrapolation test

This case study 3 uses the same time-domain measurements as case study 2. However, here the maximum instantaneous magnitude of the input signal in the validation and extraction subsets were chosen to be equals. Additionally, some extrapolation is present, as shown in Table 5.27, since the minimum and maximum instantaneous values of the in-phase I_x signal and maximum instantaneous value of the quadrature Q_x signal in the validation subset are not inside their respective ranges in the extraction subset.

Table 5.27: Range of the input signals in the extraction and validation subsets

Input-output data subset	minimum of I_x	maximum of I_x	minimum of Q_x	maximum of Q_x	maximum of $ \tilde{x}(t) $
Extraction	-0.7720	0.8319	-0.9477	0.7451	1.0000
Validation	-0.9547	0.8677	-0.8021	0.8951	1.0000

Several dynamic deviation (DD) models with $R = 2$, different memory length M and different truncation factor P , for RF Poly models, and P_0 , for BB Poly models, were extracted to model the relationship between the complex-valued envelopes measured at the PA input and output. Table 5.28 shows the NMSE and ACEPR results, as well as the number of complex-valued parameters N in each case.

For the same memory length M and truncation factor $P = P_0$, Table 5.28 shows that the DD models with BB Poly have always superior performance (NMSE and ACEPR FoMs) than the DD model with RF Poly. In the case without extrapolation, as the number of parameters increased, the improvements of the BB Poly model over the RF Poly model reduced. Here, the extrapolation of the RF Poly is clearly worse than the extrapolation of the BB Poly, and huge differences between the two different polynomial approximations are observed when higher polynomial order is used. Particularly, the BB Poly with $P_0 = 5$ and $M = 4$ improves 18.5 dB in NMSE, 6.6 dB and 7.5 dB in ACEPR_{LW} and ACEPR_{UP}, respectively, for $\Delta_f = 5$ MHz and 8.0 dB and 9.3 dB in ACEPR_{LW} and ACEPR_{UP}, respectively, for $\Delta_f = 10$ MHz with respect to the RF Poly with $P = 5$ and $M = 4$.

In Figure 5.66 is shown the measured instantaneous AM-AM conversion as well as the estimated instantaneous AM-AM conversions by the DD models with $P = P_0 = 5$ and $M = 4$ for both RF Poly and BB Poly. The instantaneous AM-AM conversion estimated by the DD model with RF Poly confirms its catastrophic extrapolation behavior. On the other hand, the instantaneous AM-AM conversion estimated by the DD model with BB Poly is still close to the measured one, even in this context of weak extrapolation.

The power spectral densities (PSDs) of the measured output signal and modeled output signals by the DD models with $P = P_0 = 5$ and $M = 4$ for both RF Poly and BB Poly are shown in Figure 5.67, as well as the PSDs of the error signals between measured

Table 5.28: NMSE and ACEPR results for DD models with $R = 2$ and different polynomial approximations

Model	P or P_0	M	N	NMSE (dB)	ACEPR _{LW} (dB) $\Delta_f =$ 10 MHz	ACEPR _{LW} (dB) $\Delta_f =$ 5 MHz	ACEPR _{UP} (dB) $\Delta_f =$ 5 MHz	ACEPR _{UP} (dB) $\Delta_f =$ 10 MHz
RF Poly	2	3	26	-32.35	-42.84	-38.23	-39.33	-41.85
BB Poly	2	3	20	-40.56	-49.83	-45.57	-48.76	-52.61
RF Poly	2	4	40	-32.30	-42.76	-38.39	-39.26	-41.76
BB Poly	2	4	30	-40.63	-50.26	-45.73	-48.94	-52.66
RF Poly	3	3	54	-38.18	-49.91	-46.83	-45.47	-48.22
BB Poly	3	3	42	-41.91	-51.41	-47.84	-50.93	-53.75
RF Poly	3	4	85	-37.29	-49.15	-47.29	-44.91	-47.46
BB Poly	3	4	65	-42.54	-52.43	-48.05	-51.64	-52.67
RF Poly	4	3	82	-35.83	-52.16	-46.97	-46.72	-52.08
BB Poly	4	3	64	-43.72	-56.11	-51.35	-51.37	-56.10
RF Poly	4	4	130	-33.57	-51.59	-45.73	-45.26	-49.66
BB Poly	4	4	100	-44.41	-55.22	-51.81	-51.63	-55.42
RF Poly	5	3	110	-30.13	-51.38	-47.89	-48.03	-51.68
BB Poly	5	3	86	-43.55	-56.46	-51.58	-51.63	-56.84
RF Poly	5	4	175	-25.73	-48.13	-45.22	-43.95	-46.66
BB Poly	5	4	135	-44.24	-56.10	-51.82	-51.42	-55.96
RF Poly	6	3	138	-26.70	-43.32	-39.61	-40.63	-44.46
BB Poly	6	3	108	-41.44	-55.57	-51.47	-51.38	-56.08
RF Poly	6	4	220	-24.20	-40.78	-37.18	-37.53	-41.44
BB Poly	6	4	170	-39.86	-55.74	-52.34	-51.67	-54.90

and modeled outputs. The error signal for the BB Poly is clearly lower than the error signal for the RF Poly at the whole measured spectrum.

The in-phase and quadrature time-domain waveforms measured and estimated at the PA output by the DD models with $P = P_0 = 5$ and $M = 4$ for both RF Poly and BB Poly are shown in Figure 5.68. A very good agreement is observed in both the in-phase

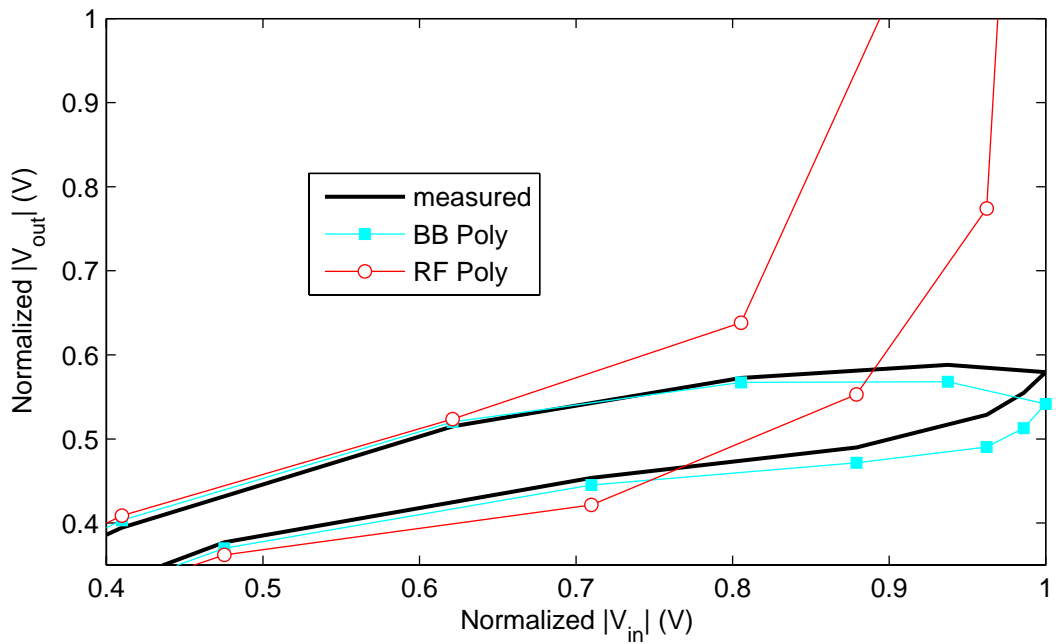


Figure 5.66: Samples of instantaneous AM-AM conversions: measured and estimated by DD models with $P = P_0 = 5$, $M = 4$, $R = 2$ and different polynomial approximations

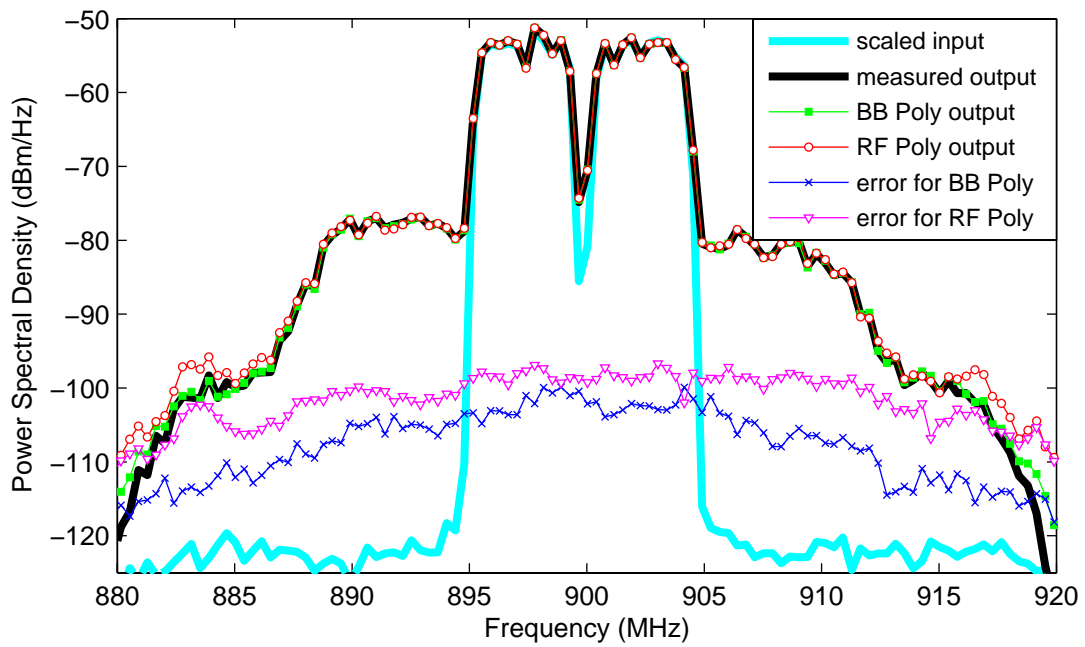


Figure 5.67: PSDs for DD models with $P = P_0 = 5$, $M = 4$, $R = 2$ and different polynomial approximations

and quadrature components between the measured and BB Poly modeled output signals. On the other hand, the effects of extrapolation are clearly visible in both the in-phase and quadrature components of the modeled output signal by the RF Poly DD model.

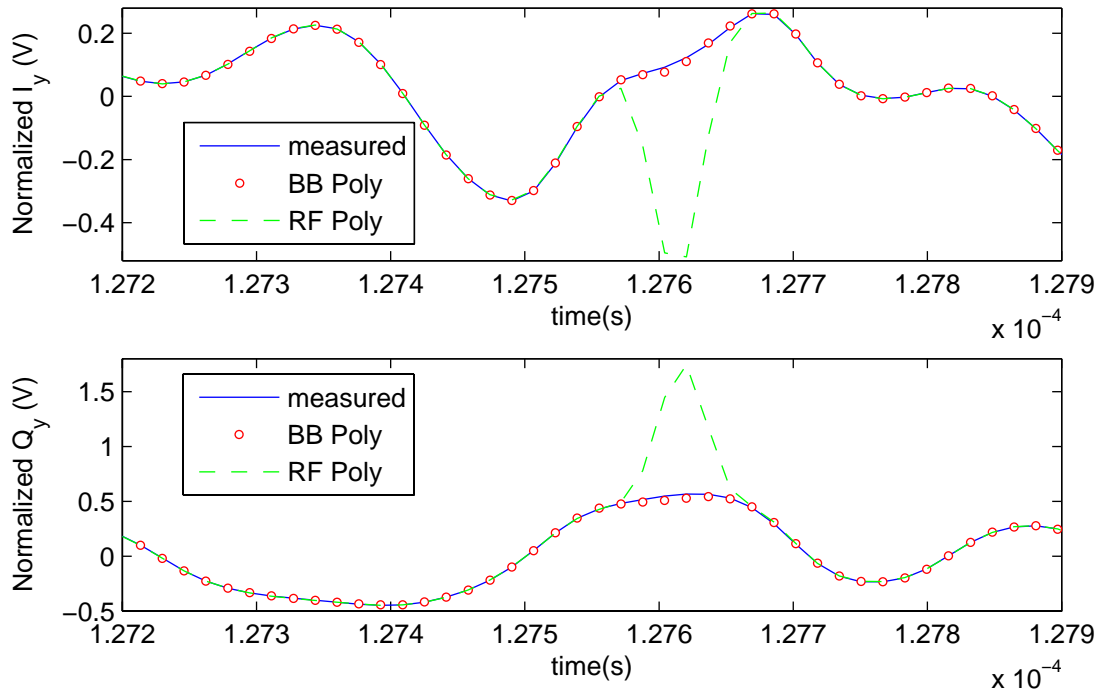


Figure 5.68: Time-domain waveforms of the in-phase and quadrature components of the output signal: measured and estimated by DD models with $P = P_0 = 5$, $M = 4$, $R = 2$ and different polynomial approximations

Chapter 6

Digital Base-band Predistortion of RF Power Amplifiers

In modern wireless communication systems, the information modulates both the amplitude and the phase of a carrier to improve the spectral efficiency. Amplitude modulation demands for linearity to avoid crosstalk between adjacent channels and so very stringent linearization specifications are imposed by regulatory agencies. On the other hand, the power amplifier (PA) in the transmission chain is more power efficient if operating near saturation, where its nonlinear behavior can not be neglected. Unless a linearization scheme is implemented, the PA must be back-off, e.g. driven at lower input levels to satisfy these linearity requirements, causing the detriment of the power efficiency and, for instance, increasing the size and weight consumed by the battery in a handset. If a linearization scheme is present, then the PA back-off can be considerably reduced whereas the linearity specifications are still satisfied. Among the linearization techniques, digital base-band predistortion (DPD) is a cost-effective solution. It consists in the distortion of the signal prior to amplification, so that the amplified signal is a linear scaled and delayed copy of the original signal.

Both PA behavioral modeling and DPD are fields of study concerning the same physical RF PA, even though with different scopes, specifically its representation or its compensation. Theoretically, the relationship between these two fields of study can be established into two different contexts, intimately related to the philosophy adopted for the DPD topology selection. In one hand, if the DPD topology is chosen as the inverse of a PA

behavioral model, then DPD can be seen as a field of study which involves, among others, the application of PA behavioral modeling. On the other hand, if the DPD topology is arbitrarily *a priori* chosen without the knowledge of any PA model, then DPD and PA behavioral modeling can be seen as two close related, but distinct fields of study, that apply the same mathematical tools, for instance system identification techniques.

This chapter is organized as follows. Starting by the basic concepts of predistortion, then a state-of-the-art description of available DPD schemes, focusing on DPD topology and parameter identification, is presented. Later, the effectiveness of different DPD schemes in improving linearization metrics of RF PAs are experimentally proved.

6.1 Basic concepts in predistortion schemes

The objective of a predistortion scheme is that the output signal in a cascade (or series) connection of the predistorter (PD) followed by a power amplifier (PA) be a scaled and delayed version of the input signal applied to the series connection [88] and [2]. A typical cascade connection is shown in Figure 6.1.

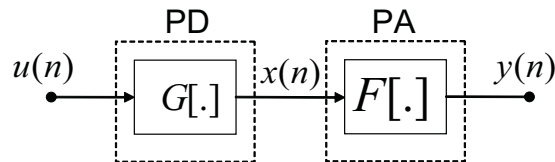


Figure 6.1: Cascade connection of a predistorter followed by a power amplifier

If the signals at the PA input, $x(n)$, and output, $y(n)$, are related by $y = F[x]$ and the signals at the PD input, $u(n)$, and output, $x(n)$, are related by $x = G[u]$, then the relationship between the input and output signals in the cascade connection of a PD followed by a PA is given by:

$$y = F[x] = F\{G[u]\} \quad (6.1)$$

On the other hand, the objective of a PD scheme is that:

$$y(n) = ku(n - d) \quad (6.2)$$

where k is a constant gain and d is a constant delay. Equaling (6.1) and (6.2), the PD and PA characteristics are related to:

$$G[u(n)] = F^{-1}[ku(n - d)] \quad (6.3)$$

Therefore, the PD must have, apart from constant gain and delay, the inverse characteristic of the PA. If the operator $F[.]$ is a linear filter, then $F^{-1}[.]$ exists (in the sense it is a BIBO stable linear operator) if $F[.]$ has minimal phase, e.g. all the poles and zeros of $F[.]$ are in the left-half of the s-plane for continuous systems or inside the unit circle in the z-plane for discrete systems. If the operator $F[.]$ is a static nonlinearity, then $F^{-1}[.]$ exists if $F[.]$ is a one-to-one mapping in the range of interest. However, in the more general case of an operator $F[.]$ that is both nonlinear and dynamic, there is no such general conditions for the existence of $F^{-1}[.]$, and the analysis, if possible, are limited to the particular analyzed topology. For instance, in the case of block-oriented topologies where the linear dynamic and nonlinear static behaviors of the operator $F[.]$ are separated and connected in a cascade structure, the existence of $F^{-1}[.]$ is guaranteed if each subsystem individually satisfies the above requirements. The AM-AM conversions of an arbitrary nonlinear dynamic operator $F[.]$, its inverse operator $F^{-1}[.]$ and their cascade connection are shown in Figure 6.2.

The predistortion scheme can be implemented at RF or base-band levels. In the former, analog hardware is mandatory. In the latter, both digital and analog implementations are possible. This work is limited to the digital implementation of a predistortion at base-band level, referred to as DPD.

6.2 DPD topology selection

The DPD topology selection is the first step to be addressed in the design. In the previous section, it was shown that the DPD must have the inverse characteristic of a PA. At base-band level, this means that if the operator $\tilde{F}[.]$ relating the complex-valued envelopes at the PA input and output is known, then the DPD operator $\tilde{G}[.]$, if exists, is the inverse of the operator $\tilde{F}[.]$.

Since such operator $\tilde{F}[.]$ is not known *a priori*, a first approach consists in the use of the low-pass equivalent PA behavioral models studied in previous chapters to represent

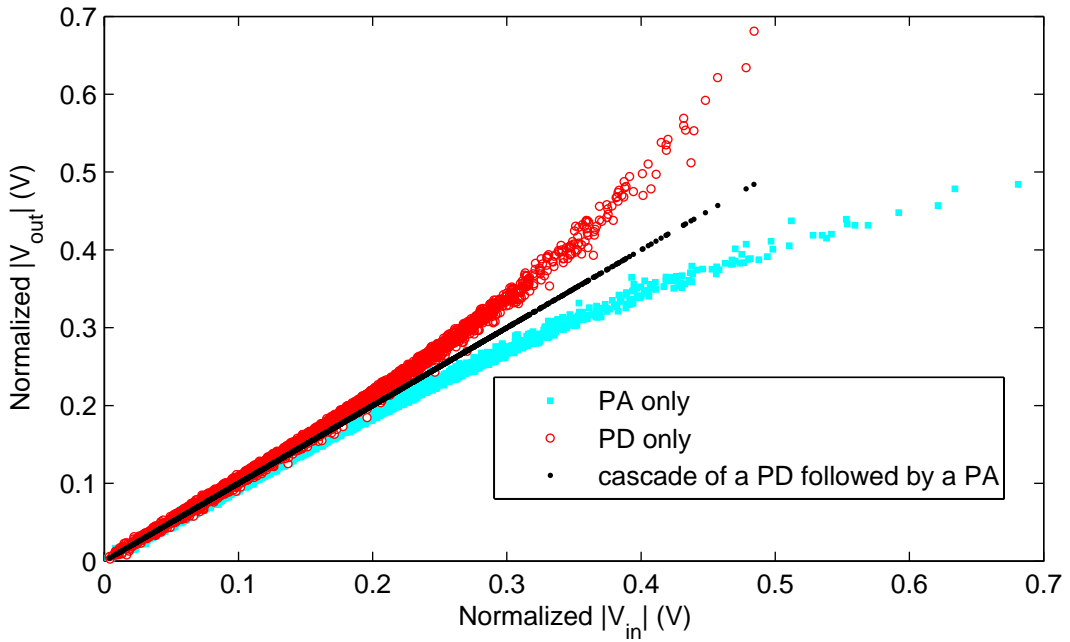


Figure 6.2: Example of AM-AM conversions in a PD scheme

the operator $\tilde{F}[\cdot]$. In this approach, the DPD topology selection is divided into two steps. First, a PA behavioral model is selected among the available ones. Second, the inverse characteristic of the chosen PA behavioral model, if exists, is adopted as the DPD topology. For the success of this approach, the PA behavioral model must accurately represent the physical system and its inverse must exist and be deductible.

Alternatively, a pure black-box oriented approach could be applied to the DPD topology selection, and then an arbitrarily *a priori* chosen topology is assumed for the DPD. The motivations can be different. First, a PA behavioral model is available and its accuracy proved, however the inverse characteristic is not available – either because can not be deduced analytically or because its deduction and possible implementation is too complex to justify its development – or does not exist. Second, most of the PA behavioral modeling approaches also are based in a black-box oriented approach. In this context of *a priori* arbitrary topology selection, if it is done for the PA or for the DPD topologies constitutes, again, another arbitrary choice with no direct implications in performance. Specifically, if the same topology is chosen for both PA and DPD models, performance comparison can be done only based on empirical results and so of no general applicability. If this is the adopted approach, the behavioral models presented in the previous chapters

– apart from the ones exploiting physical knowledge, in which the inverse characteristic must be used if it is intended to keep the support from physical analysis – can be applied as well to model a DPD. Indeed, a similar comparative study of the different modeling approaches, as the one presented in Chapter 5 for their application to model a PA, could also be done to validate, in comparative terms, their accuracy when used to model a DPD.

For the linearization of a PA exhibiting memory effects, a DPD topology should also include memory effects to provide an effective compensation. The use of a DPD with memoryless topology only achieves limited improvements for the compensation of a PA exhibiting memory effects [8].

Besides the detailed simplifications of the general Volterra series presented in Chapter 2, three additional simplifications reported in literature [89], [90], [91] and applied specifically to DPD purposes, are now briefly presented. In [90], it is proposed a simplified Volterra-based model that includes additional multi-dimensional terms, there referred to as envelope memory terms, to the MP model. Unfortunately, the proposed model does not retain the linearity in the parameters of the general Volterra series. A so-called generalized MP model is proposed in [89]. It is a simplified Volterra-based model that estimates the output by the sum of separable two-dimensional, 2D, functions that are linear in one argument, while the nonlinear dependence on the other argument is of polynomial nature. A further simplification of the generalized MP model leads to the envelope-memory polynomial model presented in [91]. Specifically, the envelope-memory polynomial model only retains the terms in the generalized MP model that are memoryless or that involve just the magnitude of delayed input samples, e.g. the dependence on the phase of the delayed complex-valued input samples is neglected.

Moreover, the additional odd-order terms included in the BB Poly models with respect to the traditional RF Poly models, theoretically justified within the new approach in deriving PA behavioral models proposed in Chapter 4, and whose improvements in PA behavioral modeling were experimentally verified in Chapter 5, if also included in DPD models, can provide similar improvements. Indeed, using the same mathematical tools and following the same reasoning as done in Chapter 4, it can be shown that both RF Poly DPD and BB Poly DPD models do not violate the odd parity constraint imposed by the band-pass nature of RF devices, and so are full effective (in the sense that all

individual contributions are pertinent) for the compensation of RF systems. Again, the RF Poly DPD imposes an additional parity constraint, by no means associated to any physical behavior observed in real RF systems but only due to the original polynomial format assumed at RF level, and if this unnecessary parity requirement is removed, BB Poly DPD is obtained. Comparison between BB Poly and RF Poly MP models as *a priori* choices for DPD topologies were already performed in [80] and [81]. However, in [80] and [81], the additional terms of the BB Poly with respect to RF Poly were misunderstood as even-order terms and only the results for the linearization of a simulated PA were reported.

The description of non polynomial PA behavioral models presented in previous chapters was limited to the tapped delay neural networks (TDNN). The use of a TDNN as *a priori* chosen topology for a DPD has been receiving little attention in DPD literature, mostly because of its high computational complexity, both for training and real-time processing. On the other hand, two additional non polynomial models also addressing memory effects, namely LUT-based models [92], [93], [94],[95],[96], and piecewise approximations [97],[98],[99], have been receiving particular attention in DPD literature. One of the motivations for their study resides in the PA architectures adopted in recent transmission chains to improve the power efficiency, for example the envelope tracking technique and the Doherty architecture [100], in which distinct behaviors observed in the PA at different power levels can no longer be accurately represented, in the whole dynamic range of the PA operation, by Volterra-based models. For instance, in a Doherty architecture is common to observe a sudden slope change in the AM-AM characteristic when the auxiliary device turns on, while in the envelope tracking technique variations in slope in the AM-AM conversion due to the dynamic changes of the voltage suppliers are frequently observed. Additionally, and concerning solely the LUT-based models, a main broader motivation is that LUT-based models significantly reduce the computational complexity for the processing of the input samples to estimate the output sample at real-time, even though a large physical memory may be allocated to store all the required data when dynamic effects are taken into account. Particularly in the memoryless case, the implementation of a LUT DPD reduces to an index calculation and a complex-valued multiplication. As a remark, in [101] extracted polynomial nonlinearities were implemented

in a field programmable gate array (FPGA) hardware by means of LUTs. Whereas standard basic techniques for LUT and piecewise models are available for the memoryless case, their extensions to include memory effects require techniques by far more sophisticated and complicated.

At this point, some strategies to include memory effects in LUT-based models are reviewed. In [92] and [93], a two-dimensional LUT was proposed to extend the traditional memoryless one-dimensional LUT, in which the second dimension is addressed based on past input samples and so is responsible for the compensation of the memory effects exhibited by the PA. In [94], a so-called filter look-up-table (FLUT) DPD was proposed in which the output of a one-dimensional LUT DPD is filtered by a discrete-time FIR whose coefficients are dependent on the magnitude of the instantaneous applied input signal. A Hammerstein cascade DPD where the static nonlinearity was implemented by a LUT, together with an augmented Hammerstein cascade, were proposed in [95]. Finally, a nested LUT topology was proposed and applied to DPD purposes in [96], which requires S^i basic one-dimensional LUTs at the i -level, where S is the number of elements stored in the basic LUT, and each level accounts for a different delayed input sample implying that $(M + 1)$ levels are required if the DPD is assumed to have a memory span equals to M .

Now, some strategies to include memory effects in piecewise models are reviewed. In [98], a DPD was modeled by a nonlinear dynamic operator that estimates the output by the sum of one-dimensional, 1D, functions driven by distinct delayed input samples, in which each nonlinear function was implemented by piecewise polynomial approximation in the form of cubic splines. In [97], a DPD was modeled by a nonlinear dynamic operator that estimates the output by the sum of separable two-dimensional, 2D, functions in which each term is linear in one argument, while the nonlinear dependence on the other argument was implemented by piecewise polynomial approximation in the form of cubic splines. A common characteristic of these approaches is that the piecewise approximation was done for 1D nonlinear functions and the inclusion of memory was separately addressed. Indeed, in piecewise curve fitting, the input signals are segmented according to their magnitude levels and processed by different functions. The loss of the information about time sequence of the input samples and, consequently, their frequency information, is

an intrinsic part of the process. To circumvent this loss of time sequence information and, in this way, allowing for the inclusion of memory effects, in [99] a vector threshold decomposition was applied to the modeling of a DPD by a piecewise Volterra-based series, specifically in its representation for dynamic-deviation (DD) reduction.

Turning back to the first approach, the next subsections will detail the inversion process of some behavioral models previously presented.

6.2.1 Inversion of static nonlinearities

This subsection is dedicated to the inverse of a static nonlinear operator $\tilde{F}[\cdot]$. The necessary and sufficient condition for the existence of an inverse operator $\tilde{F}^{-1}[\cdot]$ is that the operator $\tilde{F}[\cdot]$ be a one-to-one mapping in the range of interest. The operator $\tilde{F}[\cdot]$ is a complex-valued function if the PA exhibits both AM-AM and AM-PM conversions. Consequently, $\tilde{F}^{-1}[\cdot]$ will also be a complex-valued function to compensate for both AM-AM and AM-PM conversions. Two different operators $\tilde{F}[\cdot]$ will be studied: a nonparametric operator implemented by look-up-tables (LUTs) and a polynomial parametric operator.

In the former, two LUTs are constructed: the first, $G_{PA}(\cdot)$, to implement the AM-AM conversion and the second, $\Psi_{PA}(\cdot)$, the AM-PM conversion of a PA. The complex-valued envelope $\tilde{y}(n)$ at the PA output is related to the complex-valued envelope $\tilde{x}(n)$ at the PA input by:

$$\tilde{y}(n) = \tilde{F}[\tilde{x}(n)] = G_{PA}(|\tilde{x}(n)|) e^{j\Psi_{PA}(|\tilde{x}(n)|)} \frac{\tilde{x}(n)}{|\tilde{x}(n)|} \quad (6.4)$$

The inverse operator of $\tilde{F}[\tilde{x}(n)]$ in (6.4) is then given by:

$$\tilde{x}(n) = \tilde{F}^{-1}[\tilde{y}(n)] = G_{PD}(|\tilde{y}(n)|) e^{j\Psi_{PD}(|\tilde{y}(n)|)} \frac{\tilde{y}(n)}{|\tilde{y}(n)|} \quad (6.5)$$

where the memoryless nonlinearities $G_{PA}(\cdot)$ and $G_{PD}(\cdot)$ are related by:

$$G_{PD}(|\tilde{y}(n)|) = G_{PA}^{-1}(|\tilde{y}(n)|) \quad (6.6)$$

e.g. the operator $G_{PD}(\cdot)$ is easily obtained by just exchanging the input and output roles in the LUT implementing the operator $G_{PA}(\cdot)$, while the memoryless nonlinearities $\Psi_{PA}(\cdot)$ and $\Psi_{PD}(\cdot)$ are related by:

$$\Psi_{PD}(|\tilde{y}(n)|) = -\Psi_{PA}[G_{PD}(|\tilde{y}(n)|)] \quad (6.7)$$

In the second studied case, the operator $\tilde{F}[\cdot]$ is represented by a polynomial of complex-valued coefficients. Here, the objective is not to find the exact inverse operator $\tilde{F}^{-1}[\cdot]$, but only to find the complex-valued coefficients for an optimal polynomial approximation of degree N for $\tilde{F}^{-1}[\cdot]$. This problem can be solved analytically by imposing that the composition of two polynomials, up to order N , is linear. However, the composition will present non zero terms of order higher than N , which have different values if the polynomial disposition in the cascade connection is exchanged. The approximation degrades as the input level increases, since the effects of the unwanted higher order terms also increases [102].

6.2.2 Inversion of nonlinear dynamic 1D approximations

This subsection describes a strategy for the inversion of particular nonlinear dynamic operators that estimate the output by the sum of one-dimensional, 1D, functions driven by distinct delayed input samples and so are given by:

$$\tilde{y}(n) = \sum_{m=0}^M f_m [\tilde{x}(n-m)] \quad (6.8)$$

The above equation is a particular instance of the nonlinear auto-regressive moving average (NARMA) [103] in which the fed-back terms are neglected. The inversion of a NARMA operator was shown in [103] to be also a NARMA operator. A brief derivation of the inverse for the particular instance of the NARMA in (6.8) is now described.

First, (6.8) is rewritten as:

$$\tilde{y}(n) = f_0 [\tilde{x}(n)] + \sum_{m=1}^M f_m [\tilde{x}(n-m)] \quad (6.9)$$

where the contribution of the input at the present sample time, represented by the nonlinear function $f_0 [\tilde{x}(n)]$, was explicitly separated from those of the input at previous sample times. If now the roles of the input and output in (6.9) are inverted, then it is obtained:

$$\tilde{x}(n) = f_0^{-1} \left\{ \tilde{y}(n) - \sum_{m=1}^M f_m [\tilde{x}(n-m)] \right\} \quad (6.10)$$

In this inverted context, (6.10) estimates the PA input at the present sample time $\tilde{x}(n)$, based on the desired PA output at the present sample time $\tilde{y}(n)$ and on the PA

input at previous sample times, $\tilde{x}(n-m)$, $m = 1, 2, \dots, M$. This is exactly the constitutive equation representing the DPD, but with different signal interpretations: for predistortion purposes, $\tilde{y}(n)$ is the input signal applied to the DPD, and $\tilde{x}(n-m)$, $m = 0, 1, \dots, M$ are the DPD output at present and previous time-samples.

Since (6.10) is an explicit function of $\tilde{x}(n)$, the inverse of the operator given by (6.8) can be obtained by the inversion of just a static nonlinear function. Indeed, this peculiar explicit behavior of $\tilde{x}(n)$ is common to all models that estimate the output by the sum of 1D functions, even for recursive approximations like the NARMA [103], and independently of the expressions for the nonlinear functions. In the particular case of the memory polynomial (MP) model, obtained when the nonlinear functions f_m [.] in (6.8) are approximated by polynomials at the RF level and whose discrete-time low-pass equivalent constitutive equation was given by (2.41), the inverse has the recursive structure shown in Figure 6.3, which is here referred to as a nonlinear autoregressive scheme with exogenous inputs (NARX).

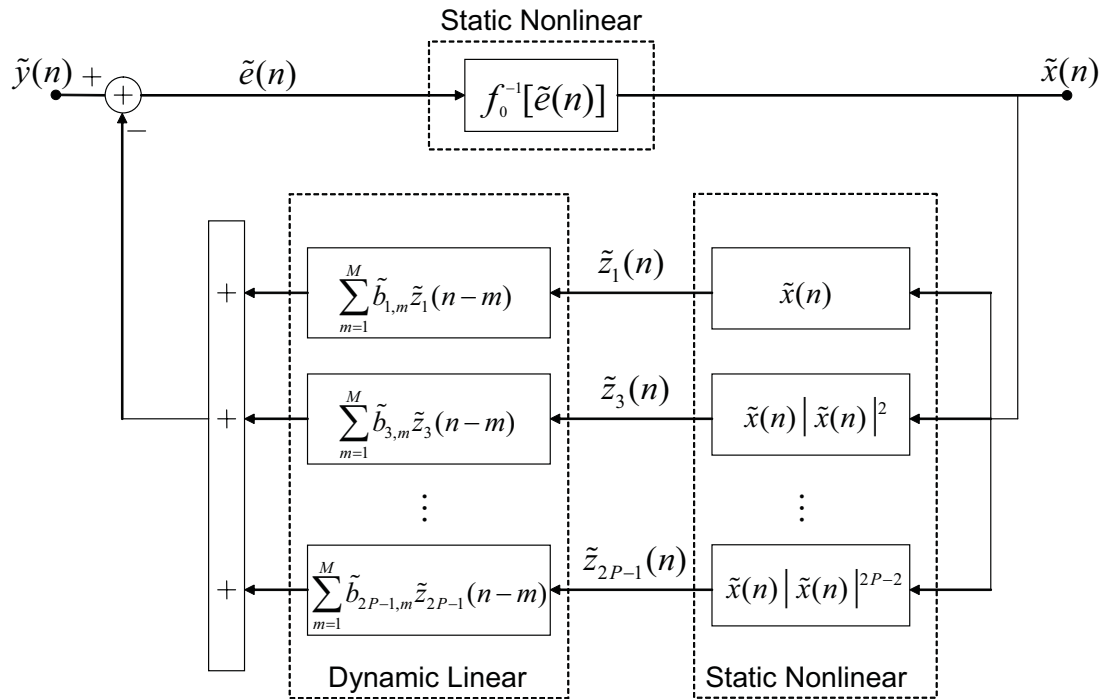


Figure 6.3: Block diagram of the NARX model

6.2.3 The p th-order inverses of Volterra series

In [104], it is presented the so-called p th-order inverse methodology for the calculation of the inverse of a Volterra series. Specifically, this method calculates the p th-order post-inverse of a nonlinear system by nulling the Volterra kernels of the cascade connection of order greater than one and less than or equal to p , and then shows that its p th-order pre-inverse is the same as its p th-order post-inverse. However, the kernels of the cascade connection for order higher than p are not considered in the algorithm and, therefore, result in non null values, generally different for the post-inverse and pre-inverse cases. They may have non negligible effects on the predistortion compensation especially for high input signal levels.

If the p th-order inverse algorithm is applied to the LPE feedback model described in Chapter 3 and shown in Figure 3.2, then a physically derived pruned version of a Volterra series DPD topology – from now on referred to as PP DPD model – is obtained. Particularly, the response of the 5th-order inverse of the LPE model, with the assumption that the linear filter in the fed-back path, $\tilde{F}_1(\Omega)$, is flat and so modeled by a complex-valued gain \tilde{f}_0 , is given by the sum of the contributions \tilde{y}_1 and \tilde{y}_2 , whose feed-forward diagrams are shown in Figures 6.4 and 6.5, respectively.

In Figures 6.4 and 6.5, the complex-valued coefficient \tilde{d}_1 is defined as:

$$\tilde{d}_1 = 1 - a_1 \tilde{f}_0 \quad (6.11)$$

As was the case for the LPE feedback model, if all the linear filters present in the PP DPD model are approximated by finite-impulse response (FIR) digital filters, parameter redundancy can be eliminated. Again, the complex-valued filter taps, \tilde{q}_{2m} , of the filter $\tilde{Q}_2(\Omega)$, and the real-valued taps, q_{0m} , of the filter $Q_0(\Omega)$, plus the real-valued polynomial coefficients a_2 and a_3 , do not need to be explicitly identified, since, without any loss in modeling capabilities, they can all be represented by just the two FIR filters, $G_0(\Omega)$ and $\tilde{G}_2(\Omega)$, whose taps, designated by g_{0m} and \tilde{g}_{2m} , respectively, are related to the original coefficients by equations (3.6) and (3.7), respectively.

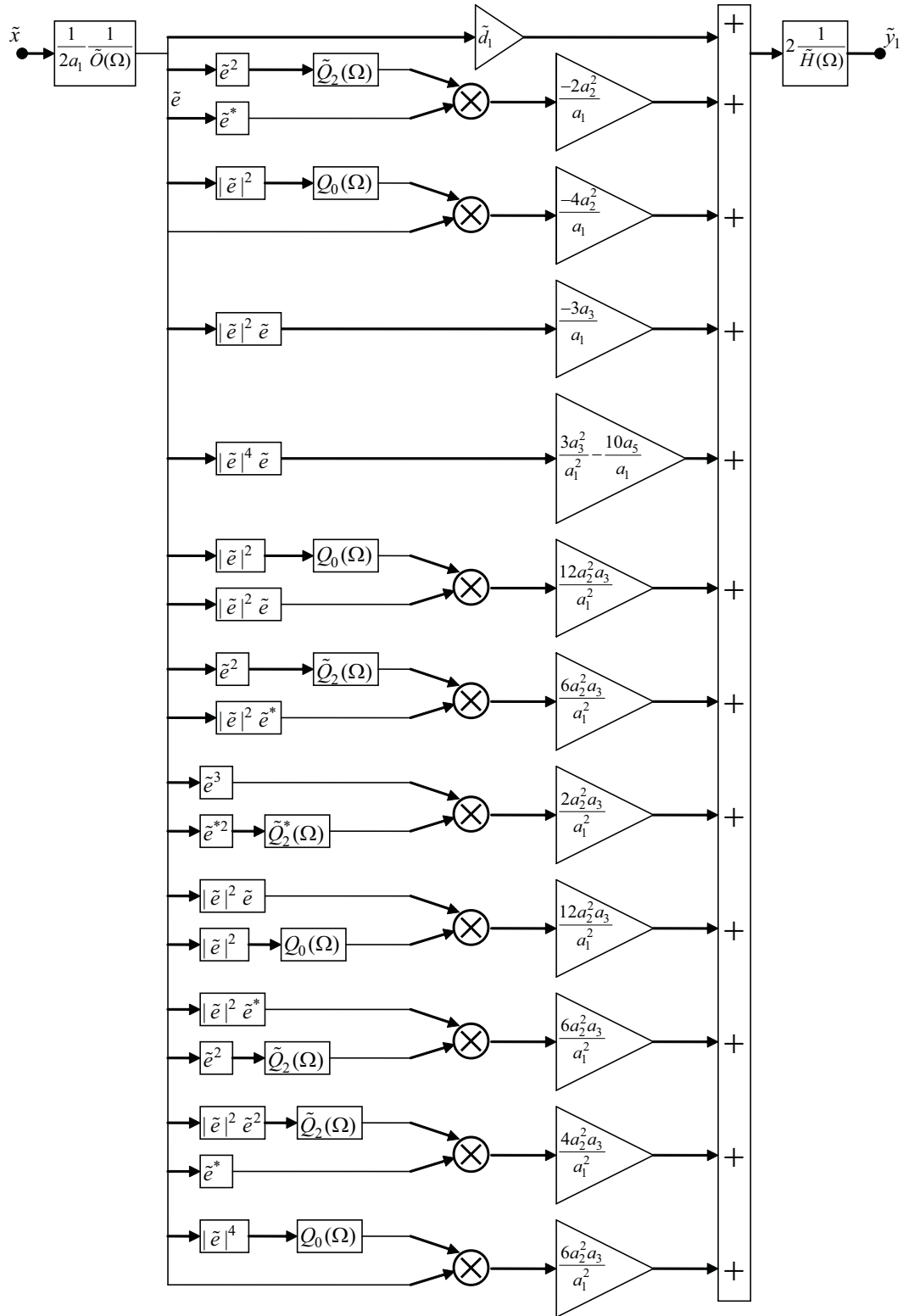


Figure 6.4: Feed-forward diagram of the 5th-order Volterra inverse of the LPE feedback model – part 1

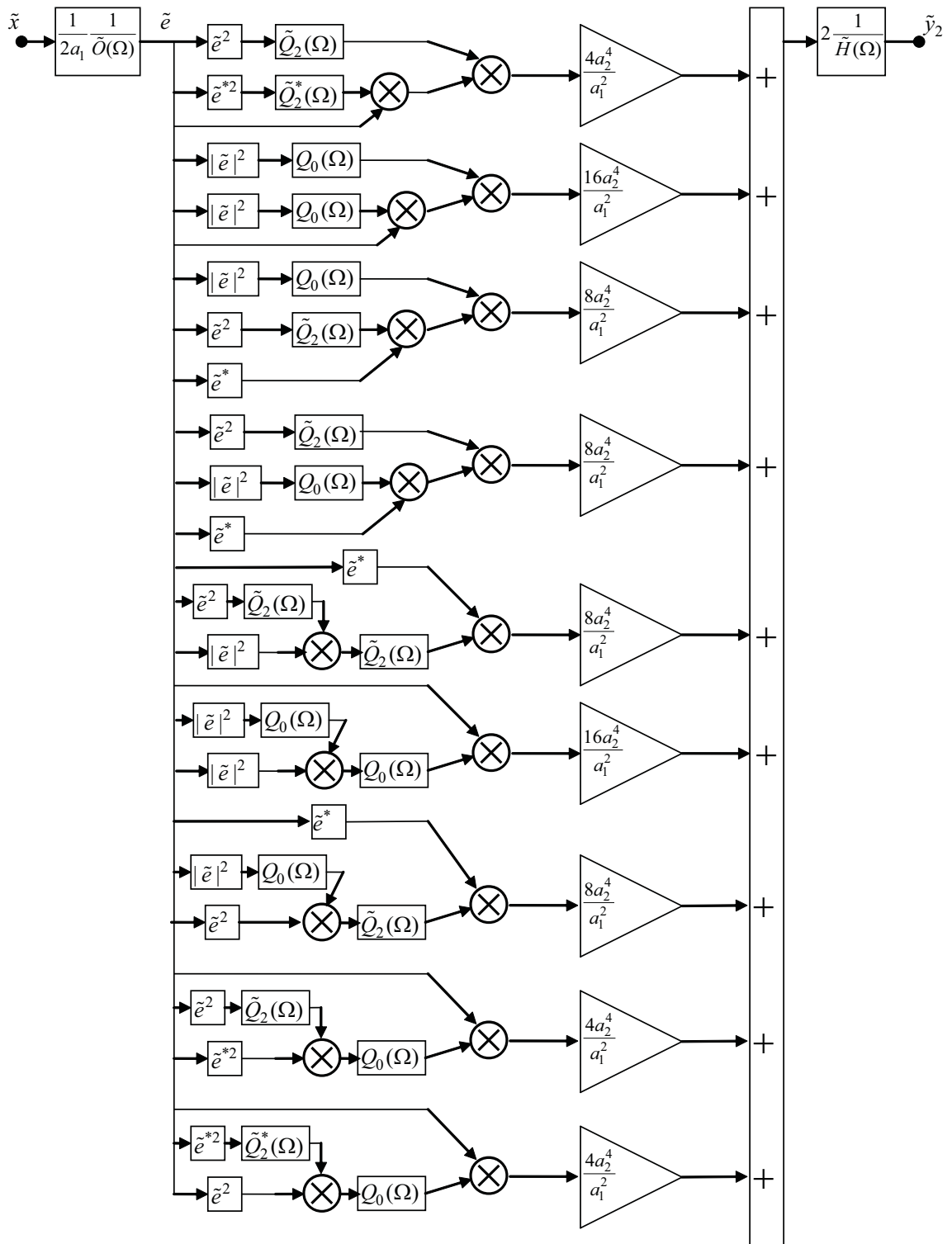


Figure 6.5: Feed-forward diagram of the 5th-order Volterra inverse of the LPE feedback model
– part 2

6.3 DPD parameter identification

The parameter identification of a given DPD topology is more difficult than the extraction of a PA behavioral model. In the case of a PA extraction, both input and output PA values are known, in the sense of applied signal and measured response, while in the DPD extraction what is known, in the sense of applied signal and desired response, is the input and output values of the cascade connection of the DPD followed by the PA. The DPD output is not available. This means that the standard system identification theory used in PA behavioral model extraction can not be directly applied to the DPD extraction.

On the other hand, the parameter identification of a given post-distorter (PoD) – an operator that has the same scope of a DPD but in the cascade connection it comes after the PA – is a standard system identification problem, since both input and output signals are available. Additionally, there is a close relationship between the PD and the PoD of a nonlinear operator. For instance, as shown in [104], the p th-order pre-inverse of a nonlinear system is the same as its p th-order post-inverse.

Those considerations have motivated the spread of two different strategies for the parameter identification of a given DPD topology. The direct learning algorithm [105], [106] addresses directly the DPD parameter extraction in the more complicated scenario in which the output is not available. The indirect learning algorithm [107] (also called translation method in [108]) first extracts a PoD using standard system identification theory, and then copies the extracted parameters to a DPD of same topology.

In the next subsections, the different learning algorithms are detailed.

6.3.1 Direct learning algorithm

The block diagram of the direct learning algorithm is shown in Figure 6.6. As stated before, standard system identification theory can not be directly applied to the extraction of the DPD parameters because the DPD output is not available. Additionally, unless the inclusion of the physical PA in a real-time optimization loop could be feasible, a model for the PA is mandatory. The direct learning is performed into two different approaches, depending on how the DPD topology was chosen.

If the DPD has an arbitrary black-box topology, the DPD parameter identification is

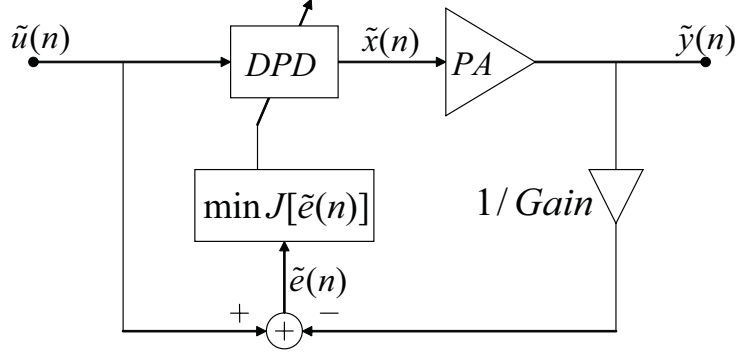


Figure 6.6: Block diagram of the direct learning

formulated as a nonlinear optimization problem, even though the chosen DPD topology is linear in its parameters. Indeed, as the error signal must be defined as the difference between desired and modeled responses at the PA output – the only available output – the PA model has to be included in the error expression. Since the PA is a nonlinear model, the minimization of some cost function of the error signal will necessarily be a nonlinear function of the DPD parameters. For that purpose, besides standard batch nonlinear optimization algorithms, like the Levenberg-Marquardt and the Gauss-Newton methods [58], nonlinear recursive algorithms were also proposed in literature, for example the nonlinear filtered-x LMS presented in [105] and applied to DPD parameter identification in [109] and [110].

On the other hand, if the DPD has a topology that is the inverse of a PA model, then its parameters can be derived from the PA ones, if analytical expressions relating them are available. Examples of DPD models whose parameters were derived from the PA parameters include the NARMA DPD presented in [103], and the NARX DPD in [111].

6.3.2 Indirect learning algorithm

The block diagram of the indirect learning algorithm is shown in Figure 6.7. The indirect learning algorithm first extracts a PoD and then copies the identified coefficients to a DPD of same topology. In fact, the cascade response of an operator and its exact inverse does not change when the operator position in the cascade connection is exchanged. On the other hand, the cascade response of an operator and its polynomial (or more generally, Volterra) approximate inverse does change if the operator disposition in the

cascade connection is exchanged. However, as shown in [104], the p th-order pre-inverse and post-inverse of a nonlinear dynamic operator are the same. Hence, the differences are due solely to higher order terms. Since in physical stable systems the numerical values of the coefficients reduce as the nonlinear order increases, if the input is kept at controllable low levels, the effects of the unwanted higher order terms can be assumed negligible and, as a consequence, the extracted parameters of the polynomial approximation for the PoD also represent an accurate estimation for the parameters of an equal topology for the DPD. Additionally, the indirect learning does not require a PA model, neither the inclusion of the physical PA in a real-time optimization loop.

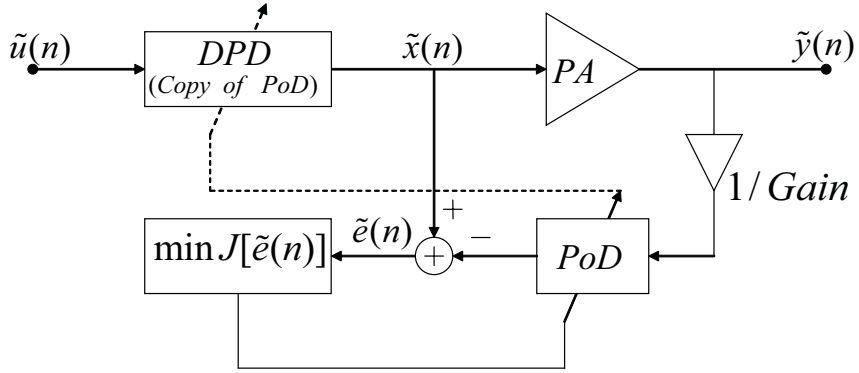


Figure 6.7: Block diagram of the indirect learning

The procedure for the PoD parameter identification is analogous to the respective one for the PA parameter extraction. Specifically, the procedures are exactly the same, if based on the same input-output data, except for exchanging the input and output roles. Therefore, all the system identification theory used in PA behavioral model extraction can be directly applied to the PoD extraction. For instance, if the PoD topology is linear in its parameter, then the PoD parameter identification can be done using linear system identification techniques, via batch algorithms like the least-squares (LS) and minimum mean-square error (MMSE), or via adaptive algorithms like least-mean-square (LMS) and recursive least-squares (RLS)[18]. Analytically, batch and recursive linear identification techniques are equivalent for the extraction of time-invariant models. The differences between them come when dealing with time-varying models, since only recursive linear identification techniques can be used for their extraction. Both applications concerned in this work, namely behavioral modeling and DPD of RF PAs, are examples of time-

invariant models, and so the choice between batch and recursive techniques would be, analytically, irrelevant. However, in practice, both algorithms could, and probably will, numerically, show different behaviors. Examples of DPD extracted via indirect learning using recursive identification techniques can be found in [107],[108],[112], while indirect learning using batch identification techniques are reported in [113], [114], [115], [101].

6.4 Experimental validation

The effectiveness of different DPD schemes in improving linearization metrics of RF PAs is experimentally assessed in this section, after an initial description of the experimental setup, as well as the definitions of the evaluated FoMs.

The experimental setup used for the input-output data collection is the same used in Chapter 5, whose schematic diagram is repeated in Figure 6.8. The in-phase $x_I(t)$ and quadrature $x_Q(t)$ components of a complex-valued base-band signal $\tilde{x}(t) = x_I(t) + jx_Q(t)$ are applied to the arbitrary waveform generator (AWG) of a Vector Signal Generator (VSG). In the VSG, an IQ modulator up-converts the base-band signals $x_I(t)$ and $x_Q(t)$ to RF. The RF signal passes through the cascade of a driver followed by the PA. A Vector Signal Analyzer (VSA) down-converts the RF signal at the PA output and stores the $y_I(t)$ and $y_Q(t)$ components of the complex-valued base-band output signal $\tilde{y}(t) = y_I(t) + jy_Q(t)$. No direct measurements of the input signal are performed. Therefore, the considered device-under-test (DUT) is the complete cascade from the VSG to the VSA channel.

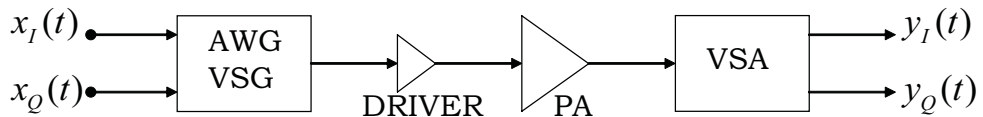


Figure 6.8: Schematic diagram of the experimental setup

Initially, an input sequence is created in a personal computer and stored in the VSG memory. A measurement of the base-band complex-valued signal at the PA output when driven by the stored sequence is performed. The created and measured sequences are used for the extraction of the parameters of a particular chosen DPD topology using the MATLAB software. Then, another input sequence, different from the one used for DPD

parameter extraction, is created. It will be used for two different purposes. First, it will be stored in the VSG memory and a measurement of the base-band complex-valued signal at the PA output is performed – it will be referred to as measured PA output without DPD. Second, it will be applied as input to the extracted DPD, the MATLAB software will process it, the predistorted sequence obtained is then stored in the VSG memory and, finally, another measurement of the base-band complex-valued signal at the PA output is performed – it will be referred to as measured PA output with DPD.

To assess the accuracy of the extracted model prior to its use as a DPD, the NMSE and ACEPR FoMs defined in Chapter 5 are used. If the scope is the accuracy assessment of a PA behavioral model, then the reference signal is the measured signal at the PA output and the test signal is the estimated signal at the PA behavioral model output when driven by the same input signal applied to the PA input. If the accuracy of a post-distorter (PoD) is addressed, then the reference signal is the applied signal to the PA input and the test signal is the estimated signal at the PoD output when driven by the measured signal at the PA output.

Two metrics are used for linearity assessment: the adjacent channel power ratio (ACPR) and the NMSE. The ACPR is defined as:

$$ACPR = 10 \log_{10} \left[\frac{\int_{adj} |Y_{ref}(f)|^2 df}{\int_{ch} |Y_{ref}(f)|^2 df} \right] \quad (6.12)$$

where $Y_{ref}(f)$ is the discrete Fourier transform of the reference signal defined as the measured signal at the PA output. The integral in the denominator is over the main channel, while the integral in the numerator is over an upper or lower adjacent channel of same bandwidth as the main channel. Two additional specifications, namely the channel bandwidth BW and the frequency separation Δ_f between the center frequencies of the main and adjacent channels, must be stated for a unique evaluation. Both ACEPR and ACPR results presented in this section uses a bandwidth of $BW = 3.84$ MHz for both main and adjacent channels. In the NMSE used for linearity assessment, the reference signal is the undistorted signal applied to the DPD input (or to the PA input if the DPD is absent) and the test signal is the measured signal at the PA output.

Additionally, the power-added efficiency (PAE) is used as metric for efficiency assess-

ment. The PAE is defined as:

$$PAE(\%) = 100 \times \frac{P_{OUT} - P_{IN}}{P_{DC}} \quad (6.13)$$

where P_{DC} is the average supplied DC power and P_{IN} and P_{OUT} are the average RF powers at the PA input and output, respectively.

As a remark, all the extracted models in this section are Volterra-based models. As shown in [86] and [87], for Volterra series identification purposes, and in [116], for the identification of Volterra series compensators, it is enough to sample the signals at a sampling frequency rate that satisfies the Nyquist rate for the undistorted input signal.

Now, the experimental results are presented in the following sequence. First, Subsection 6.4.1 proves the ability of a physically derived pruned version of a Volterra DPD topology to linearize an RF PA with GaN based technology. Then, Subsection 6.4.2 compares two MP DPD topologies – with either the RF Poly or BB Poly approximations – in terms of linearization improvements of an RF PA with GaN based technology. Finally, Subsection 6.4.3 investigates the impact on linearization metrics of a LDMOS PA if a particular arbitrary topology selection is done for the PA or for the DPD topologies.

6.4.1 Case study 1: physically derived pruned Volterra DPD topology

This subsection uses experimental time-domain measurements performed in a class AB PA with GaN based technology. The VSG used in the experimental setup was a Rohde & Schwarz SMU200A VSG, while the VSA was a Rohde & Schwarz FSQ. The sampling frequency was set to 61.44 MHz.

The objective here is to investigate the effectiveness of the physically derived pruned version of a Volterra series DPD topology, presented in Subsection 6.2.3 and from now on referred to as PP DPD model, in improving linearization metrics of the presented PA. For that scope, the parameters of the 5th order PP DPD model shown in Figures 6.4 and 6.5 were extracted using the indirect learning architecture, e.g. first the parameters of a PoD of same topology were extracted and then the identified coefficients were copied to the DPD. Specifically, the coefficients of the PP PoD model were all extracted at once via a nonlinear minimization of the norm-2 of the error signal defined as the difference

between the applied PA input signal and the PoD modeled output signal when driven by the measured signal at the PA output. In the extracted PP DPD model, according to Figures 6.4 and 6.5, the linear filter $\tilde{O}(\Omega)$ was neglected, but the linear filter $\tilde{H}(\Omega)$ was included to compensate for the memory effects observed in small-signal operation and attributed both to the PA driver used in the experimental setup and the PA input matching network. Each linear filter was modeled by a finite-impulse response (FIR) digital filter with four taps. The real-valued parameters a_2 and a_3 were not explicitly extracted, but just included in the $\tilde{G}_2(\Omega)$ and $G_0(\Omega)$ filters according to (3.6) and (3.7).

Additionally, a 5th order general Volterra series DPD topology with $P = 3$ and $M = 3$, and its particular memoryless instance, were also extracted using the indirect learning architecture and via LS.

Initially, a WCDMA 3GPP signal of bandwidth 3.84 MHz and peak-to-average power ratio (PAPR) of 11.6 dB was applied to the PA input. For extraction purposes, the signal at the PA output was acquired for an average output power of 26 dBm. The NMSE and ACEPR results obtained for the extracted PP, Volterra and memoryless PoD models, as well as their respective number of real-valued parameters N are reported in Table 6.1.

Table 6.1: NMSE and ACEPR results for different PoDs extracted by the indirect learning architecture

Model	N	NMSE (dB)	ACEPR _{LW} (dB) $\Delta_f =$ 10 MHz	ACEPR _{LW} (dB) $\Delta_f =$ 5 MHz	ACEPR _{UP} (dB) $\Delta_f =$ 5 MHz	ACEPR _{UP} (dB) $\Delta_f =$ 10 MHz
memoryless	6	-32.66	-62.47	-44.08	-43.86	-65.60
Volterra	488	-44.13	-67.81	-54.23	-54.12	-66.39
PP	24	-34.71	-67.18	-49.53	-49.75	-64.87

In Table 6.1 is shown that the PP PoD model presents intermediate results in the used FoMs. Specifically, it improves the memoryless results in NMSE by 2.1 dB and in ACEPR_{LW} and ACEPR_{UP} for $\Delta_f = 5$ MHz by 5.5 dB and 5.9 dB, respectively, but deteriorates the Volterra results in NMSE by 9.4 dB and in ACEPR_{LW} and ACEPR_{UP} for $\Delta_f = 5$ MHz by 4.7 dB and 4.4 dB, respectively. Figure 6.9 shows the measured and modeled instantaneous AM-AM conversions by the PoD models presented in Table 6.1.

The instantaneous AM-AM conversions modeled by both PP and Volterra PoD are very close to the measured one.

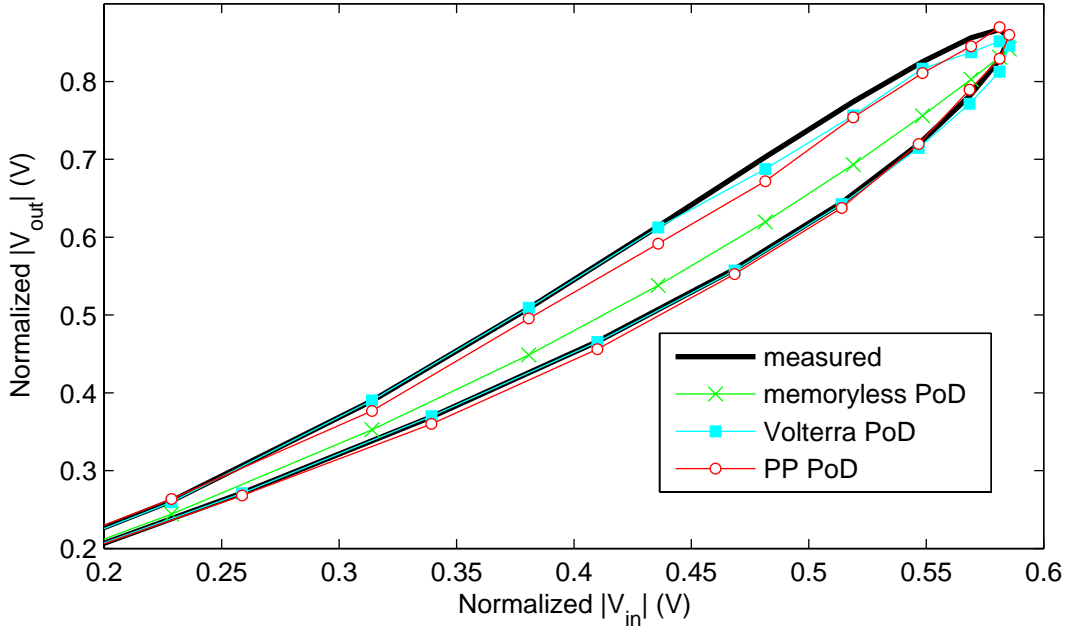


Figure 6.9: Samples of instantaneous AM-AM conversions: measured and estimated by the PoD behavioral models reported in Table 6.1

At this point, the extracted PoD parameters are copied to identical topologies, but implemented as DPDs in the Matlab software. Another realization of a one-carrier WCDMA 3GPP signal with similar characteristics with respect to the one used for PoD extraction was applied as input to the DPDs and the respective predistorted sequences were then used for driving the PA. Table 6.2 presents the ACPR of the measured signal at the PA output, for an average output power of 23 dBm, when the PA was driven by different input sequences.

The inclusion of a DPD memoryless improved by 7.3 dB and 9.0 dB the ACPR_{LW} and ACPR_{UP}, respectively, for $\Delta_f = 5$ MHz with respect to the measured PA output signal for the same average output signal but without DPD. Furthermore, with the incorporation of memory effects in the DPD topologies, additional improvements superior to 2.3 dB were observed in both ACPR_{LW} and ACPR_{UP} for $\Delta_f = 5$ MHz. The PP DPD model using less than 5% of the total number of real-valued parameters required by the Volterra series increases the ACPR, in comparison to the Volterra DPD, by just 1.7 dB and 0.3 dB for

Table 6.2: ACPR of the measured signals at the PA output for an average output power of 23 dBm

Configuration	N	ACPR_{LW} (dB) $\Delta_f =$ 10 MHz	ACPR_{LW} (dB) $\Delta_f =$ 5 MHz	ACPR_{UP} (dB) $\Delta_f =$ 5 MHz	ACPR_{UP} (dB) $\Delta_f =$ 10 MHz
without DPD	—	-64.68	-37.72	-38.63	-64.44
with memoryless DPD	6	-64.23	-44.99	-47.61	-65.31
with Volterra DPD	488	-63.93	-49.09	-50.61	-65.44
with PP DPD	24	-63.81	-47.35	-50.36	-65.00

the lower and upper channels at $\Delta_f = 5$ MHz, respectively. This confirms that the PP DPD model is an effective strategy for Volterra DPD parameter reduction. The PSDs of the measured output signals for the different PA driven conditions, shown in Figure 6.10, are in accordance with the ACPR results reported in Table 6.2.

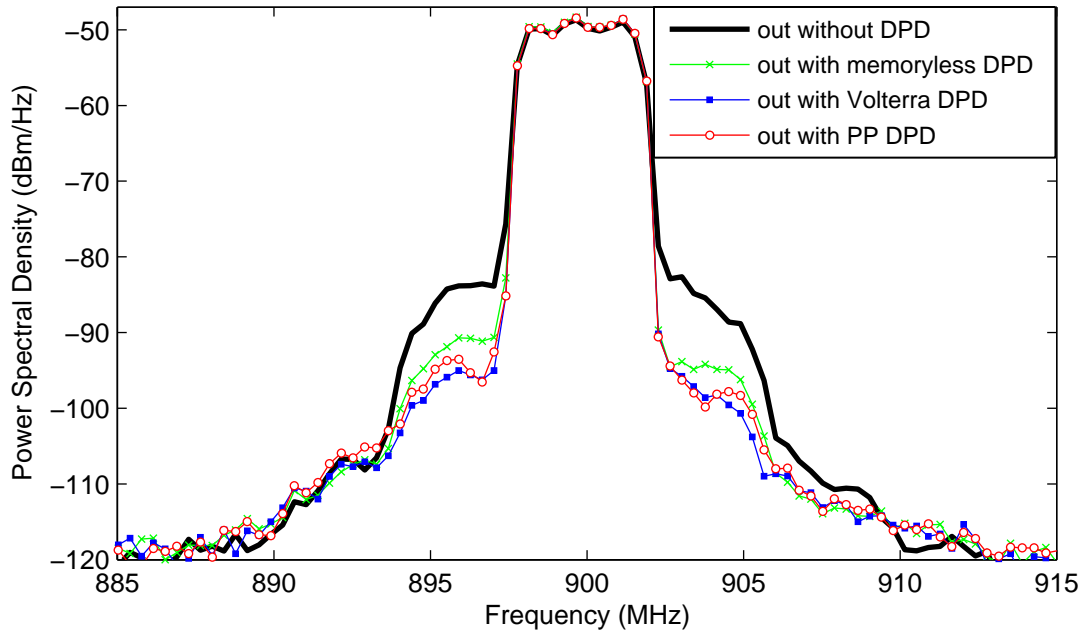


Figure 6.10: PSDs of measured PA output signals for an average output power of 23 dBm: without DPD and in the presence of different fifth-order DPD models

The NMSE between the undistorted WCDMA signal applied to the input of the DPD and the normalized signal measured at the PA output is shown in Table 6.3. Again, the

presence of a DPD significantly reduces the NMSE with respect to the case of only PA. Further reductions in NMSE are obtained if the DPD includes memory effects.

Table 6.3: NMSE results between applied input signal and normalized measured PA output signal for an average output power of 23 dBm

Configuration	N	NMSE (dB)
without DPD	—	-24.89
with memoryless DPD	6	-34.23
with Volterra DPD	488	-37.50
with PP DPD	24	-36.91

In Figure 6.11 is shown the measured instantaneous AM-AM conversions of the cascade connection of a DPD followed by a PA. Whereas all the used DPD models reduced the compression observed in the AM-AM conversion of the PA alone, only the DPD models with memory allow for an AM-AM conversion of the cascade almost memoryless, e.g. a curve with almost negligible hysteresis. Furthermore, the measured instantaneous AM-AM conversions in the presence of the PP and Volterra DPDs are almost indistinguishable.

The 3GPP WCDMA standard [1] imposes very stringent linearity requirements in the transmitter chain. Specifically, the ACPR defined for an adjacent channel of bandwidth 3.84 MHz, with a 5 MHz frequency separation between the center frequencies of the main and adjacent channels, must be lower than -45 dB, whereas the ACPR also for an adjacent channel of bandwidth 3.84 MHz, but with a 10 MHz frequency separation between the center frequencies of the main and adjacent channels, must be lower than -50 dB. To be more rigorous, the 3GPP standard refers to adjacent channel leakage ratio (ACLR), which is slightly different from the ACPR in the sense that the ACLR takes into account the raised cosine receiver filter used in the 3GPP WCDMA systems. However, only ACPR results are provided in this work. The PA in the presence of either a PP DPD or a Volterra DPD meets the required ACPR specifications with an average output power of about 4.5 dB higher than the respective average output power with similar ACPR specifications when no DPD is present. Since the efficiency of a PA also increases as the average output power increases, significant improvements in power efficiency are obtained

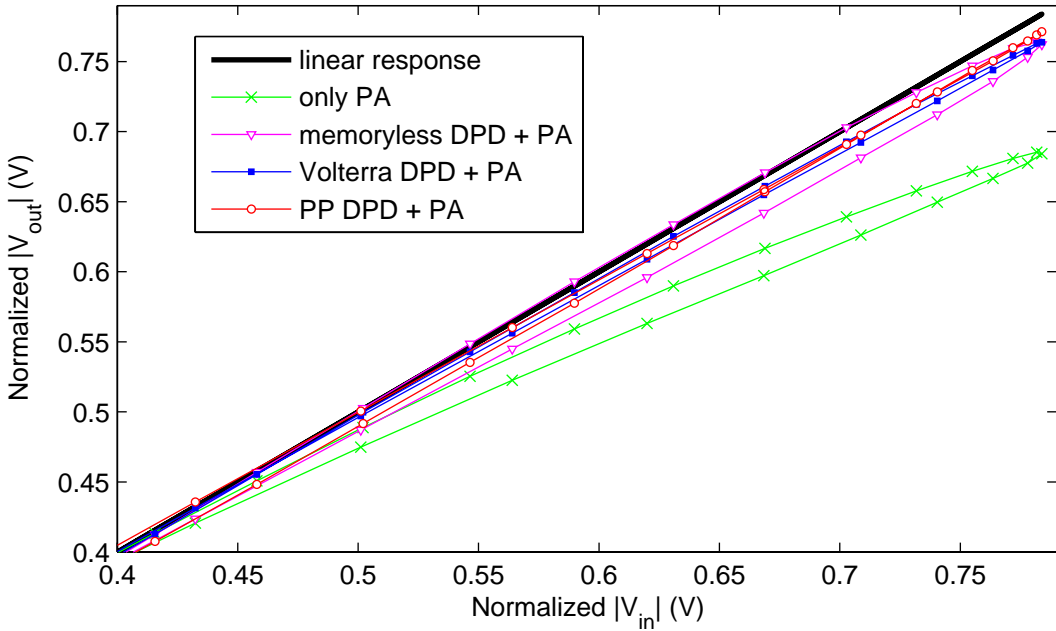


Figure 6.11: Instantaneous AM-AM conversions of the cascade connection of a DPD followed by a PA for an average output power of 23 dBm

by the use of either the PP or Volterra DPD.

The same models, using the same parameter identification strategies, were again extracted and validated but now for a two carrier WCDMA 3GPP input signal of bandwidth 3.84 MHz each carrier, with carrier frequency separation of 5 MHz and PAPR of 11 dB. For extraction purposes, the signal at the PA output was acquired for an average output power of 26 dBm. The NMSE and ACEPR results obtained for the extracted PP, Volterra and memoryless PoD models, as well as their respective number of real-valued parameters N are reported in Table 6.4.

In Table 6.4 is shown, once again, that the PP PoD model presents intermediate results in the used FOMs. Specifically, it improves the memoryless results in NMSE by 9.1 dB and in ACEPR_{LW} and ACEPR_{UP} for $\Delta_f = 5$ MHz by 8.9 dB and 7.4 dB, respectively, but deteriorates the Volterra results in NMSE by 8.4 dB and in ACEPR_{LW} and ACEPR_{UP} for $\Delta_f = 5$ MHz by 10.6 dB and 9.0 dB, respectively. Figure 6.12 shows the measured and modeled instantaneous AM-AM conversions by the PoD models presented in Table 6.4. The instantaneous AM-AM conversion modeled by the Volterra PoD is very close to the measured one, while the instantaneous AM-AM conversion modeled by the PP PoD differs

Table 6.4: NMSE and ACEPR results for different PoDs extracted by the indirect learning architecture

Model	N	NMSE (dB)	ACEPR_{LW} (dB) $\Delta_f = 10 \text{ MHz}$	ACEPR_{LW} (dB) $\Delta_f = 5 \text{ MHz}$	ACEPR_{UP} (dB) $\Delta_f = 5 \text{ MHz}$	ACEPR_{UP} (dB) $\Delta_f = 10 \text{ MHz}$
memoryless	6	-26.14	-41.64	-32.47	-34.27	-44.40
Volterra	488	-43.69	-54.24	-51.98	-50.67	-54.15
PP	24	-35.26	-50.07	-41.39	-41.65	-50.28

from the measured one at high input power levels.

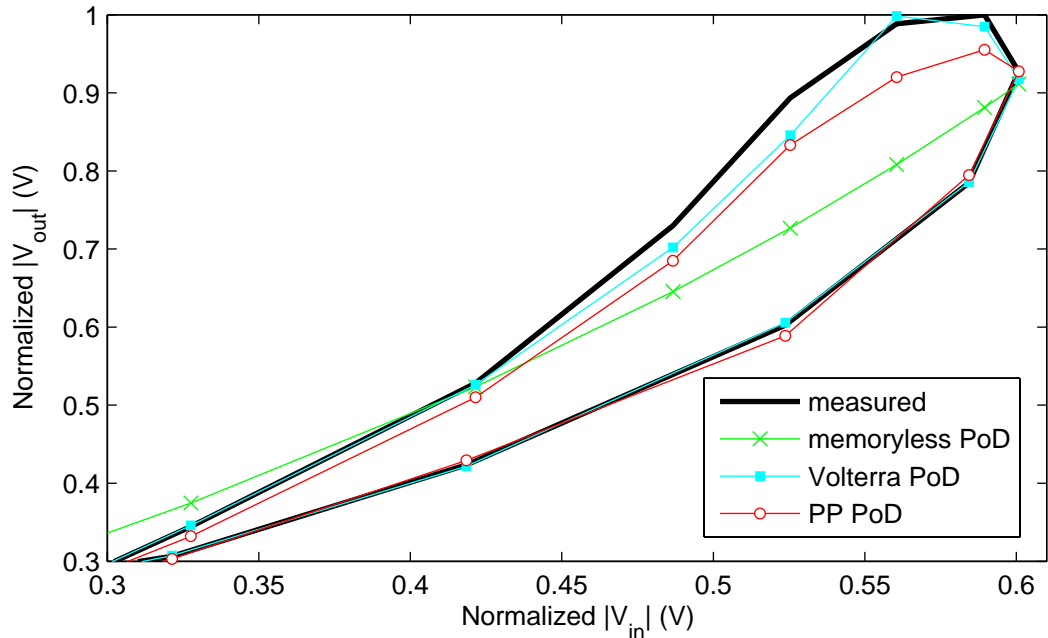


Figure 6.12: Samples of instantaneous AM-AM conversions: measured and estimated by the PoD behavioral models reported in Table 6.4

At this point, the extracted PoD parameters are copied to identical topologies, but implemented as DPDs in the Matlab software. Table 6.5 presents the ACPR of the measured signal at the PA output, for an average output power of 23 dBm, when the PA was driven by different input sequences, whereas the NMSE between the undistorted WCDMA signal applied to the input of the DPD, and the normalized signal measured at the PA output is shown in Table 6.6.

Table 6.5: ACPR of the measured signals at the PA output for an average output power of 23 dBm

Configuration	N	ACPR _{LW} (dB) $\Delta_f =$ 10 MHz	ACPR _{LW} (dB) $\Delta_f =$ 5 MHz	ACPR _{UP} (dB) $\Delta_f =$ 5 MHz	ACPR _{UP} (dB) $\Delta_f =$ 10 MHz
without DPD	—	-37.91	-28.40	-30.06	-38.65
with memoryless DPD	6	-39.92	-30.61	-33.78	-40.93
with Volterra DPD	488	-42.96	-36.75	-38.93	-45.97
with PP DPD	24	-39.48	-36.97	-42.40	-46.29

The memoryless DPD improves only slightly the linearization metrics. Specifically, improvements of 2.2 dB and 3.7 dB in ACPR_{LW} and ACPR_{UP}, respectively, for $\Delta_f = 5$ MHz and of 3.3 dB in NMSE were observed in the measured PA output with the memoryless DPD with respect to the measured PA output signal for the same average output signal but without DPD. However, the presence of DPDs that account for memory effects significantly reduced both ACPR for $\Delta_f = 5$ MHz and NMSE – reductions always superior to 8.3 dB – with respect to the case of only PA. Particularly, the PP DPD in comparison to the Volterra DPD shown similar improvements in both ACPR_{LW} for $\Delta_f = 5$ MHz and NMSE, and even superior improvements in the order of 3.5 dB in ACPR_{UP} for $\Delta_f = 5$ MHz. This reinforces the previous statement that the PP DPD model is an effective strategy for Volterra DPD parameter reduction. The PSDs of the measured output signal for the different PA driven conditions, shown in Figure 6.13, are in accordance with the ACPR results reported in Table 6.5.

Additionally to what was done previously, all PoD models were extracted again but now using the measured signal at the PA output when driven by the predistorted sequences generated by the respective previously extracted DPDs, since it represents a closer sample of the intended PA operation condition, e.g. the PA driven by a distorted signal for having an undistorted signal at its output. The NMSE and ACEPR results obtained for the second extracted PP, Volterra and memoryless PoD models, as well as their respective number of real-valued parameters N are reported in Table 6.7.

A comparison between the FoMs reported in Tables 6.4 and 6.7 shows that a better

Table 6.6: NMSE results between applied input signal and normalized measured PA output signal for an average output power of 23 dBm

Configuration	N	NMSE (dB)
without DPD	–	-22.56
with memoryless DPD	6	-25.89
with Volterra DPD	488	-31.39
with PP DPD	24	-31.88

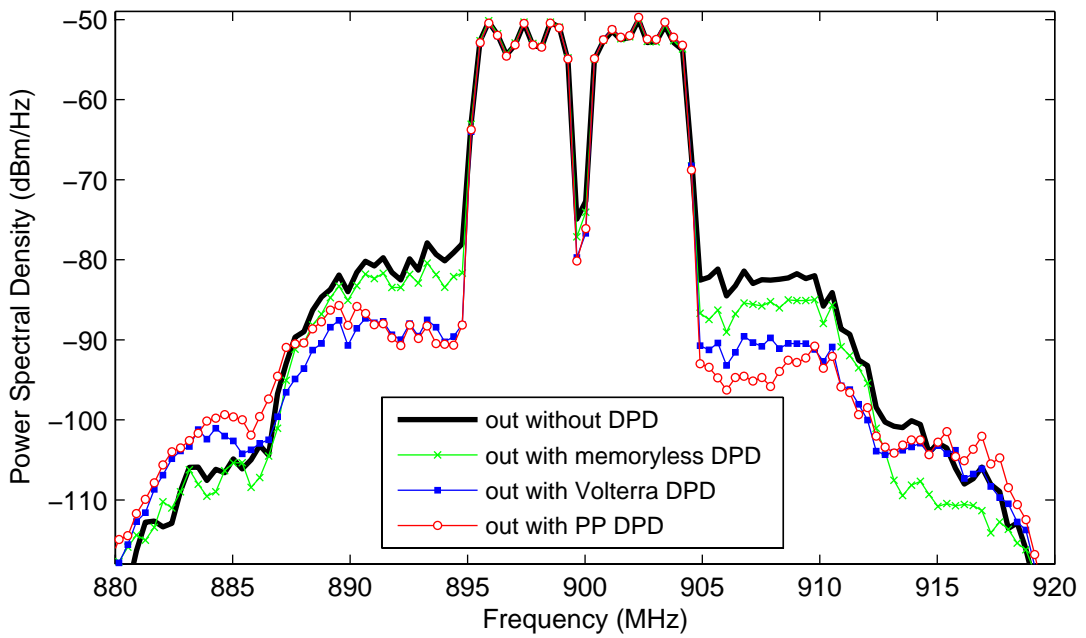


Figure 6.13: PSDs of measured PA output signals for an average output power of 23 dBm: without DPD and in the presence of different fifth-order DPD models

modeling accuracy was obtained for the second extracted PoDs in the case of the Volterra and memoryless models, whereas the first extracted PP PoD presents a lower error with respect to its second extracted counterpart.

The second extracted PoD parameters are also copied to equal topologies, again implemented as DPDs in the Matlab software. Table 6.8 presents the ACPR of the measured signal at the PA output, for an average output power of 23 dBm, when the PA was driven by different input sequences, whereas the NMSE between the undistorted WCDMA signal

Table 6.7: NMSE and ACEPR results for different PoDs extracted by the indirect learning architecture

Model	N	NMSE (dB)	ACEPR _{LW} (dB) $\Delta_f =$ 10 MHz	ACEPR _{LW} (dB) $\Delta_f =$ 5 MHz	ACEPR _{UP} (dB) $\Delta_f =$ 5 MHz	ACEPR _{UP} (dB) $\Delta_f =$ 10 MHz
memoryless DPD (2 nd extraction)	6	-26.80	-43.59	-34.20	-34.82	-44.52
Volterra DPD (2 nd extraction)	488	-44.40	-55.45	-55.54	-53.25	-54.70
PP DPD (2 nd ex- traction)	24	-33.21	-49.28	-39.62	-40.17	-49.30

applied to the input of the DPD and the normalized signal measured at the PA output is shown in Table 6.9.

Table 6.8: ACPR of the measured signals at the PA output for an average output power of 23 dBm

Configuration	N	ACPR _{LW} (dB) $\Delta_f =$ 10 MHz	ACPR _{LW} (dB) $\Delta_f =$ 5 MHz	ACPR _{UP} (dB) $\Delta_f =$ 5 MHz	ACPR _{UP} (dB) $\Delta_f =$ 10 MHz
without DPD	—	-37.91	-28.40	-30.06	-38.65
with memoryless DPD (2 nd extraction)	6	-41.72	-32.37	-35.26	-42.25
with Volterra DPD (2 nd extraction)	488	-45.41	-37.09	-40.02	-47.64
with PP DPD (2 nd ex- traction)	24	-41.45	-38.51	-42.83	-47.03

For the three implemented DPDs, inferior ACPR values, between 0.3 dB and 2.5 dB, for both lower and upper adjacent channels, either for $\Delta_f = 5$ MHz or $\Delta_f = 10$ MHz, were obtained when the second extracted PoDs are used. Figure 6.14 shows the PSDs of the measured PA output signals when the PA was driven by the predistorted sequences generated by both extracted PP DPDs. Besides the measured input-output data used for

Table 6.9: NMSE results between applied input signal and normalized measured PA output signal for an average output power of 23 dBm

Configuration	N	NMSE (dB)
without DPD	–	-22.56
with memoryless DPD (2 nd extraction)	6	-26.56
with Volterra DPD (2 nd extraction)	488	-32.85
with PP DPD (2 nd extraction)	24	-31.87

the second PoD extraction represent a closer match to the PA operation condition in a DPD scheme, these improvements in linearization metrics can be also attributed, in part, by the easier and more accurate post processing (synchronization and phase correction) of the acquired signal measured at the PA output. Indeed, the measured PA output signal used for the second PoD extraction is closer to the undistorted input WCDMA signal than the measured PA output signal used for the first PoD extraction. In terms of NMSE, both the second extracted memoryless and Volterra PoDs presented lower values, whereas no differences are observed for the PP DPD.

In Figure 6.15 is shown the measured instantaneous AM-AM conversions of the cascade connection of a DPD followed by a PA, using the second extracted DPDs. The DPD models with memory shown a further reduction of the compression observed in the AM-AM conversion of the PA alone with respect to the DPD memoryless model, additionally to the expected curve with a lower hysteresis.

The PSDs of the measured PA output signals for different PA driven conditions, using the second extracted DPD models, are shown in Figure 6.16. They are in accordance to the ACPR results reported in Table 6.8.

6.4.2 Case study 2: DPD topologies with polynomial approximations at base-band and RF levels

This subsection describes experimental time-domain measurements performed in a class AB PA with GaN based technology. The experimental setup uses the same instruments

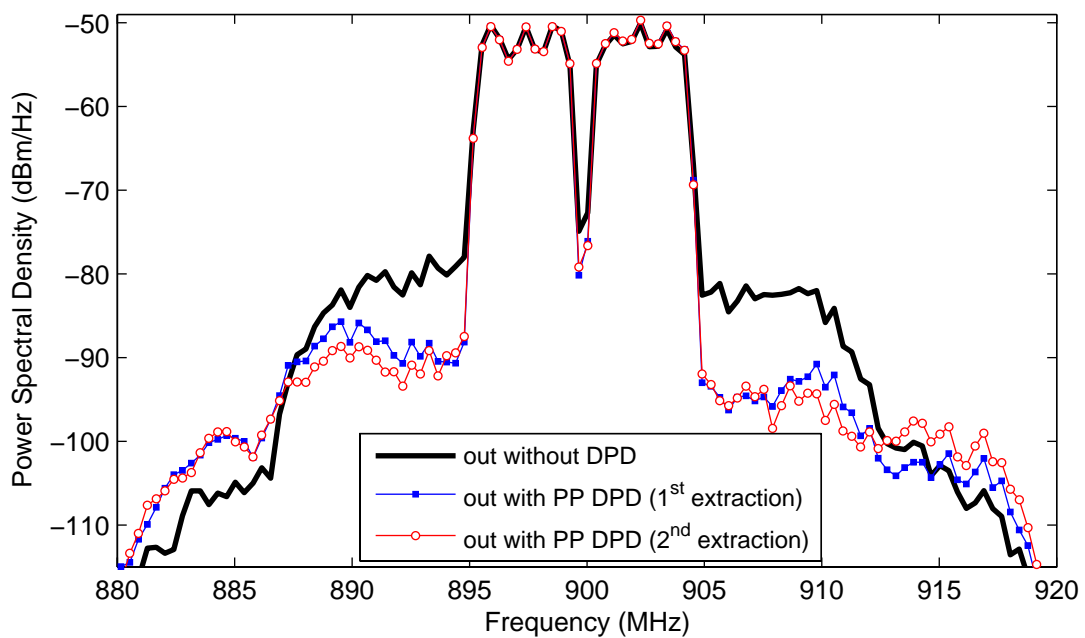


Figure 6.14: PSDs of measured PA output signals for an average output power of 23 dBm: without DPD and in the presence of a fifth-order PP DPD model

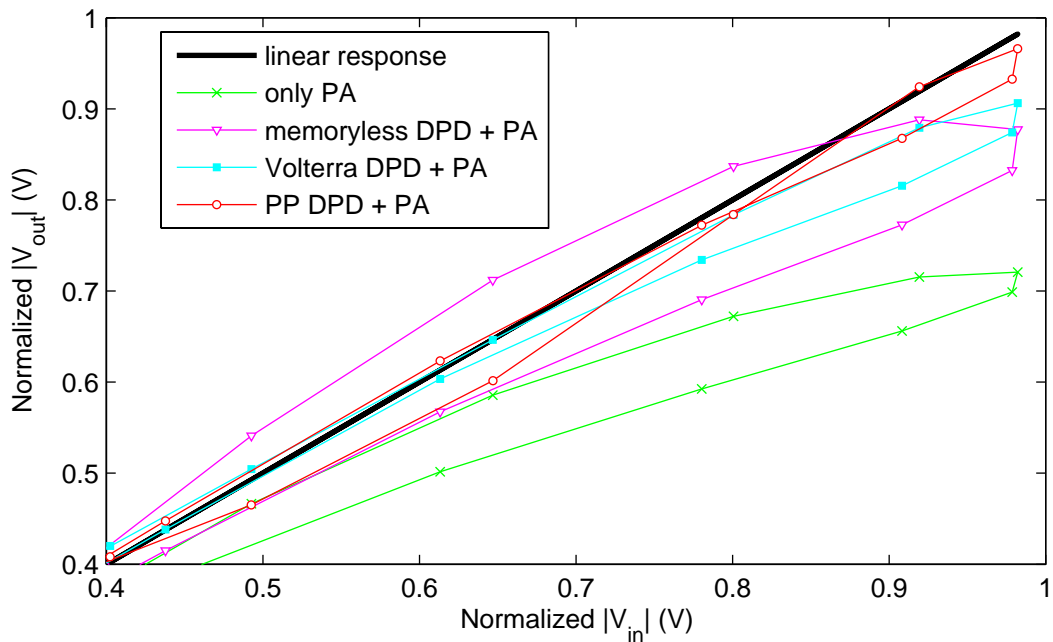


Figure 6.15: Instantaneous AM-AM conversions of the cascade connection of a DPD followed by a PA for an average output power of 23 dBm

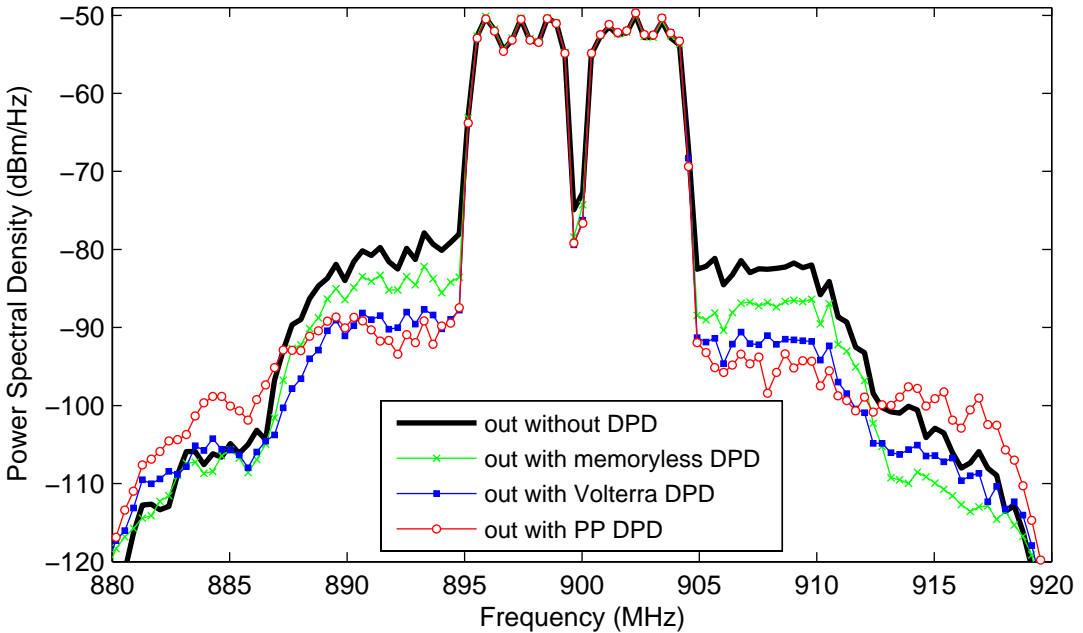


Figure 6.16: PSDs of measured PA output signals for an average output power of 23 dBm: without DPD and in the presence of different fifth-order DPD models

as the case study 1. In the analysis presented here, the considered input signal was a WCDMA 3GPP signal of bandwidth 3.84 MHz and peak-to-average power ratio (PAPR) of 11.6 dB. For extraction purposes, the signal at the PA output was acquired for an average output power of 26 dBm. The sampling frequency was set to 61.44 MHz.

In this subsection, it is investigated the differences in DPD schemes, in terms of improvements in linearization metrics, by assuming a polynomial approximation at RF level or at base-band level for the DPD topology. The theory behind these two approaches has been presented in Chapter 4, focusing on PA behavioral modeling. Nevertheless, as pointed out in Section 6.2, the same reasoning also applies to DPD purposes.

For that scope, memory polynomial (MP) models with different truncation factor P , for RF Poly models, and P_0 , for BB Poly models, and with fixed memory length $M = 3$ were arbitrarily chosen as the *a priori* topologies for the DPDs. Their parameter extraction was performed using the indirect learning architecture, via a LS. Table 6.10 shows the NMSE and ACEPR results, as well as the number of complex-valued parameters N required in each case.

Differently from what happened in PA behavioral modeling, for a same number of

Table 6.10: NMSE and ACEPR results for MP PoDs extracted by the indirect learning architecture

Model	P or P_0	M	N	NMSE (dB)	ACEPR _{LW} (dB) $\Delta_f =$ 10 MHz	ACEPR _{LW} (dB) $\Delta_f =$ 5 MHz	ACEPR _{UP} (dB) $\Delta_f =$ 5 MHz	ACEPR _{UP} (dB) $\Delta_f =$ 10 MHz
RF Poly	2	3	08	-36.38	-59.08	-46.36	-50.26	-62.70
BB Poly	2	3	08	-32.00	-55.94	-42.19	-44.88	-57.27
RF Poly	3	3	12	-38.99	-62.98	-52.41	-51.32	-64.12
BB Poly	3	3	12	-38.47	-59.79	-51.63	-50.88	-62.53
RF Poly	4	3	16	-39.93	-64.93	-53.59	-55.47	-64.85
BB Poly	4	3	16	-39.43	-64.05	-53.44	-52.53	-62.29
RF Poly	5	3	20	-40.43	-65.29	-55.70	-56.69	-65.10
BB Poly	5	3	20	-40.04	-64.21	-54.19	-55.46	-64.34
RF Poly	6	3	24	-40.45	-65.51	-55.71	-56.77	-65.06
BB Poly	6	3	24	-40.44	-65.44	-55.70	-56.97	-64.91
RF Poly	7	3	28	-40.55	-68.33	-56.53	-57.25	-65.64
BB Poly	7	3	28	-40.52	-67.62	-56.25	-57.44	-65.69

complex-valued parameters and $P = P_0 < 6$, the MP model with RF Poly has superior performance (NMSE and ACEPR FoMs) than the MP model with BB Poly. The largest difference, specifically 4.4 dB in NMSE and 4.2 dB and 5.4 dB in ACEPR_{LW} and ACEPR_{UP}, respectively, for $\Delta_f = 5$ MHz is observed in the case with $P = P_0 = 2$ and $M = 3$. However, it is worth to point out that neither approximations with $P = P_0 = 2$ could accurately model the measured AM-AM, as shown in Figure 6.17. Similarly to the case of PA behavioral modeling, as the number of parameters increases, the differences between the two polynomial approximations reduce. An equivalent performance for both RF Poly and BB Poly is observed for $P = P_0 = 7$ and $M = 3$, not only on the evaluated FoMs but also on the modeled AM-AM conversions, as shown in Figure 6.18.

For the same polynomial order truncation, $2P - 1 = P_0$, Table 6.10 shows that the MP model with BB Poly has always superior performance (NMSE and ACEPR FoMs) than the MP model with RF Poly. For instance, the BB Poly with $P_0 = 5$ and $M = 3$ improves

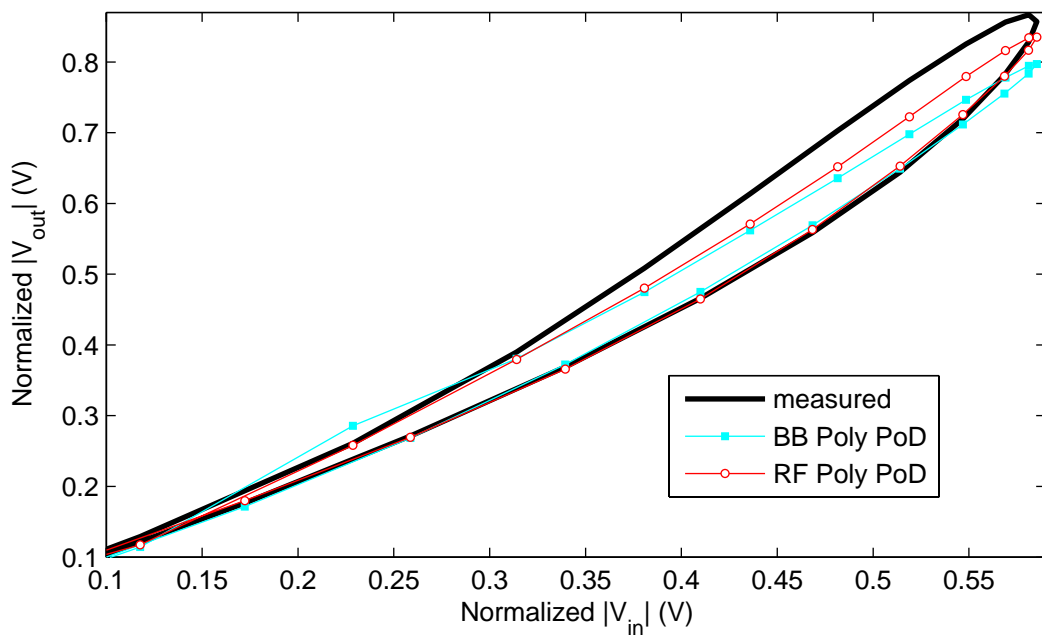


Figure 6.17: Samples of instantaneous AM-AM conversions: measured and estimated by MP PoD behavioral models with $P = P_0 = 2$, $M = 3$ and different polynomial approximations

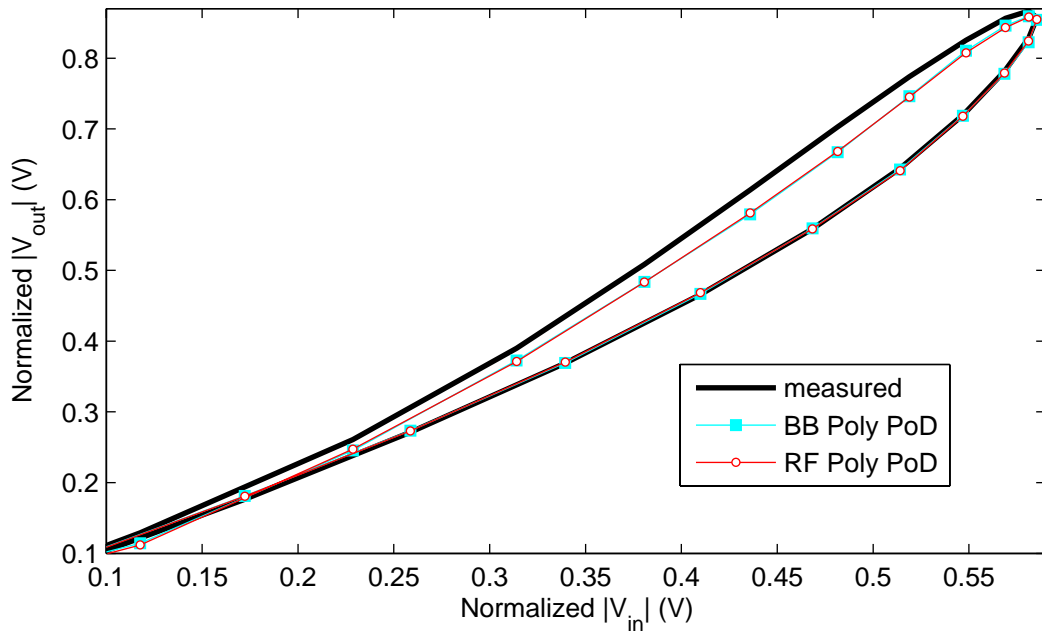


Figure 6.18: Samples of instantaneous AM-AM conversions: measured and estimated by MP PoD behavioral models with $2P - 1 = P_0 = 7$, $M = 3$ and different polynomial approximations

1.1 dB in NMSE and 1.8 dB and 4.1 dB in ACEPR_{LW} and ACEPR_{UP}, respectively, for $\Delta_f = 5 \text{ MHz}$ with respect to the RF Poly with $P = 3$ and $M = 3$.

At this point, some of the extracted PoD parameters are copied to equal topologies, but implemented as DPDs in the Matlab software. Table 6.11 presents the ACPR of the measured signal at the PA output, for an average output power of 23 dBm, when the PA was driven by different input sequences, whereas the NMSE between the undistorted WCDMA signal applied to the input of the DPD and the normalized signal measured at the PA output is shown in Table 6.12.

Table 6.11: ACPR of the measured signals at the PA output for an average output power of 23 dBm

Configuration	P or P_0	M	N	ACPR _{LW} (dB) $\Delta_f =$ 10 MHz	ACPR _{LW} (dB) $\Delta_f =$ 5 MHz	ACPR _{UP} (dB) $\Delta_f =$ 5 MHz	ACPR _{UP} (dB) $\Delta_f =$ 10 MHz
without DPD	-	-	-	-64.68	-37.72	-38.63	-64.44
with MP RF Poly DPD	3	3	12	-64.42	-49.44	-50.65	-64.70
with MP BB Poly DPD	3	3	12	-57.10	-47.58	-50.93	-63.95
with MP RF Poly DPD	4	3	16	-64.74	-52.00	-54.72	-64.51
with MP BB Poly DPD	4	3	16	-64.56	-50.19	-51.51	-61.06
with MP RF Poly DPD	5	3	20	-64.12	-53.84	-55.70	-64.55
with MP BB Poly DPD	5	3	20	-63.71	-52.89	-54.84	-63.76
with MP BB Poly DPD	7	3	28	-65.78	-55.50	-57.51	-66.17

According to Table 6.11, the inclusion of any of the extracted DPD MP models are fully justified, since improvements of at least 9.9 dB and 12.0 dB in the ACPR_{LW} and ACPR_{UP}, respectively, for $\Delta_f = 5 \text{ MHz}$ are observed with respect to the measured PA output signal for the same average output signal but without DPD.

For the same number of complex-valued parameters, and so $P = P_0$, if a DPD MP model with RF Poly is used, the signal measured at the PA output presents better linearization indicators on both ACPR and NMSE with respect to the use of a DPD MP model with BB Poly. The largest differences, specifically 2.7 dB in NMSE and 1.9 dB and 0.3 dB in ACPR_{LW} and ACPR_{UP}, respectively, for $\Delta_f = 5 \text{ MHz}$ are observed in the case

Table 6.12: NMSE results between applied input signal and normalized measured PA output signal for an average output power of 23 dBm

Configuration	P or P_0	M	N	NMSE (dB)
without DPD	—	—	—	-19.87
with MP RF Poly DPD	3	3	12	-37.29
with MP BB Poly DPD	3	3	12	-34.55
with MP RF Poly DPD	4	3	16	-40.69
with MP BB Poly DPD	4	3	16	-38.21
with MP RF Poly DPD	5	3	20	-39.00
with MP BB Poly DPD	5	3	20	-38.55
with MP BB Poly DPD	7	3	28	-43.04

with $P = P_0 = 3$ and $M = 3$. As the number of parameters increases, the differences in the linearization metrics of the signal measured at the PA output between the use of DPD with the two polynomial approximations reduce. Figure 6.19 show the PSDs of the measured PA output signal when the PA is driven by predistorted signals generated by MP DPDs with both RF Poly and BB Poly approximations having $P = P_0 = 5$ and $M = 3$.

For the same polynomial order truncation, $2P-1 = P_0$, Tables 6.11 and 6.12 show that if a DPD MP model with BB Poly is used, the signal measured at the PA output presents better linearization indicators (ACPR and NMSE) with respect to the use of a DPD MP model with RF Poly. This proves that the additional odd-order terms included in the BB Poly approximation do contribute to the compensation of the nonlinear dynamic effects exhibited by the PA. For instance, the BB Poly with $P_0 = 7$ and $M = 3$ improves 2.4 dB in NMSE and 3.5 dB and 2.8 dB in ACPR_{LW} and ACPR_{UP}, respectively, for $\Delta_f = 5$ MHz with respect to the RF Poly with $P = 4$ and $M = 3$. Figure 6.20 shows the PSDs of the measured PA output signal when the PA is driven by predistorted signals generated by MP DPD models with both RF Poly and BB Poly approximations having $2P-1 = P_0 = 7$ and $M = 3$.

In Figure 6.21 is shown the measured instantaneous AM-AM conversions of the cas-

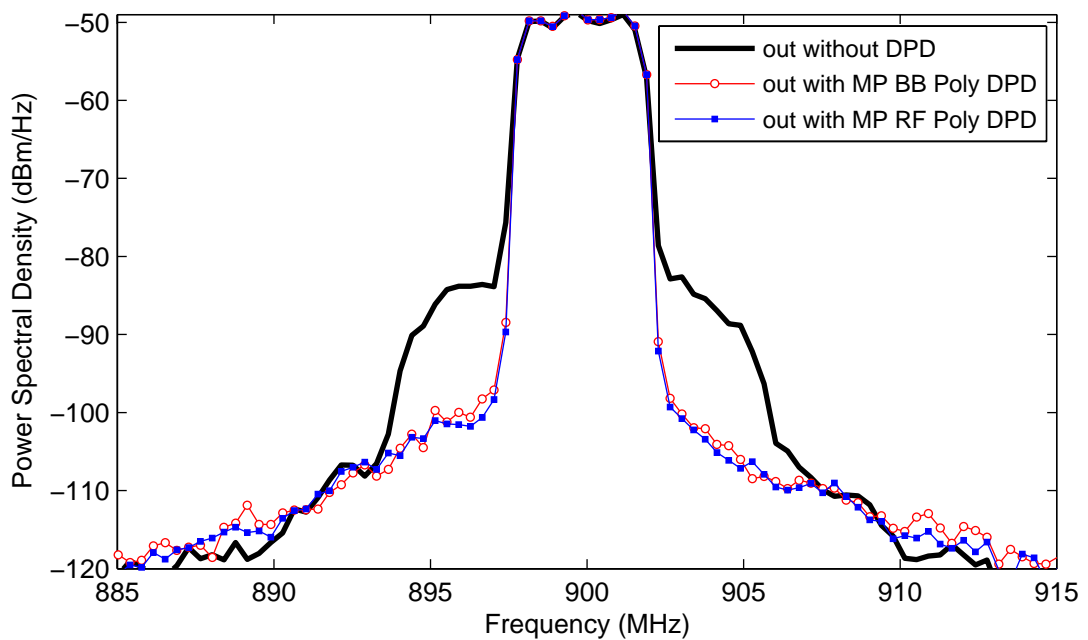


Figure 6.19: PSDs of measured PA output signals for an average output power of 23 dBm: without DPD and in the presence of MP DPD models truncated to $P = P_0 = 5$ and $M = 3$

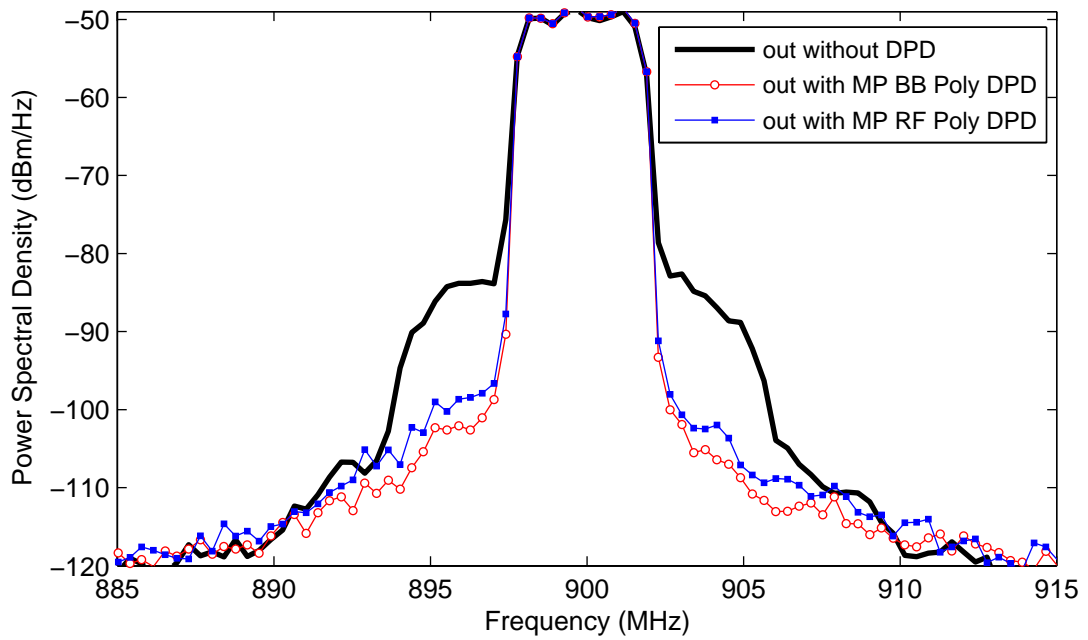


Figure 6.20: PSDs of measured PA output signals for an average output power of 23 dBm: without DPD and in the presence of MP DPD models truncated to $2P - 1 = P_0 = 7$ and $M = 3$

cade connection of a DPD followed by a PA, when MP DPD models with both RF Poly and BB Poly approximations having $2P - 1 = P_0 = 7$ and $M = 3$ are used. Both DPD models reduced the compression observed in the AM-AM conversion of the PA alone, and also allowed for an AM-AM conversion of the cascade connection almost memoryless, e.g. a curve with almost negligible hysteresis. Furthermore, the measured instantaneous AM-AM conversions in the presence of the MP DPD models with both RF Poly and BB Poly are almost indistinguishable.

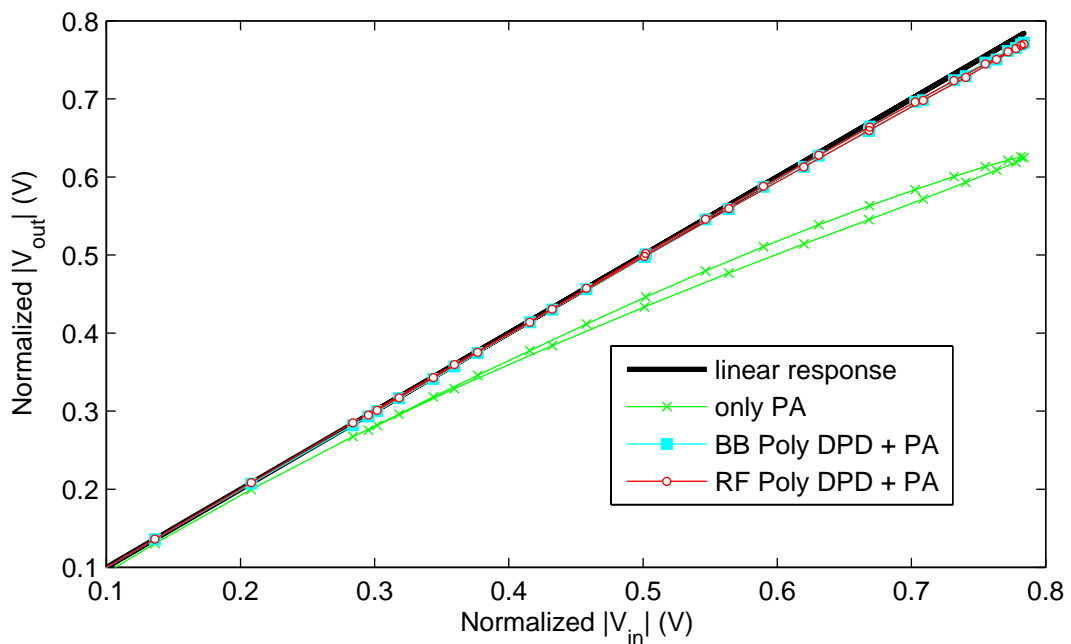


Figure 6.21: Instantaneous AM-AM conversions of the cascade connection of a DPD followed by a PA for an average output power of 23 dBm: MP DPD models have $2P - 1 = P_0 = 7$, $M = 3$ and different polynomial approximations

6.4.3 Case study 3: arbitrary topology selection for the PA or for the DPD models

This subsection is based on experimental time-domain measurements performed in a class AB LDMOS PA with second harmonic output tuning [117]. The VSG used in the experimental setup was an Agilent ESG E4433B, while the VSA was an Agilent MXA N9020A. The sampling frequency was set to 30.72 MHz. In the analysis presented in this sub-

section, WCDMA 3GPP signals of bandwidth 3.84 MHz but with two distinct PAPRs, namely 3.5 dB and 11 dB are considered.

The objective here is to investigate the possible differences, in terms of linearization improvements achieved by a DPD scheme, if a particular arbitrary topology selection is done for the PA model or for the DPD model. The *a priori* arbitrary topology chosen was the MP RF Poly – for simplicity of notation, it will be referred to just as MP model. Its inverse, as described in Subsection 6.2.2, is of recursive nature and designated as NARX. For that scope, the linearization indicators of the signal measured at the PA output are compared when either a MP DPD model, extracted instead using the indirect learning algorithm, or a NARX DPD model, whose parameters are derived from a MP PA behavioral model, are used.

First of all, the parameters of MP models were extracted, via LS, to model both a MP PA behavioral model, e.g. the complex-valued envelope measured at the PA output as a function of the applied input complex-valued envelope, and a MP PoD model, e.g. the complex-valued envelope applied to the PA input as a function of the complex-valued envelope measured at the PA output. Tables 6.13 and 6.14 show the NMSE and ACEPR results obtained when the MP models were extracted to fit measured data at the PA output for an average output power of 37.5 dBm (input signal having $PAPR = 3.5$ dB), and for an average output power of 31.5 dBm (input signal having $PAPR = 11$ dB), respectively. In the fourth columns, N indicates the number of complex-valued parameters required by the respective MP models. Memoryless polynomial PoDs were also extracted and their performances included in the Tables 6.13 and 6.14.

Despite the different number of required fitting parameters, the MP shown a similar accuracy when employed for the distinct purposes. Particularly, differences in terms of NMSE and ACEPR for $\Delta_f = 5$ MHz not higher than 1.2 dB were observed when the extraction was based on the input signal having PAPR equals 3.5 dB and, not higher than 0.2 dB, when the extraction was based on the input signal having PAPR of 11 dB. Nevertheless, whereas the MP models could provide an accurate prediction of the measured AM-AM conversions for the input signal having PAPR of 11 dB, as shown in Figures 6.22 and 6.23, the same was not true for the input signal having 3.5 dB of PAPR. In fact, Figures 6.24 and 6.25 show that both the PA MP and PoD MP fail the estimation of the

Table 6.13: NMSE and ACEPR results for MP modeling with distinct purposes when the input signal had $PAPR = 3.5$ dB

Model	P	M	N	NMSE (dB)	ACEPR _{LW} (dB) $\Delta_f =$ 10 MHz	ACEPR _{LW} (dB) $\Delta_f =$ 5 MHz	ACEPR _{UP} (dB) $\Delta_f =$ 5 MHz	ACEPR _{UP} (dB) $\Delta_f =$ 10 MHz
memoryless PoD	7	0	7	-32.50	-55.03	-39.82	-40.39	-52.19
MP PoD	7	2	21	-36.38	-57.43	-47.15	-45.93	-56.45
MP PA	11	2	33	-36.78	-60.74	-46.84	-47.12	-60.61

Table 6.14: NMSE and ACEPR results for MP modeling with distinct purposes when the input signal had $PAPR = 11$ dB

Model	P	M	N	NMSE (dB)	ACEPR _{LW} (dB) $\Delta_f =$ 10 MHz	ACEPR _{LW} (dB) $\Delta_f =$ 5 MHz	ACEPR _{UP} (dB) $\Delta_f =$ 5 MHz	ACEPR _{UP} (dB) $\Delta_f =$ 10 MHz
memoryless PoD	7	0	7	-34.77	-54.76	-41.61	-42.16	-54.57
MP PoD	7	2	21	-38.12	-59.69	-51.00	-50.82	-59.55
MP PA	11	2	33	-38.30	-61.04	-51.04	-50.86	-61.67

measured instantaneous AM-AM conversions even at low input power levels.

Repeating the steps performed in the previous case studies, the extracted MP PoD parameters are copied to another MP of same truncation factors which implements a DPD in the Matlab software. Moreover, a DPD NARX whose parameters are derived from the extracted MP PA behavioral, according to the procedure described in Subsection 6.2.2, is also implemented in the Matlab software. Another realization of a one-carrier WCDMA 3GPP signal with similar characteristics, including PAPRs, with respect to the ones used for the extraction was applied as input to the DPDs and the respective predistorted sequences were then used for driving the PA. Tables 6.15 and 6.16 present the ACPR of the measured signal at the PA output, with and without DPDs, when the applied input signal is a WCDMA having 3.5 dB and 11 dB of PAPR, respectively.

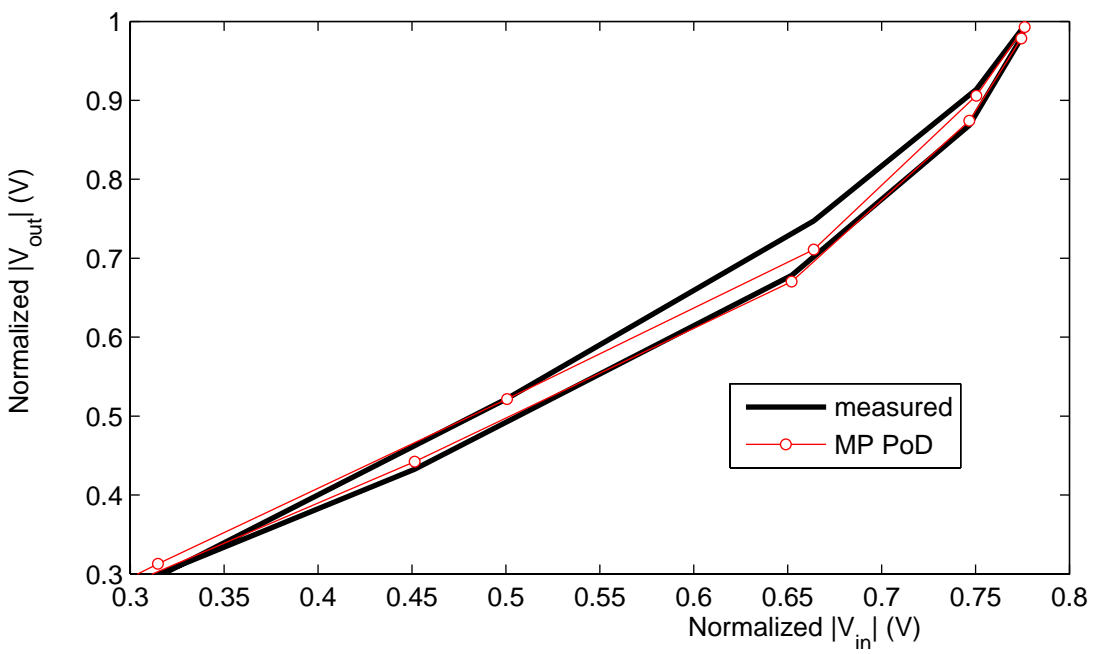


Figure 6.22: Samples of instantaneous AM-AM conversions: measured and estimated by a MP PoD behavioral model with $P = 7$ and $M = 2$, when the input signal had $PAPR = 11$ dB

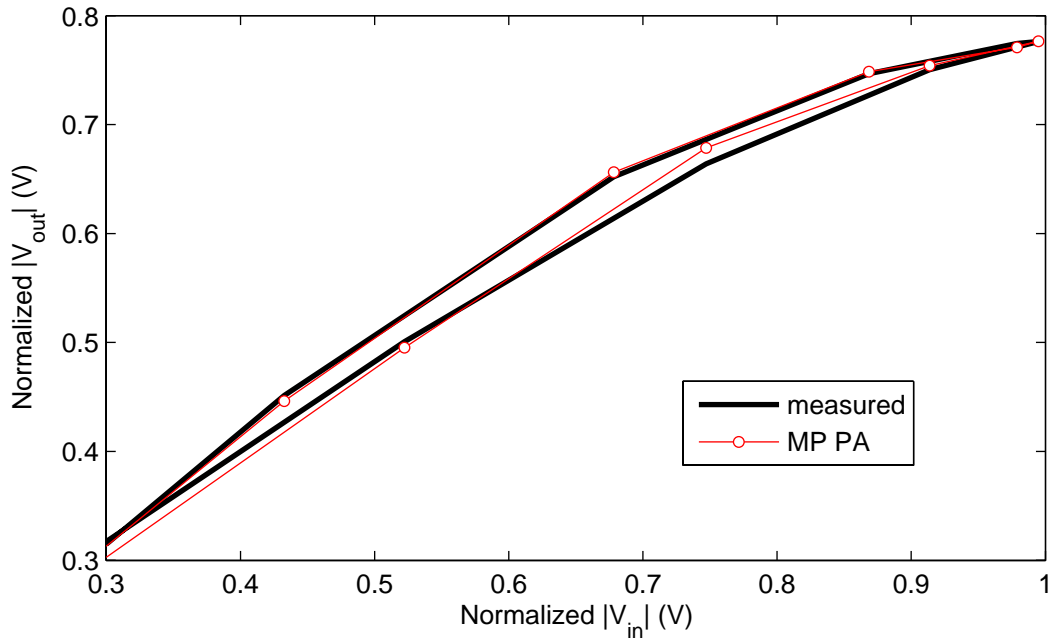


Figure 6.23: Samples of instantaneous AM-AM conversions: measured and estimated by a MP PA behavioral model with $P = 11$ and $M = 2$, when the input signal had $PAPR = 11$ dB

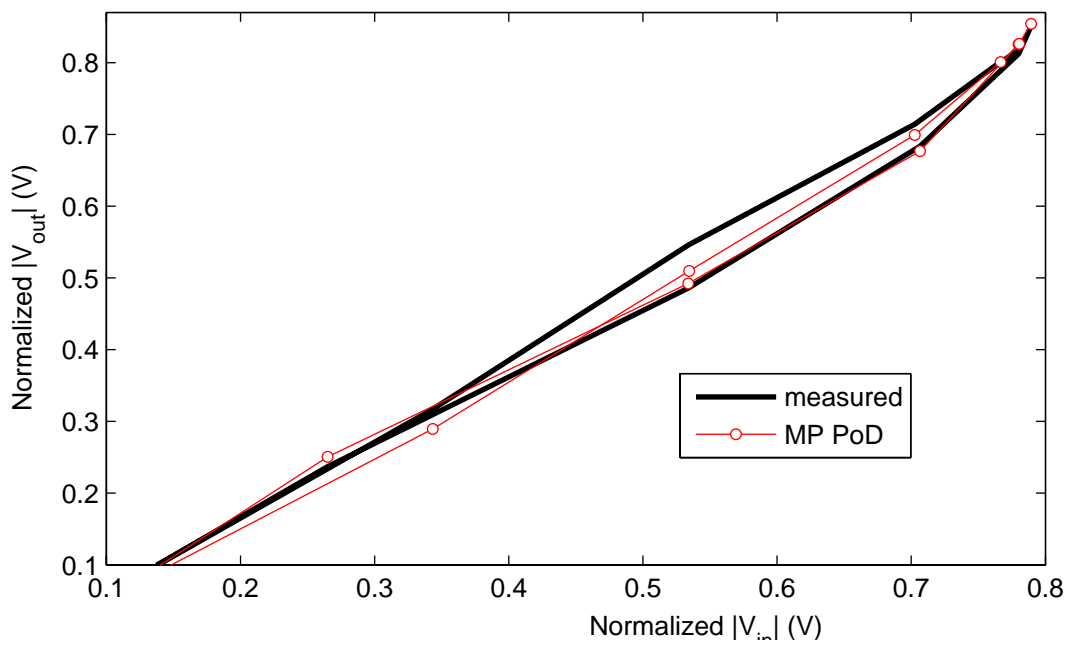


Figure 6.24: Samples of instantaneous AM-AM conversions: measured and estimated by a MP PoD behavioral model with $P = 7$ and $M = 2$, when the input signal had $PAPR = 3.5$ dB

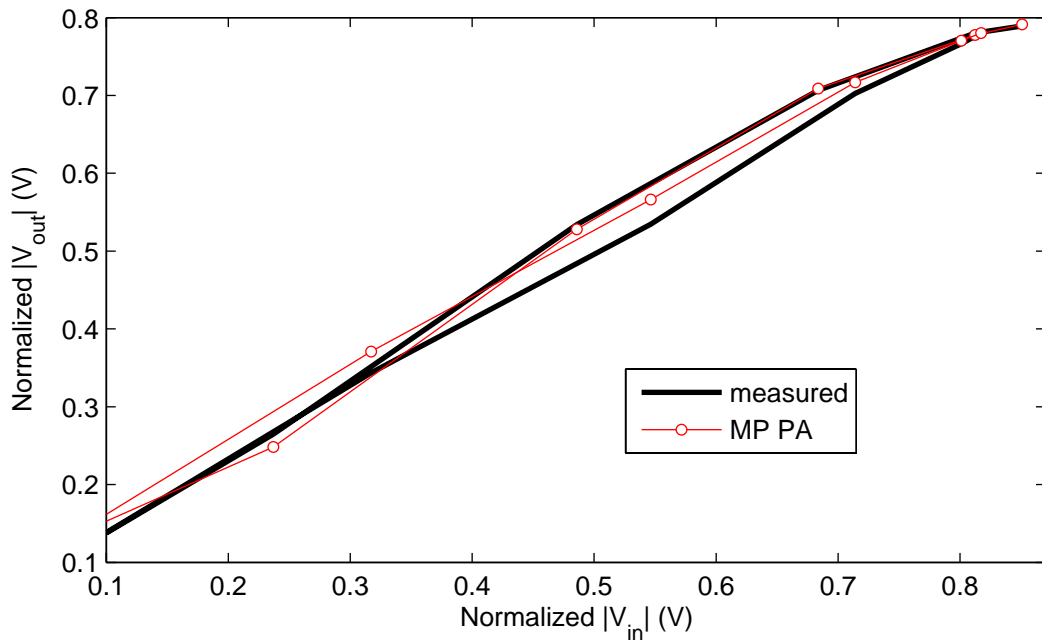


Figure 6.25: Samples of instantaneous AM-AM conversions: measured and estimated by a MP PA behavioral model with $P = 11$ and $M = 2$, when the input signal had $PAPR = 3.5$ dB

Table 6.15: ACPR of the measured PA output signal when the input signal had $PAPR = 3.5$ dB and for an average output power of 36 dBm

Configuration	ACPR _{LW} (dB) $\Delta_f =$ 10 MHz	ACPR _{LW} (dB) $\Delta_f =$ 5 MHz	ACPR _{UP} (dB) $\Delta_f =$ 5 MHz	ACPR _{UP} (dB) $\Delta_f =$ 10 MHz
without DPD	-49.89	-39.58	-33.69	-52.80
with MP DPD	-57.69	-47.21	-46.49	-59.18
with NARX DPD	-53.45	-40.03	-40.92	-58.49

Table 6.16: ACPR of the measured PA output signal when the input signal had $PAPR = 11$ dB and for an average output power of 29.5 dBm

Configuration	ACPR _{LW} (dB) $\Delta_f =$ 10 MHz	ACPR _{LW} (dB) $\Delta_f =$ 5 MHz	ACPR _{UP} (dB) $\Delta_f =$ 5 MHz	ACPR _{UP} (dB) $\Delta_f =$ 10 MHz
without DPD	-52.81	-40.82	-39.56	-52.54
with memoryless DPD	-55.50	-43.10	-43.24	-55.02
with MP DPD	-59.22	-52.93	-52.78	-59.42
with NARX DPD	-59.72	-51.36	-50.59	-59.66

Particularly for the input WCDMA having PAPR equals to 11 dB and according to Table 6.16, the DPD memoryless improves only slightly the linearization metrics. Specifically, improvements of 2.3 dB and 3.7 dB in ACPR_{LW} and ACPR_{UP}, respectively, for $\Delta_f = 5$ MHz were observed in the measured PA output with the memoryless DPD with respect to the measured PA output signal for the same average output signal but without DPD. However, the presence of DPDs that account for memory effects significantly reduces the ACPR both for $\Delta_f = 5$ MHz and for $\Delta_f = 10$ MHz – reductions always superior to 10.5 dB and 6.4 dB for $\Delta_f = 5$ MHz and $\Delta_f = 10$ MHz, respectively – with respect to the case of PA only. Since the MP models could provide an accurate prediction for both PA and PoD purposes, similar linearization metrics (differences in ACPR not higher than 2.2 dB) were obtained for the signal measured at the PA output in the presence of either the MP DPD or the NARX DPD. The PSDs of the measured output signals for the

different PA driven conditions, shown in Figure 6.26, are in accordance with the ACPR results reported in Table 6.16. In conclusion, since the *a priori* MP topology was a good choice either for the PA and DPD topologies, no direct impact on linearization metrics were observed by the specific decision on which topology, PA or DPD, it was done.

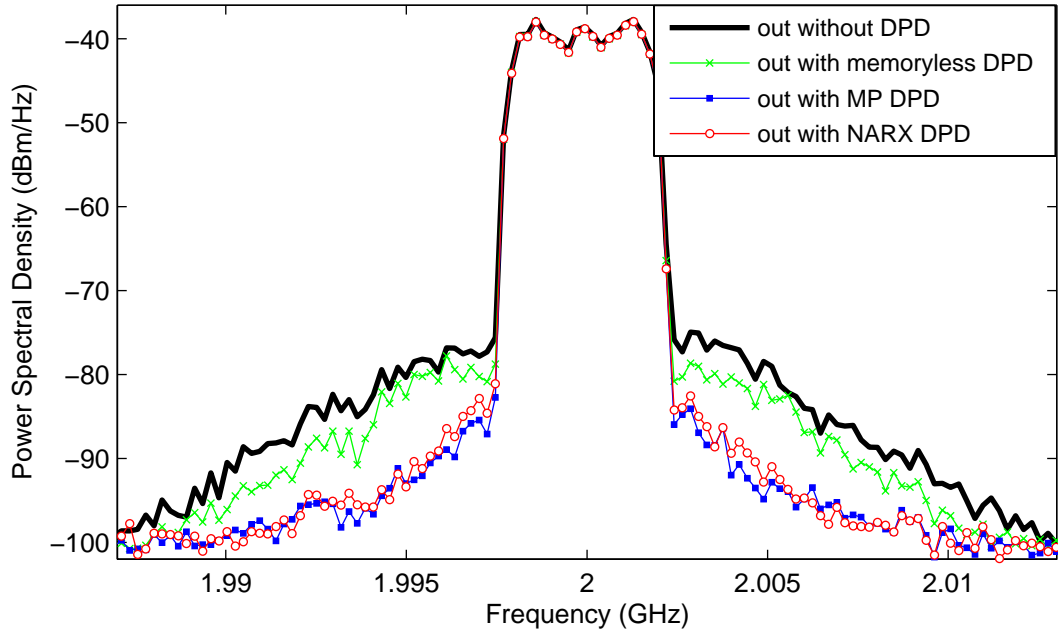


Figure 6.26: PSDs of measured PA output signals, with and without DPD, when the input signal had $PAPR = 11$ dB and for an average output power of 29.5 dBm: DPD NARX with $P = 11$, $M = 2$ and DPD MP with $P = 7$, $M = 2$

On the other hand, for the input WCDMA having 3.5 dB of PAPR, in which the MP models could not provide a good prediction, neither for the PA nor for the PoD, better linearization metrics were obtained for the signal measured at the PA output in the presence of the MP DPD in comparison to when the NARX DPD was present. Specifically, the MP DPD reduces 7.2 dB and 5.6 dB in $ACPR_{LW}$ and $ACPR_{UP}$, respectively, for $\Delta_f = 5$ MHz with respect to the NARX DPD. In the PSDs of the measured PA output signal when the PA is driven by predistorted signals generated by the MP DPD and the NARX DPD, shown in Figure 6.27, it is observed that the NARX DPD was only able to compensate for the strong asymmetries of the distortion introduced by the PA, while the MP DPD was much more effective in reducing the spectral regrowth at the PA output. This is not surprising, since while the DPD MP has a functionality close to the extracted PoD model

(both PoD and DPD mimics expansive behaviors), the NARX DPD not only is used in a completely different environment from the extracted PA model, in which additional fitting errors may be introduced during the model inversion, but also presents a recursive topology which will never completely forget previously inserted errors.

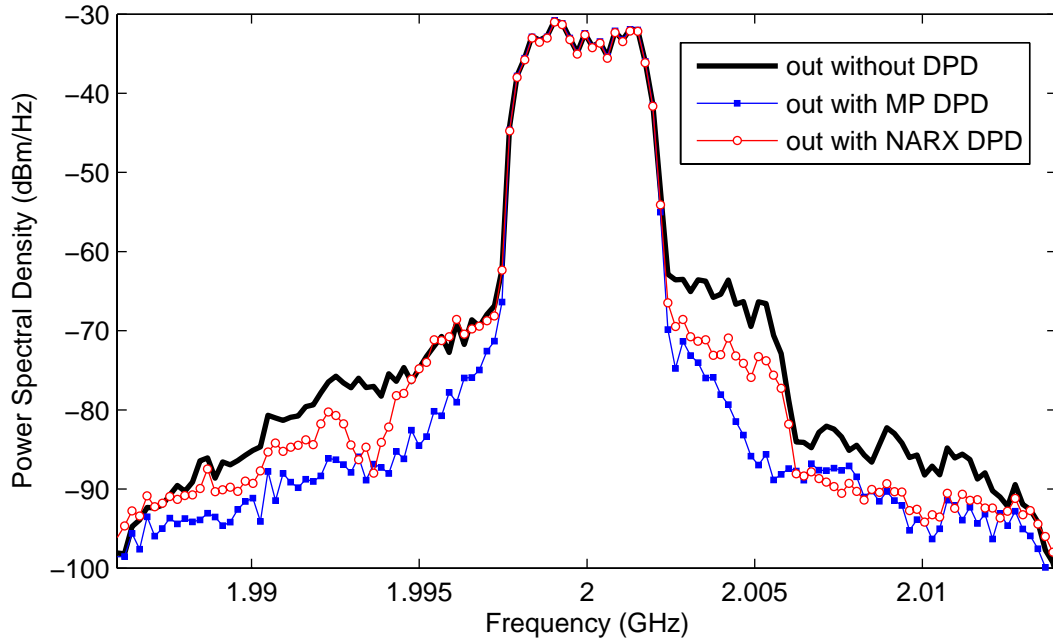


Figure 6.27: PSDs of measured PA output signals, with and without DPD, when the input signal had $PAPR = 3.5$ dB and for an average output power of 36 dBm: DPD NARX with $P = 11$, $M = 2$ and DPD MP with $P = 7$, $M = 2$

The NMSE between the undistorted WCDMA signal applied to the input of the DPD and the normalized signal measured at the PA output is shown in Table 6.17. Again, the presence of a DPD has reduced the NMSE with respect to the case of only PA.

In Figure 6.28 is shown the measured instantaneous AM-AM conversions of the cascade connection of a DPD followed by a PA, when the applied input signal is a WCDMA having a PAPR equals to 3.5 dB. The measured instantaneous AM-AM conversion in the presence of the NARX DPD initially presents a small compression and then a small expansion. These slightly slope changes are responsible for the increasing in ACPR results for the upper adjacent channel with respect to the measured output in the presence of the MP DPD, shown in Figure 6.27.

Moreover, for the specific input WCDMA signal having PAPR equals to 11 dB, the

Table 6.17: NMSE results between applied input signal and normalized measured PA output signal

Configuration	NMSE, dB	
	PAE 38% ($PAPR = 3.5$ dB)	PAE 18% ($PAPR = 11$ dB)
without DPD	-28.09	-28.86
with memoryless DPD	-	-34.95
with MP DPD	-31.80	-34.37
with NARX DPD	-31.29	-30.15

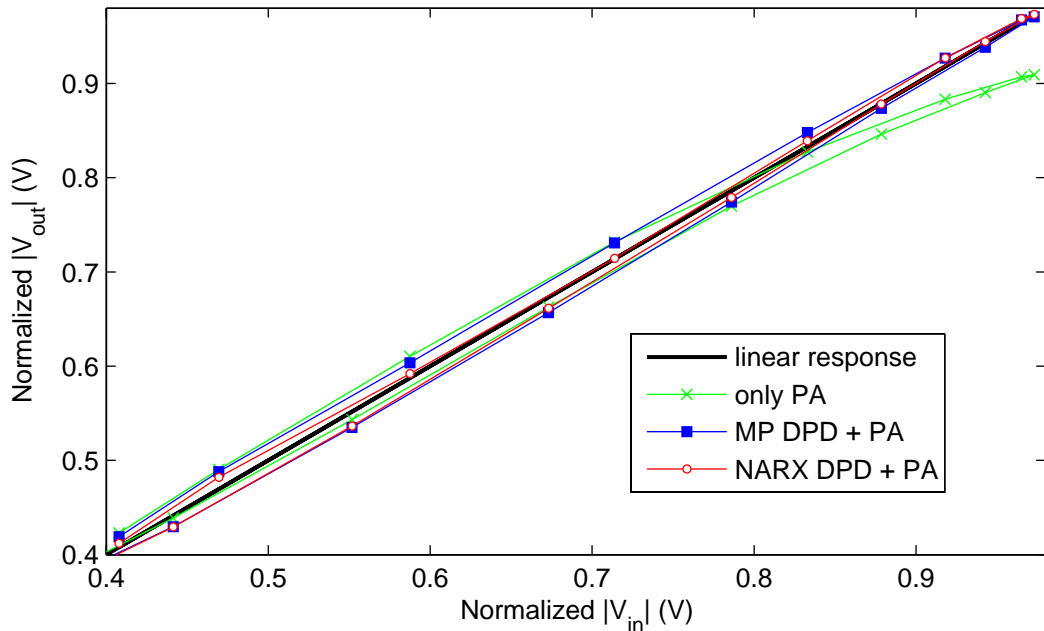


Figure 6.28: Instantaneous AM-AM conversions of the cascade connection of a DPD followed by a PA when the input signal had $PAPR = 3.5$ dB and for an average output power of 36 dBm. The MP PA has $P = 11$ and $M = 2$, while the MP PoD has $P = 7$ and $M = 2$

unpredistorted LDMOS PA meets the required ACPR specifications, previously reported in Subsection 6.4.1, only with a 20 dB of input back-off (IBO). That results in an average PAE of about 3%. The presence of either the MP or NARX DPD models lower to 9 dB the IBO needed to meet the ACPR specifications, resulting in a much larger PAE of about 18%.

6.5 Practical implementation and adaptive strategies

A practical real-time implementation of a DPD scheme requires a dedicated hardware. Among common choices for dedicated hardware suitable for real-time implementation of a DPD scheme are digital signal processings (DSPs), application-specific integrated circuits (ASICs) and field programmable gate arrays (FPGAs) [88]. Additional practical implementation topics need to be addressed [101], for instance the power consumption of the DPD itself. Furthermore, adaptive strategies are often required to sense and compensate for the PA variation with time due temperature changes and component aging [88]. A peculiar characteristic of these adaptive DPD schemes is that they implement a time-invariant DPD model, whose coefficients are updated in times to times, sometimes using information on previously identified coefficients [101], sometimes not [115]. The specific updating policies can be at fixed intervals of time and/or triggered by an environmental or operational condition changing. In other words, such adaptive DPD models involves a two different time scales: one in the order of the coefficient update, and the other in the order of the sampling interval in a real-time implementation of a DPD model. Just the sampling interval that must satisfy the Nyquist rate of the modulation signal is usually written in the DPD model equations and, with respect to this time scale, the model is time-invariant. Such strategy has been reported to work well in adaptive schemes [101], [115] since the variation of the PA characteristics with time is very slowly compared to the sample rate required by the real-time processing of a DPD model, imposed by the bandwidth of the input signal, usually in the order of several MHz. Moreover, available hardware processing speed and required sampling frequency in real-time DPD applications do not make feasible real-time DPD implementing time-varying models. Mixed DSP/FPGA architectures, FPGA in charge of the real-time DPD processing and DSP for the adaptation of the DPD parameters, was reported in [101].

Chapter 7

Conclusions

This thesis was dedicated to the behavioral modeling and digital base-band predistortion of RF PAs. Emphasis was put on model topology selection and parametric identification procedures, both for PA behavioral modeling and DPD purposes. Particular attention was paid to the use of Volterra (or polynomial) models and most of the models implemented in the Matlab software belongs to this class. Non polynomial models have also been investigated in specific parts of the work. In fact, two particular non polynomial models, namely a feedback model and tapped-delay neural networks were also implemented in the Matlab software. Careful validation results for the considered models, based on experimental input-output data measured in RF laboratories and for both PA behavioral modeling and DPD purposes, were presented. Whenever applicable, conclusive analysis were presented together with the respective simulation or experimental results.

The contributions contained in this work include:

- A detailed comparative study of the PA behavioral models that derive from polynomial approximations at RF level, using experimental data measured in an RF laboratory, and focusing on the effectiveness (trade-off between complexity and modeling capabilities) of the different approaches followed to the reduction of the number of parameters in a Volterra series.
- Additional results to further confirm the validity of the low-pass equivalent PA behavioral model with feedback topology, proposed in [4], to describe experimental data measured in a physical RF PA, when an alternative parameter extraction

procedure was adopted.

- A new approach, experimentally validated, to the derivation of PA behavioral models, also applicable to DPD purposes. Specifically, instead of approximating the RF system by a polynomial operator and then looking for the components that fall in the PA pass-band to obtain a low-pass equivalent behavioral model, a direct derivation of a base-band PA behavioral model is proposed in which a polynomial approximation is done at base-band level.
- Experimental validation of the effectiveness of different DPD schemes in improving linearization metrics of RF PAs.

Bibliography

- [1] W. C. Y. Lee, *Mobile Communications Engineering Theory and Applications*. New York: McGraw-Hill, 1998.
- [2] F. H. Raab, P. Asbeck, S. Cripps, P. B. Kenington, Z. B. Popovic, N. Potheccary, J. F. Sevic, and N. O. Sokal, “RF and microwave power amplifier and transmitter technologies – part 1,” *High Frequency Electronics*, vol. 2, no. 3, pp. 22–36, May 2003.
- [3] J. C. Pedro and S. A. Maas, “A comparative overview of microwave and wireless power-amplifier behavioral modeling approaches,” *IEEE Trans. Microw. Theory Tech.*, vol. 53, no. 4, pp. 1150–1163, Apr. 2005.
- [4] T. R. Cunha, J. C. Pedro, and E. G. Lima, “Low-pass equivalent feedback topology for power amplifier modeling,” in *IEEE MTT-S Int. Microwave Symp. Dig.*, Atlanta, GA, Jun. 2008, pp. 1445 –1448.
- [5] J. C. Pedro, N. B. Carvalho, and P. M. Lavrador, “Modeling nonlinear behavior of band-pass memoryless and dynamic systems,” in *IEEE MTT-S Int. Microwave Symp. Dig.*, Philadelphia, PA, Jun. 2003, pp. 2133–2136.
- [6] J. C. Pedro and N. B. Carvalho, *Intermodulation Distortion in Microwave and Wireless Circuits*. Norwood, MA: Artech House, 2003.
- [7] J. H. K. Vuolevi, T. Rahkonen, and J. P. A. Manninen, “Measurement technique for characterizing memory effects in RF power amplifiers,” *IEEE Trans. Microw. Theory Tech.*, vol. 49, no. 8, pp. 1383–1389, Aug. 2001.

- [8] W. Bosch and G. Gatti, “Measurement and simulation of memory effects in pre-distortion linearizers,” *IEEE Trans. Microw. Theory Tech.*, vol. 37, no. 12, pp. 1885–1890, Dec. 1989.
- [9] P. M. Asbeck, H. Kobayashi, M. Ywamoto, G. Hanington, S. Nam, and L. E. Larson, “Augmented behavioral characterization for modeling the nonlinear response of power amplifiers,” in *IEEE MTT-S Int. Microwave Symp. Dig.*, Seattle, WA, Jun. 2002, pp. 135–138.
- [10] P. M. Cabral, J. C. Pedro, and N. B. Carvalho, “Dynamic AM-AM and AM-PM behavior in microwave PA circuits,” in *Proc. Asia-Pacific Microwave Conf.*, Suzhou, China, Dec. 2005.
- [11] ——, “Bias networks impact on the dynamic AM/AM contours in microwave power amplifiers,” in *Proc. 2006 Workshop on Integrated Nonlinear Microwave and Millimeter-wave Circuits*, Aveiro, Portugal, Jan. 2006, pp. 38–41.
- [12] S. Benedetto, E. Biglieri, and R. Daffara, “Modeling and performance evaluation of nonlinear satellite links – a Volterra series approach,” *IEEE Trans. Aerosp. Electron. Syst.*, vol. 15, no. 4, pp. 494–507, Jul. 1979.
- [13] J. B. Minkoff, “Intermodulation noise in solid-state power amplifiers for wideband signal transmission,” in *Proc. 9th AIAA International Communications Satellite System Conference*, 1982, pp. 304–313.
- [14] M. C. Jeruchim, P. Balaban, and K. S. Shanmugan, *Simulation of Communication Systems – Modeling, Methodology, and Techniques*. New York: Kluwer Academic/Plenum Publishers, 2000.
- [15] A. Saleh, “Frequency-independent and frequency-dependent nonlinear models of TWT amplifiers,” *IEEE Trans. Commun.*, vol. 29, no. 11, pp. 1715–1720, Nov. 1981.
- [16] M. T. Abuelma’atti, “Frequency-dependent nonlinear quadrature model for TWT amplifiers,” *IEEE Trans. Commun.*, vol. 32, no. 8, pp. 982–986, Aug. 1984.

- [17] M. Isaksson, D. Wisell, and D. Ronnow, “A comparative analysis of behavioral models for RF power amplifiers,” *IEEE Trans. Microw. Theory Tech.*, vol. 54, no. 1, pp. 348–359, Jan. 2006.
- [18] V. Mathews and G. Sicuranza, *Polynomial Signal Processing*. New York: Wiley, 2000.
- [19] Y. Fang, M. C. E. Yagoub, F. Wang, and Q.-J. Zhang, “A new macromodeling approach for nonlinear microwave circuits based on recurrent neural networks,” *IEEE Trans. Microw. Theory Tech.*, vol. 48, no. 12, pp. 2335–2344, Dec. 2000.
- [20] K. Hornik, M. Stinchcombe, and H. White, “Multilayer feedforward networks are universal approximators,” *Neural Networks*, vol. 2, no. 5, pp. 359–366, Jul. 1989.
- [21] N. Benvenuto, F. Piazza, and A. Uncini, “A neural network approach to data pre-distortion with memory in digital radio systems,” in *Proc. IEEE Int. Conf. Comm. ICC 93*, May 1993, pp. 232–236.
- [22] T. Liu, S. Boumaiza, and F. M. Ghannouchi, “Dynamic behavioral modeling of 3G power amplifiers using real-valued time-delay neural networks,” *IEEE Trans. Microw. Theory Tech.*, vol. 52, no. 3, pp. 1025–1033, Mar. 2004.
- [23] M. Isaksson, D. Wisell, and D. Ronnow, “Nonlinear behavioral modeling of power amplifiers using radial-basis function neural networks,” in *IEEE MTT-S Int. Microwave Symp. Dig.*, Long Beach, CA, Jun. 2005, pp. 1967–1970.
- [24] D. Rumelhart, G. Hinton, and R. J. Williams, “Learning internal representations by error propagation,” in *Parallel Data Processing*, D. Rumelhart and J. McClelland, Eds. Cambridge, MA: The M.I.T. Press, 1986, vol. 1, ch. 8, pp. 318–362.
- [25] S. Chen, C. F. N. Cowan, and P. M. Grant, “Orthogonal least squares learning algorithm for radial basis function networks,” *IEEE Trans. Neural Netw.*, vol. 2, no. 2, pp. 302–309, Mar. 1991.
- [26] H. Leung and S. Haykin, “The complex backpropagation algorithm,” *IEEE Trans. Signal Process.*, vol. 39, no. 9, pp. 2101–2104, Sep. 1991.

- [27] M. Schetzen, “Nonlinear system modeling based on the Wiener theory,” *Proc. IEEE*, vol. 69, no. 12, pp. 1557–1573, Dec. 1981.
- [28] M. J. Korenberg, “Parallel cascade identification and kernel estimation for nonlinear systems,” *Ann. Biomed. Eng.*, vol. 19, no. 4, pp. 429–455, 1991.
- [29] S. Boyd and L. O. Chua, “Fading memory and the problem of approximating nonlinear operators with Volterra series,” *IEEE Trans. Circuits Syst.*, vol. 32, no. 11, pp. 1150–1161, Nov. 1985.
- [30] R. E. Bellman, *Adaptive Control Processes*. Princeton, NJ: Princeton University Press, 1961.
- [31] C. Moler, *Numerical Computing with MATLAB*. Philadelphia: SIAM, 2004.
- [32] N. Wiener, *Nonlinear Problems in Random Theory*. New York: Wiley, 1958.
- [33] W. J. Rugh, *Nonlinear system theory, the Volterra/Wiener approach*. Baltimore: Johns Hopkins University Press, 1981.
- [34] P. M. Lavrador, J. C. Pedro, and N. B. Carvalho, “A new Volterra series based orthogonal behavioral model for power amplifiers,” in *Proc. Asia-Pacific Microwave Conf.*, Suzhou, China, Dec. 2005.
- [35] C. Siviero, P. M. Lavrador, and J. C. Pedro, “A frequency domain extraction procedure of low-pass equivalent behavioural models of microwave PAs,” in *Proc. 1st European Microwave Integrated Circuits Conf.*, Manchester, UK, 2006, pp. 253–256.
- [36] J. C. Pedro, P. M. Lavrador, and N. B. Carvalho, “A formal procedure for microwave power amplifier behavioral modeling,” in *IEEE MTT-S Int. Microwave Symp. Dig.*, San Francisco, CA, Jun. 2006, pp. 848–851.
- [37] V. Z. Marmarelis, “Identification of nonlinear biological systems using Laguerre expansions of kernels,” *Ann. Biomed. Eng.*, vol. 21, no. 6, pp. 573–589, Nov. 1993.
- [38] A. Zhu and T. J. Brazil, “RF power amplifier behavioral modeling using Volterra expansion with Laguerre functions,” in *IEEE MTT-S Int. Microwave Symp. Dig.*, Long Beach, CA, Jun. 2005, pp. 963–966.

- [39] M. Isaksson and D. Ronnow, “A Kautz-Volterra behavioral model for RF power amplifiers,” in *IEEE MTT-S Int. Microwave Symp. Dig.*, San Francisco, CA, Jun. 2006, pp. 485–488.
- [40] M. J. Korenberg, “Statistical identification of parallel cascades of linear and non-linear systems,” in *IFAC Symp. Ident. Sys. Param. Est.*, 1982, pp. 669–674.
- [41] I. W. Hunter and M. J. Korenberg, “The identification of nonlinear biological systems: Wiener and Hammerstein cascade models,” *Biol. Cybern.*, vol. 55, no. 2–3, pp. 135–144, Nov. 1986.
- [42] H. Ku, M. D. McKinley, and J. S. Kenney, “Quantifying memory effects in RF power amplifiers,” *IEEE Trans. Microw. Theory Tech.*, vol. 50, no. 12, pp. 2843–2849, Dec. 2002.
- [43] V. Z. Marmarelis and X. Zhao, “Volterra models and three-layer perceptrons,” *IEEE Trans. Neural Netw.*, vol. 8, no. 6, pp. 1421–1433, Nov. 1997.
- [44] M. Asdente, M. C. Pascucci, and A. M. Ricca, “Modified Volterra-Wiener functional method for highly nonlinear systems,” *Alta Frequenza*, vol. 45, no. 12, pp. 756–760, Dec. 1976.
- [45] F. Filicori, G. Vannini, and V. A. Monaco, “A nonlinear integral model of electron devices for HB circuit analysis,” *IEEE Trans. Microw. Theory Tech.*, vol. 40, no. 7, pp. 1456–1465, Jul. 1992.
- [46] D. Mirri, F. Filicori, G. Iuculano, and G. Pasini, “A non-linear dynamic model for performance analysis of large-signal amplifiers in communication systems,” in *IEEE Instrumentation and Measurement Technology Conf.*, Venice, Italy, May 1999, pp. 193–197.
- [47] E. Ngoya, N. L. Gallou, J. M. Nébus, H. Burêt, and P. Reig, “Accurate RF and microwave system level modeling of wideband nonlinear circuits,” in *IEEE MTT-S Int. Microwave Symp. Dig.*, Boston, MA, Jun. 2000, pp. 79–82.

- [48] N. L. Gallou, E. Ngoya, H. Berêt, D. Barataud, and J. M. Nébus, “An improved behavioral modeling technique for high power amplifiers with memory,” in *IEEE MTT-S Int. Microwave Symp. Dig.*, Phoenix, AZ, May 2001, pp. 983–986.
- [49] A. Zhu, J. C. Pedro, and T. J. Brazil, “Dynamic deviation reduction-based Volterra behavioral modeling of RF power amplifiers,” *IEEE Trans. Microw. Theory Tech.*, vol. 54, no. 12, pp. 4323–4332, Dec. 2006.
- [50] K. S. Narendra and P. G. Gallman, “An iterative method for the identification of nonlinear systems using a Hammerstein model,” *IEEE Trans. Autom. Control*, vol. 11, no. 3, pp. 546–550, Jul. 1966.
- [51] D. T. Westwick and R. E. Kearney, “Separable least squares identification of nonlinear Hammerstein models: Application to stretch reflex dynamics,” *Ann. Biomed. Eng.*, vol. 29, no. 8, pp. 707–718, Aug. 2001.
- [52] G. Chrisikos, C. Clark, A. Moulthrop, M. Muha, and C. Silva, “A nonlinear ARMA model for simulating power amplifiers,” in *IEEE MTT-S Int. Microwave Symp. Dig.*, Baltimore, MD, Jun. 1998, pp. 733–736.
- [53] C. J. Clark, G. Chrisikos, M. S. Muha, A. A. Moulthrop, and C. P. Silva, “Time-domain envelope measurement technique with application to wideband power amplifier modeling,” *IEEE Trans. Microw. Theory Tech.*, vol. 46, no. 12, pp. 2531 – 2540, Dec. 1998.
- [54] M. S. Muha, C. J. Clark, A. Moulthrop, and C. P. Silva, “Validation of power amplifier nonlinear block models,” in *IEEE MTT-S Int. Microwave Symp. Dig.*, Anaheim, CA, Jun. 1999, pp. 759–762.
- [55] T. Liu, S. Boumaiza, M. Helaoui, H. B. Nars, and F. M. Ghannouchi, “Behavior modeling procedure of wideband RF transmitters exhibiting memory effects,” in *IEEE MTT-S Int. Microwave Symp. Dig.*, Long Beach, CA, Jun. 2005, pp. 1983–1986.
- [56] H. Poza, Z. Sarkozy, and H. Berger, “A wideband data link computer simulation model,” in *Proc. NAECON Conf.*, Dayton, OH, Jun. 1975, pp. 71–78.

- [57] C. P. Silva, C. J. Clark, A. Moulthrop, and M. S. Muha, “Optimal-filter approach for nonlinear power amplifier modeling and equalization,” in *IEEE MTT-S Int. Microwave Symp. Dig.*, Boston, MA, USA, Jun. 2000, pp. 437–440.
- [58] J. Dennis Jr., “Nonlinear least-squares,” in *State of the Art in Numerical Analysis: Conference Proceedings*, D. A. H. Jacobs, Ed. London: Academic Press, 1977, pp. 269–312.
- [59] G. H. Golub and V. Pereyra, “The differentiation of pseudo-inverses and nonlinear least squares problems whose variables separate,” *SIAM J. Numer. Anal.*, vol. 10, no. 2, pp. 413–432, Apr. 1973.
- [60] J. Sjoberg and M. Viberg, “Separable non-linear least-squares minimization – possible improvements for neural net fitting,” in *Proc. IEEE Wkshp Neural Nets Sig. Process.*, Sep. 1997, pp. 345–354.
- [61] *ADS Ptolemy Simulation*, Agilent Technologies, Inc., Palo Alto, CA, Jan. 2007.
- [62] *Visual System Simulator System Block Catalog*, Applied Wave Research, Inc., El Segundo, CA, Jul. 2006, version 7.
- [63] P. Stoica, “On the convergence of an iterative algorithm used for Hammerstein system identification,” *IEEE Trans. Autom. Control*, vol. 26, no. 4, pp. 967–969, Aug. 1981.
- [64] H. C. Yuan, D. T. Westwick, E. P. Ingenito, K. R. Lutchen, and B. Suki, “Parametric and nonparametric nonlinear system identification of lung tissue strip mechanics,” *Ann. Biomed. Eng.*, vol. 27, no. 4, pp. 548–562, Jul. 1999.
- [65] J. Kim and K. Konstantinou, “Digital predistortion of wideband signals based on power amplifier model with memory,” *Electron. Lett.*, vol. 37, no. 23, pp. 1417–1418, Nov. 2001.
- [66] M. S. Heutmaker, E. Wu, and J. R. Welch, “Envelope distortion models with memory improve the prediction of spectral regrowth for some RF amplifiers,” in *48rd ARFTG Conf. Dig.*, Clearwater, FL, Dec. 1996, pp. 10–15.

- [67] H. Ku and J. S. Kenney, “Behavioral modeling of nonlinear RF power amplifiers considering memory effects,” *IEEE Trans. Microw. Theory Tech.*, vol. 51, no. 12, pp. 2495–2504, Dec. 2003.
- [68] M. Isaksson and D. Wisell, “Extension of the Hammerstein model for power amplifier applications,” in *63rd ARFTG Conf. Dig.*, Fort Worth, TX, Jun. 2004, pp. 131–137.
- [69] A. Soury, E. Ngoya, and J. M. Nébus, “A new behavioral model taking into account nonlinear memory effects and transient behaviors in wideband SSPAs,” in *IEEE MTT-S Int. Microwave Symp. Dig.*, Seattle, WA, Jun. 2002, pp. 853–856.
- [70] A. Soury, E. Ngoya, J. M. Nébus, and T. Reveyrand, “Measurement based modeling of power amplifiers for reliable design of modern communication systems,” in *IEEE MTT-S Int. Microwave Symp. Dig.*, Philadelphia, PA, Jun. 2003, pp. 795–798.
- [71] A. Walker, M. Steer, K. Gard, and K. Gharaibeh, “Multi-slice behavioral model of RF systems and devices,” in *Proc. IEEE Radio Wireless Conf.*, Atlanta, GA, Sep. 2004, pp. 71–74.
- [72] T. R. Cunha, J. C. Pedro, P. M. Cabral, and A. Zhu, “General nonlinear feed-forward RF model for power amplifiers,” in *IEEE MTT-S Int. Microwave Symp. Dig.*, Honolulu, HI, Jun. 2007, pp. 2027–2030.
- [73] C. Crespo-Cadenas, J. Reina-Tosina, and M. J. Madero-Ayora, “Volterra behavioral model for wideband RF amplifiers,” *IEEE Trans. Microw. Theory Tech.*, vol. 55, no. 3, pp. 449–457, Mar. 2007.
- [74] P. Draxler, I. Langmore, T. P. Hung, and P. M. Asbeck, “Time domain characterization of power amplifiers with memory effects,” in *IEEE MTT-S Int. Microwave Symp. Dig.*, Philadelphia, PA, Jun. 2003, pp. 803–806.
- [75] M. B. Steer, K. Gard, K. Gharaibeh, A. Walker, and W. Jang, “Deterministic and stochastic behavioral modeling of RF front ends,” in *Proc. 2006 Workshop on Integrated Nonlinear Microwave and Millimeter-wave Circuits*, Aveiro, Portugal, Jan. 2006, pp. 150–153.

- [76] D. Wisell and M. Isaksson, “Derivation of a behavioral RF power amplifier model with low normalized mean-square error,” in *Proc. 37th European Microwave Conf.*, Munich, Germany, Oct. 2007, pp. 485–488.
- [77] A. Zhu, J. C. Pedro, and T. R. Cunha, “Pruning the Volterra series for behavioral modeling of power amplifiers using physical knowledge,” *IEEE Trans. Microw. Theory Tech.*, vol. 55, no. 5, pp. 813–821, May 2007.
- [78] T. R. Cunha, J. C. Pedro, and P. M. Cabral, “Design of a power-amplifier feed-forward RF model with physical knowledge considerations,” *IEEE Trans. Microw. Theory Tech.*, vol. 55, no. 12, pp. 2747–2756, Dec. 2007.
- [79] A. S. Householder, *Principles of Numerical Analysis*. New York: McGraw-Hill, 1953.
- [80] L. Ding and G. T. Zhou, “Effects of even-order nonlinear terms on predistortion linearization,” in *Proc. 10th IEEE DSP Workshop*, Pine Mountain, GA, Oct. 2002, pp. 1–6.
- [81] ——, “Effects of even-order nonlinear terms on power amplifier modeling and predistortion linearization,” *IEEE Trans. Veh. Technol.*, vol. 53, no. 1, pp. 156–162, Jan. 2004.
- [82] N. M. Blachman, “Band-pass nonlinearities,” *IEEE Trans. Inf. Theory*, vol. 10, no. 2, pp. 162–164, Apr. 1964.
- [83] J. C. Mason and D. C. Handscomb, *Chebyshev Polynomials*. Boca Raton, FL: Chapman & Hall/CRC, 2002.
- [84] N. M. Blachman, “Detectors, bandpass nonlinearities, and their optimization: Inversion of the Chebyshev transform,” *IEEE Trans. Inf. Theory*, vol. 17, no. 4, pp. 398–404, Jul. 1971.
- [85] L. Ljung, *System Identification: Theory for the User*. Englewood Cliffs, NJ: Prentice Hall, 1999.

- [86] Y.-M. Zhu, “Generalized sampling theorem,” *IEEE Trans. Circuits Syst. II*, vol. 39, no. 8, pp. 587–588, Aug. 1992.
- [87] W. A. Frank, “Sampling requirements for Volterra system identification,” *IEEE Signal Process. Lett.*, vol. 3, no. 9, pp. 266–268, Sep. 1996.
- [88] P. B. Kenington, *High Linearity RF Amplifier Design*. Norwood, MA: Artech House, 2000.
- [89] D. Morgan, Z. Ma, J. Kim, M. Zierdt, and J. Pastalan, “A generalized memory polynomial model for digital predistortion of RF power amplifiers,” *IEEE Trans. Signal Process.*, vol. 54, no. 10, pp. 3852–3860, Oct. 2006.
- [90] L. Ding, Z. Ma, D. Morgan, M. Zierdt, and J. Pastalan, “A least-squares/Newton method for digital predistortion of wideband signals,” *IEEE Trans. Commun.*, vol. 54, no. 5, pp. 833–840, May 2006.
- [91] O. Hammi, F. Ghannouchi, and B. Vassilakis, “A compact envelope-memory polynomial for RF transmitters modeling with application to baseband and RF-digital predistortion,” *IEEE Microw. Wireless Compon. Lett.*, vol. 18, no. 5, pp. 359 –361, May 2008.
- [92] Z.-Y. He, J.-H. Ge, S.-J. Geng, and G. Wang, “An improved look-up table predistortion technique for HPA with memory effects in OFDM systems,” *IEEE Trans. Broadcast.*, vol. 52, no. 1, pp. 87–91, Mar. 2006.
- [93] B. Ai, Z.-X. Yang, C.-Y. Pan, S.-G. Tang, and T.-T. Zhang, “Analysis on LUT based predistortion method for HPA with memory,” *IEEE Trans. Broadcast.*, vol. 53, no. 1, pp. 127–131, Mar. 2007.
- [94] P. Jardin and G. Baudoin, “Filter look up table method for power amplifiers linearization,” *IEEE Trans. Veh. Technol.*, vol. 56, no. 3, pp. 1076–1087, May 2007.
- [95] T. Liu, S. Boumaiza, and F. M. Ghannouchi, “Augmented Hammerstein predistorter for linearization of broad-band wireless transmitters,” *IEEE Trans. Microw. Theory Tech.*, vol. 54, no. 4, pp. 1340–1349, Apr. 2006.

- [96] O. Hammi, F. Ghannouchi, S. Boumaiza, and B. Vassilakis, “A data-based nested LUT model for RF power amplifiers exhibiting memory effects,” *IEEE Microw. Wireless Compon. Lett.*, vol. 17, no. 10, pp. 712 –714, Oct. 2007.
- [97] N. Safari, T. Roste, P. Fedorenko, and J. Kenney, “An approximation of volterra series using delay envelopes, applied to digital predistortion of RF power amplifiers with memory effects,” *IEEE Microw. Wireless Compon. Lett.*, vol. 18, no. 2, pp. 115 –117, Feb. 2008.
- [98] N. Safari, P. Fedorenko, J. Kenney, and T. Roste, “Spline-based model for digital predistortion of wide-band signals for high power amplifier linearization,” in *IEEE MTT-S Int. Microwave Symp. Dig.*, Atlanta, GA, Jun. 2008, pp. 1441 –1444.
- [99] A. Zhu, P. J. Draxler, C. Hsia, T. J. Brazil, D. F. Kimball, and P. M. Asbeck, “Digital predistortion for envelope-tracking power amplifiers using decomposed piecewise Volterra series,” *IEEE Trans. Microw. Theory Tech.*, vol. 56, no. 10, pp. 2237–2247, Oct. 2008.
- [100] F. H. Raab, P. Asbeck, S. Cripps, P. B. Kenington, Z. B. Popovic, N. Potheccary, J. F. Sevic, and N. O. Sokal, “RF and microwave power amplifier and transmitter technologies – part 3,” *High Frequency Electronics*, vol. 2, no. 5, pp. 34 –48, Sep. 2003.
- [101] P. Gilabert, A. Cesari, G. Montoro, and J. M. Bertran, E. and Dilhac, “Multi-lookup table FPGA implementation of an adaptive digital predistorter for linearizing RF power amplifiers with memory effects,” *IEEE Trans. Microw. Theory Tech.*, vol. 56, no. 2, pp. 372–384, Feb. 2008.
- [102] R. González-Cardel, M. F. and Díaz-Uribe, “An analysis on the inversion of polynomials,” *Rev. Mex. Fís.*, vol. E52, no. 2, pp. 163–171, Dec. 2006.
- [103] G. Montoro, E. Gilabert, P. L. and Bertran, A. Cesari, and D. D. Silveira, “A new digital predictive predistorter for behavioral power amplifier linearization,” *IEEE Microw. Wireless Compon. Lett.*, vol. 17, no. 6, pp. 448–450, Jun. 2007.

- [104] M. Schetzen, “Theory of p th-order inverses of nonlinear systems,” *IEEE Trans. Circuits Syst.*, vol. CAS-23, no. 5, pp. 285–291, May 1976.
- [105] Y. H. Lim, Y. S. Cho, I. W. Cha, and D. H. Youn, “An adaptive nonlinear prefilter for compensation of distortion in nonlinear systems,” *IEEE Trans. Signal Process.*, vol. 46, no. 6, pp. 1726–1730, Jun. 1998.
- [106] G. Baudoin and P. Jardin, “Adaptive polynomial pre-distortion for linearization of power amplifiers in wireless communications and WLANS,” in *Proc. IEEE International Conference on Trends in Communications*, Bratislava, Slovakia, Jul. 2001, pp. 157–160.
- [107] C. Eun and E. J. Powers, “A new Volterra predistorter based on the indirect learning architecture,” *IEEE Trans. Signal Process.*, vol. 45, no. 1, pp. 223–227, Jan. 1997.
- [108] R. Marsalek, P. Jardin, and G. Baudoin, “From post-distortion to pre-distortion for power amplifiers linearization,” *IEEE Commun. Lett.*, vol. 7, no. 7, pp. 308–310, Jul. 2003.
- [109] D. Zhou and V. E. DeBrunner, “Novel adaptive nonlinear predistorters based on the direct learning algorithm,” *IEEE Trans. Signal Process.*, vol. 55, no. 1, pp. 120–133, Jan. 2007.
- [110] H. W. Kang, Y. S. Cho, and D. H. Youn, “On compensating nonlinear distortions of an OFDM system using an efficient adaptive predistorter,” *IEEE Trans. Commun.*, vol. 47, no. 4, pp. 522–526, Apr. 1999.
- [111] V. Camarchia, P. Colantonio, S. Donati Guerrieri, R. Giofrè, E. G. Lima, M. Pirola, and R. Quaglia, “Base-band predistortion linearization scheme of high efficiency power amplifiers for wireless applications,” in *Proc. 2008 Workshop on Integrated Nonlinear Microwave and Millimeter-wave Circuits*, Malaga, Spain, Nov. 2008.
- [112] A. Zhu and T. J. Brazil, “An adaptive Volterra predistorter for the linearization of RF high power amplifiers,” in *IEEE MTT-S Int. Microwave Symp. Dig.*, Seattle, WA, Jun. 2002, pp. 461–464.

- [113] L. Ding, R. Raich, and G. T. Zhou, “A Hammerstein predistortion linearization design based on the indirect learning architecture,” in *Proc. IEEE Int. Conf. Acoustics, Speech, Signal Processing*, Orlando, FL, May 2002, pp. 2689–2692.
- [114] L. Ding, G. T. Zhou, D. Morgan, Z. Ma, J. Kenney, J. Kim, and C. Giardina, “A robust digital baseband predistorter constructed using memory polynomials,” *IEEE Trans. Commun.*, vol. 52, no. 1, pp. 159 –165, Jan. 2004.
- [115] A. Zhu, P. J. Draxler, J. J. Yan, T. J. Brazil, D. F. Kimball, and P. M. Asbeck, “Open-loop digital predistorter for RF power amplifiers using dynamic deviation reduction-based Volterra series,” *IEEE Trans. Microw. Theory Tech.*, vol. 56, no. 7, pp. 1524–1534, Jul. 2008.
- [116] J. Tsimbinos and K. Lever, “Input Nyquist sampling suffices to identify and compensate nonlinear systems,” *IEEE Trans. Signal Process.*, vol. 46, no. 10, pp. 2833–2837, Oct. 1998.
- [117] E. Cipriani, P. Colantonio, and R. Giannini, F.and Giofrè, “A second harmonic tuned power amplifier in LDMOS technology,” in *Prod. XVII International Conference on Microwaves, Radar and Wireless Communications*, Wroclaw, Poland, May 2008, pp. 519–522.